

UC Berkeley

UC Berkeley Electronic Theses and Dissertations

Title

Quantifying Radiative Heat Transfer Scaling Distortions: System Code Development and a Scaling Methodology for Fluoride-Salt-Cooled High-Temperature Reactors

Permalink

<https://escholarship.org/uc/item/6p78d8d1>

Author

Johnson, Ishak

Publication Date

2022

Peer reviewed|Thesis/dissertation

Quantifying Radiative Heat Transfer Scaling Distortions: System Code Development and a
Scaling Methodology for Fluoride-Salt-Cooled High-Temperature Reactors

by

Ishak Mudrikah Banin Johnson

A dissertation submitted in partial satisfaction of the

requirements for the degree of

Doctor of Philosophy

in

Nuclear Engineering

in the

Graduate Division

of the

University of California, Berkeley

Committee in charge:

Professor Per F. Peterson, Chair
Assistant Professor Raluca Scarlat
Associate Professor Massimiliano Fratoni
Professor of the Graduate School Ralph Greif

Spring 2022

Quantifying Radiative Heat Transfer Scaling Distortions: System Code Development and a
Scaling Methodology for Fluoride-Salt-Cooled High-Temperature Reactors

Copyright 2022

by

Ishak Mudrikah Banin Johnson

Abstract

Quantifying Radiative Heat Transfer Scaling Distortions: System Code Development and a Scaling Methodology for Fluoride-Salt-Cooled High-Temperature Reactors

by

Ishak Mudrikah Banin Johnson

Doctor of Philosophy in Nuclear Engineering

University of California, Berkeley

Professor Per F. Peterson, Chair

Radiative heat transfer (radHT) is the reason we exist. For life, we need energy, and for that energy, we turn to the sun. Thermal radiation, another term for radHT, simply provides the means to transfer the sun's energy to us. On Earth, we interact with radHT as well — we bask in the heat of a fire from across the room, we see metals glow red hot, we feel the evening warmth from buildings heated by the day as we walk past, and we see sunbeams through water turn blue and eventually peter out. All of these examples, both earthly and stellar, are driven by the transfer of energy via photons.

The amount of thermal radiation emitted by an object scales rapidly (to the fourth power) with temperature — the reason why the fire across the room feels hotter than the building we pass by, loosely speaking. The proportion of radiation a body interacts with or absorbs varies as well — the reason why sunlight travels mostly unabated through the atmosphere but attenuates noticeably in water. These two factors, temperature dependence and proportional interaction of various media, are important to consider when analyzing radHT in any system.

Of particular interest to this dissertation, is the consideration of these two factors within heat transfer analysis for nuclear reactors. The system temperatures and participating media interaction of conventional light water reactors are too low to render thermal radiation a significant heat transfer mechanism, less extraordinary circumstances. However, advanced reactors utilize significantly higher temperatures and non-water coolants that have the potential for increased radiative interaction. The fluoride-salt-cooled high-temperature reactor (FHR) is one such advanced reactor concept.

This dissertation addresses the impacts of radHT in FHRs through two means, introduced and contextualized by [Chapter 1](#). On one hand, FHR development requires scaled-down experiments, in which low temperatures and surrogate fluids render radHT insignificant. The proportional impact of thermal radiation will be distorted compared to the prototypical re-

actor. [Chapter 2](#) presents a scaling methodology to scale the system-level thermal-hydraulic behavior of FHR systems, with particular emphasis on quantifying radHT distortions. On the other hand, thermal radiation will serve as an important heat transfer mechanism in some full-scale FHR scenarios. Thus, radHT modeling must be included in FHR safety analyses to determine if thermal radiation plays a significant heat transfer role, and requires further consideration, or is low enough to be neglected. [Chapter 3](#) details the development process of radHT simulation capabilities for System Analysis Module (SAM), a system-level thermal hydraulics code being developed for advanced reactor modeling. [Chapter 4](#) then ties together the work conducted in [Chapters 2](#) and [3](#) by laying out a proposed demonstration of the FHR scaling methodology and utilizing system-level modeling for radHT distortion quantification. The FHR scaling methodology and SAM radHT simulation tools presented in this dissertation can be used to address the impact of radHT in FHR systems. It is my hope this work will be utilized to facilitate FHR development and help realize the dream of building FHRs for clean energy production.

To Mother Nature.
By the power of atoms,
may her rage be quenched.

Acknowledgments

Out of all parts of my dissertation, this is the one I've dreaded writing the most. When I get to the end of this page, I'll conclude my time at UC Berkeley — a time that's held many of my greatest experiences and facilitated much personal growth, all with some of the best people I've had the pleasure to know. Furthermore, there's no way my writing can do justice to the support I've received, nor to all the folks who made it happen. Regardless, I wouldn't've made it this far without those others, so I must try.

First and foremost, the unconditional position of support from my immediate family — Mom, Dad, Grandma — is the foundation for my success. Your unabated backing, whether I was pursuing music performance or nuclear energy, meant the world to me. The support and encouragement from other Stillwater family has been just as important. Tok Zah (my other grandma) and Tok Allen, Auntie Vickie and Auntie Marie, thank you for everything. You've been there since the beginning, and I wouldn't be who I am without you. To the Lambert Family, thank you for taking me in, for all you've taught me, and for sharing so many experiences with me.

Before moving to Berkeley, I was just as passionate about nuclear energy as I am now. However, I must credit my adviser, Dr. Peterson, for introducing me to the specific technology I've been so passionate about since. Moreover, you enabled me to research my favorite technical topic — something I don't take for granted. Thank you for guiding me towards these topics, thank you for sharing your enthusiasm for thermal hydraulics, and thank you for encouraging me while still showing such support and patience along the way. I benefited immensely from interactions with other professors as well. In the Berkeley Nuclear Department, namely Max and Raluca. You were always willing and available to help. Thank you for caring and taking time out of your schedules to give such meaningful, valuable advice. Dr. Greif, the pandemic robbed me of many discussions I wished we had. Nevertheless, thank you for your kind words of encouragement throughout. Beyond Berkeley, I gained an incredible mentor in Ling Zou during my internship at Argonne. Your advice and guidance has been a critical factor in enabling some of my most meaningful academic accomplishments. I'm still amazed at your willingness to hold those impromptu mini-lessons in your office to answer any question I had. Thank you for teaching me so much.

Being part of the Thermal Hydraulics Lab has been a truly special experience. Our collaborative atmosphere is something I've continually highlighted as a key contributor to my success at Berkeley. I've enjoyed the camaraderie in 4118 even more than the coffee. Chris, Clara, Dane, James, Omar, Shane, Theo, thank you for your friendship and thank you for making the Lab such a great place to be. I've had some truly amazing friendships in Berkeley. I cannot possibly hope to list all those here, and some others I've already mentioned. I'll simply name those few so crucial to my experience here, I couldn't've made it without: Joey, Lee Van, Maria, Zahmiria. A "thank you" doesn't do it justice.

Contents

Contents	iii
List of Figures	vi
List of Tables	viii
Nomenclature	ix
1 Radiative Heat Transfer Distortion between FHRs and their Experiments and its Impact on Scaled Heat Transfer Behavior	1
1.1 Scaled Experiments for FHRs	3
1.1.1 Scaling analysis theory pertinent to FHR experiments	6
1.2 Radiative Heat Transfer in FHRs and their Experiments	8
1.2.1 Radiative heat transfer physics pertinent to FHRs	8
1.2.2 Role of thermal radiation in FHR heat transfer	16
1.2.3 Role of thermal radiation in scaled experimental heat transfer	19
1.3 Quantification of Radiative Heat Transfer Scaling Distortion for FHRs	20
2 A System-Level Scaling Methodology for FHRs with an Emphasis on Radiative Heat Transfer Scaling Distortion Quantification	21
2.1 Previous Methodologies for Nuclear Reactor Scaling Analysis	22
2.1.1 LWR scaling methodologies	22
2.1.2 FHR scaling methods	24
2.1.3 An FHR scaling methodology for radiative heat transfer distortion	25
2.2 Fluid Momentum Scaling Parameters for Forced Circulation Fluid Flow	26
2.2.1 Fully-derived ND momentum equation for forced circulation fluid flow	34
2.2.2 Component scaling considerations for forced circulation fluid flow	36
2.2.3 Integral system scaling considerations for forced circulation fluid flow	37
2.2.4 Characteristic parameters for forced circulation fluid flow scaling	37
2.3 Fluid Momentum Scaling Parameters for Natural Circulation Fluid Flow	39
2.3.1 Fully-derived ND momentum equation for natural circulation fluid flow	43
2.3.2 Component scaling considerations for natural circulation fluid flow	44

2.3.3	Integral system scaling considerations for natural circulation fluid flow	44
2.3.4	Characteristic parameters for natural circulation fluid flow scaling . .	45
2.4	Fluid Energy Scaling Parameters	53
2.4.1	Fully-derived ND energy equation for fluid energy	59
2.4.2	Component scaling considerations for fluid energy	61
2.4.3	Integral system scaling considerations for fluid energy	65
2.4.4	Characteristic parameters for fluid energy scaling	66
2.5	Solid-Structure Energy Scaling Parameters	66
2.5.1	Fully-derived ND energy equation for solid-structure energy	68
2.5.2	Component scaling considerations for solid-structure energy	70
2.5.3	Alternative solid-structure energy scaling parameters	72
2.5.4	Characteristic parameters for solid-structure energy scaling	73
2.6	A Three-Step Scaling Methodology for FHRs	75
2.6.1	Scaling methodology framework	76
2.6.2	Scaling relations for scaled system design	77
2.6.3	Use of inertia numbers in transient scaling	82
2.6.4	Distortions between FHRs and their scaled experiments	84
2.6.5	Residence time scaling distortion	85
2.6.6	Parasitic heat loss scaling distortion	87
2.6.7	Thermal inertia scaling distortion	88
2.6.8	Radiative heat transfer scaling distortion	89
2.7	Quantifying Radiative Heat Transfer Scaling Distortion	90
2.8	This Scaling Methodology and FHR Development	93
3	The Development of Radiative Heat Transfer Simulation Capabilities for System Analysis Module	94
3.1	System Codes	95
3.1.1	SAM and its need for radiative heat transfer modeling	96
3.1.2	Previous radiative heat transfer modeling in system codes	99
3.1.3	Other prominent radiative heat transfer modeling methods	101
3.2	SAM Radiative Heat Transfer Code Development	102
3.2.1	Adapting the net radiation method for SAM	104
3.2.2	Code framework considerations for adapting Rad++ to SAM	108
3.2.3	Deriving transmittance calculations for RadiativeHeatTransfer	112
3.2.4	Enabling RadiativeHeatTransfer compatibility with SAM components	133
3.2.5	Restructuring RadiativeHeatTransfer with a userObject	145
3.2.6	Developing RadiativeHeatTransfer rate postProcessors	148
3.3	RadiativeHeatTransfer Verification Studies	154
3.4	How to Use RadiativeHeatTransfer	161
3.5	SAM Radiative Heat Transfer Simulation Capabilities	163

4	The Mk.II Initiative or: System-Level Modeling of Scaled-Up FHRs to Demonstrate the Three-Step FHR Scaling Methodology	165
4.1	The Mk.II Initiative	166
4.2	CIET Scaling Analysis for the Mk.II	167
4.2.1	Description of SAM models	167
4.2.2	CIET primary loop forced circulation scaling analysis	172
4.2.3	CIET DRACS loop natural circulation scaling analysis	174
4.3	Scaling Up to a Mk.II Design	176
4.3.1	Mk.II primary loop	177
4.3.2	Mk.II DRACS loop	179
4.4	Realizing the Mk.II Initiative	181
4.5	Final Words	183
	Bibliography	185

List of Figures

1.1	Diagram of the Mk.I FHR primary loop	2
1.2	Mk.I FHR core vessel size comparison	4
1.3	CIET heater section size comparison	5
1.4	Analogy for idealized scaling analysis	6
1.5	Analogy for realistic scaling analysis with distortions	7
1.6	Simplified radiative behavior of a grey surface	9
1.7	Bay Area views exemplifying participating and non-participating media	10
1.8	Radiative behavior of a grey participating medium	12
1.9	Blackbody emission spectra for FHR and LWR temperatures	13
1.10	Absorption coefficient of water across the visible spectrum	14
1.11	Spectral emissive power from the sun received by the earth	15
1.12	Generic absorption behavior of halide salts	18
2.1	Differential friction pressure drop in axial flow	27
2.2	Non-dimensional convection term values in the CIET \dot{Q} -step experiment	31
2.3	Idealized ND pressure term dictating the forced circulation height-scale	39
2.4	Idealized ND buoyancy term dictating the natural circulation height-scale	46
2.5	Impact of PHL on natural circulation velocity-scale	52
2.6	Three-step FHR scaling methodology framework	77
3.1	Radial slice of the Mk.I FHR downcomer	97
3.2	Two-body constraint infographic	109
3.3	Three-body constraint infographic	110
3.4	RadiativeHeatTransfer code framework	111
3.5	Radiative path length in a pipe demonstrating axial temperature dependence	115
3.6	Two-dimensional Lambert cosine law	117
3.7	Energy emitted from $d\ell_i$ towards $d\ell_j$	118
3.8	Cylinder radiative enclosure cross-section	119
3.9	Dissection of the Cylinder radiative geometry	120
3.10	Cylinder transmittance contribution per emission angle	121
3.11	Cylinder transmittance comparison with 3D mean beam length method	122
3.12	Annulus radiative enclosure cross-section	123
3.13	Dissection of the Annulus radiative geometry for outer- to outer-surface transfer	124

3.14	Dissection of the Annulus radiative geometry for inner- to outer-surface transfer	126
3.15	Annulus transmittance contribution per emission angle	128
3.16	Annulus transmittance comparison with 3D mean beam length method	129
3.17	Convergence of the Cylinder \bar{t}_{11} trapezoidal integration approximation	131
3.18	Convergence of the Annulus \bar{t}_{12} trapezoidal integration approximation	132
3.19	RadiativeHeatTransfer-PBHeatExchanger compatibility testing geometry	135
3.20	PBHeatExchanger simulation with convection	137
3.21	PBHeatExchanger-RadiativeHeatTransfer simulation with bug	139
3.22	PBHeatExchanger-RadiativeHeatTransfer simulation corrected	141
3.23	PBHeatExchanger-RadiativeHeatTransfer compatibility testing differences	142
3.24	RadiativeHeatTransfer-PBCoreChannel compatibility testing geometry	143
3.25	PBCoreChannel-RadiativeHeatTransfer compatibility testing differences	144
3.26	RadiativeHeatTransfer userObject code framework	147
3.27	RadHTHeatRemovalRate verification testing geometry	152
3.28	Concentric pipes energy balance test geometry	155
3.29	Semi-infinite slab test geometry	156
3.30	Semi-infinite slab test results	158
3.31	Pipe heating and cooling test wall temperature profile	159
3.32	Pipe heating and cooling test results	160
3.33	RadiativeHeatTransfer geometry options	161
4.1	CIET primary loop flow path and characteristic parameters	168
4.2	CIET power step change experiment data and SAM validation test results	169
4.3	CIET natural circulation loop flow paths and characteristic parameters	170
4.4	DHX-DRACS coupled-loop experiment natural circulation development	171
4.5	12 unit Mk.I FHR nuclear power plant reference site	184

List of Tables

1.1	Prototypical and experimental design characteristics for FHR scaling	3
2.1	Numerical evidence for neglecting the convection term	32
2.2	Numerical evidence for refraining from the Boussinesq approximation	33
2.3	Numerical evidence for assuming a constant thermal expansion coefficient	43
2.4	Intra-component scaling parameters for system fluids	78
2.5	Intra-component scaling parameters for solid structures	79
2.6	Non-dimensional variables for inter-component scaling	80
2.7	Compatibility scaling parameters for producing scaled integral system criteria	81
2.8	Residence time scaling distortion examples	86
2.9	Radiative heat transfer scaling distortion quantification example St values	92
3.1	User-desired capabilities for SAM radiative heat transfer modeling	108
3.2	RadiativeHeatTransfer-PBHeatExchanger compatibility simulation parameters	136
3.3	PBHeatExchanger-RadiativeHeatTransfer coupling bug search	140
3.4	Convective coupling temperature matrix used for \dot{Q} postProcessor calculation	149
3.5	PostProcessor testing simulation parameters and verification results	153
3.6	Simulation parameters and analytical solution for concentric pipes testing	156
3.7	Simulation parameters and analytical solution for slab enclosure testing	157
4.1	Component-specific characteristic parameters for CIET primary loop heater	172
4.2	Intra-component scaling parameters of interest for CIET primary loop heater	173
4.3	Inter-component scaling characteristic variable uniformity for CIET primary loop	173
4.4	Integral-system characteristic parameters for CIET primary loop	174
4.5	Compatibility scaling parameters of interest for CIET primary loop	174
4.6	Characteristic parameters for CIET DRACS loop scaling and distortion analyses	175
4.7	Intra-component scaling parameters of interest for CIET DRACS loop DHX	175
4.8	Compatibility scaling parameters of interest for CIET DRACS loop	176
4.9	Mk.II core parameters determined via component scaling of CIET heater	178
4.10	Mk.II primary loop at steady-state full-power	179
4.11	Mk.II primary loop in a post-SCRAM scenario	180
4.12	Mk.II DRACS loop in a post-SCRAM scenario	181

Nomenclature

Acronyms & Abbreviations

1D	One-Dimensional
2D	Two-Dimensional
3D	Three-Dimensional
ANL	Argonne National Laboratory
BC	Boundary Condition
CFD	Computational Fluid Dynamics
CIET	Compact Integral Effects Test
CRAB	Comprehensive Reactor Analysis Bundle
DHX	DRACS HX
DOE	United States Department of Energy
DRACS	Direct Reactor Auxiliary Cooling System
EOS	Equation(s) of State
FEI	Fluid Energy Inertia
FEM	Finite Element Method
FHR	Fluoride-Salt-Cooled High-Temperature Nuclear Reactor
Flibe	Molten Li_2BeF_4 Salt
FMI	Fluid Momentum Inertia
H2TS	Hierarchical Two-Tiered Scaling
HX	Heat Exchanger

IC	Initial Condition
IET	Integral Effects Test
LHS	Left-Hand Side
LWR	Light Water Reactor
Mk.I	Mark 1
Mk.II	Mark 2
MOOSE	Multiphysics Object Oriented Simulation Environment
MSR	Molten Salt Reactor
ND	Non-Dimensional
NRC	United States Nuclear Regulatory Commission
P-V	Power-to-Volume
PHL	Parasitic Heat Loss
Rad++	Rad+ “plus” a participating fluid
Rad+	Net Radiation Method “plus” non-grey surfaces
radHT	Radiative Heat Transfer
RHRA	Reduced-Height, Reduced-Area
RHS	Right-Hand Side
s2f	Solid-to-Fluid
s2s	Solid-to-Solid
SAM	System Analysis Module
SCRAM	Safety Control Rod Axe Man
SEI	Solid-Structure Energy Inertia
SET	Separate Effect Test
TRISO	Tri-structural Isotropic
UC Berkeley	University of California, Berkeley

Variables & Symbols

$\% \Delta$	Percent Difference
α	Fluid Emittance
α_s	Thermal Diffusivity
α_{rad}	Surface Absorptivity
β	Fluid Thermal Expansion Coefficient — or — Placeholder Angle for Trigonometric Manipulation
Bi	Biot Number
ΔT	Temperature Difference
Δ	Change — or — Difference
δ	Geometric Width (e.g. Solid-Structure Thickness)
δ_{kj}	Kronecker Delta
\dot{m}	Mass Flow Rate
\dot{Q}	Power — or — Heat Transfer Rate
ℓ	Length
ϵ	Void Fraction
Eu	Euler Number
\mathcal{F}	Friction Number
Fr	Froude Number
κ	Absorption Coefficient
λ	Wavelength
\dot{u}	Non-Dimensional Mass Flow Rate
μ	Dynamic Viscosity
Nu	Nusselt Number
ν	Kinematic Viscosity
\oint	Loop Integral

Ω	Solid Angle
$\mathcal{O}(\psi)$	Order of Magnitude (e.g. on the order 10^ψ)
Σ	Loop Sum
$\bar{\psi}$	Geometrically- or Spectrally-Averaged Parameter (e.g. ψ)
Pe	Peclet Number
Ψ	Non-Dimensional Pressure
Pr	Prandtl Number
\mathcal{B}	Non-Dimensional Heat Generation
\mathcal{B}'''	Non-Dimensional Volumetric Heat Generation
Re	Reynolds Number
ρ	Reflectivity — or — Density
Ri	Richardson Number
σ	Stefan-Boltzmann Constant
St	Stanton Number
τ	Non-Dimensional Time
θ	Non-Dimensional Fluid Temperature — or — Angle
ε	Emissivity
φ	Non-Dimensional Solid-Structure Temperature
$\vec{\mathbf{g}}$	Gravity Vector
\mathcal{X}	Non-Dimensional Distance along 1D Axial Flow
ξ	Non-Dimensional Relative Elevation
A	Area (Cross-sectional — or — Surface)
c_p	Specific Heat Capacity
D	Diameter
D_h	Hydraulic Diameter

d_p	Pebble Diameter
E	Radiative Emissive Power
f	Friction Factor (or “Flow Loss Coefficient”)
$f(\psi)$	Function of Some Variable (e.g. ψ)
F_{ij}	View Factor from Surface (e.g. “ i ”) to Surface (e.g. “ j ”)
G	Incident Radiation
g	Gravity Scalar Acting in the Direction of Flow (Equal to $g_x = \vec{\mathbf{g}} \cdot \hat{x}$)
H	Total Height
h	Heat Transfer Coefficient
h_{pump}	Pump Head
I	Radiative Intensity
J	Radiosity
K	Form Loss Coefficient
k	Thermal Conductivity
L	Total Axial Length
m	Mass
O	Origin
P	Pressure
p_h	Heated Perimeter
p_w	Wetted Perimeter
q''	Heat Flux
q'''	Volumetric Heat Rate (e.g. of Emission, Generation, Source, Transfer)
r	Radius — or — Directional Coordinate in the Radial Direction
S	Radiative Path Length
T	Temperature

t	Transmittance — or — Time
u	Fluid Velocity
V	Volume
x	Distance Along 1D Axial Flow Path — or — Directional Coordinate Along 1D Axial Flow Path
y and z	Directional Coordinate Orthogonal to 1D Axial Flow
z	Relative Elevation (Compared to the Lowest Point in the System/Loop) — or — Directional Coordinate Opposite to the Direction of Gravity
N_{ψ}	Nondescript Non-Dimensional Parameter (or e.g. “ ψ Number”)
“ \equiv ”	Verbally Defined as . . .

Subscript-Use of Symbols

0	Initial (or “Naught”)
λ	Wavelength (or “Spectral”)
<i>alt</i>	Alternative
<i>anal</i>	Analytical
<i>aug</i>	Augmented
b	Blackbody — or — Bulk Fluid
C	Cold
c	Component
<i>conv</i>	Convective
DC	Downcomer
e	Experiment
f	Fluid — or — Flow
<i>fric</i>	Friction
<i>gen</i>	Generation
H	Hot

<i>HX</i>	Heat Exchanger
<i>i</i>	Inner
<i>in</i>	Inlet
<i>k</i>	Surface
<i>LM</i>	Log-Mean
<i>mod</i>	Modified
<i>n</i>	Node
<i>o</i>	Characteristic (for Scaling Analysis) — or — Outer
<i>p</i>	Prototype
<i>p – m</i>	Participating Media
<i>postP</i>	PostProcessor
<i>R</i>	Ratio (<i>e/p</i>)
<i>r</i>	Radial
<i>rad</i>	Radiative
<i>refl.</i>	Reflector
<i>res</i>	Residence
<i>s</i>	Solid-Structure
<i>tot</i>	Total
<i>w</i>	Wall
<i>x / ж</i>	Axial — or — Local Value Along 1D Axial Flow Path

Chapter 1

Radiative Heat Transfer Distortion between FHRs and their Experiments and its Impact on Scaled Heat Transfer Behavior

The fluoride-salt-cooled high-temperature reactor (FHR) is a promising advanced nuclear reactor concept incorporating a novel configuration of design characteristics [1, 2] — the core is filled with TRISO pebble fuel elements, which permits online refueling, and produces anywhere from 100 MW_e [3] to 150 MW_e [4, 5] as opposed to the conventional light water reactor (LWR) value of ≈ 1000 MW_e; high temperature (500 °C to 700 °C instead of ≈ 300 °C in LWRs) molten salt coolant transfers heat between the reactor core and primary heat exchanger (HX); and natural circulation passive safety loops remove decay heat from the core in the case of a reactor SCRAM. The molten salt typically considered for FHRs is Li₂BeF₄ (FLiBe or flibe), which has melting and boiling points around 460 °C and 1400 °C respectively, a high volumetric heat capacity, and is chemically inert with air, water, and soluble fission products [1]. These characteristics result in multiple benefits. Firstly, FHRs can be operated at near-atmospheric pressure (instead of ≈ 16 MPa in LWRs), reducing system complexity, structural materials, and cost, while minimizing the energy available for rapid release events [6]. Secondly, system max temperature safety margins are constrained by allowable solid-structure operating temperatures rather than fluid boiling (as is conventional when using a water coolant), enabling higher operating temperatures, which generally translates to higher thermodynamic efficiency. Thirdly, compact system design further enhances the economic benefits of building small reactors, primarily by inhibiting the large initial cost overruns commonly associated with large 1000 MW LWR builds [7]. Moreover, inherently requiring more reactor units per plant to reach comparable electric output promotes long-term cost reductions through iterative unit construction.

The FHR design has progressed beyond academia and is now under active commercial development [8], backed by strong support from the United States Department of Energy [9–13]. A critical step in the licensing process for new nuclear reactors is the validation of important safety analysis codes, such as those pertaining to system-level thermal hydraulics. To validate codes' simulation capabilities for specific reactor types, experimental data are necessary — data which typically come from separate effect tests (SETs) and integral effects tests (IETs).

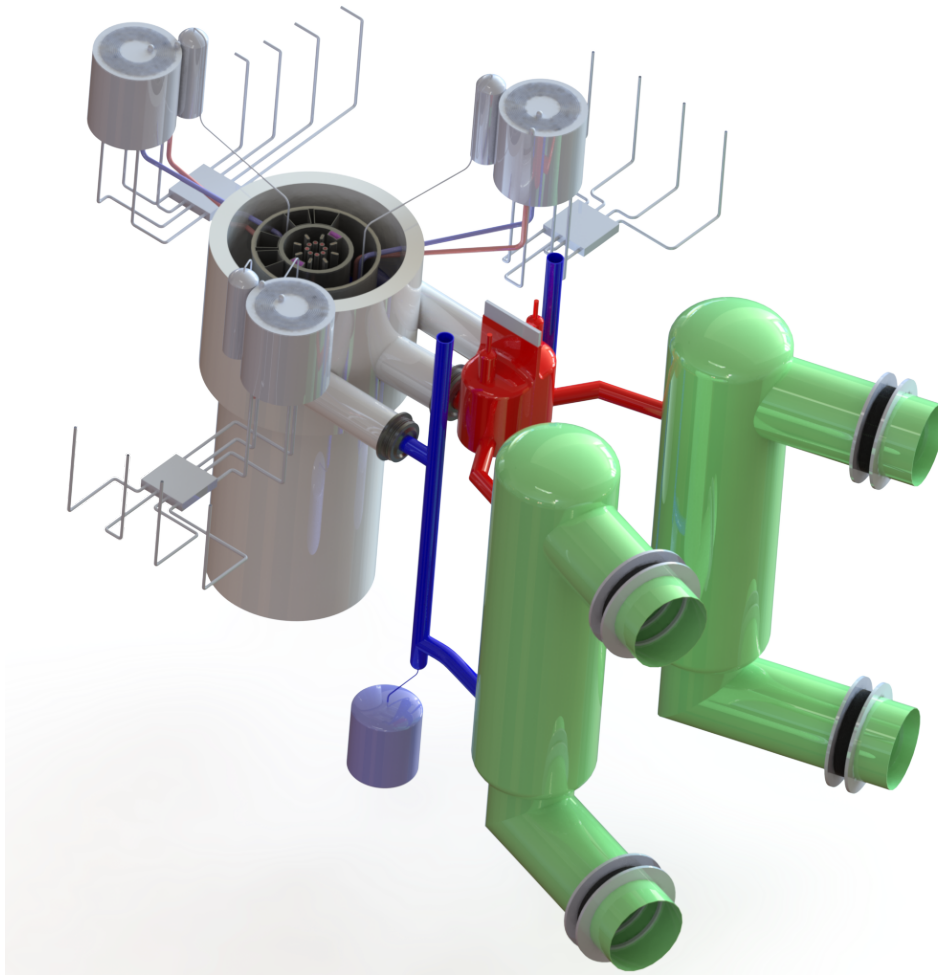


Figure 1.1: Mark 1 (Mk.I) FHR primary loop supplemented by three passive cooling natural circulation loops. The core cavity structure is represented in grey, the hot leg is shown in red, the cold leg in blue, and the HX vessels are drawn in green. For scale, the core cavity structure is approximately 12 m tall and the HX vessels are approximately 14 m tall [3].

In the context of nuclear reactor engineering, SETs and IETs, are scaled-down experiments designed to simulate the thermal hydraulic behavior of the prototypical reactor design. In addition to the primary goal of facilitating code validation for safety analysis, SETs and IETs are vital to the reactor design process for understanding general system behavior, establishing experience in system procurement, developing instrumentation and controls, and developing operating procedures for startup, shutdown, and other postulated operating conditions.

There are some phenomenological behaviors which will be present in FHRs and cannot be reproduced in scaled experiments, such as heat transfer via thermal radiation. It is expected radiative heat transfer (radHT) will be significant in some FHR scenarios, leading to its classification as an important topic of study. If scaled experiments cannot properly capture the impact of radHT, there must be methods for determining this contribution. This chapter will describe the discordant nature of radHT between FHRs and their experiments, followed up by a discussion on how to address that discrepancy.

1.1 Scaled Experiments for FHRs

To set the stage for delving into the impact of radHT in FHRs and their scaled experiments, it is helpful to more thoroughly discuss scaled experiments in general. As discussed previously, there are a number of benefits to building SETs/IETs, which all *could* be achieved with FHRs instead. However, building reduced scale experiments provides a more feasible pathway to meeting those goals — building reduced-scale experiments is more practical and safer than building first of a kind FHR systems, which would be costly, complicated, and potentially dangerous without preliminary experience.

Table 1.1: Select prototypical FHR design characteristics and their corresponding aspects implemented in scaled experiments.

FHR Prototype	Scaled Experiment
• Nuclear heating	• Electric heating
• Large material inventories for both solids and fluid	• Reduced size ↳ less materials
• High energy consumption	↳ lower power
• Toxic coolant	• Surrogate fluid
• High temperatures	↳ low temperatures

In particular, the left column of [Tbl. 1.1](#) summarizes several less-manageable FHR characteristics that complicate the construction and operation of prototypical systems. These characteristics can be avoided by scaling the prototype down to a reduced size SET/IET with electrical heating and a surrogate fluid. [Table 1.1](#)'s right column shows which experimental characteristics replace which of those less-manageable FHR characteristics.

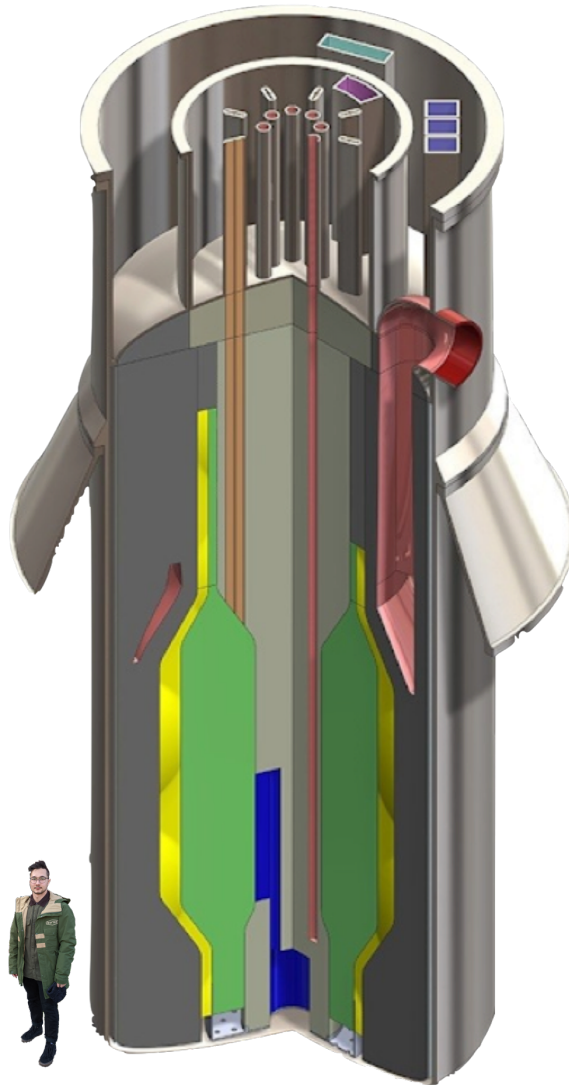


Figure 1.2: An isometric cutaway view of the Mk.I FHR core vessel. Me pictured for size comparison. Drawn to scale. FHR render modified from Krumwiede et al. [14].

Previous milestones in FHR development include the Mk.I pre-conceptual design [3] (shown in [Figs. 1.1](#) and [1.2](#)), which serves as a seemingly-ubiquitous reference design for FHR studies,

and the compact integral effects test (CIET) [15], the first IET built for FHR analysis — both of which were developed at UC Berkeley. Figure 1.2 shows the Mk.I FHR core with all FHR characteristics shown on the left side of Tbl. 1.1, while Fig. 1.3 shows an example IET core-equivalent section (from CIET) with all undesirable FHR characteristics replaced by the items on the right side of Tbl. 1.1. My image, superimposed to scale in both images, can be used to compare core/heater sizes between Figs. 1.2 and 1.3.

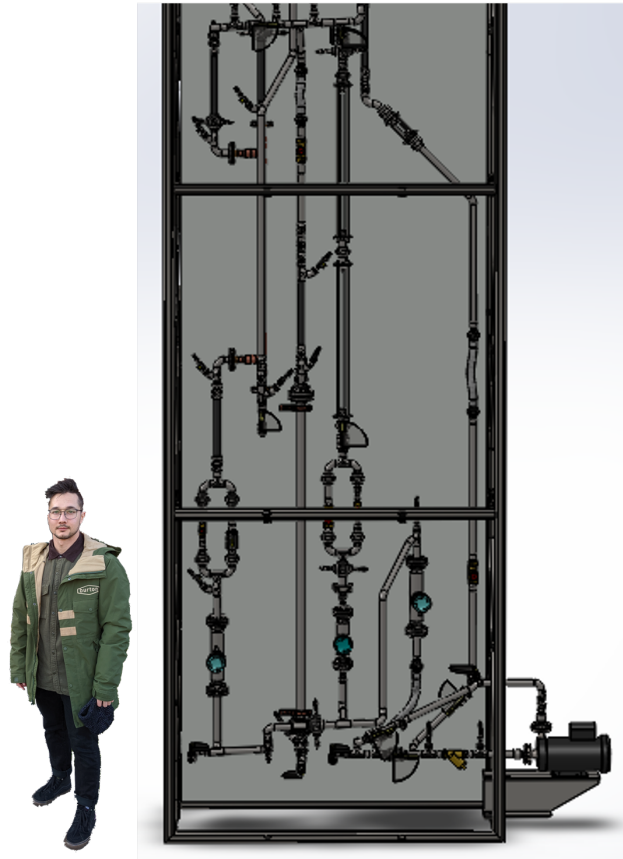


Figure 1.3: The scaled-down CIET heater section and surrounding components. Me pictured for size comparison. Drawn to scale. Compared to the Mk.I core in Fig. 1.2, CIET's heater is smaller, lower power, and filled with a low temperature surrogate fluid.

This comparison exemplifies an FHR-to-scaled-system example resulting in a much smaller system that is easier, cheaper, and safer to build and operate while still meeting the following goals:

- Validate codes for safety analysis

- Understand general system behavior
- Establish experience procuring and building system components
- Develop instrumentation and controls
- Develop reactor operating procedures

However, one cannot simply build any reduced-scale, surrogate fluid experiment and expect it to produce data pertinent to full-scale FHR behavior. Particular experimental design characteristics are required for particular prototypical designs, and those specifics of experimental design are produced by scaling analysis.

1.1.1 Scaling analysis theory pertinent to FHR experiments

Scaling analysis provides the theoretical basis for capturing full-scale prototypical reactor behavior and representing it in reduced-scale experiments. If the experimental system is designed properly, behavioral “similitude” with the prototype can be achieved. The mathematical basis behind scaling comes from nondimensionalizing (ND-izing) the governing equations for fluid flow and heat transfer. In practice, this means contextualizing behavioral phenomena in terms of characteristic system behavior. If experimental system characteristics are



Figure 1.4: Analogy for idealized scaling analysis showing prototypical behavior (large black square) perfectly represented by the scaled-down experimental behavior (small black box).

correctly chosen, the nondimensional (ND) behavior of the prototype can be made to resemble that of the experiment and vice versa. For example, Fig. 1.4 visually demonstrates the process of system scaling, where total system thermal hydraulic phenomenological interplay is represented by black boxes. Here, prototypical behavior (big black box) is perfectly represented by the experiment (smaller, but identical black box), indicating perfect similitude.

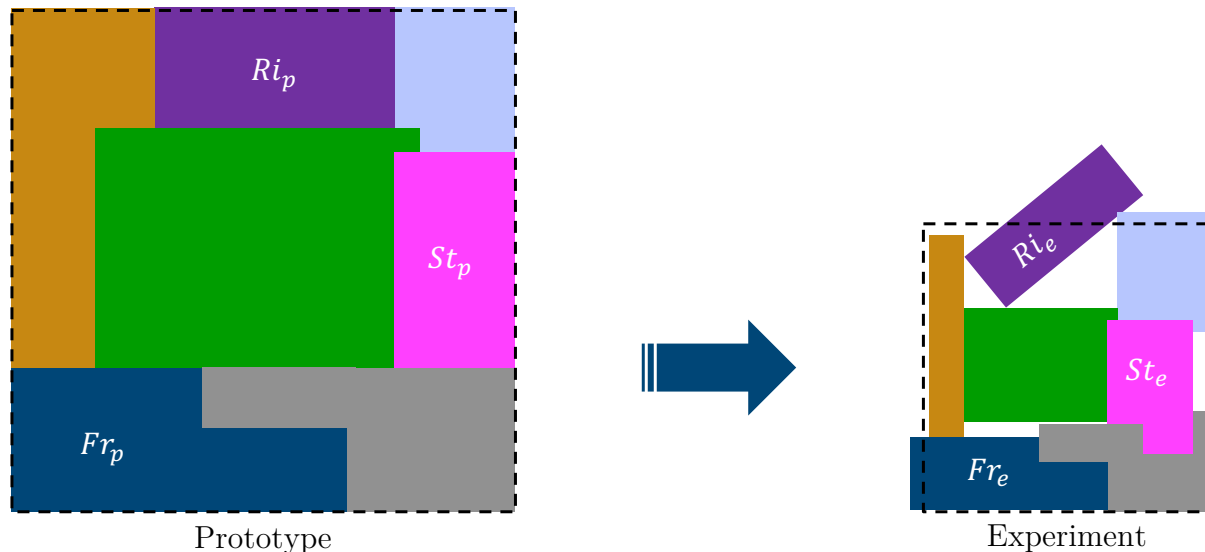


Figure 1.5: Analogy for realistic scaling analysis with scaling distortions. Prototypical behavior (dotted square) is shown decomposed into various scaling numbers (colored shapes), which do not fit together in the same way when scaled down and reassembled as the experiment. The differences between prototypical and experimental shapes, and nonconformity of experimental shapes to the dotted square, represent scaling distortions.

To facilitate the selection of system characteristics, variables used in the ND-izing process can be rearranged into ND ratios called “scaling numbers” or “scaling parameters”. The “prototype” box in Fig. 1.5, compared to the same box in Fig. 1.4, exemplifies the decomposition of prototypical behavior into scaling numbers (three of which are labeled). When scaling numbers are equated between systems, similitude is achieved. However, these scaling parameters often cannot all be matched simultaneously, resulting in discrepancies between the prototypical and experimental systems. These discrepancies, called “scaling distortions”, are visualized in Fig. 1.5 by the dissimilar arrangement of scaling numbers, resulting in an imperfectly recreated system behavior box.

Scaling distortions arise from imperfectly representing the relative significance of a phe-

nomenon in the scaled system. Of interest to FHR scaling, the relative significance of thermal radiation in system heat transfer will be inherently misrepresented by reduced-temperature, surrogate fluid experiments. The next section will discuss thermal radiation in FHRs and experiments to set the stage for quantifying radHT scaling distortion between the two.

1.2 Radiative Heat Transfer in FHRs and their Experiments

Radiative heat transfer is a phenomenon of interest for FHR scaling analysis since radHT will sometimes play a significant heat transfer role in FHRs, but an insignificant role in scaled experiments for FHRs. Capturing this discrepancy via scaling analysis requires first understanding the conditions creating that discrepancy, which requires some background discussion on the physics of radHT. In this section, I introduce radHT basics to set up ensuing discussion on how radHT differs between FHRs and their experiments.

1.2.1 Radiative heat transfer physics pertinent to FHRs

The radHT physics described in this section is an abridged discussion pertinent to the work conducted for this thesis. I repeatedly reference these concepts in later chapters, particularly in [Ch. 3](#). For more complete discussions on radHT material, I recommend textbooks on thermal radiation (e.g. Howell et al. [16] and Modest [17]). Traditional analysis of thermal radiation prioritizes the radiative behavior of interacting surfaces. I follow that precedent by discussing surface radiation before delving into participating media transfer. Both are important for FHR radHT.

Behavior of radiating surfaces

Radiative emissive power is used to describe the energy emitted by a radiating body, with the units W/m^2 . The amount of energy emitted scales with the fourth power of absolute temperature, as shown by [Eq. \(1.1\)](#). Here, σ is the Stefan-Boltzmann constant ($\approx 5.67 \times 10^{-8} \text{ W}/\text{m}^2\text{K}^4$) and ε represents surface emissivity.

$$E = \varepsilon\sigma T^4 \tag{1.1}$$

[Equation \(1.1\)](#) can be multiplied by surface area to compute emission *from* a radiatively interacting body, but does not address incoming radiation. Further characteristics are required to describe how a surface radiatively interacts with its surrounding environment. Surface characteristics can be described by the radiative parameters emissivity ε (previously introduced), reflectivity ρ , and absorptivity α_{rad} . These parameters describe a surface's propensity to emit

its own radiation, reflect incident radiation, and absorb incident radiation, respectively. All range from zero to one and all are unitless.

One common simplification in radiative heat transfer analysis, which has been assumed in the physics discussion thus far, is the so-called “grey” assumption, where radiative properties are treated as constant along wavelength (when in reality, they are not). The physical basis for this assumption is that the same molecular/atomic rotational and vibrational energy states that are available for photon-induced excitation (absorption) are also the energy states that are available for photon-releasing de-excitation (emission). The grey assumption breaks down when a radiating system contains large temperature discrepancies, as the wavelength spectra for incoming radiation (and the energy states those spectra encompass) can differ substantially from the spectrum for significant emission. For grey surfaces, this assumption equates emissivity to absorptivity, resulting in the convenient relation shown by Eq. (1.2).

$$\varepsilon = 1 - \rho \quad (1.2)$$

“Blackbodies”, or “black” surfaces in this context, are an important subset of grey surfaces, which are characterized by $\varepsilon = 1$ and therefore $\rho = 0$. In other words, all incident radiation is absorbed, and the body emits the maximum amount of radiation physically allowed for its given temperature.

Figure 1.6 shows how radiative properties are used to characterize radiation for grey surfaces. Incident radiation G , is either absorbed by the surface, $\alpha_{rad}G$, or reflected away, ρG . Emission and reflected incidence are grouped together as radiosity, J . Both G and J are designated the units W/m^2 , same as E .

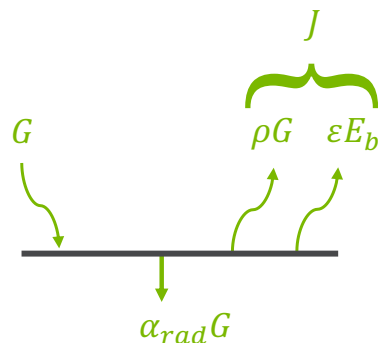


Figure 1.6: Simplified radiative behavior of some grey, opaque surface. The surface is represented by the straight, black line, while classifications of surface radiation are represented by labeled, arrow-tipped lines and squiggles.

Increasing the number of interacting surfaces can quickly increase the complexity of surface radiation analysis, as radiosity becomes dependent, not only on its own temperature and radiative properties, but also all other surfaces' temperatures and properties.



(a)



(b)

Figure 1.7: Views from East Bay overlooking the Bay with San Francisco in the distance. The (a) clear air viewed from Berkeley [18] is acting as a non-participating medium, while the (b) wildfire-smoke-filled air viewed from Oakland [19] absorbs and scatters visible light, thereby acting as a participating medium.

Participating media interaction

Radiative behavior of fluids, which are called participating media in this regard, involve a bit more intricate behavior than can be said for surfaces. Incident radiation can pass through a fluid body, interacting with the fluid along the way. [Figure 1.7](#) displays this behavior through an example all too familiar to those living in the Bay Area. On a typical clear day, such as that shown in [Fig. 1.7a](#), someone above the UC Berkeley campus can look past the Campanile and clearly see details of buildings and hills in San Francisco. Photons travelling from San Francisco to Berkeley are uninhibited by the clear air in-between — a non-participating medium, at least in the visible spectrum. [Figure 1.7b](#) reveals an entirely different story. During intense wildfires in the Autumn of 2017, heavy smoke inundated the Bay Area for several days. The smoke particles in the air substantially interacted with photons traveling through them, the result of which could be seen (or more accurately, less-clearly seen) from the Oakland Hills. The city in the distance of [Fig. 1.7b](#) is the same San Francisco seen in [Fig. 1.7a](#). Yet the buildings appear as silhouettes due to heavy absorption in the visible spectrum between those buildings and the hills, and the light beams bathing the cranes in Oakland’s harbor are clearly visible due to substantial scattering, redirecting photons in those beams towards the camera. The smoke-filled air in the Bay acts as a participating medium, absorbing and scattering light along the way.

Participating media’s radiative interaction can be described quantitatively as well. The ability of a participating fluid to interact with incoming photons, described by the attenuation coefficient β_{p-m} , is comprised of absorption κ and scattering σ_{p-m} . Similar to nuclear reaction cross sections, this attenuation coefficient represents a probability of interaction. However, in this case, these are linear attenuation coefficients with units m^{-1} .

$$\beta_{p-m} = \kappa + \sigma_{p-m} \quad (1.3)$$

In many instances of radiative analysis, scattering is not considered to make up a significant source of photon attenuation and is neglected, leaving only absorption as the means of interaction between incoming radiation and participating media. This simplification aligns well with the work in this dissertation by justifying the lower-fidelity treatment of thermal radiation necessary for system-level analysis. Assuming negligible scattering, the (nondimensional) optical path seen by radiation is the path length S multiplied by the absorption coefficient of the fluid, κ . Shown as the dotted line in [Fig. 1.8](#), this absorption produces an exponential decay of incident radiation I_0 along distance, obeying [Eq. \(1.4\)](#).

$$I = I_0 \exp\left(-\int_0^S \kappa \, dS\right) \quad (1.4)$$

It should be noted [Eq. \(1.4\)](#)’s exponential term describes the proportion of incident radiation remaining at some distance S into a participating medium. This term is designated as a radiative parameter called “transmittance” and assigned the variable t . For homogeneous

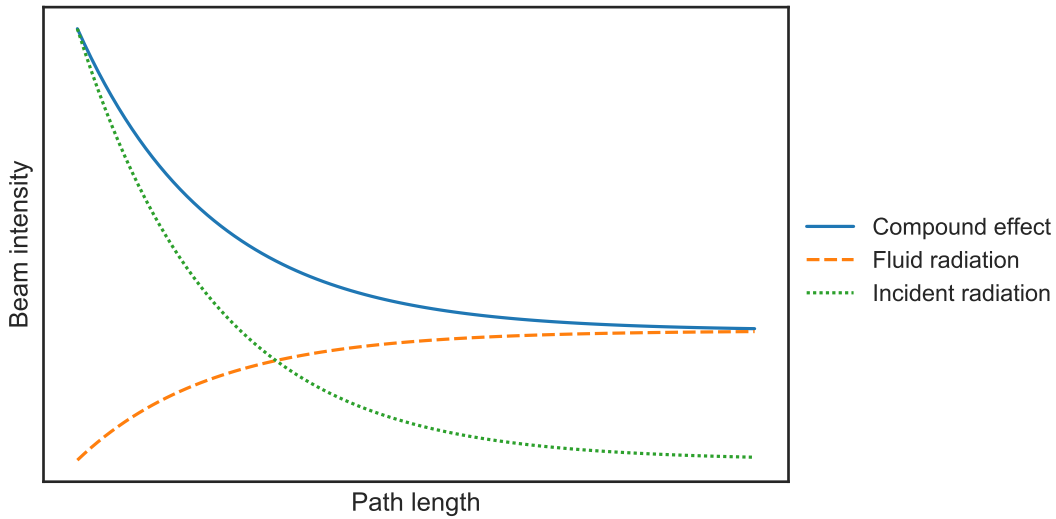


Figure 1.8: Simplified radiative behavior of some grey, homogeneous participating medium along a line of sight. The incident radiation beam is attenuated and replaced by emission from the medium itself. The medium’s contribution is attenuated as well, leading to the observed asymptote.

participating fluids, both in terms of composition and temperature, the absorption coefficient will remain constant along a line of sight, thereby simplifying the transmittance term to $\exp(-\kappa S)$. I maintain the homogeneous fluid assumption for the remainder of this thesis.

In addition to absorption, the fluid body emits thermal radiation of its own along the line of sight, which is subsequently subject to the same absorption behavior described by Eq. (1.4). The overall fluid contribution, what is emitted and remains unattenuated, is shown by the dashed line in Fig. 1.8. The magnitude of this contribution emerging from a fluid body can also be described by Eq. (1.1). However, ε here would have to be substituted with a parameter called “emittance”, which is designated in this thesis by the variable α .

Applying the grey assumption to solid surfaces generated Eq. (1.2). The convenient product of applying the grey assumption to participating media is an analogous relationship between transmittance and emittance, shown by Eq. (1.5).

$$t = 1 - \alpha \quad (1.5)$$

A participating medium blackbody has $t = 0$ and $\alpha = 1$. Revisiting Fig. 1.8, a blackbody is approximated by the “optically thick” behavior on the far right side of the plot (as opposed to the “optically thin” behavior on the left).

Wavelength dependence of radiative properties

By maintaining the grey assumption, the physics discussion up to this point has neglected a major detail of radiative transfer — wavelength dependence of radiative properties. When properly treated, the grey assumption can greatly simplify radHT analysis while still maintaining a level of accuracy sufficient for safety analysis. However, proper treatment requires understanding the wavelength-dependent nature of radHT first. The reality is emission, attenuation, re-emission, reflection, etc. all behave differently at different wavelengths for different materials at different temperatures in different systems.

The first relation I discussed in this section was emissive power, Eq. (1.1). For a blackbody, total $E_b = \sigma T^4$ is found as the integral of spectral emissive power, Eq. (1.6). This equation, called Planck's law, reveals the theoretical maximum limits of radiative emission for any wavelength at a given temperature. When plotted across the appropriate wavelength spectrum, this equation manifests a Boltzmann distribution, as seen in Fig. 1.9. In Eq. (1.6), h_P is Planck's constant, c_o is the speed of light in a vacuum, and k_B is the Boltzmann constant.

$$E_{\lambda,b} = \frac{2\pi h_P c_o^2}{\lambda^5 \left[\exp\left(\frac{h_P c_o}{\lambda k_B T}\right) - 1 \right]} \quad (1.6)$$

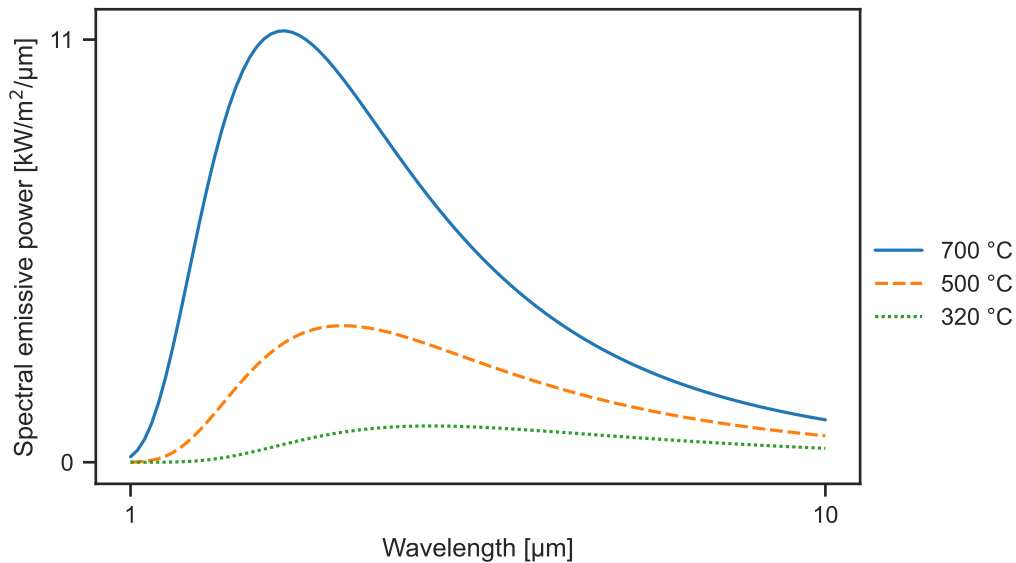


Figure 1.9: Total hemispherical blackbody emission spectra in the infrared region shown for bounding FHR temperatures (solid and dashed) and a characteristic LWR hot leg temperature (dotted).

The distribution peaks in Fig. 1.9 clearly shift towards shorter wavelengths at higher temperatures (see Wien’s displacement law). For radiative systems, the implication is that significant wavelength-regions of emitted radiation depend entirely on the constituents’ temperatures. However, real-world emission exhibits some proportion of Planck’s law all along wavelength, which can alter wavelength-regions of interest for radHT. The wavelength-dependent proportion of Planck’s law, $E_\lambda/E_{\lambda,b}$, is characterized by spectral emissivity, ε_λ .

Radiative absorption varies along wavelength as well. For opaque surfaces, incoming radiation at a given wavelength that isn’t absorbed gets reflected — characterized by spectral reflectivity, ρ_λ . For translucent bodies and participating media, spectral transmission battles spectral absorption, both of which are dictated by κ_λ . A great example of this interplay is demonstrated by the absorption coefficient of water in the visible range, which is responsible for producing the blue color we see when looking through water. As can be ascertained from Fig. 1.10, water absorbs red light (~ 700 nm) at a rate orders of magnitude higher than blue (~ 400 nm), leading to substantial blue shift of light traveling through it.

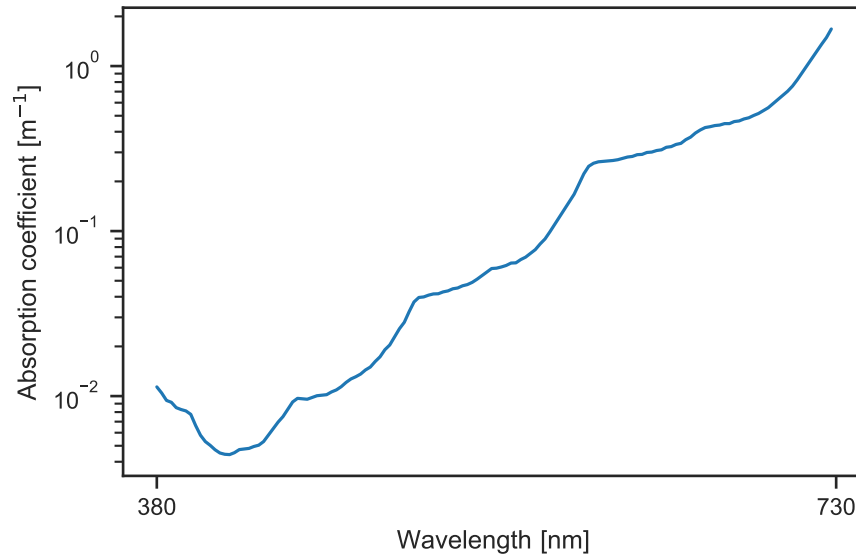


Figure 1.10: Absorption coefficient of water across the visible spectrum showing preferential absorption of red light (around 700 nm). Plot generated using data from Pope [20].

Thus far, all examples have examined the wavelength-dependent nature of one radiative property at a time, despite the real complication arising from interplay between various materials at different temperatures with their own wavelength-dependent properties affecting system radiation in their own ways. A great example of multi-variable wavelength-dependent thermal radiation comes from the sun’s interaction with our atmosphere. The dashed Boltz-

mann distribution in Fig. 1.11 shows an approximation of the wavelength-dependent emission from the sun, as it arrives at the edge of Earth’s exosphere. Approximating the sun as a blackbody at 5777 K, a commonly-made assumption, works well for thermal emission, particularly for red and infrared wavelengths. The solid curve shows the final outcome of the wavelength-dependent absorption in Earth’s atmosphere in the primary range of the sun’s emission. Atmospheric absorption of sunlight occurs primarily due to ozone, water, and carbon dioxide [21], and accounts for approximately 23% of the sun’s energy that reaches Earth [22].

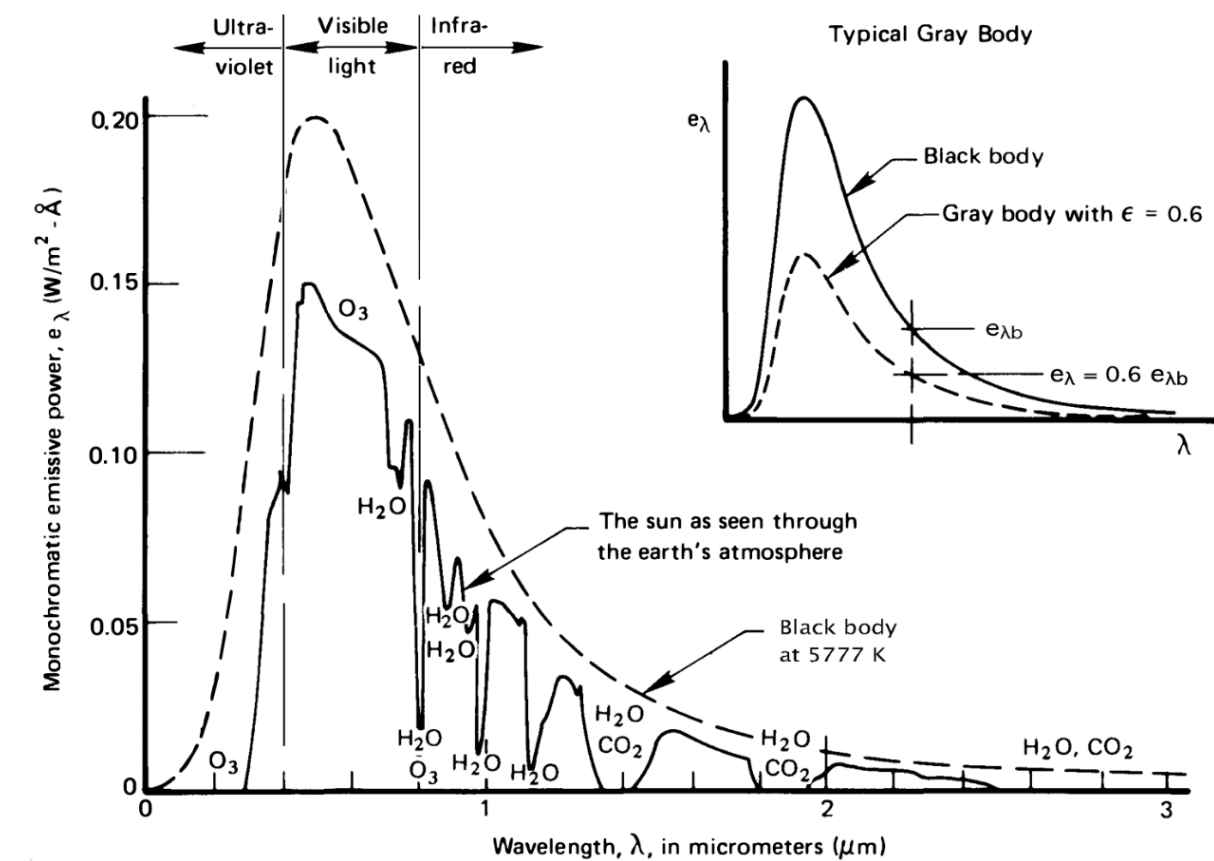


Figure 1.11: Spectral emissive power from the sun received by the earth’s surface (solid) compared to the energy that would be received if there was no atmospheric attenuation and the sun was replaced by a perfect blackbody (dashed). The dips in energy received are effects of atmospheric absorption bands and are respectively labeled with the gas(es) responsible. Figure from Lienhard [22].

Radiative emission from the earth occurs primarily in the 4-40 μm region. Gaseous absorption of thermal radiation across this wavelength band substantially influences Earth’s

energy balance, impacting our daily lives. Ozone, water vapor, carbon dioxide, methane, and nitrous oxide contribute substantially to radiative absorption in this spectrum [22], with their respective absorption bands trapping earthborn heat bound for space. These gases' wavelength-specific absorption between 4 and 40 μm is called the greenhouse effect. As human activity increases the atmospheric concentrations of these gases, the greenhouse effect will strengthen, further limiting Earth's ability to jettison heat. The steady-state temperature of Earth, an outcome of balancing atmospheric absorption and reflection in the region of the sun's radiation with atmospheric absorption and transmission in the region of earthborn radiation, will continue to rise as long as we emit more greenhouse gases into the atmosphere.

$$\bar{\psi} = \frac{\int_{\lambda_1}^{\lambda_2} \psi(\lambda) I_{\lambda} d\lambda}{\int_{\lambda_1}^{\lambda_2} I_{\lambda} d\lambda} \quad (1.7)$$

To accurately describe radiative behavior of a system without solving an entirely separate set of equations for each wavelength band, spectral averaging of radiative properties is required. Spectral averaging, performed for some generic parameter via Eq. (1.7), is conducted with incoming or outgoing spectral intensity, I_{λ} , depending on which phenomena the parameter of interest quantifies. All surface and fluid radiative parameters must be spectrally-averaged in their applicable wavelength ranges to be used in ensuing analysis. While methods for spectral averaging are outside the scope of this thesis, the readers are referred to Howell, et al. [16] and Modest [17] for further information. Further discussion in this thesis assumes spectrally-averaged radiative properties.

1.2.2 Role of thermal radiation in the heat transfer behavior of FHRs

Based on the physics discussion in the previous section, FHRs' high prototypical temperatures (anywhere from 500 $^{\circ}\text{C}$ - 700 $^{\circ}\text{C}$) and the use of a participating medium coolant (flibe) could lead to thermal radiation being a significant mode of heat transfer in some scenarios. I will discuss how these factors contribute to an increased contribution from radHT, starting with temperature.

The strong temperature dependence in Eq. (1.1) has serious implications for high temperature reactor systems, such as FHRs. Neglecting differences in emissivity, Fig. 1.9 and Eq. (1.1) reveal an FHR operating at 700 $^{\circ}\text{C}$ [3] has more than seven times the blackbody emissive power than a current generation LWR operating at 320 $^{\circ}\text{C}$ [23]. For this reason, while LWR safety analyses do not typically consider radiative heat transfer less extraordinary temperature excursions, some FHR analyses might even need to consider thermal radiation during regular operation.

For FHRs, scenarios with non-insignificant radHT contributions will typically be characterized as such by diminished convective contributions, or otherwise by inflated radiation effects approaching those from convection. Therefore a good local metric of comparison for the significance of radHT can be made by normalizing blackbody emissive power by convective flux, shown by Eq. (1.8).

$$\frac{E_b}{q''_{conv}} \approx \frac{\sigma(T_{H,o}^4 - T_{C,o}^4)}{h(T_{H,o} - T_{C,o})} \quad (1.8)$$

This metric can be used to approximate low and high bounds on radiative heat transfer interaction. Based on the physics discussion Sec. 1.2.1, regions of *least* impact for radHT will have high convective heat transfer and short optical paths — conditions which exist in a pebble bed. Applying the Wakao correlation [24] to the Mk.I core [3] during steady-state operation, a heat transfer coefficient of $h = 4.7 \times 10^3 \text{ W}/(\text{m}^2 \text{ K})$ results in Eq. (1.8) bounding FHR radHT on the low end at $E_{b,FHR}/q''_{conv} \approx 4 \times 10^{-2}$. This number, at two orders of magnitude below unity, indicates FHR cores will likely be excluded from radHT scaling distortion analysis during steady-state conditions. However, when talking about a nuclear reactor with $\dot{Q} = 320 \text{ MW}_{th}$ [5], the 4×10^{-2} low bound translates to almost 13 MW — a significant figure that warrants consideration for some analyses.

The previous example was simply an order of magnitude comparison, and is not fit for highlighting extraordinary scenarios of significant radHT. Take for example a loss of forced cooling transient, where convection reduces to a negligible heat transfer phenomenon. For these important scenarios, more-detailed participating fluid analyses are required. Extrapolating the participating media discussion in Sec. 1.2.1 to wavelengths outside the visible range, and to fluids other than air and water, one can imagine how the wavelength-dependent nature of radiative properties can impact radiative heat transfer in FHRs.

To understand fluid absorption in FHR coolant, the specific radiative behavior of flibe must be investigated. However, the absorption coefficient for flibe has not yet been well characterized [25]. One workaround to this lack of data is approximating flibe’s absorption characteristics by drawing estimate fits to connect previously-measured values in disparate wavelength bands [26]. However, previous data sets are incomplete and disjointed, leading to potentially significant errors. As a substitute, given flibe is a halide salt, the generic radiative behavior of halide salts can provide insights on how fluid absorption will behave in FHRs. Figure 1.12 shows this generic absorption behavior, dominated by two absorption cutoff “tails” enclosing a “plateau” of low absorption.

Flibe’s level of absorption will depend on where its absorption tails sit in relation to the FHR emission spectra drawn in Fig. 1.9. Observing Bendow’s various plots for transmission spectra of BeF_2 glass (as BeF_2 is a constituent molecule of flibe), the ultraviolet absorption cutoff sits at $\sim 0.2 \mu\text{m}$ whereas the infrared cutoff sits at $\sim 4 \mu\text{m}$ [27]. Superimposing

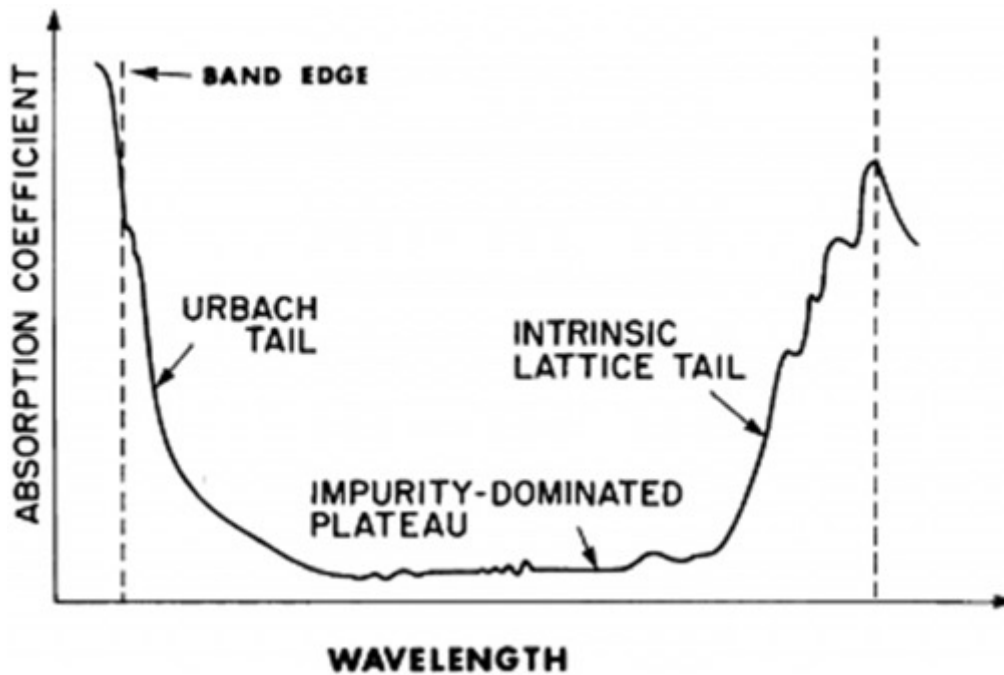


Figure 1.12: Generic absorption behavior of halide salts. The intrinsic lattice tail can be assumed to sit in the near infrared region plotted in Fig. 1.9. Original figure from Bendow [27] and modified by Chaleff et al. [28].

these absorption step-changes on Fig. 1.9, the ultraviolet cutoff can be ignored entirely. However, BeF_2 's intrinsic lattice tail sits somewhere near the middle of that plot, subjecting a substantial wavelength region of radiative emission to high fluid absorption. *For FHR blackbody emission, this roughly translates to $\approx 55\%$ of thermal radiation being emitted in highly absorbing wavelength regions and $\approx 45\%$ more emitted with substantial sensitivity to the impurity-dominated plateau.*

Shifting from BeF_2 to flibe, the expected “intrinsic lattice tail” step-change in absorption could substantially impact the magnitude of radHT in FHRs depending on how much it overlaps with the dominant wavelength region of radiative emission at prototypical FHR conditions. Additionally, absorption and emission characteristics of participating media can vary substantially with impurity concentration [29], which further complicates radiative heat transfer analysis with participating media. In Fig. 1.12’s “impurity-dominated plateau”, narrow but tall absorption bands at wavelengths greater than $1\ \mu\text{m}$ could greatly enhance solid-to-fluid radHT in FHRs.

Bardet conducted a high-level approximation for FHR radHT by considering flibe absorption bands [6]. Normalizing radHT by convective transfer, in a similar manner to Eq. (1.8), Bardet estimates a figure as high as 40% in flibe-filled HXs. This is despite the fact that flibe acts

as a fluxing agent, keeping HX (metal) surfaces shiny and low in emissivity. There will likely be non-steady-state scenarios in which this figure will be even higher. Therefore, thermal radiation is a heat transfer phenomena significant enough to consider in scaling analysis for FHRs.

1.2.3 Role of thermal radiation in the scaled heat transfer behavior of FHR experiments

In contrast to FHRs, scaled-down experiments are designed to operate at much lower temperatures, typically rendering radHT negligible. Utilizing Eq. (1.8) for CIET at steady-state full power, 80 °C to 110 °C, results in $h = 469 \text{ W}/(\text{m}^2 \text{ K})$ and $E_{b,CIET}/q''_{conv} \approx 2.4 \times 10^{-2}$. In this heat transfer example, normalized radHT is 40 % weaker in CIET than in the Mk.I. However, this metric was conjured to compare local heat transfer effects. A global metric of comparison, normalizing emissive power by total system power as shown below, could be a more useful scaled heat transfer benchmark.

$$\left(\frac{E_b A_w}{\dot{Q}} \right)_R = \left(\frac{T_{avg}^4}{(\rho c_p)_o L_o u_o \Delta T_o} \right)_R \quad (1.9)$$

For convenience, the above equation borrows nomenclature from more detailed discussions in Ch. 2. Briefly, the subscript $_R$ denotes a “ratio”, evaluating the expression at experimental conditions and dividing it by its evaluation at prototypical conditions. The subscript $_o$ indicates “characteristic” values. Additionally, some of the parameters for the experiment are dictated by scaling relations yet to be discussed (assuming half-height, geometric similitude, and Fr matching). For more discussion on these borrowed elements or variable definitions, see Ch. 2. Evaluating Eq. (1.9) produces a value of about two-thirds, indicating the conditions facilitating radiative heat transfer are, contextually, 52 % more significant for prototypical FHRs than their experiments. Furthermore, the level of participating fluid effects are not captured here. Assuming the transparent heat transfer oils used as surrogate fluids in FHR IETs are optically thin, the figure of 52 % can be interpreted as a underapproximation.

Scenarios characterized by diminished convective heat transfer effects, mentioned previously, will likely exaggerate the normalized contribution of radHT even further for FHRs compared to the equivalent scenarios in scaled experiments. To properly understand the discrepancy between prototypical and experimental radHT, both convective and radiative contributions must be evaluated and compared. However, the aforementioned metrics are simply rough order of magnitude benchmarks incapable of answering just how exaggerated that discrepancy will be. A more desirable parameter would focus on conditionally dependent, participating fluid heat transfer to enable quantifying the radHT distortion between FHRs and their experiments.

1.3 Quantification of the Radiative Heat Transfer Scaling Distortion between FHRs and their Scaled Experiments

Given what has been discussed in [Secs. 1.1](#) and [1.2](#), radHT is a phenomenon significant enough to FHR heat transfer to require analysis, scaled experiments are necessary for FHR development, and scaled-down experiments for FHRs will have substantially lower radHT effects than their prototypical counterparts. Taking these factors into consideration, it was necessary to develop an FHR scaling methodology capable of supporting radHT distortion quantification. Furthermore, to carry out this quantification, it is necessary to capture the system-level impacts of radHT. As the in situ measurement of radHT is neither feasible in FHRs nor their experiments, this must be carried out by system-level thermal hydraulics simulations. However, system codes previously lacked the ability to model participating media radHT [30], so it was necessary to develop these code capabilities to support the scaling methodology development. Due to the lack of radiative property data for flibe, accurate quantification of system-level radHT is not yet possible for FHR analysis. Therefore, system codes can serve the temporary role of approximating system-level radHT impacts for distortion quantification until reliable absorption data are acquired. Following this milestone, system codes, backed by validation efforts and radiative property measurement experiments, can be used to quantify FHR-to-experiment radHT distortion using scaling methods.

Before I carried out the work presented in this dissertation, neither the scaling methodology nor system-level modeling capabilities necessary to assess radHT scaling distortion for FHRs existed. This thesis presents the development of both. [Chapter 2](#) introduces an FHR scaling methodology developed to highlight and investigate radHT scaling distortion, and [Ch. 3](#) details the development of system-level radHT modeling capabilities to support distortion quantification. These concepts are then tied together in practice by [Ch. 4](#), which lays out a proposed demonstration of the scaling methodology, utilizing system-level modeling tools to quantify radHT distortion.

Chapter 2

A System-Level Scaling Methodology for FHRs with an Emphasis on Radiative Heat Transfer Scaling Distortion Quantification

System-level scaling, as defined in this chapter, is a form of scaling analysis that analyzes various thermal hydraulic phenomena in terms of their impact on total system behavior. As discussed in [Sec. 1.1](#), the purpose of analyzing ND behavior is to compare the behavior of entirely different systems, such as nuclear reactors and their experiments. The system-level approach is taken so this scaled behavior is evaluated on a scale pertinent to informing system-level design. After all, the ultimate goal of scaling analysis is informing separate effect test (SET) and integral effects test (IET) design.

To adhere to a system-level approach, the zoomed-in, micro-scale, boundary layer approach to thermal hydraulics is abandoned. Instead, for the purpose of deriving scaling parameters, a radially- and azimuthally-uniform one-dimensional (1D) approach is taken for fluid flow, while a pseudo-two-dimensional (2D) approach is employed for solid-structures.

The term “system-level scaling” should not be confused with “integral system scaling” (sometimes shortened to “system scaling”) — a scaling methodology step which will be discussed later in this chapter. Component scaling for SET applications is still permitted by a system-level scaling approach.

In this chapter, I develop a system-level scaling methodology for fluoride-salt-cooled high-temperature nuclear reactors (FHRs) with the intent of enabling analysis and quantification of radiative heat transfer (radHT) scaling distortion. In general, the derived non-dimensional (ND) “scaling equations” produce scaling parameters generalizable to the analysis of any loop-type heat transfer system with a single-phase coolant — for instance, the ND fluid

momentum equations. I derived these scaling equations to capture hydraulic behavior of both the forced (Sec. 2.2) and natural (Sec. 2.3) varieties for pump-driven and buoyancy-driven loops, respectively. The FHR-centric scaling approach begins to reveal itself when deriving scaling parameters for the fluid coolant (Sec. 2.4) and solid-structures (Sec. 2.5) — I assume solid fuel elements, high temperatures, and a radiatively participating fluid. The first of those assumptions dictates the solid and fluid heating terms, whereas the latter two assumptions are used to introduce radHT terms. Each of these four sections starts off by deriving a generalizable ND scaling equation and discussing the scaling numbers produced before delving into derivation considerations specifically for component and integral system scaling. These derivations are each followed by a discussion on characteristic parameter selection.

Following the scaling parameter derivation sections, I discuss the derived scaling parameters in the context of the overarching scaling methodology (Sec. 2.6), i.e. which parameters to use for various scaling scenarios. After a short discussion on transient scaling considerations (Sec. 2.6.3), I introduce prominent scaling distortions which will arise in SETs and IETs specifically as a result of applying this methodology to FHRs (Sec. 2.6.4). Of these distortions, the focus sits heavily on radHT scaling distortion (Sec. 2.7).

2.1 Previous Methodologies for Nuclear Reactor Scaling Analysis

I conducted a literature review on previous scaling methods and methodologies for nuclear reactors to show the expectations and capabilities of what has come before. The substantial bulk of scaling work was conducted for light water reactors (LWRs), which has laid the groundwork for all nuclear reactor scaling. I discuss the evolution of LWR scaling in the context of lessons learned for FHR scaling. As the FHR concept was first posed in 2003 [1], there has been substantially less time to make progress on FHR scaling analysis compared to that of LWRs. Therefore, my discussion on FHR scaling expands beyond holistic, complete methodologies developed for specific IETs to incorporate standalone scaling analysis methods as well. In general, the literature lacks focus on the scaling distortion originating from discrepancies in radHT between nuclear reactor prototypes and their associated experiments. Through this section, I make clear the motivations for particular aspects of this dissertation’s scaling methodology as well as how this methodology supports radHT distortion analysis and quantification.

2.1.1 LWR scaling methodologies

For the purposes of this work, it helps to break down LWR scaling methodologies into three categories — power-to-volume (P-V) scaling, three-step methodologies, and hierarchical two-tiered scaling (H2TS) methodologies. Power-to-Volume scaling was one of the first

approaches taken for LWR scaling, with the purpose being reducing the size, complexity, and cost of IETs. Examples of early IETs designed via P-V include the LSTF of the ROSA-IV program [31] and the Semiscale facility, an experiment built at Idaho National Laboratory beginning in the 1960s for the Atomic Energy Commission [32]. Semiscale operated at prototypical pressure, but reduced fluid inventory and core power by a factor of 1705, strictly by reducing the loop flow area. Interestingly, as a result of reduced area, Semiscale faced a substantial scaling distortion in heat transfer between the fluid and solid structures in the experiment downcomer [33, 34]. This distortion is of interest to FHR scaling analysis due to reduced area experiments and the relatively high thermal inertia of solid structures in prototypical FHR cores (discussed later in Secs. 2.5.3, 2.6.6 and 2.6.7). Both LSTF and Semiscale were full-height, reduced-area, reduced power, electrically-heated IETs. While the P-V approach does not capture additional aspects of modern scaling analysis, it did lay the foundation for later methodologies.

One of the approaches built off P-V scaling, which has been widely utilized, is the H2TS approach. This approach was developed by Zuber at the United States Nuclear Regulatory Commission (NRC) under the Severe Accident Scaling Methodology development program [35], and owes its success in part to its integration in the NRC's licensing strategy for LWRs [36]. Zuber's H2TS methodology is based on sets of phenomenological time ratios, each posed as a ND number. By formulating scaling numbers in this way, Zuber "provides a quantitative measure for evaluating the effect of the process on the system" [36].

The H2TS methodology has been well-utilized for the design of LWR IETs, notably at Oregon State University. Reyes and Hochreiter described their scaling analysis conducted to procure the design of the APEX experimental facility as "the first, and most comprehensive, application of [H2TS]" [37]. APEX was an IET built to provide system codes validation data for the Westinghouse AP600 emergency core cooling system during a loss of coolant accident. Using H2TS, this facility was designed with reduced-height, reduced-area (RHRA), reduced power (electric), accelerated time, and reduced pressure (not of consequence to FHR scaling). Another, more modern, application of H2TS was conducted to design Oregon State University's MASLWR facility [38, 39], the IET predecessor to NuScale's small modular LWR. This IET utilized RHRA scaling, electrical power, but maintained full-pressure and non-accelerated time.

Another approach built off experiences from P-V scaling is the three-step scaling approach. With forced circulation scaling relations for LWRs already well-established, Ishii (interestingly, one of Zuber's PhD students [40]) and Kataoka presented methods for scaling single- and two-phase natural circulation [41]. Ishii et al. then incorporated these relations into a cohesive, three-step scaling methodology, by which the PUMA IET was designed [42]. Using this methodology, PUMA was designed to represent the prototype (GE's Simplified Boiling Water Reactor) with an experiment utilizing RHRA, reduced power, and accelerated time, while keeping an eye on the quantification of pertinent distortions [43]. While this approach

does not share the level of use H2TS has, it does have precedence in facilitating the design of an IET that successfully investigated the behavior of a prototypical reactor design and provided pertinent test data to the NRC [42].

As natural circulation, an integral system phenomena, serves as the theoretical motivation behind the scaling relations developed by Ishii, the focus of this methodology is on integral system scaling. As such, Ishii's step one of the three steps is "integral response function scaling", which is conducted in conjunction with the second step, "control volume and boundary flow scaling". Step three acts separately from the first two "top down" scaling steps by analyzing local phenomena scaling from the "bottom up". This three-step framework motivates the framework implemented in this chapter's methodology. However, I made several tweaks to fit the purposes of my work, which are discussed further in [Sec. 2.6](#).

2.1.2 FHR scaling methods

Scaled experiments for FHRs have slightly different requirements than their LWR-based counterparts. The desirable experimental characteristics are listed below:

- RHRA
- Reduced power electrical heating
- Single-phase coolant
- Surrogate fluid

Reduced-pressure in experiments is not necessary, as FHRs operate at near-atmospheric conditions. Additionally, two-phase considerations are typically neglected, which simplifies analysis considerably compared to that of LWR severe accidents. The new requirement, use of surrogate fluids, is necessary due to the corrosive properties of molten Li_2BeF_4 (flibe) coolant [29], toxicity [2], and high temperatures at prototypical conditions [1]. There is precedence for single-phase, surrogate fluid scaling analysis. Heisler developed a scaling methodology for natural circulation in liquid metal reactors, which included the use of water in experiments as a surrogate for sodium and sodium-potassium reactor coolants [44]. However, water cannot provide both hydro- and thermo-dynamic similitude simultaneously for either sodium nor sodium-potassium. Heisler's work was commonly cited by Ishii [41, 42] and provides useful insights for FHR scaling analysis, but this chapter's scaling methodology will enable true similitude with a surrogate fluid.

Other scaling methods for FHRs, primarily developed at the University of California, Berkeley (UC Berkeley), all provide useful insights for developing a cohesive FHR scaling methodology. Bardet and Peterson were first suggested the use of Therminol[®] as a true surrogate fluid for flibe [6]. They found that at experimental conditions, Therminol[®] can be led to

match the Reynolds, Froude, Prandtl, and Grashof numbers simultaneously for flibe at prototypical FHR conditions. This was later numerically confirmed by Seo [45]. Quite apt to the work in this dissertation, Bardet and Peterson also provide discussion on thermal radiation scaling for surrogate fluid FHR experiments [6], which was previously unprecedented to my knowledge. Huddar et al. explored FHR-to-experiment scaling for the purpose of applying frequency response methods to a pebble bed heat transfer experiment [33]. Scarlet performed substantial work in developing scaling methods for natural circulation in FHRs [46], which I reference continually throughout this chapter. Liu, during his time at UC Berkeley, built off the foundation established by Scarlet, incorporating influences from Huddar et al., and composed a well-organized set of scaling relations for FHR natural circulation [47]. Of particular interest, Liu performed numerical simulations of scaled systems to explore the impact of surrogate fluids and parasitic heat loss (PHL) in FHR experiments. Despite the aforementioned developments in FHR scaling methods, none of those pieces of work were specifically produced for the purpose of designing a particular IET. The scaling work designed to produce FHR experiments is discussed below.

The product of scaling work conducted for the Compact Integral Effects Test (CIET), the first IET for FHRs, was described by Bickel et al. [15]. I make the distinction to avoid calling this work a “methodology” because equations are seemingly presented as if utilizing previous methods for producing CIET’s design characteristics. Nevertheless, CIET successfully captured the ND behavior of an early pre-conceptual FHR design [48] using RHRA, reduced power electrical heating, and, most importantly, a surrogate fluid coolant [49, 50]. There does currently exist one properly cohesive scaling methodology for designing experiments for an FHR prototype. That methodology was developed by Kairos Power to produce IETs with all the required characteristics of FHR scaling [51, 52]. Interestingly, Kairos Power developed their methodology as an application of H2TS. One of the reasons Zuber’s methods were adopted came down to the “pedigree” [52] of his work, which serves as ample justification considering Kairos is attempting to license a reactor with the very entity that integrated H2TS into their licensing process (the NRC). However, there remains one glaring omission from this methodology, as well as other FHR scaling methods previously discussed — radHT distortion quantification.

2.1.3 Need for an FHR scaling methodology that supports radiative heat transfer distortion analysis and quantification

Radiative heat transfer scaling analysis has been conducted, albeit rarely. In 2004, Kottke et al. investigated the ND interplay between thermal radiation and convection, stating “scale analysis has not previously been applied with radiation included” [53]. However, that ND analysis, among others (e.g. [25]), explored the local effects of radiation at interfaces with a surrounding medium. Boundary layer analysis has no role in system-level scaling. Incorporating Kottke’s relations would seek to achieve similitude in radiative transfer on the local level, whereas I sought to capture the system-level effects of radiation for distortion

quantification. The theoretical dissonance between previous ND radHT analysis and this chapter’s radHT distortion quantification methods is well summed up by the term “non-scalability of phenomena”, which D’Auria and Galassi applied to “phenomena [that] are not reproducible in different IETs and at different scales” [54]. Radiative heat transfer is one such non-scalable phenomenon. However, as I previously stated, I pursued radHT in scaling only for the purpose of distortion quantification. Therefore, radHT scaling analysis such as Kottke’s was not useful for my purposes, and I needed to draw exclusively from previous scaling methodologies instead.

Scaling methodologies for LWRs are not directly applicable to FHR scaling analysis, but laid the groundwork for developing FHR scaling methods and methodologies, such as Kairos Power’s based on Zuber’s H2TS approach. However, all FHR scaling methods and methodologies fail to address radHT distortion analysis and quantification. Due to the inherent distortion inevitable between high-temperature flibe systems and low-temperature surrogate fluid systems, radHT distortion is a necessary aspect for FHR scaling methodologies to incorporate. Taking lessons learned from this literature review, I developed a scaling methodology that fills this gap. Ensuing sections show how this methodology’s scaling relations are derived, followed by a description of the encompassing framework in [Sec. 2.6](#).

2.2 Fluid Momentum Scaling Parameters for Forced Circulation Fluid Flow

I begin with deriving scaling parameters for preserving fluid flow similitude in forced circulation flow loops. For FHRs, and nuclear reactors in general, forced circulation is enforced by fluid pumps. I allude to this sometimes by referring to forced circulation flow as “pump-driven” flow. For FHR scaling, these parameters would be applicable to the primary loop during scenarios with forced flow, such as regular operation conditions. Additionally, FHRs with intermediate salt loops between the primary- and power-production-sides could incorporate the derived parameters in those secondary loops.

I begin my derivation with Cauchy’s momentum equation. As the starting point, I have left the bolded vector variables in formulation. Here, $\vec{\mathbf{u}}$ contains three-dimensional fluid velocity information, $\vec{\mathbf{b}}$ represents external body forces acting on the fluid, and \mathbf{T} is the stress tensor. Of the external body forces, gravity $\vec{\mathbf{g}}$ is the only one expected to be acting on FHR systems. The stress tensor can be separated into pressure P and viscous forces $\vec{\boldsymbol{\tau}}$.

$$\begin{aligned} \rho \frac{D\vec{\mathbf{u}}}{Dt} &= \rho \vec{\mathbf{b}} + \nabla \cdot \mathbf{T} \\ &= -\nabla P + \rho \vec{\mathbf{g}} + \nabla \cdot \vec{\boldsymbol{\tau}} \end{aligned} \tag{2.1}$$

The Cauchy momentum equation can then be reduced to represent 1D flow in the axial x -direction. Using Cartesian coordinates, where $u = \vec{\mathbf{u}} \cdot \hat{x}$, all vector terms can be simplified to the system-level analysis pertinent to this scaling methodology. However, I have elected to retain the gravity vector $\vec{\mathbf{g}}$ because gravity does not act on 1D flow orthogonal to the direction of gravity. The multi-dimensional vector is kept for convenience and will be resolved later.

$$\rho \frac{\partial u}{\partial t} + \rho u \frac{\partial u}{\partial x} = -\frac{\partial P}{\partial x} + \rho \vec{\mathbf{g}} - \rho \nu \left(\frac{\partial^2 u}{\partial x^2} + \frac{\partial^2 u}{\partial y^2} + \frac{\partial^2 u}{\partial z^2} \right) \quad (2.2)$$

The last term on the right-hand side (RHS) of Eq. (2.2) represents shear forces acting on the fluid. Technically, this expression is only correct for laminar flow. For shear forces in turbulent flow, one can introduce a fluctuating velocity component to produce turbulent convection terms that remain in formulation for the y - and z - coordinates. A turbulent shear stress term equivalent in form to its laminar counterpart can then be achieved by time-averaging the entire equation. For brevity, I will leave that exercise to the reader and assume the shear term in Eq. (2.2) represents both laminar and turbulent shear forces. This term needs to be replaced anyways because the system-level analysis employed here does not allow for variation in u with respect to any direction besides the axial direction. Below, I show how to replace this term with one describing the equivalent impact of (laminar and turbulent) shear forces on 1D flow.

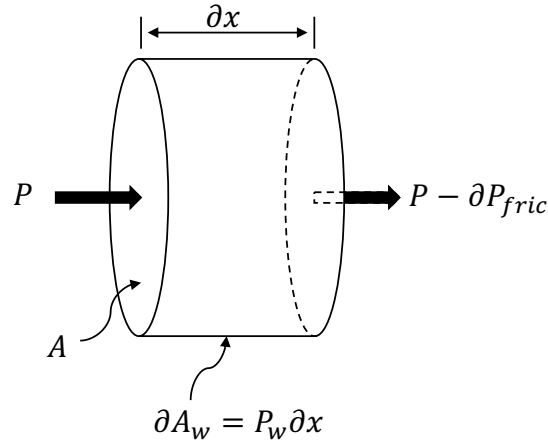


Figure 2.1: Cross section of axial flow down a cylinder showing a differential wall section inflicting a differential pressure drop due to friction.

I have included Fig. 2.1 to assist in visualizing how a differential wall section with some friction factor f' , induces friction shear forces, ∂F_{fric} . These forces can then be characterized

as a pressure gradient expression to replace the shear force term in Eq. (2.2) for describing wall friction.

$$A \partial P_{fric} = \partial F_{fric} = \left(\frac{1}{2} \rho u^2 \right) f' \partial A_w \quad (2.3)$$

$$\begin{aligned} \partial P_{fric} &= \frac{\rho u^2}{2} \frac{f' p_w}{A} \partial x \\ \frac{\partial P_{fric}}{\partial x} &= \frac{\rho u^2}{2} \frac{f}{D_h} \end{aligned} \quad (2.4)$$

$$\text{where } D_h = \frac{4A}{p_w}, \quad f = 4f'$$

$$\rho \nu \left(\frac{\partial^2 u}{\partial y^2} + \frac{\partial^2 u}{\partial z^2} \right) = \frac{\partial P_{fric}}{\partial x} = \frac{\rho u^2}{2} \frac{f}{D_h} \quad (2.5)$$

Inserting Eq. (2.5) into Eq. (2.2) produces the Navier-Stokes equation for 1D fluid flow. To quickly allude to work in later chapters, Eq. (2.6) serves as the basis for system-level fluid modeling, particularly in Argonne National Laboratory's System Analysis Module (SAM) system-level thermal hydraulics code. This is significant because the hydraulic physics captured by this equation are identical to physics captured by SAM simulations. Beyond acting as a confirmation checkpoint for the derivation thus far, this means any *scaled* behavior derived from this equation will align with SAM-simulated behavior as well. Therefore SAM can be used as a tool in conjunction with this methodology to probe system-level scaled behavior of FHRs.

$$\rho \frac{\partial u}{\partial t} + \rho u \frac{\partial u}{\partial x} = -\frac{\partial P}{\partial x} + \rho \vec{g} - \frac{\rho u^2}{2} \frac{f}{D_h} \quad (2.6)$$

Change in velocity	+	Convection term	=	Pressure term	+	Body force term	+	Friction term
-----------------------	---	--------------------	---	------------------	---	--------------------	---	------------------

Continuing with the derivation, it is useful to replace velocity u with mass flow rate \dot{m} to complement the prevalence of flow meters for measuring fluid movement in hydraulic systems. Typically, fluid does not accumulate in particular system locations, meaning mass flow rates are generally constant throughout flow loop (or loop branches). Compared to velocity, which is dependent on flow geometry and temperature, \dot{m} provides a more helpful metric for capturing fluid flow throughout a system.

Mathematically, velocity is related to mass flow rate by

$$u = \frac{\dot{m}}{\rho A} \quad (2.7)$$

Substituting this relation into Eq. (2.6) and dividing through by ρ ,

$$\frac{\partial \dot{m}}{\partial t \rho A} + \frac{\dot{m}}{\rho A} \frac{\partial \dot{m}}{\partial x \rho A} = \frac{-1}{\rho} \frac{\partial P}{\partial x} + \vec{g} - \frac{\dot{m}^2}{2\rho^2 A^2} \frac{f}{D_h} \quad (2.8)$$

By integrating along the flow path x , the integral form is found.

$$\int \frac{\partial \dot{m}}{\partial t} \frac{\partial x}{\rho A} + \int \frac{\dot{m}}{\rho A} \partial \left(\frac{\dot{m}}{\rho A} \right) = - \int \frac{\partial P}{\rho} + \sum \frac{P_{pump}}{\rho} + \int \vec{g} \partial x - \frac{\dot{m}^2}{2} \left[\int \frac{f}{D_h} \frac{\partial x}{\rho^2 A^2} + \sum K \frac{1}{\rho^2 A^2} \right] \quad (2.9)$$

Two modifications are made to supplement the integral form: first, the pressure supplied by the pump is separated out from the pressure into a standalone term conducive to representing pump contribution to the flow as point sources along the flow path. Second, the friction flow loss term incorporates the use of a form loss coefficient K to allow the description of the form losses at junctions etc.

It is now convenient to resolve the multi-dimensional gravity vector contained in the integral body force term. To do this, I introduce a new directional vector z . As opposed to the x -direction, which always aligns itself in the direction of fluid flow, the z -vector is static, always pointing opposite to the direction of gravity. Then, $\vec{g} \partial x$ can be resolved as a function of the (scalar) gravitational constant and the z -direction.

$$\int \vec{g} \partial x = \int -g \partial z \quad (2.10)$$

Non-dimensional variables can be supposed, which consist of dynamic variables (non-static in space and time) normalized by characteristic variables. To clarify the use of characteristic variables, I define “characteristic” here:

Characteristic Constant values, denoted by the subscript o , representative of the behavior of, or phenomena present in, a given system. Depending on the specifics of system behavior, the scaling analyst must determine characteristic parameters which properly characterize their system. These values can be used to normalize system behavior or relate various phenomena between (separate) distinct systems. Generally, characteristic values for a system should be selected such that ND variables will be of order unity.

$$\begin{aligned}
\dot{u} &= \frac{\dot{m}}{\rho_o u_o A_o} & \tau &= \frac{t}{L_o/u_o} & \mathfrak{X} &= \frac{x}{L_o} \\
\mathcal{Q} &= \frac{P}{\rho_o g H_o} & \mathcal{Q}_{pump} &= \frac{P_{pump}}{\rho_o g h_{pump,o}} & \xi &= \frac{z}{H_o}
\end{aligned} \tag{2.11}$$

Non-dimensional variables in Eq. (2.11) shown normalized by more than a single variable incorporate a characteristic parameter consisting of several other characteristic values. In these cases, the combined form is always written out in full. However, the single parameter can be deduced. These composite parameters are

$$\begin{aligned}
\dot{m}_o &= \rho_o u_o A_o \quad , \\
t_o &= \frac{m_o}{\dot{m}_o} = \left(\frac{\rho_o A_o}{\rho_o A_o} \right) \frac{L_o}{u_o} \quad , \\
P_o &= \rho_o g H_o \quad , \\
\text{and } P_{pump,o} &= \rho_o g h_{pump,o} \quad .
\end{aligned} \tag{2.12}$$

Substituting the non-dimensional variables from Eq. (2.11), resolving the gravity vector, and gathering terms results in the first iteration of the scaled momentum equation for fluid flow:

$$\begin{aligned}
\frac{\partial \dot{u}}{\partial \tau} \int \frac{\rho_o A_o}{\rho A} \partial \mathfrak{X} + \int \frac{\dot{u} \rho_o A_o}{\rho A} \partial \left(u \frac{\rho_o A_o}{\rho A} \right) &\overset{\ll}{=} \frac{-g H_o}{u_o^2} \left[\int \frac{\rho_o}{\rho} \partial \mathcal{Q} + \int \partial \xi \right] + \\
\frac{g h_{pump,o}}{u_o^2} \sum \frac{\rho_o}{\rho} \mathcal{Q}_{pump} - \left[\frac{L_o}{2} \int \frac{f}{D_h} \left(\frac{\rho_o A_o}{\rho A} \right)^2 \partial \mathfrak{X} + \sum \frac{K}{2} \left(\frac{\rho_o A_o}{\rho A} \right)^2 \right] &\dot{u}^2 \tag{2.13}
\end{aligned}$$

Numerical justification for neglecting ND convection term

Some terms left in Eq. (2.13) will later be selectively neglected in either component or integral system scaling analysis, but are left in formulation here to permit generalizability. However other terms, such as the second term on the left-hand side (LHS) of Eq. (2.13), are neglected entirely and removed from analysis.

For the convection term in particular, the loop integral sums to zero by definition, whereas component-specific values are considered negligible because the behavior of interest for scaling analysis does not typically include regions of large flow acceleration. Therefore, this term is removed from this scaling methodology.

To numerically demonstrate the negligible contribution supplied by the convection term, I conducted a sample calculation using validated, SAM-simulation data for a power (\dot{Q}) step

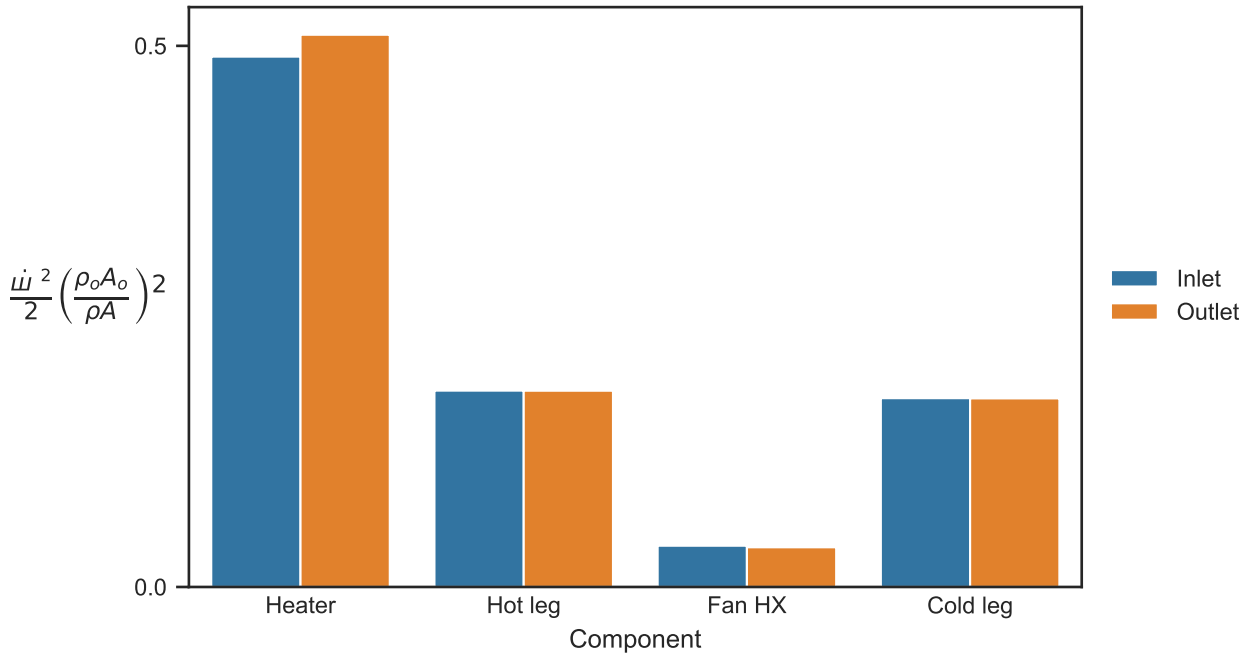


Figure 2.2: Local function values for the convection term in CIET primary loop components during the \dot{Q} -step experiment at steady-state full-power ($t = 5900\text{s}$).¹ The ND convection term is evaluated as the negligibly small differences between outlet and inlet values.

change experiment originally conducted in the CIET primary loop. I discuss these sample calculations in more detail in Secs. 4.2.1 and 4.2.2, where I use the same experiment for Mark 2 (Mk.II) scaling analysis. Assuming steady-state, with characteristic parameters taken at the heater section midpoint, Fig. 2.2 shows convection term *local* values at pipe junctions along the CIET primary loop. The ND convection term evaluated for an entire component is found as the difference between the plotted values at the component inlet and outlet. I show these component ND convection term values for CIET’s heater, hot leg, fan, and cold leg in Tbl. 2.1. The integral system value is omitted because the ND convection term loop integral sums to zero by definition. To contextualize the ND convection term, I normalize these values with the weighting factor to the $\partial \dot{u} / \partial \tau$ term, as seen in Eq. (2.13) — $\int \frac{\rho_o A_o}{\rho A} \partial \mathcal{J}$. This value is introduced as the “fluid momentum inertia number” in Sec. 2.2.1. For now, it suffices to simply say this weighting factor dictates how strongly every term impacts flow acceleration and is, therefore, an apt measure to indicate relative significance.

For a term to be significant, it would need to be at least within an order of magnitude below the weighting factor — 10% or greater when using the relative significance metric.

¹SAM validation data from simulated \dot{Q} -step experiment in CIET (described further in Sec. 4.2.1)

Table 2.1: Component-wise ND convection term and relative significance in the CIET \dot{Q} -step experiment at steady-state full-power ($t = 5900$ s).¹ The relative significance values show the convection term is negligible.

	Component			
	Heater	Hot Leg	Fan	Cold Leg
$N_{FMI}^{\circ} = \int \frac{\rho_o A_o}{\rho A} \partial \mathcal{J}$	1.00	0.90	0.22	2.57
ND convection term				
$\left(\frac{\dot{u} \rho_o A_o}{2 \rho A} \right)^2 \Big _{in}^{out}$	2×10^{-2}	-9×10^{-5}	-1×10^{-3}	-2×10^{-4}
Relative significance				
$\left \left(\frac{\dot{u} \rho_o A_o}{2 \rho A} \right)^2 \Big _{in}^{out} / N_{FMI}^{\circ} \right $	2%	0.01%	0.7%	0.008%

The convection term does not meet these requirements. The relative significance values in Tbl. 2.1 demonstrate the convection term is negligible for this analysis, which goes to support my decision to remove the ND convection term from formulation.

Numerical justification for maintaining non-unity density ratios

In scaling analysis for incompressible fluids, it is common to employ the Boussinesq approximation to neglect changes in fluid density. The justification is that density fluctuations are small and can thus be ignored (except in buoyancy terms). For this scaling methodology, employing the Boussinesq approximation would mean $\rho_o/\rho \implies 1$ and all density ratios in Eq. (2.13) would disappear.

To investigate the applicability of the Boussinesq approximation to this scaling methodology, I evaluated ND terms with and without $\rho_o/\rho = 1$ and evaluated the relative significance of the Boussinesq-induced *differences* in values. For brevity's sake, I preemptively adopt nomenclature from Eq. (2.81).

The relative significance metric used in Tbl. 2.2 to quantify the impact of the Boussinesq

approximation on each term is defined as

$$\Delta/\mathcal{N}_{FMI}^0 = \left| \frac{[\text{Term}] \Big|_{\rho=\rho_o} - [\text{Term}] \Big|_{\rho \neq \rho_o}}{\int \frac{\rho_o A_o}{\rho A} \partial \mathcal{K}} \right| \times 100 \% \quad , \quad (2.14)$$

Table 2.2: Impact of the Boussinesq approximation on various ND terms in the CIET \dot{Q} -step experiment at steady-state full-power ($t = 5900$ s).¹ The relative significance values ($\Delta/\mathcal{N}_{FMI}^0$) show the proportional difference between terms with and without a constant $\rho \approx \rho_o$ is significant.

	Component				System
	Heater	Hot Leg	Fan	Cold Leg	Loop Integral
$\mathcal{N}_{FMI}^0 = \int \frac{\rho_o A_o}{\rho A} \partial \mathcal{K}$	1.00	0.90	0.22	2.57	4.69
ND pressure term					
$\frac{-1}{Fr} \int \frac{\rho_o}{\rho} \partial \Psi$	87.28	105.83	3.01	-193.22	2.89
$\frac{-1}{Fr} \int \partial \Psi$	87.32	104.77	3.01	-195.10	0.00
$\Delta/\mathcal{N}_{FMI}^0$	4.3 %	120 %	0.90 %	73 %	62 %
ND pump driving force term					
$Eu \sum \frac{\rho_o}{\rho} \mathcal{Q}_{pump}$				53.38	53.38
$Eu \sum \mathcal{Q}_{pump}$				53.91	53.91
$\Delta/\mathcal{N}_{FMI}^0$				20 %	11 %
ND friction term					
$-\mathcal{F} \dot{u}^2 \Big _{\rho \neq \rho_o}$	-8.83	-14.03	-15.99	-16.91	-55.76
$-\mathcal{F} \dot{u}^2 \Big _{\rho = \rho_o}$	-8.89	-13.75	-16.26	-17.23	-56.13
$\Delta/\mathcal{N}_{FMI}^0$	5.8 %	31 %	125 %	12 %	8.0 %

again using \mathcal{N}_{FMI}^0 to contextualize the impact of employing an approximation. Table 2.2 shows the relative differences between $\rho = \rho_o$ terms and $\rho \neq \rho_o$ terms are significant for this analysis. Therefore, this example supports my decision that the Boussinesq approximation should not be employed in formulating the scaling equations in this methodology.

2.2.1 Fully-derived ND momentum equation for forced circulation fluid flow

A fully-derived ND equation, also referred to as a “final scaling equation”, is significant to scaling analysis because it shows the interplay between various ND terms and contains all scaling numbers derived for the physics modeled by the scenario at hand. For the pump-driven flow scenario, the final fluid momentum scaling equation is produced by simplifying remaining terms in Eq. (2.13) and gathering ND ratios into known scaling parameters.

$$\frac{\partial \dot{u}}{\partial \tau} \int \frac{\rho_o A_o}{\rho A} \partial_{\mathcal{X}} = \frac{-1}{Fr} \left[\int \frac{\rho_o}{\rho} \partial \mathcal{V} + \Delta \xi \right] + Eu \sum \frac{\rho_o}{\rho} \mathcal{V}_{pump} - \mathcal{F} \dot{u}^2 \quad (2.15)$$

ND flow acceleration	×	Fluid momentum inertia (FMI)	=	ND pressure	+	ND body force	+	ND pump driving force	+	ND friction
-------------------------	---	---------------------------------	---	----------------	---	------------------	---	--------------------------	---	----------------

For each fully-derived scaling equation in Secs. 2.2 to 2.5, newly derived scaling parameters will be discussed. For Eq. (2.15), the new scaling parameters include the Froude number (Fr), Euler number (Eu), and the Friction number (\mathcal{F}). Additionally, the FMI number (\mathcal{N}_{FMI}^0) introduces a parameter essential for transient scaling analysis and otherwise valuable for contextualizing the other scaling terms in formulation.

Fluid momentum inertia number (\mathcal{N}_{FMI}^0)

Previously, the FMI number was used as a normalizing parameter in Tbls. 2.1 and 2.2 to gauge the relative impact of various values on the ND momentum equation. In that context, \mathcal{N}_{FMI}^0 was considered a weighting factor to the ND fluid acceleration term. This is because the larger the value, the larger the deviations between other terms need to be to induce a transient. By dictating the system’s propensity to deviate from the status quo, \mathcal{N}_{FMI}^0 acts as a type of **inertia** for the ND acceleration term in the **fluid momentum** equation — hence the name.

$$\mathcal{N}_{FMI}^0 = \int \frac{\rho_o A_o}{\rho A} \partial_{\mathcal{X}} \quad (2.16)$$

The FMI number can typically be neglected in analysis performed for scaled system design. However, it is useful for analyzing the progression of system-level hydraulic behavior in transient scaling regimes. [Section 2.6.3](#) continues this discussion.

Froude number (Fr)

The Froude number impacts the ND pressure and body force terms in an inverted form.

$$\frac{1}{Fr} = \frac{gH_o}{u_o^2} \quad \text{“}\equiv\text{”} \quad \frac{\text{gravitational potential}}{\text{flow inertia}} \quad (2.17)$$

For FHRs, this Fr ratio is expected to be large due to the coolant’s low velocity (enabled by its high heat capacity). I have already numerically supported this assessment with CIET data in [Tbl. 2.2](#).

Euler number (Eu)

The Euler number only impacts the ND pump driving forced term.

$$Eu = \frac{gh_{pump,o}}{u_o^2} \quad \text{“}\equiv\text{”} \quad \frac{\text{pump force}}{\text{inertial forces}} \quad (2.18)$$

The Eu and Fr terms appear remarkable similar, one bearing the characteristic loop height and the other bearing the pump head. Both terms are required for scaling analysis due to the necessary height-scale term used for ND-ization. Without separating \mathcal{Q} out from \mathcal{Q}_{pump} , the ND pressure term becomes convoluted, as \mathcal{Q} requires ND-izing with a characteristic pressure related to the hydrostatic pressure, whereas \mathcal{Q}_{pump} benefits from normalizing the instantaneous pressure supplied by the pump to pump head — a parameter commonly used to characterize pump performance. Additionally, separating the “hydrostatic pressure term” and the “driving force term” further benefit analysis by retaining the *meaning* behind their respective ND parameters (defined in [Eqs. \(2.17\)](#) and [\(2.18\)](#)).

One might observe the density ratio ρ_o/ρ within the driving force term might seem to imply a numerical difference between the driving forces supplied by equally-strong pumps situated in the hot and cold legs of a loop. This deduction is false because this density ratio simply resolves the use of characteristic density to normalize P_{pump} in [Eq. \(2.11\)](#), $P_{pump,o} = \rho_o g h_{pump}$.

Friction number (\mathcal{F})

The friction number is a scaling number of the same vein as N_{FMI} — they include integral terms that can vary over time.

$$\mathcal{F} = \frac{L_o}{2} \int \frac{f}{D_h} \left(\frac{\rho_o A_o}{\rho A} \right)^2 \partial_{\mathcal{K}} + \sum \frac{K}{2} \left(\frac{\rho_o A_o}{\rho A} \right)^2 \quad \text{“}\equiv\text{”} \quad \frac{\text{momentum dissipation}}{\text{flow inertia}} \quad (2.19)$$

Really, \mathcal{F} is a ND term that does not need to be. The ND form is simply maintained for consistency. The *dimensional* friction term from Eq. (2.6) could be used to derive the ND \mathcal{F} instead:

$$\mathcal{F} = \frac{1}{2} \int \frac{f}{D_h} \left(\frac{u}{u_o} \right)^2 \partial x + \sum \frac{K}{2} \left(\frac{u}{u_o} \right)^2 \quad (2.20)$$

The friction number is composed of a flow loss part and form loss part. That formulation is purely an advantage, as the \mathcal{F} does not discriminate between the two parts in contributing to the sum total. This means the scaling analyst can adjust either flow losses or form losses to match their desired \mathcal{F} -value. If the ND friction for some scaled experimental design is found to be too low, it is typically easy to amend that distortion by adding sources of form losses, such as valves.

2.2.2 Component scaling considerations for forced circulation fluid flow

The generalizable scaling equation, Eq. (2.15), modifies its form when applied to component scaling. Consider a component bounded by points 1 \rightarrow 2. The component scaling equation for forced circulation fluid flow is shown as Eq. (2.21).

$$\frac{\partial \dot{u}}{\partial \tau} \int_1^2 \frac{\rho_o A_o}{\rho A} \partial_{\mathcal{K}} = \frac{-1}{Fr_c} \left[\int_1^2 \frac{\rho_o}{\rho} \partial \mathcal{Q} + \xi \Big|_1^2 \right] + Eu \sum \frac{\rho_o}{\rho} \mathcal{Q}_{pump} - \mathcal{F}_c \dot{u}^2 \quad (2.21)$$

The scaling numbers produced are $\mathcal{N}_{FMI,c}$, Fr_c , Eu , and \mathcal{F}_c . The only difference between Fr_c and Fr is that Fr_c requires component-specific characteristic parameter definitions.

$$\frac{1}{Fr_c} = \frac{gH_{o,c}}{u_{o,c}^2} \quad (2.22)$$

The entire loop “feels” fluid friction effects from everywhere, so \mathcal{F} is considered exclusively in integral system scaling. The component \mathcal{F}_c should be calculated only to help find the integral system \mathcal{F} .

If the region of analysis for component scaling does not include a pump, the ND scaling term will disappear from formulation. Therefore, it is somewhat redundant for this methodology

to consider a general Eu as well as a component-specific Eu_c , so the subscript has been dropped.

2.2.3 Integral system scaling considerations for forced circulation fluid flow

Equation (2.15) is applied to integral system scaling by evaluating integral terms around the entire loop, starting and ending at the same point. The body force term then drops out by definition, as the change in elevation is zero. The component scaling equation for forced circulation fluid flow is shown as Eq. (2.21).

$$\frac{\partial \dot{u}}{\partial \tau} \oint \frac{\rho_o A_o}{\rho A} \partial_{\mathcal{K}} = \frac{-1}{Fr} \oint \frac{\rho_o}{\rho} \partial \Psi + Eu \sum \frac{\rho_o}{\rho} \Psi_{pump} - \mathcal{F} \dot{u}^2 \quad (2.23)$$

The scaling numbers produced by Eq. (2.23) are that same as those discussed in Sec. 2.2.1. However, loop integrals slightly alter the N_{FMI}^o and \mathcal{F} expressions.

$$N_{FMI}^o = \oint \frac{\rho_o A_o}{\rho A} \partial_{\mathcal{K}} \quad (2.24)$$

$$\mathcal{F} = \frac{L_o}{2} \oint \frac{f}{D_h} \left(\frac{\rho_o A_o}{\rho A} \right)^2 \partial_{\mathcal{K}} + \sum \frac{K}{2} \left(\frac{\rho_o A_o}{\rho A} \right)^2 \quad (2.25)$$

As opposed to the component scaling parameter \mathcal{F}_c , the integral loop \mathcal{F} is an important number for integral system scaling analysis. Flow in a loop “feels” the friction effects across the entire loop, so maintaining the proportion of ND friction effects in each specific component is not necessary. Instead, the loop-wide \mathcal{F} can be coerced into matching some desired value by adding sources of flow friction into the loop.

2.2.4 Characteristic parameters for forced circulation fluid flow scaling

I introduced characteristic parameters in Eq. (2.11) for the sake of ND-izing the fluid momentum equation. However, I previously neglected to discuss how these parameters should be selected for scaling analysis. For each scaling equation derivation in Secs. 2.2 to 2.5, I will address characteristic parameters and suggest how they might be selected.

When ND variables are assigned a normalizing variable properly representative of the system behaviour, the ND variable should ideally approximate unity (~ 1) throughout the loop.

Some characteristic parameters will be obvious, depending on the scaling regime, and do not require much discussion. Others, such as the characteristic height, require more thorough investigation. In the end, the onus for characterizing system behavior with representative variables falls on the scaling analyst, but in some cases these suggestions will help.

Characteristic length-scale (L_o)

To capture an ideal length-scale, either the length of a significant heat transfer component, e.g. heater/core, or length of an entire loop should be chosen.

Characteristic area-scale (A_o)

The characteristic area should either be the average/midpoint area of a significant heat transfer component or the average area of entire loop.

Characteristic density-scale (ρ_o)

At characteristic steady-state, the characteristic fluid density should be taken at $T_{avg} = (T_H + T_C)/2$.

Characteristic velocity-scale (u_o)

At steady-state, the velocity at midpoint of significant heat transfer component, presumably at T_{avg} , could be considered characteristic. Alternatively u_o could be taken in conjunction with the characteristic density- and area-scales to achieve a total characteristic mass flow rate, $\dot{m}_o = \rho_o u_o A_o$. With ρ_o evaluated at T_{avg} , and A_o chosen otherwise, u_o can be chosen to produce a system representative \dot{m}_o .

Characteristic pump head-scale ($h_{pump,o}$)

The characteristic pump head is probably best taken as the pump head required at steady-state full-power operation.

Characteristic height-scale (H_o)

The characteristic height, embedded in the Fr , serves as a coefficient to the ND pressure term and ND body force term. For component scaling, the ND body force term hints that the characteristic height should be defined as the height difference between the component inlet and outlet. Revisiting the characteristic parameter definitions in Eq. (2.11), a H_o defined as such would result in a satisfying $\xi = [0, 1]$. For integral system scaling however, the ND body force term drops out of formulation, leaving the ND pressure term as the only remaining term impacted by the height-scale. This hints that \mathcal{V} , not ξ , should dictate the H_o definition. For the pressure term, however, the *change* in loop pressure is the important bit.

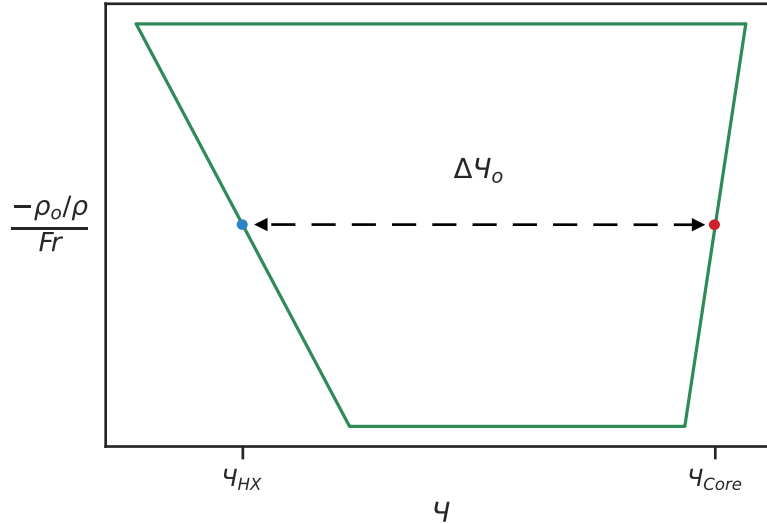


Figure 2.3: Idealized loop integral of the ND pressure term, which is evaluated as the area within the trapezoid. System-wide pressure differentials are best characterized by defining the characteristic height-scale between the midpoints of heat transfer components, shown here by the red and blue dots for the core and HX, respectively.

Figure 2.3 shows the loop-wise ND pressure term can be approximated as the area of a trapezoid, assuming linear temperature change in the heat transfer components and no PHL.

$$\frac{-1}{Fr} \oint \frac{\rho_o}{\rho} \partial \psi \approx \frac{1}{Fr} \left(\frac{\rho_o}{\rho_H} - \frac{\rho_o}{\rho_C} \right) \Delta \psi_o \quad (2.26)$$

This expression reveals $\Delta \psi_o$ — the $\Delta \psi$ between heat transfer component midpoints — is more important to integral system scaling analysis than absolute ψ values. Therefore, the normalizing variable for ψ in Eq. (2.11) should be thought of as a ΔP_o instead of simply P_o , implying the characteristic height-scale for forced circulation scenarios should be defined as the height difference between the midpoints of the loop's heat transfer components.

2.3 Fluid Momentum Scaling Parameters for Natural Circulation Fluid Flow

In the previous section, the driving force for fluid flow was supplied by a pump. A new fluid momentum scaling equation can be derived for pump-less loops in which temperature-induced density gradients, buoyancy, drive fluid flow. In FHRs, natural circulation flow loops

provide passive cooling to the core. Additionally, natural circulation back-flow scenarios can be induced following loss of forced cooling — of particular interest to FHR radHT analysis when considering heat transfer from the core barrel across the downcomer. Therefore it is of interest to this methodology to derive scaling parameters for natural circulation loops.

The 1D Navier-Stokes equation was previously derived as Eq. (2.6), and is generalizable to pump- and buoyancy-driven flows. This equation serves as a good starting point for scaling natural flow behavior. To highlight the influence of temperature variation in the buoyancy force term, I suppose

$$\rho(T) = \rho_o + \frac{\partial \rho}{\partial T}(T - T_o) \quad (2.27)$$

to separate density change expressions, where ρ_o is the characteristic fluid density which exists at $T = T_o$. The characteristic fluid density should be chosen such that it is within the range present in the system during “characteristic” operation. Investigating the use of the fluid thermal expansion coefficient, β :

$$\beta \partial T = \frac{\partial V}{V} \quad \text{where } \rho = \frac{m}{V}, \quad \text{so } \partial V = m \partial \left(\frac{1}{\rho} \right) \quad (2.28)$$

$$\beta \partial T = \rho \partial \left(\frac{1}{\rho} \right) \quad \text{where } \partial \left(\frac{1}{\rho} \right) = \frac{-\partial \rho}{\rho^2} \quad (2.29)$$

$$\begin{aligned} \beta \partial T &= \frac{-\partial \rho}{\rho} \\ \beta &= \frac{-1}{\rho} \frac{\partial \rho}{\partial T} \end{aligned} \quad (2.30)$$

Combining Eqs. (2.27) and (2.30) and inserting the expression into Eq. (2.6) produces the 1D Navier-Stokes equation with the inclusion of a buoyancy term, split off from the body force term.

$$\frac{\partial u}{\partial t} + u \frac{\partial u}{\partial x} = \frac{-1}{\rho} \frac{\partial P}{\partial x} + \frac{\rho_o}{\rho} \vec{g} - \beta(T - T_o) \vec{g} - \frac{u^2}{2} \frac{f}{D_h} \quad (2.31)$$

Following the same derivation steps followed for Eq. (2.9), velocity is replaced with mass flow rate and the integral along flow path is taken.

$$\begin{aligned} \int \frac{\partial \dot{m}}{\partial t} \frac{\partial x}{\rho A} + \int \frac{\dot{m}}{\rho A} \partial \left(\frac{\dot{m}}{\rho A} \right) &= - \int \frac{\partial P}{\rho} + \\ &\int \frac{\rho_o}{\rho} \vec{g} \partial x - \int \beta(T - T_o) \vec{g} \partial x - \frac{\dot{m}^2}{2} \left[\int \frac{f}{D_h} \frac{\partial x}{\rho^2 A^2} + \sum K \frac{1}{\rho^2 A^2} \right] \end{aligned} \quad (2.32)$$

Non-dimensional variables are supposed for normalizing variables for natural circulation scaling analysis. The ND variables here differ from those for forced circulation analysis, shown in Eq. (2.11). The ND pump pressure is abandoned, as there is no pump in this analysis, and replaced by a ND fluid temperature θ , which is necessary to capture the ND driving force in buoyancy-driven flow.

$$\begin{aligned} \dot{u} &= \frac{\dot{m}}{\rho_o u_o A_o} & \tau &= \frac{t}{L_o/u_o} & \mathfrak{X} &= \frac{x}{L_o} \\ \Psi &= \frac{P}{\rho_o g H_o} & \xi &= \frac{z}{H_o} & \theta &= \frac{T - T_o}{T_{H,o} - T_{C,o}} \end{aligned} \quad (2.33)$$

Again, as with Eq. (2.11), the composite parameters are written out in their full form but can be deduced. Here, these are

$$\begin{aligned} \dot{m}_o &= \rho_o u_o A_o \quad , \\ t_o &= \frac{m_o}{\dot{m}_o} = \left(\frac{\rho_o A_o}{\rho_o A_o} \right) \frac{L_o}{u_o} \quad , \\ P_o &= \rho_o g H_o \quad , \\ \text{and } \Delta T_o &= T_{H,o} - T_{C,o} \quad . \end{aligned} \quad (2.34)$$

Substituting the non-dimensional variables in Eq. (2.33) into Eq. (2.32), I arrive at the ND-ized Navier-Stokes equation adjusted to facilitate the analysis of natural circulation.

$$\begin{aligned} \frac{\partial \dot{u}}{\partial \tau} \int \frac{\rho_o A_o}{\rho A} \partial \mathfrak{X} + \int \dot{u} \frac{\rho_o A_o}{\rho A} \partial \left(\dot{u} \frac{\rho_o A_o}{\rho A} \right) &= \frac{-g H_o}{u_o^2} \left[\int \frac{\rho_o}{\rho} \partial \Psi + \int \frac{\rho_o}{\rho} \partial \xi \right] + \\ \frac{g \beta_o H_o \Delta T_o}{u_o^2} \int \left(\frac{\beta}{\beta_o} \right) \theta \partial \xi - \left[\frac{L_o}{2} \int \frac{f}{D_h} \left(\frac{\rho_o A_o}{\rho A} \right)^2 \partial \mathfrak{X} + \sum \frac{K}{2} \left(\frac{\rho_o A_o}{\rho A} \right)^2 \right] &\dot{u}^2 \end{aligned} \quad (2.35)$$

Again, the convection term can be considered negligible and removed from formulation. Additionally, I consider β/β_o a unity ratio while simultaneously retaining ρ_o/ρ in formulation, a seeming discrepancy which I justify shortly. In this form, Eq. (2.35) closely resembles Eq. (2.13), except with two differences resulting from the buoyancy-focused approach taken in derivation. Firstly, the new body force term $\int \rho_o/\rho \partial \mathfrak{X}$ includes a density ratio. More importantly however, this formulation includes a buoyancy force term, which can be considered the driving force term for natural circulation applications of this scaling methodology.

This term serves the same purpose as the pump-pressure driving force term in Eq. (2.13) for forced flow applications.

Justification for assuming a constant thermal expansion coefficient

There seemingly arose a discrepancy in my treatment of fluid thermal expansion in the derivation of Eq. (2.35), specifically between the Ri and Fr terms. For the buoyancy force term, I assume variation in the fluid thermal expansion coefficient β is negligible. However for the pressure and body force terms, I maintain the density ratios to capture temperature-driven changes in fluid density, thereby refraining from utilizing the Boussinesq approximation, which is commonly enforced in scaling analysis (e.g. [33, 37, 41, 44, 47, 52]).

To justify this discrepancy, it is useful to revisit the penultimate step in the derivation of Eq. (2.30). In particular, $\beta \partial T = -\partial \rho / \rho$ reveals the fluid thermal expansion is dependent on both β and temperature change. For reactor applications, ∂T provides a much more substantial contribution to proportional fluid expansion than does alterations in β . Therefore, β can be assumed constant without significantly distorting numerical expressions of thermal expansion nor the Ri . On the other hand, fluid expansion as a function of density depends only on a single variable, and therefore cannot be held constant without distorting the result.

Again, a numerical example can help support decisions in derivation. I return to using SAM-simulated validation data, this time for DHX-DRACS coupled-loop natural circulation tests originally conducted in CIET's primary and DRACS loops. These sample calculations are further discussed in Sec. 4.2.1 and used for Mk.II scaling analysis in Sec. 4.2.3. Preemptively borrowing nomenclature from Eq. (2.37) below, Tbl. 2.3 shows the loop integral ND buoyancy force evaluated with a temperature-dependent β and again with a constant β_o . The relative significance metric used here to quantify the impact of the constant thermal expansion coefficient approximation on the ND buoyancy force term is defined as

$$\Delta / \mathcal{N}_{FMI}^{\circ} = \left| \frac{[\text{Term}] \Big|_{\beta=\beta_o} - [\text{Term}] \Big|_{\beta \neq \beta_o}}{\oint \frac{\rho_o A_o}{\rho A} \partial \mathcal{K}} \right| \times 100 \% \quad . \quad (2.36)$$

The relative difference data in Tbl. 2.3 are negligibly low, particularly for the natural circulation loop of interest — the DRACS loop. These data support the decision to approximate a constant β_o for the buoyancy force term. This step in derivation has the added benefit of enabling a constant Ri to be pulled out of the buoyancy term integral, which can then be conveniently used as a constant scaling number rather than as an inconvenient variable one (such as the \mathcal{F}). Considering a constant Ri is essential to scaled system design and surrogate

Table 2.3: Impact of the constant thermal expansion coefficient approximation on the ND buoyancy force term in the CIET DHX-DRACS coupled-loop natural circulation experiment at steady-state ($\dot{Q} = 2.4 \text{ kW}$).² The relative significance values (Δ/N°_{FMI}) show the proportional difference between buoyancy terms with and without a constant $\beta \approx \beta_o$ is negligible.

	Primary Loop	DRACS Loop
$N^{\circ}_{FMI} = \oint \frac{\rho_o A_o}{\rho A} \partial_{\mathcal{K}}$	3.05	7.56
ND buoyancy force term		
$\oint Ri(\beta)_{\mathcal{K}} \theta \partial \xi$	55.3	157.98
$Ri(\beta_o) \oint \theta \partial \xi$	55.0	157.96
Δ/N°_{FMI}	9.3 %	0.21 %

fluid selection, assuming a constant β_o is necessary, even for systems with relatively high Δ/N°_{FMI} values (such as Primary Loop in Tbl. 2.3).

2.3.1 Fully-derived ND momentum equation for natural circulation fluid flow

Accepting the constant β assumption and gathering terms into scaling parameters produces the fluid momentum scaling equation for natural flow.

$$\frac{\partial \dot{u}}{\partial \tau} \int \frac{\rho_o A_o}{\rho A} \partial_{\mathcal{K}} = \frac{-1}{Fr} \left[\int \frac{\rho_o}{\rho} \partial \psi + \int \frac{\rho_o}{\rho} \partial \xi \right] + Ri \int \theta \partial \xi - \mathcal{F} \dot{u}^2 \quad (2.37)$$

ND flow acceleration	×	Fluid momentum inertia (FMI)	=	ND pressure	+	ND body force	+	ND buoyancy driving force	+	ND friction
----------------------	---	------------------------------	---	-------------	---	---------------	---	---------------------------	---	-------------

²SAM validation data from simulated DHX-DRACS coupled-loop natural circulation tests in CIET (described further in Sec. 4.2.1)

Deriving this form of the momentum equation raises the question, “is the buoyancy driving force term worth deriving for the scaled momentum equation for forced circulation?” In the end, I decided retaining the buoyancy term in formulation for forced circulation applications holds little worth. While pump-to-buoyancy driving force comparisons could be made, extra scaling terms would be introduced but hardly used for analytical design purposes. I find it best to capture the buoyancy effects within the body force term for forced circulation applications. However, this decision should be recognized should the need to investigate buoyancy effects arise (e.g. in mixed flow scenarios).

Richardson number (Ri)

The scaling parameters produced by Eq. (2.37) are almost identical to those produced for forced flow scaling. The exceptions resulting from the new derivation include a new body force integral and new driving force term, which introduces the new Ri scaling number.

$$Ri = \frac{g\beta_o H_o \Delta T_o}{u_o^2} \quad “\equiv” \quad \frac{\text{buoyancy forces}}{\text{inertial forces}} \quad (2.38)$$

This scaling parameter includes the natural circulation u_o , which is discussed starting on Pg. 46.

2.3.2 Component scaling considerations for natural circulation fluid flow

Applying Eq. (2.37) to a component bounded by points 1 \rightarrow 2:

$$\frac{\partial \dot{u}}{\partial \tau} \int_1^2 \frac{\rho_o A_o}{\rho A} \partial_{\mathcal{K}} = \frac{-1}{Fr_c} \left[\int_1^2 \frac{\rho_o}{\rho} \partial \Psi + \int_1^2 \frac{\rho_o}{\rho} \partial \xi \right] + Ri_c \int_1^2 \theta \partial \xi - \mathcal{F}_c \dot{u}^2 \quad (2.39)$$

However, it is not immediately clear what components would garner applications of this equation for scaling purposes. Besides pool-type configurations, natural circulation in reactors typically exists as an integral full-loop phenomenon. Therefore, component scaling for natural circulation flow will be ignored.

2.3.3 Integral system scaling considerations for natural circulation fluid flow

Integrating Eq. (2.37) around the entire loop produces the fluid momentum scaling equation for natural circulation. In forced circulation analysis, the body force term dropped out of formulation. Here, it is preserved on account of the density ratio within the body force integral.

$$\frac{\partial \dot{u}}{\partial \tau} \oint \frac{\rho_o A_o}{\rho A} \partial_{\mathcal{K}} = \frac{-1}{Fr} \left[\oint \frac{\rho_o}{\rho} \partial \Psi + \oint \frac{\rho_o}{\rho} \partial \xi \right] + Ri \oint \theta \partial \xi - \mathcal{F} \dot{u}^2 \quad (2.40)$$

The scaling parameters to be used in natural circulation scaling analysis are N_{FMI}^0 , Fr , Ri , and \mathcal{F} . All have been previously introduced.

2.3.4 Characteristic parameters for natural circulation fluid flow scaling

Most characteristic parameters used for ND-izing the buoyancy-driven fluid momentum equation were discussed in [Sec. 2.2.4](#). The *new* characteristic parameters are presented here.

Characteristic temperature-scale (ΔT_o)

The characteristic temperature-scale is defined as the difference between characteristic hot and cold system temperatures, $\Delta T_o = T_{H,o} - T_{C,o}$. In an ideal loop without PHL, these temperatures could be taken at the core/heater and heat exchanger (HX)/fan outlets, respectively. With PHL considered, the ΔT_o is ideally found across the core/heater section.

Characteristic temperature (T_o)

The “scale” suffix is dropped for this parameter because T_o is not used as a normalizing variable in [Eq. \(2.33\)](#). However, T_o is still necessary to characterize ND temperatures. Whether T_o is taken at $T_{avg} = (T_{H,o} + T_{C,o})/2$ or at $T_{C,o}$ is a matter of preference. The buoyancy force term integral $\int \theta \partial \xi$ will be the same regardless. I prefer using $T_o = T_{C,o}$ so θ is always positive during normal operation, but this is not necessary.

Characteristic buoyancy-scale (β_o)

Just as ρ_o is evaluated at T_{avg} , so to should β_o .

Characteristic height-scale (H_o)

The characteristic height-scale was previously discussed on [Pg. 38](#), where the ND pressure term revealed H_o should be taken as the height difference between the core/heater and HX/fan midpoints. For natural circulation scaling, the height-scale-containing buoyancy term is far more important to analysis.

Looking at [Fig. 2.4](#), the ND buoyancy driving force term can be approximated as the area of a quadrilateral, again assuming linear temperature change in heat transfer components and no PHL,

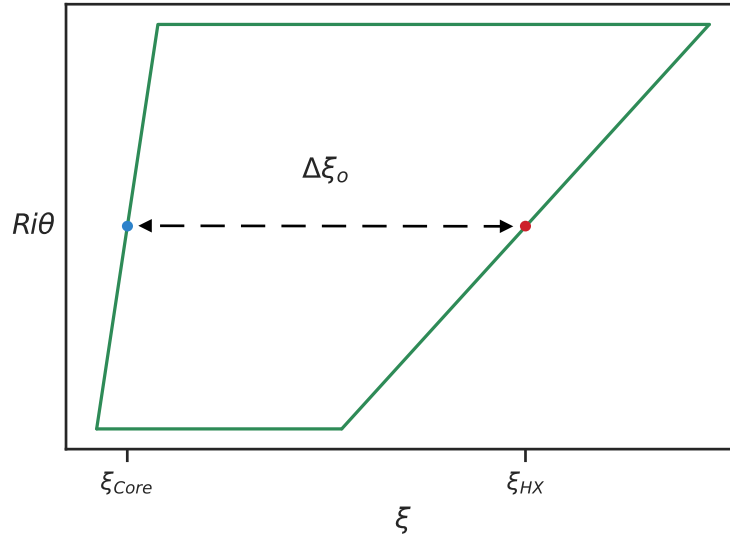


Figure 2.4: Idealized loop integral of the ND buoyancy term, which is evaluated as the area within the quadrilateral. Buoyancy forces are best captured by the Ri if the height-scale is chosen between the midpoints of heat transfer components, shown here by the red and blue dots for the core and HX, respectively.

$$Ri \oint \theta \partial \xi \approx Ri \Delta \theta_o \Delta \xi_o \quad , \quad (2.41)$$

where $\Delta \theta_o$ and $\Delta \xi_o$ are taken at the vertical sections' midpoints. If $T_{H,o}$ and $T_{C,o}$ are taken as the hot and cold leg temperatures, respectively, $\Delta \theta_o = 1$. Then the buoyancy term can be conveniently approximated as unity at characteristic conditions if $\Delta \xi_o = 1$, which *is* true if H_o is taken between the midpoints of system heat transfer components. Therefore, in agreement with forced circulation scaling, H_o should be taken just there.

Characteristic velocity-scale (u_o)

Characteristic fluid velocity u_o is ubiquitously used to ND-ize across Eq. (2.37) — it appears in the Fr in the ND pressure and body force terms, the Ri in the ND driving force term, and \dot{u}^2 in the ND friction term. Of particular importance for scaling analysis, the Fr and Ri require a u_o value. However, obtaining a characteristic u_o value for a natural circulation flow loop (especially when it is yet to be built) is not always a simple task. With forced circulation scaling analysis, the scaling analyst can almost always assume they will be able to adjust pump speed to achieve the desired Eu in their experimental loops, but for natural circulation loops the interplay between momentum and energy that generates fluid flow cannot be so

easily controlled. To justify the existing formulation of Eq. (2.37) a u_o must be practically obtainable.

I conducted a literature review, summarized below, to provide examples for how characteristic fluid velocities are determined for natural circulation systems. Based on the reviewed examples, I defined my own natural circulation u_o . The final expression is shown below, the same equation as derived in Eq. (2.59) near the end of this section.

$$u_o = \sqrt{\frac{2gH_o}{A_o^2} \left[\frac{\beta_o \Delta T_o - \left(\frac{\rho_C^2 - \rho_H^2}{\rho_C \rho_H} \right)}{\oint \frac{f}{D_h A^2} \partial x + \sum \frac{K}{A^2}} \right]} \quad (2.42)$$

Thermal hydraulicists utilizing this scaling methodology can either adopt my derived u_o definition above, follow one of the reviewed methods exactly, or simply use them as guidance for how they might determine a u_o themselves. Throughout this brief literature review, I discuss approaches for finding \dot{m}_o and u_o interchangeably.

Approaches for finding a steady-state analytical u_o : Perhaps the most unambiguous and detailed demonstration of obtaining an analytical steady-state \dot{m} that I have read comes from Appendix C of the **SAM CIET Validation** report [55]. The CIET experiment contains a primary loop, which operates under pump-driven flow conditions, and two coupled natural circulation loops. Instead of starting off by building a complicated simulation of a coupled, natural circulation system, this report produced analytical \dot{m} s for each loop and used them as preliminary benchmark values for evaluating the simulation behavior of each loop operating as if in a decoupled manner.

This report does not contain any scaling analysis, so the dimensional buoyancy forces, ΔP_B , were simply equated to the dimensional frictional forces, ΔP_F , at steady-state operation. For the scaling methodology described in this chapter, this would translate to equating the final two terms on the RHS of Eq. (2.32). In the report, they write the equivalent of

$$\Delta P_B = (\rho_C - \rho_H)gH_o \quad . \quad (2.43)$$

For fluids with an empirical expression for specific heat resembling $c_p = a + bT$, where a and b are constants,

$$\Delta P_B = \beta g \Delta T \quad ,$$

$$\text{where } \Delta T = \frac{-c_{p,C} + \sqrt{c_{p,C}^2 + 2b \frac{\dot{Q}}{\dot{m}}}}{b} \quad (2.44)$$

Then, the frictional forces are presented for the loop assuming laminar flow:

$$\Delta P_F = \sum_i \left[\left(K_i + \frac{\dot{m} L_i}{\mu_i A_i} \right) \frac{\dot{m}^2}{2 \rho_i A_i^2} \right] , \quad (2.45)$$

where μ_i and ρ_i are linearly averaged across each component i .

Equations for ΔP_B and ΔP_F are equated, and solved for \dot{m} with, “for example, a simple bisection method” [55]. The authors acknowledge the assumed linear behavior of ρ in ΔP_B introduces error in the analytical solution, as does the linearly-averaged μ_i and ρ_i in ΔP_F and neglecting to consider PHL across the system.

Using this approach for finding \dot{m} works because taking u_o from the steady-state analytical mass flow rate returns a well defined and pragmatically chosen characteristic velocity. Now, this review turns towards scaling-oriented approaches for acquiring steady-state analytical flow rates as their characteristic velocities. In general, they are quite similar to the approach already discussed.

Scarlat developed scaling methods specifically for analyzing natural circulation decay heat removal systems for FHRs [46]. Starting with the fluid momentum equation for mass flow rate rather than velocity, Scarlat employs the Boussinesq approximation to remove several terms, simplifying the ND momentum equation at steady state as a balance between the Ri buoyancy forces and \mathcal{F} friction forces. Assuming these forces balance perfectly, i.e. $Ri(\dot{m}) = \mathcal{F}$, an expression for the steady-state analytical mass flow rate was found:

$$\dot{m}_{SS}^3 = \frac{2 \rho_o^2 g \beta H_o \dot{Q}_h}{c_{p,h} F'} . \quad (2.46)$$

In the above equation, SS “ \equiv ” steady state, subscript $_h$ “ \equiv ” heated section, and F' is similar to the \mathcal{F} used in this thesis.

In **Ishii**'s scaling methodology developed for the PUMA IET [42], he defines u_o as the steady-state analytical velocity solution in the heat source component. To find this analytical solution, an expression for ΔT_o is substituted into the steady-state fluid momentum equation, which is simplified to contain only the buoyancy and friction terms. This results in an equation that can be solved for u_o ,

$$u_o = \left[\frac{4 \beta g \left(\frac{q_o''' \ell^2}{\rho c_p} \right) \left(\frac{a_{s,o}}{a_o} \right)}{\sum_i \left(\frac{f_i \ell_i}{d_i} + K_i \right) / \left(\frac{a_i}{a_o} \right)^2} \right]^{1/3} , \quad (2.47)$$

where the subscript “ o ” denotes the reference component, $a_{s,o}$ is the solid-structure surface area, a_o is the fluid cross-sectional flow area, and \sum_i is taken along each component in the loop.

Alternative approaches for finding u_o : In general, the approaches presented thus far achieve steady-state analytical u_o s or \dot{m} s which are defined in the same way, simply differing (slightly) in the equations used to calculate them. There are other definitions used for characteristic velocities in natural circulation loops. Since there is no one-size-fits-all approach to scaling analysis, and it is the scaling analyst’s responsibility to select characteristic parameters for the system being analyzed, I show some examples of “alternative” u_o s in this short literature review as well. Although I do not necessarily recommend adopting these u_o definitions outright, I will acknowledge there are circumstances in which these characteristic velocities are more than apt for the scaling analysis at hand and even preferable, primarily due to their less stringent requirements for calculating a u_o .

The scaling methodology developed by **Kairos Power** [51] follows the H2TS approach originally developed by Zuber [36], which means their methodology exists as an application of Zuber’s methodology [35] to FHR systems. This work is significant in that it “provides a basis for using surrogate fluids” in scaled experiments for molten salt systems as a topical report submission to the NRC. For this purpose, basing their scaling work off a methodology so accepted by the NRC as H2TS is a pragmatic decision.

The characteristic velocity Kairos has selected for natural circulation analysis is simply chosen to be proportional to the ratio of reactor power during normal full-power operation to the decay heat reactor power, where NC stands for “natural circulation” and FC stands for “forced circulation”.

$$u_{o,NC} = u_{o,FC} \frac{\dot{Q}_{NC}}{\dot{Q}_{FC}} \quad (2.48)$$

Kairos retains the Ri for forced circulation analysis, so their $u_{o,NC}$ relation leads to a simple comparison for the natural circulation Ri .

$$Ri_{NC} = Ri_{FC} \left(\frac{\dot{Q}_{FC}}{\dot{Q}_{NC}} \right)^2 \quad (2.49)$$

The approach taken by Kairos provides a simple method for producing an analytical u_o , but leaves a bit to be desired in terms of providing a value truly characteristic of the system, and therefore providing a Ri_R useful for scaling purely natural circulation systems. Instead, it seeks to scale power ratios at the expense of all other scaling parameters. Adjustments after

loop construction *could* be made to achieve the contrived u_o , thereby aligning Ri with its contrived value to effectively capture the characteristic buoyancy forces defined in Eq. (2.38). However, the balance between the buoyancy term and Fr -effected pressure and body force terms would no longer be correct. Thus, the balance of behavior captured by ND scaling parameters is lost in scaling analysis, and therefore cannot be preserved between systems.

In the **CIET Integrated Research Project report** [15], the authors did not seek a characteristic velocity for natural circulation. Rather, they derived a “target mass flow rate” based on target heater power and thermophysical properties calculated at targeted average fluid temperature values. Since mass flow rate is proportional to velocity, I will take the liberty of extending their methodology to the parameter of interest here, u_o .

$$u_o = \frac{\dot{m}}{\rho(T_{avg})A_{avg}} = \frac{\dot{Q}_{target}}{\rho(T_{avg})c_p(T_{avg})A_{avg}\Delta T_{target}} \quad (2.50)$$

This report, self-admittedly, will not produce a properly characteristic analytical u_o . However, “flow losses can be adjusted through needle valves on all branches of CIET 1.0 to achieve the target flow rates” [15]. In a way, this contradicts my previous claim that “the interplay. . . that generates [natural circulation] flow cannot be so easily controlled”. In the context of this scaling methodology, this approach would seek to artificially manipulate \mathcal{F} to reach a contrived u_o instead of seeking to initially determine a correct driving force (captured by Ri), effecting the balance between ND terms in Eq. (2.40). This is only a problem within the context of this scaling methodology because the Boussinesq approximation is neglected, which maintains the ND pressure and body force terms in formulation. In the same way as Kairos’s methodology, the phenomenological interplay captured by Fr would not be preserved.

Michael Heisler developed scaling methods for natural circulation experiments for sodium-cooled reactors using water as a surrogate fluid [44]. It is not practical to achieve similitude between water and sodium for both thermo- and hydro-dynamic considerations simultaneously, so the scaling approach here differs. Heisler includes multiple methods for determining $u_{o,R}$, but no method to define a system u_o . He simultaneously solves a system of five equations, some of which include the variable u_o . To this analysis, u_R can be “completely arbitrary” in determination and subsequently compensated for by manipulating the Bi to achieve a satisfactory time-scale. This approach is not quite applicable to this FHR scaling methodology, in which thermal hydraulic similitude is achievable. However, Heisler’s scaling methodology is a fellow single-phase-coolant methodology and goes to show that in some instances, selecting a properly-characteristic u_o is not so important.

Deriving a u_o for this FHR scaling methodology: The most appropriate velocity-scale for natural circulation scaling is one that captures the approximate velocity at characteristic conditions, i.e. the analytical u_o . Starting with Eq. (2.40), I impose steady-state

conditions at $\dot{u} = 1$ and approximate the ND buoyancy term integral as the ideal quadrilateral from Fig. 2.4.

$$\frac{\partial \dot{u}}{\partial \tau} \oint \frac{\rho_o A_o}{\rho A} \partial_{\mathcal{J}} = \frac{-1}{Fr} \left[\oint \frac{\rho_o}{\rho} \partial \mathcal{Y} + \oint \frac{\rho_o}{\rho} \partial \xi \right] + Ri \oint \theta \partial \xi - \mathcal{F} \dot{u}^2 \quad (2.51)$$

The ND pressure term can be approximated as the ideal quadrilateral in Fig. 2.3. It follows that the ND body force term for natural circulation can be approximated as an ideal quadrilateral in a similar fashion to the terms approximated in Figs. 2.3 and 2.4.

$$\frac{-1}{Fr} \oint \frac{\rho_o}{\rho} \partial \xi \approx \frac{-1}{Fr} \left(\frac{\rho_o}{\rho_H} - \frac{\rho_o}{\rho_C} \right) \Delta \xi_o \quad (2.52)$$

Implementing this approximation produces

$$0 = \frac{-1}{Fr} \left[\left(\frac{\rho_o}{\rho_H} - \frac{\rho_o}{\rho_C} \right) \Delta \mathcal{Y}_o + \left(\frac{\rho_o}{\rho_H} - \frac{\rho_o}{\rho_C} \right) \Delta \xi_o \right] + Ri - \mathcal{F} \quad (2.53)$$

If ρ_o is taken as the average between the densities at $T_{H,o}$ and $T_{C,o}$,

$$\rho_o = \frac{\rho_C + \rho_H}{2} \quad , \text{ and} \quad (2.54)$$

$$\left(\frac{\rho_o}{\rho_H} - \frac{\rho_o}{\rho_C} \right) = \left(\frac{\rho_C^2 - \rho_H^2}{2\rho_C\rho_H} \right) \quad , \text{ which produces} \quad (2.55)$$

$$0 = \frac{-1}{Fr} \left(\frac{\rho_C^2 - \rho_H^2}{\rho_C\rho_H} \right) + Ri - \mathcal{F} \quad (2.56)$$

The Fr ratio and Ri both include u_o^2 in the denominator. Solving the above expression for u_o produces an expression for the characteristic velocity.

$$u_o = \sqrt{\frac{gH_o}{\mathcal{F}_{anal}} \left[\beta_o \Delta T_o - \left(\frac{\rho_C^2 - \rho_H^2}{\rho_C\rho_H} \right) \right]} \quad (2.57)$$

For an analytical solution, approximating the density ratio embedded in \mathcal{F}_{anal} as unity is a practical approach.

$$\mathcal{F}_{anal} \approx \frac{A_o^2}{2} \oint \frac{f}{D_h A^2} \partial x + \sum \frac{K}{A^2} \quad (2.58)$$

The final expression for an analytical u_o for this scaling methodology is shown below.

$$u_o = \sqrt{\frac{2gH_o}{A_o^2} \left[\frac{\beta_o \Delta T_o - \left(\frac{\rho_C^2 - \rho_H^2}{\rho_C \rho_H} \right)}{\oint \frac{f}{D_h A^2} \partial x + \sum \frac{K}{A^2}} \right]} \quad (2.59)$$

Solving for u_o requires an iterative process. The friction factor is dependent on fluid velocity, and the loop ΔT_o could change as a result of changing u_o as well. Additionally, this equation will have a tendency to inflate the analytical velocity solution — specifically due to overapproximating the buoyancy driving force by neglecting PHL.

Observing Fig. 2.5, PHLs reduce the area within the ideal quadrilateral (drawn with dashed

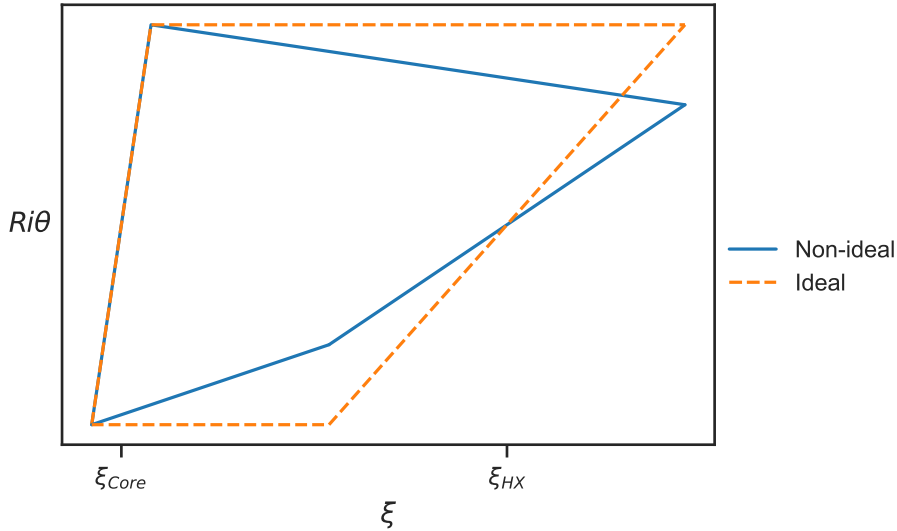


Figure 2.5: Idealized and non-idealized loop integrals of the ND buoyancy term, which are each evaluated as the area within their respective quadrilateral. The “non-ideal” term accounts for PHL, whereas the “ideal” one does not. Utilizing the ideal term for determining an analytical steady-state velocity-scale will result in an overapproximation for the characteristic natural circulation velocity-scale.

lines) to that within the non-ideal one (solid lines). This figure is similar to one of the plots in Fig. 3-5 of Scarlat’s dissertation [46]. The non-ideal degradation of $\oint \theta \partial \xi$ aptly measures the impact of PHL on system buoyancy forces. Incorporating this term into the analytical u_o expression is not entirely recommended, as the non-ideal quadrilateral area seen in Fig. 2.5 is dynamic. However, if an approximation is available, this value could serve as a factor to $\beta_o \Delta T_o$ in Eq. (2.59).

2.4 Fluid Energy Scaling Parameters

Sections 2.2 and 2.3 derived parameters for momentum scaling, whereas Secs. 2.4 and 2.5 do the same for energy scaling. The approach taken for fluid energy scaling is particularly important to this methodology for multiple reasons — firstly, it drives the component-based approach of the entire methodology and, secondly, it provides the basis for capturing and quantifying radHT scaling distortion.

Nondimensionalizing the energy equation enables the derivation of scaling parameters which can be used to preserve the proportional significance of heat transfer phenomena between systems. I ND-ize the 1D fluid energy equation and show the derivation of scaling parameters which can be used to capture the proportional relevance of convective heat transfer, radiative heat transfer, axial fluid bulk temperature change, and time on system behavior.

$$\rho c_p \frac{DT}{Dt} - \nabla(k \nabla T) = q''' \quad (2.60)$$

Equation (2.60), which is commonly referred to as the “energy equation” throughout this thesis, can be considered the starting point for fluid energy scaling. The first LHS term captures the change of fluid enthalpy in time and space. By interpreting the substantial derivative to the first spacial dimension, I obtain an expression for 1D fluid flow, which is desirable for system-level scaling analysis.

$$\frac{DT}{Dt} \xrightarrow{1D} \left(\frac{\partial T}{\partial t} + u \frac{\partial T}{\partial x} \right) \quad (2.61)$$

The second LHS term captures fluid conduction, which can be assumed negligible within the fluid. However, evaluating this term at solid-to-fluid boundaries expresses convective energy addition to the fluid. Evaluating at a fluid boundary (or wall w), the conduction term produces a “convective source” term q'''_{conv} , called as such because it appears in formulation,

and acts upon the 1D fluid in such a manner, identical to the fluid source term in Eq. (2.60).

$$\nabla(k\nabla T) \approx \frac{k}{r} \frac{\partial}{\partial r} \left(r \frac{\partial T}{\partial r} \right) + k \frac{\partial^2 T}{\partial x^2} \ll \quad (2.62)$$

$$\left. \frac{k}{r} \frac{\partial}{\partial r} \left(r \frac{\partial T}{\partial r} \right) \right|_w = q'''_{conv} \quad (2.63)$$

The RHS term in Eq. (2.60) expresses the volumetric heat source, or energy added to the fluid volume. This term is general enough to capture all heat gained or lost by the fluid through non-convective means, expressed by q'''_{gen} . While the subscript nomenclature is primarily chosen to represent fission heat generation, q'''_{gen} also captures energy deposition from neutron moderation and gamma heating. For the purposes of this scaling methodology, this is also where radiative heat transfer enters the energy equation, which can be made clear by segregating q'''_{rad} from the total q'''_{gen} definition. Quantifying and analyzing radiative heat transfer scaling distortion begins with the introduction of q'''_{rad} , which can be seen in the 1D fluid energy equation — Eq. (2.64).

If this methodology were to be used for integral-fuel-type molten salt reactors (fission energy generation within the fluid itself), the fluid heat source would be retained in full as $q''' = q'''_{rad} + q'''_{gen}$. However, FHRs do not utilize integral fuel salt and therefore do not generate fission energy within the coolants. Instead of retaining q'''_{gen} as neutron and gamma heating, it is conventional to assume all that energy is deposited in the solid structures. Therefore, volumetric heat generation q'''_{gen} is considered negligible and removed from formulation.

$$\frac{\partial T}{\partial t} + u \frac{\partial T}{\partial x} = \frac{1}{\rho c_p} (q'''_{conv} + q'''_{rad}) \quad (2.64)$$

Change in temperature	+	Advection term	=	Energy gain via convection	+	Energy gain via radiation
--------------------------	---	-------------------	---	-------------------------------	---	------------------------------

For the sake of calculating fluid energy source terms, it is common to break them down into expressions compatible with Nusselt number heat transfer correlations. For the convective heat source:

$$\begin{aligned} q'''_{conv} &= \frac{h_x p_h (T_w - T)}{A} \\ &= \frac{4Nu_x k (T_w - T)}{D_h^2} \end{aligned} \quad (2.65)$$

where $Nu_x = \frac{h_x D_h}{k}$, $D_h = \frac{4A}{p_w}$

The nomenclature introduced in Eq. (2.65) includes the local heat transfer coefficient h_x , the local Nusselt number Nu_x , heated perimeter p_h , and $(T_w - T)$, which is translated as the difference between the wall and fluid temperatures.

To facilitate radHT analysis in a comparable fashion to that of convective heat transfer, I suppose a local radiative heat transfer coefficient $h_{x,rad}$ of the same form as the convective h_x . Assuming the heated perimeter is equal to the wetted perimeter,

$$h_{x,rad} = \frac{D_h}{4} \frac{q'''_{rad}}{T_w - T} \quad . \quad (2.66)$$

Using Eq. (2.66), a Nu -compatible radHT expression can be derived identical in form to Eq. (2.65) but with $h_{x,rad}$ replacing h_x .

$$\begin{aligned} q'''_{rad} &= \frac{h_{x,rad} p_h (T_w - T)}{A} \\ &= \frac{4Nu_{x,rad} k (T_w - T)}{D_h^2} \end{aligned} \quad (2.67)$$

where $Nu_{x,rad} = \frac{h_{x,rad} D_h}{k}$

It is useful to note here the temperature difference $(T_w - T)$ in Eq. (2.67) seems to imply radHT occurs exclusively between a participating fluid and a single surface (or multiple surfaces at the same temperature). However, solid-to-fluid radHT in FHRs will inevitably occur in geometries with multiple surfaces at various temperatures — e.g. salt flowing through the downcomer, where the core barrel surface will typically be hotter than that of the reactor vessel. I seek to capture radHT in those scenarios as well, so the aforementioned homogeneous-surface-temperature interpretation is undesirable. I rectify that misinterpretation on Pg. 61, where I discuss how to apply the fluid energy scaling equation to multiple surfaces in a single component.

For the sake of brevity, when the combined heat transfer effects of convection and radiation can be analyzed together, the Nu expressions from Eqs. (2.65) and (2.67) can be recombined into a total Nusselt number, where $Nu_{tot} = Nu + Nu_{rad}$. Inserting this new definition, along with the unity ratio $\frac{\mu/\rho}{\nu}$, into Eq. (2.64) produces a form with three ND numbers in the RHS energy gain term.

$$\frac{1}{u} \frac{\partial T}{\partial t} + \frac{\partial T}{\partial x} = \frac{4}{uD_h^2} \frac{k}{\rho c_p} Nu_{x,tot} (T_w - T) \left[\frac{\mu/\rho}{\nu} \right] \quad (2.68)$$

$$= \frac{4}{D_h} Re^{-1} Pr^{-1} Nu_{x,tot} (T_w - T) \quad , \quad (2.69)$$

$$\text{where } Re = \frac{\rho u D_h}{\mu} \quad \text{and} \quad Pr = \frac{\nu}{k/\rho c_p} \quad .$$

The Reynolds number (Re) and Prandtl number (Pr) are familiar parameters to the thermal hydraulicist and commonly used in scaling analysis. In fact, the Pr similarity between fiber at characteristic FHR temperatures and Therminol[®] VP-1 at experimentally-practical temperatures [6] motivated the use of Therminol[®] as the surrogate fluid in CIET [50]. Nusselt number correlations commonly incorporate Re and Pr , so matching these two parameters can be vital for energy scaling when heat transfer geometries are maintained between systems, such as for heat transfer SETs. In this methodology, these numbers appear multiplied together, which produces the Peclet number (Pe).

$$\begin{aligned} Pe &= Re Pr \\ &= \frac{uD_h}{\alpha_s} \end{aligned} \quad (2.70)$$

Incorporating this definition and integrating along flow path x produces the integral energy equation for 1D fluid flow.

$$\int \frac{\partial T}{\partial t} \frac{1}{u} \partial x + \int \partial T = \int \frac{4}{D_h} \frac{Nu_{x,tot}}{Pe} (T_w - T) \partial x \quad (2.71)$$

I suppose non-dimensional variables to normalize variables in Eq. (2.71). Note the ND fluid and wall temperatures, θ and φ_w respectively, are normalized by $\Delta T_o = T_{H,o} - T_{C,o}$.

$$\begin{aligned} \theta &= \frac{T - T_o}{\Delta T_o} & \varphi_w &= \frac{T_w - T_o}{\Delta T_o} \\ \tau &= \frac{t}{L_o/u_o} & \kappa &= \frac{x}{L_o} \end{aligned} \quad (2.72)$$

Substituting ND variables into Eq. (2.71) results in the 1D fluid ND energy equation.

$$\Delta T_o \int \frac{\partial \theta}{\partial \tau} \frac{u_o}{u} \partial \mathcal{X} + \Delta T_o \int \partial \theta = \Delta T_o \int \frac{4L_o}{D_h} \frac{Nu_{x,tot}}{Pe} (\varphi_w - \theta) \partial \mathcal{X} \quad (2.73)$$

Variables on the RHS of Eq. (2.73) can be gathered into a local Stanton number, $St_{\mathcal{X}}$.

$$\frac{\partial \theta}{\partial \tau} \int \frac{u_o}{u} \partial \mathcal{X} + \int \partial \theta = \int St_{\mathcal{X}} (\varphi_w - \theta) \partial \mathcal{X} \quad (2.74)$$

Reformulating with a component-integral St

The $St_{\mathcal{X}}$ in Eq. (2.74) exists as an axially dependent, local parameter due to its incorporation of a local Nu_x . In this form, local heat transfer coefficients must be used in conjunction with local temperature data in $(\varphi_w - \theta)$. However, it is not common to adopt a local Nu to characterize heat transfer throughout an entire component. Typically, component-integral heat transfer correlations are used. Additionally, for scaling analysis, the ability to compare a component-mean St between systems is much more beneficial than being required to compare $St_{\mathcal{X}}$ at every \mathcal{X} -value. To achieve this, a component-integral St must be pulled out of the integral term.

$$\frac{\partial \theta}{\partial \tau} \int \frac{u_o}{u} \partial \mathcal{X} + \int \partial \theta = St \int (\varphi_w - \theta) \partial \mathcal{X} \quad (2.75)$$

There is one theoretical inconsistency with pulling out a component St — variable thermophysical properties of the fluid, contained within the Pe , must be replaced by their characteristic counterparts. One option is multiplying $St_{\mathcal{X}}$ by a Pe_o unity ratio, leading to Pe remaining within the RHS integral of Eq. (2.74). However, when compared to the treatment of the Nu , this step would seem rather superfluous. Component-integral Nu correlations contain the Re and Pr numbers, constituents of the Pe , averaged in various ways depending on the correlation specifications. Thus, it is perfectly reasonable to extend that treatment to the thermophysical properties contained in the Pe , and average those in the same way as those of the component-integral Nu correlation in use.

The formulation above accommodates heat transfer regions where the thermal hydraulicist would like to utilize component-mean Nu correlations to describe heat transfer behavior. However, it is not uncommon for the temperature difference associated with the component Nu correlation (ΔT_{Nu}) to be something other than the local wall-to-fluid temperature difference, which is contained in the numerator of the RHS term in the equation above as

$$\begin{aligned}
\int (\varphi_w - \theta) \partial_{\mathcal{K}} &= \int \frac{T_w - T}{\Delta T_o} \partial_{\mathcal{K}} \\
&= \frac{\Delta T_{avg}}{\Delta T_o} \int \partial_{\mathcal{K}} \quad .
\end{aligned} \tag{2.76}$$

For example, some Nu correlations require a log-mean temperature difference, ΔT_{LM} , while others depend on a bulk fluid temperature difference, $\Delta T_{b,f}$. To accommodate these correlation-mandated ΔT s, it is necessary to pull a ND temperature difference out of the RHS integral as well.

$$\frac{\partial \theta}{\partial \tau} \int \frac{u_o}{u} \partial_{\mathcal{K}} + \Delta \theta = St (\overline{\varphi_w - \theta}) \int \partial_{\mathcal{K}} \tag{2.77}$$

The new ND temperature difference definition here is

$$(\overline{\varphi_w - \theta}) \equiv \frac{\Delta T_{Nu}}{\Delta T_o} \quad , \tag{2.78}$$

where ΔT_{Nu} can be substituted with various temperature difference formulations. I show example ND temperature difference expressions below using the three examples of ΔT_{Nu} mentioned thus far.

$$(\overline{\varphi_w - \theta}) = \begin{cases} \overline{\varphi_w - \theta} & , \Delta T_{Nu} = \Delta T_{avg} \\ \theta_{out} - \theta_{in} & , \Delta T_{Nu} = \Delta T_{b,f} \\ \frac{(\overline{\varphi_w - \theta_{in}}) - (\overline{\varphi_w - \theta_{out}})}{\ln\left(\frac{\overline{\varphi_w - \theta_{in}}}{\overline{\varphi_w - \theta_{out}}}\right)} & , \Delta T_{Nu} = \Delta T_{LM} \end{cases} \tag{2.79}$$

For scenarios in which the user wants to utilize a local heat transfer coefficient or Nu correlation but still pull out a component mean St for scaling comparison, the RHSs of Eqs. (2.74) and (2.81) can be compared, using the local wall-to-fluid temperature difference, to produce

$$\overline{St} = \frac{\int St_{\mathcal{K}} (\varphi_w - \theta) \partial_{\mathcal{K}}}{\overline{\varphi_w - \theta} \Delta_{\mathcal{K}}} \quad , \tag{2.80}$$

2.4.1 Fully-derived ND energy equation for fluid energy

Incorporating the changes made to allow a component integral St , the ND energy equation achieves its final form.

$$\frac{\partial \theta}{\partial \tau} \int \frac{u_o}{u} \partial_{\mathcal{K}} + \Delta \theta = St (\overline{\varphi_w} - \theta) \Delta_{\mathcal{K}} \quad (2.81)$$

$$\boxed{\text{ND fluid heating}} \times \boxed{\text{Fluid energy inertia (FEI)}} + \boxed{\text{ND advection}} = \boxed{\text{ND heat transfer}}$$

The ND advection term is used to capture the proportional change in fluid temperature across a component of interest. I specify “component” because the advection term is not present in integral system scaling analysis due to the loop integral of this term summing to zero by definition. When normalized by the N_{FEI}^o term, this ratio describes the ability of a component’s temperature gradient to alter the thermal energy contained in the fluid, either component- or system-wide depending on which N_{FEI}^o is used ($N_{FEI,c}^o$ or N_{FEI}^o , respectively). Barring poor selection of characteristic parameters, this ratio should have an order of magnitude that justifies the ND advection term’s retention in analysis.

The ND heat transfer term is used to capture a component’s ability to transfer heat in or out of the fluid and, when normalized by $N_{FEI,c}^o$, the ability of this proportional heat transfer to induce a transient in the component. When normalized by the integral system N_{FEI}^o , this ratio measures the ability of a given component’s heat transfer to induce a system-wide transient.

Due to the highly-specific applicability requirements for heat transfer correlations, the scaling parameters derived from the fluid energy equation are component specific by nature. The implication is that the energy equation is useful for component scaling of heat transfer, but less so for integral system scaling. For the purpose of integral system heat transfer scaling, I have derived an alternative to Eq. (2.81) in Sec. 2.4.3, which includes an alternative ND heat transfer term. The discrepancy between scaling equation forms is useful to keep in mind when selecting scaled system design/operational parameters.

Stanton number (St)

Terms in the RHS integral of Eq. (2.73) are consolidated into the total Stanton number — an essential parameter for analyzing radHT scaling distortion in this methodology. This parameter is slightly modified from its conventional form by a ratio of $4L_o/D_h$ and, as a collection of several other ND numbers, has several acceptable equivalent expressions. For the purposes of calculating the total St , any of the formulas shown in Eq. (2.82) may be used. Depending on available information, one form might be easier to calculate than another.

$$\begin{aligned}
St &= St_{mod} + St_{rad} \\
&= \frac{4L_o}{D_h} \left(\frac{Nu_{tot}}{Pe} \right) = \frac{4L_o}{D_h} \left(\frac{Nu + Nu_{rad}}{RePr} \right) \\
&= \frac{4L_o}{k} \left(\frac{h_{tot}}{Pe} \right) = \frac{4L_o}{k} \left(\frac{h + h_{rad}}{RePr} \right) \\
&= \frac{L_o}{\rho u c_p} \left(\frac{4h_{tot}}{D_h} \right) = \frac{L_o}{\rho u c_p} \left(\frac{4h}{D_h} + \frac{q'''_{rad}}{T_w - T} \right)
\end{aligned} \tag{2.82}$$

The theoretical implication of splitting the St into a convective St_{mod} and a radiative St_{rad} is that the definition of the St must change. Under “regular”, convection-dominant behavior, the St is defined with a focus on the fluid. For this methodology, that definition remains for the St_{mod} .

$$St_{mod} \quad \text{“}\equiv\text{”} \quad \frac{\text{heat transfer with the fluid}}{\text{advection by the fluid}} \tag{2.83}$$

This definition holds true because the heat transfer being described comes exclusively from the interaction of a single surface with some given fluid. The fluid-centric St definition stands when the heat transfer to the fluid is equal to the heat transfer from the wall. However, this equivalence is not necessarily true for multi-surface geometries in which radHT plays a significant role. Whereas $St_{mod,k} = f(T_{w,1}, T_f)$, $St_{rad,k} = f(T_{w,1}, T_{w,2}, T_f)$. To accommodate this multi-surface dependency, a new definition for St should be defined such that all phenomena are captured by its description.

$$St = St_{mod} + St_{rad} \quad \text{“}\equiv\text{”} \quad \frac{\text{net heat transfer from the surface}}{\text{advection from the surface}} \tag{2.84}$$

This definition captures both St_{mod} and St_{rad} . Only when St_{rad} values for all surfaces are summed together, or when there is only a single surface interacting with the fluid, can the definition from Eq. (2.83) be correctly applied to the total St just as well as the definition in Eq. (2.84).

Radiative Stanton number (St_{rad})

The combined form of the St in Eq. (2.82), capturing scaled convection and thermal radiation, is possible due to Eqs. (2.66) and (2.67) casting radHT as dependent on a radiative heat transfer coefficient, h_{rad} . While this parameter is convenient for generating Nu_{rad} , it is a contrived one and not actually physical. Starting with q'''_{rad} , calculating St_{rad} would be

easier without needlessly back-calculating Nu_{rad} . For this purpose, I derived a new formula for St_{rad} starting with Eq. (2.64) but preserving q'''_{rad} .

$$St_{rad} (\overline{\varphi_w - \theta}) = \frac{L_o}{\Delta T_o} \int \frac{q'''_{rad}}{\rho u c_p} \partial \mathcal{K} \quad (2.85)$$

A standalone St_{rad} would inevitably adopt $(\overline{\varphi_w - \theta}) = \Delta T_{avg}/\Delta T_o$. For the purposes of combining or comparing Eq. (2.85) with St_{mod} , such as shown in Eq. (2.82), the Nu -dictated $(\overline{\varphi_w - \theta})$ (from Eq. (2.78)) should be adopted. The combined form is shown below.

$$\begin{aligned} St &= St_{mod} + St_{rad} \\ &= \frac{4L_o}{D_h} \left(\frac{Nu}{Pe} \right) + \frac{L_o}{\Delta T_{Nu}} \int \frac{q'''_{rad}}{\rho u c_p} \partial \mathcal{K} \end{aligned} \quad (2.86)$$

2.4.2 Component scaling considerations for fluid energy

Assuming a component is bounded by points $1 \rightarrow 2$, taking the integral of Eq. (2.81) between those points produces produces the component scaling equation for fluid energy. I drop the subscript $_c$ from the St because the anticipated application of fluid energy scaling is already implied to be component scaling.

$$\frac{\partial \theta}{\partial \tau} \int_1^2 \frac{u_o}{u} \partial \mathcal{K} + \theta \Big|_1^2 = St (\overline{\varphi_w - \theta}) \mathcal{K} \Big|_1^2 \quad (2.87)$$

Calculating St with multiple surfaces in a single component

Equation (2.87) is straightforward in application for scenarios with a single surface with known temperature data. However, some scenarios such as annular enclosures or pebble beds include multiple surfaces. To understand how to adjust Eq. (2.87) for these multi-surface analyses, it is useful to look at various Nu correlations for annuli and pebble beds.

Nusselt correlations for annular geometries: Dirker and Meyer [56] reviewed eleven correlations for smooth concentric annuli. All utilize a single $\Delta T = T_w - T$ for the temperature difference definition, which seems to suggest the most agreement with $(\overline{\varphi_w - \theta}) = \overline{\varphi_w - \theta}$. These authors define a Nu_i for the inner wall and a separate Nu_o for the outer wall. Gnielinski [57] defines a single Nu for the entire test length, which utilizes a ΔT_{LM} . The final definition of $(\overline{\varphi_w - \theta})$ in Eq. (2.79) is appropriate for this correlation. Jianfeng et al. [58] were specifically interested in defining a transition-flow-regime Nu correlation for molten

salt heating by the inner wall of an annulus. They modified Gnielinski's correlation for this purpose, but altered the ΔT to resemble those found in Dirker and Meyer. Another author who utilized Gnielinski's correlation, including the ΔT_{LM} , was W. van Zyl [59]. He defined both a local Nu_x and total mean Nu . For the local Nu_x , the test section was divided up into control volumes, each of which was assigned its own $T_{b,i}$ and $T_{b,o}$.

Nusselt correlations for pebble beds: Wakao [24], Summers [60], and Limin [61]. The widely-used Nu correlation from Wakao [24] defined the temperature difference between the fluid and particle (pebble) surface, assuming constant heat generation within the pebbles and constant surface temperatures. Various relations for a constant ΔT are provided in Wakao's Appendix A [24]. Summers [60] took a different approach by incorporating a ΔT_{LM} and a bulk fluid temperature found by quadratic averaging of radial temperature measurements. Limin Liu [61] defined local and total approaches to finding a pebble bed Nu . For both, a linear-average value was assigned to the fluid and solid temperatures, which would be incorporated in this methodologies analysis as $(\overline{\varphi_w - \theta}) = \overline{\varphi_w} - \theta$.

The Nu correlation review above sufficiently demonstrates the use of various T_f and T_w formulations, further supporting the decision to separate out the $(\overline{\varphi_w - \theta})$ term. With this adaptable formulation provided by Eq. (2.87), any temperature difference definition can be incorporated. Additionally, it shows the St should be adjusted to capture the use of various Nu formulations. A bulleted summary of deductions from approaches is described here.

- For geometries with two surfaces, some heat transfer correlations utilize a single Nu along with the lone *heated* wall temperature and bulk fluid temperature for the ΔT . For these cases, the single St should make use of a D_h that captures the wetted perimeter of both walls.
- For two-surface geometries which utilize a separate Nu correlation for each wall, two separate Sts should be used as well. This necessitates a $\Delta T_1 = T_{w,1} - T_f$ and a $\Delta T_2 = T_{w,2} - T_f$. The D_h accompanying each St should only capture the wetted perimeter of the wall corresponding to its respective Nu .
- For a multi-surface enclosure with many surfaces, such as a pebble bed, a single Nu is typically used. For these formulations, a D_h describing the entire geometry and all surfaces is used.

The only substantial differences between approaches is how D_h and ΔT is defined. However, to make clear the option to use multiple St terms for multiple surfaces, Eq. (2.87) can be altered using the relation below to explicitly address how the separate St terms appear, one for every surface k .

$$St(\overline{\varphi_w - \theta}) = \sum_k St_k(\overline{\varphi_w - \theta})_k \quad (2.88)$$

Defining St_{rad} for multiple surfaces: If surface-specific St_k s are sought for multi-surface ND convection heat transfer analysis, as shown in Eq. (2.88), it is necessary to define how to generate surface-specific $St_{rad,k}$ parameters as well. I will show how to split up Eq. (2.85) for multiple surfaces.

System-level radHT analysis, which is appropriate for this scaling methodology, evaluates thermal radiation in terms of enclosures. It is convenient then to consider any given heat transfer component as its own radiative enclosure. For each component, the total radiative energy absorbed by the component fluid must be equal to the net radiation emitted by the component surfaces.

$$\int_1^2 q'''_{rad} dV_f = \sum_k \int_1^2 q''_{rad,k} dA_k \quad (2.89)$$

This relation can be used to generate a q'''_{rad} along the ND flow path, where p_w is the wetted perimeter of surface k and A is the cross-sectional fluid area.

$$\begin{aligned} \int_1^2 q'''_{rad} \partial\mathcal{K} &= \sum_k \int_1^2 \frac{q''_{rad,k} p_w}{A} \partial\mathcal{K} \\ &= \sum_k \int_1^2 \frac{4q''_{rad,k}}{D_{h,k}} \partial\mathcal{K} \end{aligned} \quad (2.90)$$

Substituting this relation into Eq. (2.85) produces a practically accessible St expression for multiple surfaces in the same enclosure.

$$St_{rad}(\overline{\varphi_w - \theta}) = \frac{4L_{o,c}}{\Delta T_{o,c}} \sum_k \int \frac{1}{\rho u c_p} \frac{q''_{rad,k}}{D_{h,k}} \partial\mathcal{K} \quad (2.91)$$

Alternative time-scale derivation for the ND fluid energy equation

Thus far, the ND-ization of fluid momentum and energy equations has always defined the characteristic time as $t_o = L_o/u_o$ (see τ denominator in Eqs. (2.11), (2.33) and (2.72)). When simultaneously analyzing the ND thermo- and hydro-dynamic behavior of a system, utilizing identical time-scale definitions between equations is necessary. Without that consistency,

momentum and energy data gathered during transients would not align chronologically. However, if the experimental analyst is exclusively concerned with thermodynamic behavior, the time-scale does not need to resemble that of the ND momentum equation. Take for instance a natural circulation heat transfer experiment in an SET, in which the ND fluid velocity varies through some transient in a manner inconsistent with the prototypical reactor. For a situation such as this, it could be more helpful to directly tie the chronological progression of the experiment to the dynamic mass flow rate instead of accepting some inescapable distortion present between the SET transient and that of the full-scale prototype, which exists due to the static time-scale binding time progression in both systems.

I have derived an alternate ND fluid energy equation for such circumstances. By omitting the ND time τ in Eq. (2.72), a dimensional time cascades down the derivation. The alternate version of Eq. (2.73) appears as

$$\Delta T_o \int \frac{\partial \theta}{\partial t} \frac{\rho A L_o}{\dot{m}} \partial_{\mathcal{K}} + \Delta T_o \int \partial \theta = \Delta T_o \int \frac{4 L_o}{D_h} \frac{Nu_{x,tot}}{Pe} (\varphi_w - \theta) \partial_{\mathcal{K}} \quad . \quad (2.92)$$

Note the partial derivative with respect to dimensional time in the first term. This alternative ND change in energy term can be simplified in the context of component scaling analysis as

$$\begin{aligned} \int_1^2 \frac{\partial \theta}{\partial t} \frac{\rho A L_o}{\dot{m}} \partial_{\mathcal{K}} &= \frac{\partial \theta}{\partial t} \frac{m_c}{\dot{m}} \\ &= \frac{\partial \theta}{\partial \tau_{alt}} \quad , \end{aligned} \quad (2.93)$$

where $\tau_{alt} = \frac{t}{t_{res,c}} \quad .$

Utilizing this alternative ND time, normalized by the component fluid residence time, results in a new component scaling equation, alternative to Eq. (2.87).

$$\frac{\partial \theta}{\partial \tau_{alt}} + \theta \Big|_1^2 = St (\overline{\varphi_w - \theta}) \mathcal{K} \Big|_1^2 \quad (2.94)$$

As can be seen, the only difference induced in Eq. (2.94) is the alternative τ_{alt} and lack of a $N_{FEI,c}$. Instead, the alternative fluid energy time-scale is inherently linked to the mass flow rate, even as that parameter changes over time. Again, this alternative component scaling equation is most likely only useful for analyzing transient experiments in heat transfer SETs. Recall the static scaled fluid momentum equation time-scale — attempting to use a dynamic τ_{alt} in energy scaling while using a static τ in momentum scaling would lead to mismatched time progression of phenomena in the same experiment during transients.

2.4.3 Integral system scaling considerations for fluid energy

Taking the loop integral of Eq. (2.81) provides a integral system fluid energy scaling equation. However, this form provides little insight. Using this equation to match the heat transfer behavior of an entire loop would be unnecessarily tedious. Specifically, the task of matching a loop-wide St is not recommended. The Stanton number is better suited for component heat transfer analysis. Instead, a different form of the ND energy equation can be derived to better capture metrics commonly used to characterize loop-wide heat transfer rates — power, or \dot{Q} -values. The total system thermal power, either via fission in a reactor core or via electric heater in the experiment is represented by \dot{Q}_{gen} , while the HX/fan heat removal rate is \dot{Q}_{HX} .

Starting by modifying Eq. (2.71), I neglect modifications made to the fluid energy gains term. In other words, by ignoring changes previously described by Eqs. (2.65) to (2.69), the integral form of the energy equation becomes

$$\int \frac{\partial T}{\partial t} \frac{1}{u} \partial x + \int \partial T = \int \frac{q_f'''}{\rho c_p u} \partial x \quad , \quad (2.95)$$

$$\text{where } \oint q_f''' \partial x = \frac{\dot{Q}_{gen} - \dot{Q}_{HX}}{m_f/\rho} \quad .$$

For this derivation, only two ND variables are necessary, time and axial distance.

$$\tau = \frac{t}{L_o/u_o} \quad \mathcal{X} = \frac{x}{L_o} \quad (2.96)$$

The resulting ND equation taken over the entire loop is shown below.

$$\frac{\partial \theta}{\partial \tau} \oint \frac{u_o}{u} \partial \mathcal{X} = \frac{L_o (\dot{Q}_{gen} - \dot{Q}_{HX})}{m_f \Delta T_o} \oint \frac{\partial \mathcal{X}}{c_p u} \quad (2.97)$$

Equation (2.97) allows for the use of system-wide known \dot{Q} -values instead of component-specific heat transfer correlations, which are more characteristic of integral system heat transfer analysis. Assuming a constant specific heat capacity, the loop integrals cancel out and Eq. (2.97) is simplified down to

$$\frac{\partial \theta}{\partial \tau} = \frac{L_o (\dot{Q}_{gen} - \dot{Q}_{HX})}{m_f u_o c_{p,o} \Delta T_o} \quad (2.98)$$

2.4.4 Characteristic parameters for fluid energy scaling

All characteristic parameters used for ND-izing the fluid energy equation were previously discussed in Secs. 2.2.4 and 2.3.4. Fluid energy scaling will be applied on the component level. Therefore, characteristic parameters should be defined to reflect intracomponent heat transfer except where it is desirable to contextualize behavior in terms of the whole system. An example could be scaling analysis for the HX in a system where characteristic parameters were defined by the core section. Switching over to an $L_{o,c}$ defined by the HX length is perfectly fine. However, keeping ΔT_o and $t_o = L_o/u_o$ consistent with the core would typically be advisable.

2.5 Solid-Structure Energy Scaling Parameters

The derivation of energy scaling parameters for solid-structures begins the same way as it began for fluids — the energy equation, Eq. (2.60). The only difference is specifying the solid-structure temperature T_s to replace the fluid temperature.

$$\rho c_p \frac{DT_s}{Dt} - \nabla(k \nabla T_s) = q''' \quad (2.99)$$

Assuming all solid structures are stationary (FHR pebbles move slowly enough to be considered stationary, e.g. 60 day pebble core residence time in the Mark 1 (Mk.I) [3] compared to a fluid loop residence time on the order of minutes), the substantial derivative does not retain any spacial terms. Approximating constant thermal conductivity as a function of temperature, the second LHS term can be evaluated for 2D conduction in cylindrical coordinates (axially symmetric, so no azimuthal variation).

$$\nabla(k \nabla T_s) \approx \frac{k}{r} \frac{\partial}{\partial r} \left(r \frac{\partial T_s}{\partial r} \right) + k \frac{\partial^2 T_s}{\partial x^2} \ll \quad (2.100)$$

At solid-to-fluid interfaces, this term can be replaced by an equivalent boundary condition that makes use of commonly-used heat transfer coefficients. Here, I account for both con-

vective and radiative heat transfer with the fluid.

$$\begin{aligned} \nabla(k\nabla T_s) \Big|_w &= -\nabla(q''_{conv} + q''_{rad}) \\ &= -\nabla[(h_x + h_{x,rad})(T_w - T)] \end{aligned} \quad (2.101)$$

$$\text{where } h_{x,tot} = h_x + h_{x,rad}, \quad h_{x,rad} = \frac{q''_{rad}}{T_w - T}$$

$$= -\frac{\partial}{\partial r}[h_{x,tot}(T_w - T)] - \frac{\partial}{\partial x} \ll [h_{x,tot}(T_w - T)] \quad (2.102)$$

Axial derivative terms are considered negligible because temperature gradients across solid structures and fuel elements (in the radial direction) are typically much greater than axial temperature gradients. Representing volumetric heat generation from fission, gamma deposition, and neutrons as q_s''' and multiplying the boundary term by a unity ratio k/k , I arrive at the 2D solid energy equation.

$$\frac{\partial T_s}{\partial t} = \frac{\alpha_s}{r} \frac{\partial}{\partial r} \left(r \frac{\partial T_s}{\partial r} \right) - \frac{[k/k]}{\rho c_p} \frac{\partial}{\partial r} (h_{x,tot}(T_w - T)) + \frac{q_s'''}{\rho c_p} \quad (2.103)$$

Change in temperature	=	Internal conduction	-	Boundary conditions	+	Fission, gamma, neutron heating
--------------------------	---	------------------------	---	------------------------	---	------------------------------------

Integrating Eq. (2.103) in the radial r and axial x directions produces the integral solid-structure energy equation.

$$\begin{aligned} \iint \frac{\partial T_s}{\partial t} r \, dr \, dx &= \iint \alpha_s \frac{\partial}{\partial r} \left(r \frac{\partial T_s}{\partial r} \right) dx - \\ &\quad \iint \frac{[k/k]}{\rho c_p} r_w \frac{\partial}{\partial r} (h_{x,tot}(T_w - T)) dx + \iint \frac{q_s'''}{\rho c_p} r \, dr \, dx \end{aligned} \quad (2.104)$$

Below, I suppose characteristic variables for ND-izing Eq. (2.104). Note use of the previously-utilized fluid temperature-scale $\Delta T_o = T_{H,o} - T_{C,o}$, a characteristic solid time-scale $t_{o,s}$ that has yet to be defined, and a characteristic solid thickness used as the radial length-scale.

$$\begin{aligned} \varphi &= \frac{T_s - T_o}{\Delta T_o} & \theta &= \frac{T - T_o}{\Delta T_o} & \mathcal{B}''' &= \frac{q_s'''}{(\rho c_p)_o \Delta T_o / t_{o,s}} \\ \tau_s &= \frac{t}{t_{o,s}} & \mathcal{R} &= \frac{r}{\delta_o} & \mathcal{X} &= \frac{x}{L_o} \end{aligned} \quad (2.105)$$

Substituting ND variables into Eq. (2.104), approximating $k \approx k_o$ and $\rho c_p \approx (\rho c_p)_o$, and interpreting the inner boundary term integral as a summation of boundary conditions over w solid-to-fluid interfaces.

$$\iint \frac{\partial \varphi}{\partial \tau_s} \mathcal{A} \partial \mathcal{A} \partial \mathcal{K} = \frac{\alpha_{s,o} t_{o,s}}{\delta_o^2} \int \Delta \left(\mathcal{A} \frac{\partial \varphi}{\partial \mathcal{A}} \right) \partial \mathcal{K} - \frac{\alpha_{s,o} t_{o,s}}{\delta_o^2} \int \sum_w \frac{h_{x,tot} \delta_o}{k_o} (\varphi_w - \theta) \mathcal{A}_w \partial \mathcal{K} + \iint \mathcal{B}''' \mathcal{A} \partial \mathcal{A} \partial \mathcal{K} \quad (2.106)$$

2.5.1 Fully-derived ND energy equation for solid-structure energy

Simplifying and gathering remaining terms into scaling parameters produces the final energy scaling equation for solid structures. This expression generates two scaling parameters — the Fo and Bi . The Bi , which consists of both a convective and radiative part, can incorporate heat transfer correlations of various forms, some of which do not use the axial temperature difference $\varphi_w(\mathcal{K}) - \theta(\mathcal{K})$. Therefore, it is beneficial to pull out a component average ND temperature difference $(\overline{\varphi_w - \theta})$ to complement the component integral Bi . I conducted this step in the same manner as was done for the component integral St , the details of which were previously discussed in Eqs. (2.76), (2.78) and (2.79).

$$\frac{\partial \varphi}{\partial \tau_s} \iint \mathcal{A} \partial \mathcal{A} \partial \mathcal{K} = Fo \left[\int \Delta \left(\mathcal{A} \frac{\partial \varphi}{\partial \mathcal{A}} \right) \partial \mathcal{K} - \sum_w Bi_w (\overline{\varphi_w - \theta}) \mathcal{A}_w \Delta \mathcal{K} \right] + \iint \mathcal{B}''' \mathcal{A} \partial \mathcal{A} \partial \mathcal{K} \quad (2.107)$$

ND solid heating	×	Solid energy inertia (SEI)	=	ND internal conduction	−	ND boundary heat transfer	+	ND solid heating
------------------	---	----------------------------	---	------------------------	---	---------------------------	---	------------------

Fourier number (Fo)

Depending on the time-scale selected, the definition of the Fo will change to reflect the phenomena captured by that characteristic time. However, it is still helpful to have a general Fo definition that accompanies the use of a general $t_{o,s}$.

$$Fo = \frac{\alpha_{s,o} t_{o,s}}{\delta_o^2} \quad \text{“}\equiv\text{”} \quad \frac{\text{internal energy dissipation}}{\text{thermal inertia}} \quad (2.108)$$

Biot number (Bi)

This number resembles the St in that it is specific for each surface and varies through time. One can acquire a characteristic value by assuming a characteristic h_o evaluated at steady-

state conditions or another representative scenario.

$$Bi = \frac{h_{tot}\delta_o}{k_o} \quad \text{“}\equiv\text{”} \quad \frac{\text{external heat transfer}}{\text{internal conduction}} \quad (2.109)$$

In its full form, Eq. (2.107) ND boundary heat transfer term holds a $Fo \times Bi$ term for every solid-to-fluid interface.

$$FoBi = \frac{h_{tot}t_{o,s}}{(\rho c_p)_o\delta_o} \quad \text{“}\equiv\text{”} \quad \frac{\text{external heat transfer}}{\text{thermal inertia}} \quad (2.110)$$

Effects of various time-scales on the ND solid-structure energy equation

The solid-structure time-scale $t_{o,s}$ has thus far remained ambiguous so Eq. (2.107) can remain adaptable to numerous scenarios characterized by various time-scales. Depending on the time-scale selected, and the value of Fo and Bi , Eq. (2.107) will be altered. Options for $t_{o,s}$ are discussed on Pg. 74. In summary, there are three options:

1. Fluid time-scale: $t_{o,s} = \frac{L_o}{u_o}$
2. Conduction time-scale: $t_{o,s} = \frac{\delta_o^2}{\alpha_{s,o}}$
3. Boundary transfer time-scale: $t_{o,s} = \frac{(\rho c_p)_o\delta_o}{h_{tot,o}}$

When using the fluid time-scale $t_{o,s}$ option, the Fo changes to $Fo = \alpha_{s,o}L_o/\delta_o^2u_o$. One way to view this new form is a comparison between fluid residence time and solid-structure conduction time. With this time-scale option, the only thing that changes in Eq. (2.107) is the subscript dropping from τ_s ($\partial\varphi/\partial\tau_s \implies \partial\varphi/\partial\tau$) to resemble the ND time used in the ND fluid equations.

The second time-scale option is the solid-structure conduction time. Using this definition, $Fo = 1$ and Eq. (2.107) changes to

$$\frac{\partial\varphi}{\partial\tau_s} \iint_{\mathcal{A}} \partial_{\mathcal{A}} \partial_{\mathcal{K}} = \int \Delta \left(\mathcal{A} \frac{\partial\varphi}{\partial\mathcal{A}} \right) \partial_{\mathcal{K}} - \sum_w Bi_w (\overline{\varphi_w - \theta})_{\mathcal{A}_w} \Delta_{\mathcal{K}} + \iint \mathcal{B}'''_{\mathcal{A}} \partial_{\mathcal{A}} \partial_{\mathcal{K}} \quad . \quad (2.111)$$

The third, “lumped capacitance”, time-scale option inherently implies $Bi \ll 1$ and is therefore negligible. However, the ND boundary transfer term from Eq. (2.107), which contains Bi

does not directly drop out of formulation as a result. Instead, the Fo is altered to $Fo = Bi_o^{-1} = k_o/h_{tot,o}\delta_o$, where

$$Bi_o = \frac{h_{tot,o}\delta_o}{k_o} \quad . \quad (2.112)$$

Note the static $h_{tot,o}$. Thus the entire ND solid energy equation changes accordingly.

$$\begin{aligned} \frac{\partial\varphi}{\partial\tau_s} \iint \mathcal{A} \partial\mathcal{A} \partial\mathcal{K} &= \frac{1}{Bi_o} \int \Delta \left(\mathcal{A} \frac{\partial\varphi}{\partial\mathcal{A}} \right) \partial\mathcal{K} \\ &\quad - \sum_w \frac{h_{tot}}{h_{tot,o}} (\overline{\varphi_w - \theta})_{\mathcal{A}_w} \Delta\mathcal{K} + \iint \mathcal{B}''' \mathcal{A} \partial\mathcal{A} \partial\mathcal{K} \quad (2.113) \end{aligned}$$

In this formulation, $Bi_o^{-1} = Fo \gg 1$, resulting in numerical emphasis on the ND internal conduction term. For the opposite scenario, $Fo \ll 1$, less emphasis is placed on the use of Eq. (2.107). New ND ratios are formed to describe solid-structure thermal inertia and are discussed separately in Sec. 2.5.3.

2.5.2 Component scaling considerations for solid-structure energy

To apply Eq. (2.107) to solid structures within a component, the bounds of integration need to be identified. Determining axial bounds is simple — the component inlet to outlet are represented by axial points 1 \rightarrow 2. However, there is some variability in how the radial integrals should be taken. One bound will always be taken at the solid-to-fluid interface (or wall w). The other bound depends on the solid structures being analyzed within the component of interest. For the purpose of writing a generalizable formulation, I will denote the radial bounds using the nomenclature BC_i for “inner boundary condition” and BC_o for “outer boundary condition”. However, the terminology used here should not conflate the meaning of the internal conduction term and the boundary transfer term. The integral $\partial\varphi/\partial\mathcal{A}$ still describes the internal solid-structure temperature gradient evaluated at the boundary.

$$\begin{aligned} \frac{\partial\varphi}{\partial\tau_s} \int_1^2 \int_{BC_i}^{BC_o} \mathcal{A} \partial\mathcal{A} \partial\mathcal{K} &= Fo_c \int_1^2 \left(\mathcal{A} \frac{\partial\varphi}{\partial\mathcal{A}} \right) \Big|_{BC_i}^{BC_o} \partial\mathcal{K} - \\ &\quad \sum_w Fo_c Bi_w (\overline{\varphi_w - \theta})_{\mathcal{A}_w} \mathcal{K} \Big|_1^2 + \int_1^2 \int_{BC_i}^{BC_o} \mathcal{B}''' \mathcal{A} \partial\mathcal{A} \partial\mathcal{K} \quad (2.114) \end{aligned}$$

To better visualize the meaning behind terms, it is helpful to extrapolate the ND radius to ND circumference \mathfrak{C} , ND surface area $\mathfrak{A}_\mathfrak{C}$, ND solid-structure cross-sectional area \mathfrak{A} , and ND solid-structure volume \mathfrak{V} .

$$\begin{aligned}
\mathfrak{D} &= 2\pi\mathfrak{A} & \mathfrak{D} &= \pi(\mathfrak{A}_{BC_o}^2 - \mathfrak{A}_{BC_i}^2) \\
\mathfrak{D}_{\mathfrak{D}} &= 2\pi\mathfrak{A}\mathfrak{J} & \mathfrak{V} &= \pi(\mathfrak{A}_{BC_o}^2 - \mathfrak{A}_{BC_i}^2)\mathfrak{J}
\end{aligned} \tag{2.115}$$

Incorporating these ND spacial parameters into Eq. (2.114) and multiplying both sides by a factor of 2π produces a simplified version of Eq. (2.114) with easily understandable applications of the radial bounds, BC_i and BC_o . This simplified form was only achieved by approximating $\partial\varphi/\partial\mathfrak{A}$ and \mathfrak{B}''' as constants through ND space, which is not a proper assumption. Therefore, this formula should not be used for any purpose besides deciphering the radial bounds $BC_i \rightarrow BC_o$.

$$\begin{aligned}
\frac{\partial\varphi}{\partial\tau_s} \int_1^2 \mathfrak{D} \partial\mathfrak{J} &= F\partial_c \int_1^2 \left(\mathfrak{D} \frac{\partial\varphi}{\partial\mathfrak{A}} \right) \Big|_{BC_i}^{BC_o} \partial\mathfrak{J} \\
&\quad - \sum_w F\partial_c Bi_w (\overline{\varphi_w - \theta}) \mathfrak{D}_w \mathfrak{J} \Big|_1^2 + \int_1^2 \mathfrak{B}''' \mathfrak{D} \partial\mathfrak{J} \tag{2.116}
\end{aligned}$$

$$\frac{\partial\varphi}{\partial\tau_s} \mathfrak{V}_c = F\partial_c \left(\mathfrak{D}_{\mathfrak{D}} \frac{\partial\varphi}{\partial\mathfrak{A}} \right) \Big|_{BC_i}^{BC_o} - \sum_w F\partial_c Bi_w (\overline{\varphi_w - \theta}) \mathfrak{D}_{\mathfrak{D},w} + \mathfrak{B}_c \tag{2.117}$$

In the component scaling equation, Eq. (2.117), I introduce the total component-integral ND heat generation \mathfrak{B}_c . I will now apply this equation to various solid-structure geometries and explain the various interpretations for the radial bounds $BC_i \rightarrow BC_o$:

- A **cylindrical pipe** containing internal and/or external flow is the most straightforward application of $BC_i \rightarrow BC_o$. For a component of this geometry, $\mathfrak{D}_{\mathfrak{D},BC_i}$ must describe the entire ND inner surface area of the pipe, while $\mathfrak{D}_{\mathfrak{D},BC}$ must describe the ND outer surface area. Therefore BC_i corresponds to the inner pipe surface (referred to as wall w) and BC_o corresponds to the outer pipe surface. At steady-state conditions, $(\partial\varphi/\partial\mathfrak{A})_w/(\partial\varphi/\partial\mathfrak{A})_{BC_o} = \mathfrak{D}_{\mathfrak{D},BC_o}/\mathfrak{D}_{\mathfrak{D},w}$, and the ND conduction term will drop out entirely. If the pipe is subjected to both internal and external flow, two boundary condition terms will need to be provided. An array of many pipes, such as in a HX, could be represented by a single instance of Eq. (2.114) assuming a practically achievable average $\partial\varphi/\partial\mathfrak{A}$. For this example application, each $\mathfrak{D}_{\mathfrak{D}}$ must capture all HX tubes combined.

- A **solid sphere** surrounded by fluid flow, such as a fuel pebble, warrants some special consideration. Here, $\mathcal{A}_\ominus = 4\pi\mathcal{r}^2$ and $V = (4/3)\pi\mathcal{r}^3$. The center of the sphere is referred to as BC_i , where both \mathcal{A}_\ominus and $\partial\varphi/\partial\mathcal{r}$ equal zero. All that remains of the ND conduction term is $Fo_c\mathcal{A}_{\ominus,w}(\partial\varphi/\partial\mathcal{r})_w$, which should be equal in magnitude to that sphere’s total ND heat generation \mathcal{B} at steady state. To capture an entire pebble bed, one would require a separate Eq. (2.114) for each pebble. However, simplifications could be made to capture entire regions of pebbles in the pebble bed, in which all pebbles have a similar $(\partial\varphi/\partial\mathcal{r})_w$, with a single equation. For this scenario, $\mathcal{A}_{\ominus,w}$ and \mathcal{B} would both need to account for all pebbles in that region.
- A **solid cylinder** surrounded by fluid flow, such as a fuel rod, is treated very similarly to the solid sphere example with the only difference being non-spherical formulas required to calculate \mathcal{A}_\ominus and \mathcal{B} . The only bound with a non-zero value is $BC_o = w$.

With the bounds of integration for Eq. (2.114) clarified, this equation can be utilized as a generalized solid-structure equation for component scaling. To correctly capture ND heat transfer behavior, the BCs and solid time-scale (effects of which are discussed on Pg. 69) need to be properly determined before use.

2.5.3 Alternative solid-structure energy scaling parameters

Scaling transient conduction across an entire loop would be a time- and effort-intensive process with little reward compared to component scaling. Therefore, it is strongly encourage to apply solid-structure scaling on a component-by-component basis — similar in approach to fluid energy scaling, but primarily focusing on heat transfer in components with thermal response time constants comparable to the transient times of interest. For this reason, the scope of Eq. (2.107) applicability will be limited to the component scaling discussion in Sec. 2.5.2.

Instead, as a compensation for the impracticality of capturing important system-level thermal behaviors of solid structures with the equations derived thus far, parameters will be supposed for just that purpose and can be applied when and where the thermal hydraulicist deems them fit.

Thermal inertia number (\mathcal{N}_{ThI})

I have previously discussed the impact of $Fo \gg 1$ on solid-structure scaling, which begs the question, ‘what about when $Fo \ll 1$?’ Going back to the definition of the Fo in Eq. (2.108), this condition describes scenarios when the the solid-structure thermal inertia serves as the dominant phenomenon at play. Large amounts of heat could be stored in solid structures with a relatively slow ‘release time’. Over the course of these energy release times, heat transfer will be limited less by how energy is made available for release and more by the

sheer capacity for storing it. It follows then, that a relationship comparing the thermal inertias of solids-to-fluids should be constructed.

The thermal inertia of a body is defined as $\int \rho c_p dV$, which has units [J/K]. However, to make this parameter more practical to calculate, it is helpful to approximate $\rho c_p \approx (\rho c_p)_o$. Then, taking a ratio of solid-to-fluid thermal inertias within a component, the thermal inertia number ($\mathcal{N}^{\circ}_{ThI}$) is born.

$$\mathcal{N}^{\circ}_{ThI} = \frac{(\rho c_p)_{s,o} V_s}{(\rho c_p)_{f,o} V_f} \quad \text{“}\equiv\text{”} \quad \frac{\text{solid-structure resistance to temperature change}}{\text{fluid resistance to temperature change}} \quad (2.118)$$

The component-specific nature of $\mathcal{N}^{\circ}_{ThI}$ is not articulated by Eq. (2.118). However, it is assumed this parameter will only be applied for component scaling.

Parasitic heat loss number ($\mathcal{N}^{\circ}_{PHL}$)

The term “parasitic heat loss” (PHL) is assigned to heat leakage occurring beyond purposeful heat removal within heat transfer components. An example of PHL is heat leakage from hot leg piping to the ambient. It is helpful to normalize parasitic losses against a meaningful measure, characteristic system thermal power. I call this supposed ratio the “PHL number”.

$$\mathcal{N}^{\circ}_{PHL} = \frac{h_{\infty} \sqrt{A_{o,c}} L_{o,c} \Delta T_{\infty}}{\dot{m}_o c_{p,o} \Delta T_o} \quad \text{“}\equiv\text{”} \quad \frac{\text{parasitic heat losses}}{\text{system thermal power}} \quad (2.119)$$

In this equation, $A_{o,c}$ is the characteristic fluid area, which provides only an approximation for outer-surface diameter when taken at the square root value. The subscript “ ∞ ” denotes external interaction with ambient conditions, typically a layer of insulation. An empirically determined h_{∞} accounts for heat transfer with adjacent insulation. As this parameter is dependent on many factors, it should be empirically extracted from experiment data. For practicality’s sake, the temperature difference parameter should be taken as the difference between the characteristic fluid temperature and that of the ambient air: $\Delta T_{\infty} = T_o - T_{\infty}$.

The $\mathcal{N}^{\circ}_{PHL}$ captures parasitic loss behavior as it pertains to the solid structures. For the detrimental impact of PHL on buoyancy-driven flow, see Fig. 2.5 and surrounding discussion.

2.5.4 Characteristic parameters for solid-structure energy scaling

All characteristic variables have been introduced previously. However, the characteristic time-scale will receive further attention here because additional considerations can be taken when defining this parameter for solid-structure scaling.

Characteristic time-scale ($t_{o,s}$)

ND fluid behavior is obviously characterized by the time required to flow through a region of interest — residence time. For solid structures, there is no one-size-fits-all approach for ascertaining time-scales. Instead, depending on the scenario at hand, a $t_{o,s}$ should be derived to capture pertinent phenomena at play in the system.

Selecting the correct solid-structure time-scale requires analyzing which phenomena at play are dominant in the system and then deciding how solid-structure heat transfer behavior should be contextualized. There are essentially three obvious options (listed below) for selecting a solid-structure characteristic time. See Pg. 69 for how these various time-scales impact the terms present in the solid-structure ND energy equation.

1. Matching the fluid time-scale: $t_{o,s} = \frac{L_o}{u_o}$
2. Adopting an internal-conduction-centric time-scale: $t_{o,s} = \frac{\delta_o^2}{\alpha_{s,o}}$
3. Adopting an external-heat-transfer-centric time-scale: $t_{o,s} = \frac{(\rho c_p)_o \delta_o}{h_{tot,o}}$

As seen in the fluid Eqs. (2.11), (2.33) and (2.72), the fluid characteristic time-scale is $t_o = L_o/u_o$, where u_o represents the characteristic fluid velocity. By equating the solid-structure time-scale to the fluid time-scale, the scaling analyst is choosing to directly relate solid-structure heat transfer behavior to the thermal *hydraulic* behavior of the system. This approach is recommended for situations when heat transfer within the component of interest actively engages the fluid and solid structures. In other words, when solid heat transfer and fluid heat transfer should not be treated separately.

For some instances, conduction within solid structures serves as the primary heat transfer mechanism of concern. Instead of allowing the fluid body to dictate system time-scales, a characteristic time can be produced from the conduction-driven diffusion characteristics of the material properties and the system geometry, $t_{o,s} = \delta_o^2/\alpha_{s,o}$. One might notice this ratio is already previously captured in Eq. (2.108), the *Fo* definition.

There are scenarios in which the ND solid-structure heat transfer behavior should be contextualized in terms of interface heat transfer. One example scenario is when internal conduction is so dominant, the thermal behavior of the solid structure of interest is primarily dictated by external transfer. The common term used for these scenarios is “lumped capacitance”, where transient temperature of an object can be approximated as

$$\frac{T_s - T}{T_0 - T} = \exp\left(\frac{-th}{\rho c_p \delta}\right) \quad , \quad (2.120)$$

where T represents the fluid temperature and T_0 is the initial lumped solid temperature. The exponential can be viewed as holding a ND time ratio $\exp(-t/t_s)$, giving rise to the third time-scale definition, $t_{o,s} = (\rho c_p)_o \delta_o / h_{tot,o}$.

2.6 A Three-Step Scaling Methodology for System- and Component-Level Scaling Analysis for FHRs

In Secs. 2.2 to 2.5, I show how scaling parameters for this methodology are derived and how considerations are taken for various modes of scaling. In this section, I tie those derived parameters into a cohesive methodology for FHR scaling.

The framework for this methodology was selected to support and emphasize radHT scaling distortion analysis. Taking the methodologies and other FHR scaling methods discussed in Sec. 2.1 into consideration, I decided to choose between Ishii's three-step approach or Zuber's H2TS approach as a starting point. I would then adapt it to my methodology by incorporating progress made in FHR scaling methods along the way. In the end, I decided to adapt Ishii's framework for several reasons. The primary reason was that I found the three-step methodology more intuitive to those less familiar with scaling analysis. Scaling numbers derived within a H2TS framework incorporate built in time-scales, which numerically indicate the significance of that parameter. In some ways, this feature satisfies multiple requirements for scaling at once — capturing ND phenomenological interplay and revealing the significance of that interplay to the system during the transient of interest. While this multipurpose feature might be convenient for the scaling analyst, I have found it also acts as a barrier to understanding. As I prefer this FHR scaling methodology to be accessible to more than just experienced thermal hydraulicists, it is desirable to separate the processes of identifying scaling relations and determining their significance. Ishii's three-step scaling approach accomplishes the task of scaling parameter identification, while primarily leaving the responsibility of determining phenomenological significance to separate analysis such as Phenomena Identification and Ranking Tables (PIRTs), a thorough description of which is provided by Wulff [62].

It is likely radHT will not play a significant role in many FHR scenarios. Radiative heat transfer scaling parameters derived from H2TS would be inherently minimized by system time-scales. For scaled system design, such as that in support of a reactor licensing approach, that minimization is rightfully done. However, this scaling methodology seeks to emphasize radHT scaling distortions, not neglect them. Utilizing Ishii's framework in this regard provides a more versatile approach — radHT scaling distortion can be emphasized to whatever extent the scaling analyst sees fit.

I took Ishii's three-step methodology, but adjusted it to emphasize radHT scaling parameters even further. As derived in Sec. 2.4.1, St_{rad} is applied on a component-by-component basis.

Taken purely in Ishii’s methodology, radHT would be but one of many phenomena analyzed in the “bottom-up” third step, almost as an afterthought for distortion analysis. However, I want the SET/IET design process to acknowledge these distortions early on, even enabling design alterations if deemed fit. In opposition to this, Ishii sought to emphasize integral system scaling, making it the first “top-down” approach. By switching the order of his steps one and three, and dropping the “top-down, bottom-up” nomenclature, I adapt Ishii’s three-step methodology to meet my goal of emphasizing radHT scaling distortion quantification.

I should mention I conducted most of this work before Kairos Power released their FHR scaling methodology [51]. If I had conducted this work following the release of that report, I would have probably built off their H2TS-based framework instead of Ishii’s, not because it better suits radHT distortion analysis, but because it would increase the likelihood of my developed methods being utilized in the short term for FHR SET/IET design and analysis. For those utilizing Kairos’s scaling methodology, equivalent radHT distortion quantification parameters can be derived to match the H2TS approach using the process outlined in [Sec. 2.4.1](#). Regardless, I present my FHR scaling methodology below, which enables the design of FHR SETs and IETs with all desirable experimental characteristics:

- **RHRA** to reduce experiment complexity and cost of materials
- **Reduced power electrical heating** to avoid nuclear heating and reduce energy costs
- **Surrogate fluids** to avoid complications and costs stemming from flibe toxicity and high melting point
- **Distortion quantification** methods pertinent to FHR scaling, including that for radHT distortion
- **Accelerated time** to shorten time necessary for running experiments, if desired

2.6.1 Scaling methodology framework

This methodology supports both component scaling and integral system scaling for FHRs. Briefly, component scaling enables scaled component design and produces SET test parameters, while integral system scaling is used for total scaled system design and IET testing. To allow for both of these modes, this methodology utilizes three steps (modeled after Ishii’s scaling methodology for LWRs [41, 42]), and can therefore be referred to as a “three-step” scaling methodology consisting of: step 1) intra-component scaling, step 2) inter-component scaling, and step 3) compatibility scaling. The methodology framework is summarized in [Fig. 2.6](#).

Energy scaling, both for fluids and solid structures, is heavily oriented towards component scaling. Therefore it is strongly encouraged to begin the scaling process with step one of the

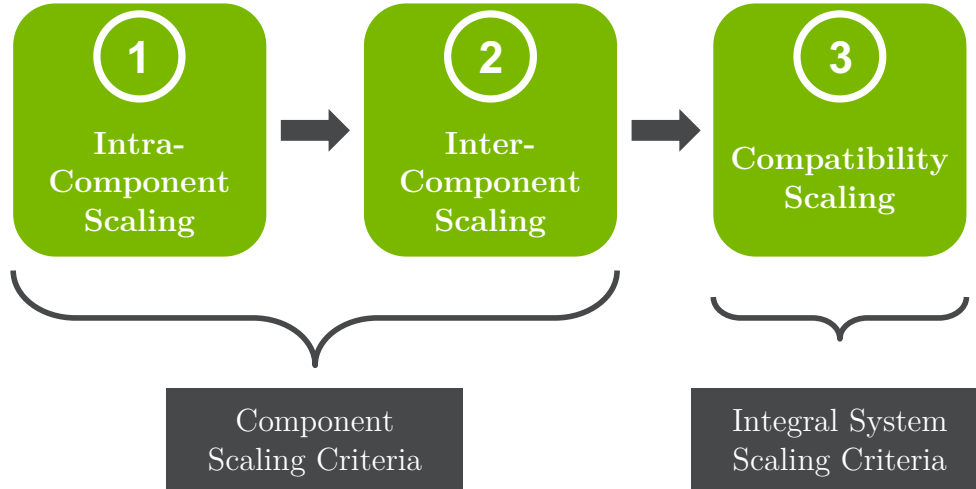


Figure 2.6: Three-step FHR scaling methodology framework consisting of the intra- and inter-component scaling steps for the purposes of component scaling and the compatibility scaling step for integral system scaling.

methodology applied to heat transfer components, regardless of the end goal. If the goal is SET design, intra-component scaling suffices. To analyze a component in the context of the system, the extra step of inter-component scaling is necessary. Even if the end goal is IET design and testing, the component-based nature of this methodology requires major heat transfer components be analyzed with intra- and inter-component scaling before completing the final step of compatibility scaling. However, in anticipation of compatibility scaling, some characteristic parameters chosen for intra-component scaling can be defined to capture integral system behavior during the component scaling steps.

2.6.2 Scaling relations for scaled system design

This section will discuss the scaling parameters included in each step of the scaling methodology. Additionally, summary tables will define scaling numbers to clarify the characteristic parameters contained within each scaling number, which reveals how scaling numbers constrain certain parameters for SET and IET design.

To compare ND behavior of prototypical FHRs and their experiments, I introduce scaling ratios represented by the subscript “ R ”. Scaling ratios are defined as the value of a given experimental scaling number divided by the value of the corresponding prototypical scaling number. An example scaling ratio, using a generic ND number N^e , is written below.

$$N^e_R = \frac{N^e_e}{N^e_p} \quad (2.121)$$


A $N_R = 1$ indicates phenomenological similarity between the experimental and prototypical systems for the behavioral interplay captured by that N . For scaling analysis, all numbers presented in Tbls. 2.4, 2.5 and 2.7 should be utilized in the context of Eq. (2.121) to compare experimental and prototypical behavior.

Step 1) Intra-component scaling

Intra-component scaling captures ND behavior pertinent to a single component at a time, primarily through choosing component-specific characteristic variables. Scaling parameters pertinent to component scaling will be produced in this step. In that vein, intra-component scaling neglects some ND numbers entirely.

Fluid momentum and energy scaling parameters for intra-component scaling are shown in Tbl. 2.4. Depending on the component, not all of these parameters are used. For instance, the Eu is not used if the component under analysis is not, or does not contain, a pump, while the St is typically used exclusively for heat transfer components. The St_{rad} is used to quantify radHT scaling distortion (discussed in Sec. 2.7).


Table 2.4: Intra-component scaling parameters for system fluids.

	Scaling Number	Definition
	Fr_c^{-1}	$\frac{gH_{o,c}}{u_{o,c}^2}$
	Eu	$\frac{gh_{pump,o}}{u_{o,c}^2}$
	St_{mod}	$\frac{4L_{o,c}}{D_h} \left(\frac{Nu}{Pe} \right)$
	St_{rad}	$\frac{L_{o,c}}{\Delta T_{Nu}} \int_1^2 \frac{q_{rad}'''}{\rho u c_p} \partial \mathcal{X}$
	$St (\overline{\varphi_w - \theta})$	$(St_{mod} + St_{rad}) \frac{\Delta T_{Nu}}{\Delta T_{o,c}}$

Utilizing these ND numbers in scaling analysis requires scaling ratios, previously defined as the experimental scaling number divided by the prototypical reactor number. For the Fr_c , it is assumed $g_R = 1$ (unless the scaling analyst has the profound distinction of designing earth-based scaled experiments for a moon- or Mars-based FHR), and $Fr_{c,R}^{-1}$ simplifies to

$(H_{o,c}/u_{o,c}^2)_R$. The Eu_R is simplified in the same way. The St_R is dependent on which heat transfer phenomena are anticipated to be present in the analyzed component.

Table 2.5: Intra-component scaling parameters for solid structures.

	Scaling Number	Definition
	Fo	$\frac{\alpha_{s,o} t_{o,s}}{\delta_o^2}$
	$FoBi$	$\frac{h_{tot} t_{o,s}}{(\rho c_p)_o \delta_o}$
	N_{ThI}^o	$\frac{(\rho c_p)_{s,o} V_s}{(\rho c_p)_{f,o} V_f}$
	N_{PHL}^o	$\frac{h_\infty \sqrt{A_{o,c}} L_{o,c} \Delta T_\infty}{\dot{m}_o c_{p,o} \Delta T_o}$

The intra-component scaling parameters for solid structures are shown in [Tbl. 2.5](#). The first two parameters, Fo and $FoBi$, are derived from the solid-structure energy equation and are therefore useful for scaling solid structures. The latter two parameters, N_{ThI}^o and N_{PHL}^o , were contrived separate from the energy equation with the intention of capturing thermal impacts of solid structures on the system fluid — specifically, impacts present in FHRs and known to be potential sources of scaling distortion in FHR experiments. Despite their lack of derivation from first principles, these parameters are important for FHR scaling analysis and will be discussed further in [Secs. 2.6.6](#) and [2.6.7](#).

Step 2) Inter-component scaling

Inter-component scaling begins to reconcile differences generated by separately analyzing individual components in intra-component scaling. To accomplish this, mass and energy balances are evaluated at component boundaries, justified by the ND fluid acceleration term in [Eqs. \(2.15\)](#) and [\(2.37\)](#) and the ND fluid heating term in [Eq. \(2.81\)](#). Solid structures are not considered in inter-component scaling because discontinuities between components' solids are permitted due to axial conduction being considered negligible between [Eqs. \(2.99\)](#) and [\(2.103\)](#).

Inter-component scaling differs from other steps in this methodology in that scaling numbers are not plugged into [Eq. \(2.121\)](#). Instead, characteristic variables between components are

set equal to each other. However, inter-component scaling is still considered part of the scaling process because this step relates scaled component behavior to that of surrounding components.

To ensure uniform ND mass and energy balances between adjacent components, \dot{u} , θ , and τ must have equal values at component boundaries, made apparent by the $\partial\dot{u}/\partial\tau$ and $\partial\theta/\partial\tau$ terms in the ND fluid momentum and ND fluid energy equations, respectively. Uniformity is accomplished by adopting the same characteristic variable definitions for multiple components.

Table 2.6: Non-dimensional variables for inter-component scaling. Matching these variables at component boundaries requires inter-component uniformity for the associated characteristic variables.


	ND Variable	Characteristic Variable(s)
	\dot{u}	$\rho_{o,c}, u_{o,c}, A_{o,c}$
	θ	$T_{C,o,c}, T_{H,o,c}$
	τ	$L_{o,c}, u_{o,c}$
		— OR —
		$w_{o,c}$

Table 2.6 shows which characteristic variables must adopt uniform values for which ND component boundary parameters. Two options exist for uniformly normalizing time because

$$t_o = \frac{L_o}{u_o} \left(\frac{\rho_o A_o}{\rho_o A_o} \right)^{ (=1)} = \frac{w_o}{\dot{u}_o} \quad , \quad (2.122)$$

and if $\dot{u}_{o,c}$ has already been given a uniform value, adopting a consistent $w_{o,c}$ can be used to preserve adjacent components' proportion of total system fluid residence time.


The responsibility of selecting values that properly capture characteristic behavior across multiple components falls to the scaling analyst. Possible tactics for this process include simply appropriating characteristic variables from the more important component or treating connected components as one and following the same approach taken for selecting intra-component scaling characteristic variables.

Step 3) Compatibility scaling

Compatibility scaling works to capture integral system thermal hydraulic phenomena. In this step, differences introduced by separate applications of intra-component scaling are fully reconciled. Component-specific characteristic variables are replaced by those reflecting integral system behavior. Additionally, some scaling parameters, which were ignored by intra- and inter-component scaling, are considered for analysis. This step is necessary for IET design.

Compatibility scaling parameters are shown in Tbl. 2.7. The Fr has been redefined with integral-system characteristic parameters, and two scaling numbers have been introduced — the Ri for buoyancy driven natural circulation flow and the \mathcal{F} , which captures loop-wide friction effects. In addition to the characteristic variables shown in Tbl. 2.7, all characteristic parameters should be redefined in the compatibility scaling step to characterize total system behavior. This includes the characteristic variables discussed in inter-component scaling (Tbl. 2.6).

Table 2.7: Compatibility scaling parameters for producing scaled integral system criteria.

	Scaling Number	Definition
	Fr^{-1}	$\frac{gH_o}{u_o^2}$
	Ri	$\frac{g\beta_o H_o \Delta T_o}{u_o^2}$
	\mathcal{F}	$\frac{L_o}{2} \oint \frac{f}{D_h} \left(\frac{\rho_o A_o}{\rho A} \right)^2 d\mathcal{K} + \sum \frac{K}{2} \left(\frac{\rho_o A_o}{\rho A} \right)^2$

As assumed for intra-component scaling, $g_R = 1$, which simplifies the Froude ratio to $Fr_R^{-1} = (H_o/u_o^2)_R$. If this ratio is properly resolved to unity between the prototype and experiment, the Ri ratio can be additionally simplified to $Ri_R = (\beta_o \Delta T_o)_R$. For natural circulation IETs, this simplified Ri_R can be essential for selecting a temperature range and T_{avg} (at which β_o is typically evaluated). The use of surrogate fluids for FHR IETs can be further supported by this parameter as well.

The \mathcal{F} contains density-area ratios, which have been preserved by neglecting the Boussinesq approximation in derivation of the scaled fluid momentum equations. The ratios assisted in determining which terms could be neglected and which should be kept in formulation.

However in the \mathcal{F} , these ratios introduce a complication which could make determining an accurate \mathcal{F} impractical. If desired, this scaling number can be simplified to

$$\mathcal{F} \approx \frac{L_o}{2} \oint \frac{f}{D_h} \partial_{\mathcal{K}} + \sum \frac{K}{2} \quad . \quad (2.123)$$

2.6.3 Use of inertia numbers in transient scaling

There are two distinct time regimes in scaling analysis: steady-state scaling and transient scaling. Thus far, this chapter has discussed scaling parameters and the ND equations that produce them with a strong emphasis on the steady-state regime. That can be seen by the majority of discussion being about the derivation of the scaling parameters themselves. Take for example this simplified, generic ND equation for some variable ψ in a form resembling the scaled Eqs. (2.15), (2.37), (2.81) and (2.107).

$$\frac{\partial \psi}{\partial \tau}(\text{WF}) = \mathcal{N}_A + \mathcal{N}_B$$

ND change term	×	Weighting factor (WF)	=	ND A term	+	ND B term
-------------------	---	--------------------------	---	--------------	---	--------------

For steady-state scaling analysis, the LHS goes to zero, the weighting factor (WF) can be neglected, and scaling terms need only be compared to other scaling terms in the equation. More specifically for this example, when matching numbers between systems one need only preserve the ratio ($\mathcal{N}_A/\mathcal{N}_B$). However for transient scaling analysis, the LHS remains in formulation, thereby preserving the weighting factor. Transient scaling is much more stringent because the outright values of each scaling parameter must be heeded separately to maintain similitude in $\partial\psi/\partial\tau$. For this regime, the scaling analyst must either match \mathcal{N}_A , \mathcal{N}_B , and WF, or match the ratios (\mathcal{N}_A/WF) and (\mathcal{N}_B/WF) to achieve thermal hydraulic similitude. Enabling transient scaling with this methodology is the reason scaling parameters summarized in Sec. 2.6.2 are presented as individual numbers (i.e. like \mathcal{N}_A , \mathcal{N}_B) rather than as more flexible ratios (i.e. like $\mathcal{N}_A/\mathcal{N}_B$).

In practice however, scaling analysis is more complicated than what is shown by the above generic example for ψ . The WF, which exists as a integral coefficient to the ND change term, varies over time during transients. Similarly, the ND A and B terms have time-dependant integral coefficients which act to modify the effect of \mathcal{N}_A and \mathcal{N}_B on $\partial\psi/\partial\tau$. While these integral terms are too variable to incorporate into scaled system design, they can be used during transient experiments to help describe ND thermal hydraulic behavior. This section will explain and demonstrate how these previously derived weighting factors, or “inertia numbers”, can be used in transient analysis.

Throughout the derivation of scaling parameters for this methodology, several inertia numbers have arisen as coefficients to the ND change terms — the fluid momentum inertia number $\mathcal{N}_{FMI}^{\circ}$ in Eqs. (2.23) and (2.40), the fluid energy inertia number $\mathcal{N}_{FEI}^{\circ}$ in Eq. (2.81), and the solid-structure energy inertia number $\mathcal{N}_{SEI}^{\circ}$ in Eq. (2.107). These inertia numbers are summarized below.

$$\mathcal{N}_{FMI}^{\circ} \equiv \int \frac{\rho_o A_o}{\rho A} \partial \mathcal{J} \quad (2.124)$$

$$\mathcal{N}_{FEI}^{\circ} \equiv \int \frac{u_o}{u} \partial \mathcal{J} \quad (2.125)$$

$$\mathcal{N}_{SEI}^{\circ} \equiv \iint \mathcal{J} \partial \mathcal{J} \quad (2.126)$$

It can be noted $\mathcal{N}_{FEI}^{\circ}$ calculates ND residence time and $\mathcal{N}_{SEI}^{\circ}$ calculates ND solid-structure volume. The $\mathcal{N}_{FMI}^{\circ}$ produces a ND residence frequency when applied to a length equal to $L = L_o$, as shown below.

$$\begin{aligned} \mathcal{N}_{FMI}^{\circ} &= \int \frac{\rho_o A_o}{\rho A} \partial \mathcal{J} \\ &= \int \frac{\dot{m}_o}{u_o} \frac{u}{\dot{m}} \partial \mathcal{J} = \int \frac{u}{u_o} \partial \mathcal{J} \end{aligned} \quad (2.127)$$

$$\mathcal{N}_{FMI}^{\circ} \Big|_0^{L_o} = \frac{u}{L_o} \frac{L_o}{u_o} \quad (2.128)$$

Interestingly, this expression reveals $\mathcal{N}_{FMI}^{\circ}$ and $\mathcal{N}_{FEI}^{\circ}$ are inversely related (loosely). Therefore, as the mass flow rate departs from \dot{m}_o throughout a transient, the scaled momentum equation will become more sensitive to its respective ND terms while the scaled energy equation becomes less sensitive, or vice versa.

Equations (2.124) to (2.126) are all referred to as “inertia numbers” because they act as weighting factors to changes in temperature and fluid flow. The higher these numbers are, the more drastic differences between other terms in formulation need to be to induce heating/cooling or flow acceleration/deceleration.

The nomenclature used here is similar to that used by Scarlat [46], where she refers to the total ND change term multiplied by its associated inertia number as the “inertia term”. In contrast, I elected to separate the inertia number from the ND change term so the weighting factor can serve a purpose at steady-state conditions. Throughout Secs. 2.2 to 2.4, I have demonstrated that purpose. I used inertia numbers as normalizing factors in numerical

demonstrations (Tbls. 2.1 to 2.3) to justify decisions made in derivation. Numerically this use makes sense — each inertia number serves as a coefficient to its respective ND change in momentum or energy, so comparing any other term’s order to that of the inertia number returns a quantified metric for that term’s ability to influence the thermal hydraulic behavior of the system. Moreover, these inertia numbers are necessary for analyzing ND behavior during transient conditions as well.

Inertia numbers have an inversely-related impact on $\partial\psi$. To force transient behavior to align between prototypical and experimental systems, *all* scaling terms in the ND scaled equations would have to be adjusted by quotients of their respective inertia numbers throughout the entire transient. Another option is maintaining all time-variable inertia numbers between prototype and experiment. Realistically however, both of these expectations are completely unreasonable to practically incorporate into scaling analysis. Inertia numbers are too variable and difficult to control. Transient scaling distortions will exist and impact ND phenomena throughout transients.

The good news is these inertia numbers, assuming proper selection of characteristic parameters, should cause limited distortion between prototype and experiment. Instead of attempting to force these numbers into ideal values for the sake of scaling transient behavior between systems, it is more practical to simply track their impact on ND system behavior throughout transients. Scaling parameters from Tbls. 2.4 to 2.7 will be adjusted by their respective inertia terms, in addition to their time-variable coefficients. Instead of providing multiple tables of transient scaling terms, I recommend revisiting Eqs. (2.15), (2.37), (2.81) and (2.107) to use for forced circulation, natural circulation, fluid energy, and solid energy transient scaling, respectively.

2.6.4 Distortions between FHRs and their scaled experiments

This scaling methodology provides the mathematical means to capture ND-ized behavior of nuclear reactors, specifically FHRs, and replicate that behavior in reduced-scale experiments. However, no scaling methodology can replicate phenomenological similitude perfectly. There will inevitably be discrepancies, called “scaling distortions”, between the prototypical ND behavior and the experimental behavior meant to mimic the former.

There are two ways to look at scaling distortions. Discrepancies in ND behavior between scaled systems can be seen by comparing the values of entire ND terms from the scaled momentum and energy equations. I refer to this interpretation as operational mode distortion. However, operational mode distortion analysis can only be carried out when operational data is available for both systems are available, hence the name. The conventional practice observes distortions in scaling numbers only. This interpretation can be carried out with characteristic parameters only, making it practical for designing scaled systems. Therefore I call this interpretation design mode distortion analysis.

To understand how scaling distortions affect experimental system behavior, it is necessary to quantify the impact of each distortion. Building on the generic example for scaling number ratios represented in Eq. (2.121), design mode scaling distortion of a generic ND number N^o is shown by Eq. (2.129) in units of %. To capture operational mode distortions, the generic N^o s would need to be replaced by whole ND terms normalized by their respective inertia numbers.

$$N^o_{dist} = (1 - N^o_R) \times 100 \% \quad (2.129)$$

In some cases, the practice of distortion quantification can highlight shortcomings in scaled system design and lead to the mitigation of distortions. Additionally, the metrics used for distortion quantification can facilitate experimental augmentation for the purpose of compensating for scaling distortions, such as increasing SET/IET convective heat transfer to compensate for decreases in radiative heat transfer.

For FHR experiments designed with this scaling methodology, there are four primary sources of scaling distortion: accelerated time, PHL, thermal inertia, and radHT (or rather, lack thereof). I discuss these sources of distortion in Secs. 2.6.5 to 2.6.8. These ensuing sections will address how to quantify and compensate for each prominent FHR-to-experiment scaling distortion discussed. The focus of this thesis is radHT scaling distortion, so discussion on quantifying those effects is granted a standalone section as Sec. 2.7.

2.6.5 Residence time scaling distortion

The residence time distortion is not one particular to FHR experiments. In fact, any system-level scaling analysis used to design reduced-height experiments will face this issue. In this case, the Fr introduces a complication due to the mismatch between exponents of H_o and u_o^2 . If the Fr is preserved between systems,

$$\begin{aligned} \left(\frac{1}{Fr} \right)_R &= \frac{gH_{o,R}}{u_{o,R}^2} = 1 \\ \implies u_{o,R} &= \sqrt{H_{o,R}} \quad . \end{aligned} \quad (2.130)$$

Substituting this relation into the definition characteristic time produces the metric for plugging into Eq. (2.129) to quantify the residence time scaling distortion.

$$\begin{aligned} t_{o,R} &= \frac{L_{o,R}}{u_{o,R}} \\ t_{o,R} \Big|_{Fr_R=1} &= \frac{L_{o,R}}{\sqrt{H_{o,R}}} \end{aligned} \quad (2.131)$$

Deduced from Eq. (2.131), $t_{o,R}$ will not be equal to one if the same value is adopted for experimental height- and length-scales. If this discrepancy is not accounted for by adjusting non-vertical lengths in the scaled experiment, τ_e and τ_p will not match, and a time distortion will exist between systems.

Unlike other FHR scaling distortions, the residence time distortion can be seen as an advantage. This distortion can be utilized to decrease the amount of real-world time taken to

Table 2.8: Residence time scaling distortion examples between hypothetical prototypes and IETs of various dimensions. System diagrams are drawn to scale, with red dots indicating \dot{Q}_{gen} component center points and blue dots indicating \dot{Q}_{HX} component center points. Characteristic time ratios less than one indicate accelerated time.

Prototype	IET	$L_{o,R}$	$H_{o,R}$	$t_{o,R}$
		$\frac{1}{2}$	$\frac{1}{4}$	1
		$\frac{1}{2}$	$\frac{1}{2}$	0.71
		$\frac{1}{3}$	$\frac{3}{4}$	0.38

simulate prototypical behavior with experiments, hence the name “accelerated time”. For example, if $H_{o,R} = L_{o,R}$, some prototypical reactor scenario spanning four hours could be simulated in full by a quarter-scale experiment in the accelerated time span of two hours. Another advantage of tweaking accelerated time could result in the alignment of chronological progression between coupled loops with discrepant time-scales. Further examples of preserved and accelerated time-scale distortion are shown in Tbl. 2.8.

2.6.6 Parasitic heat loss scaling distortion

As with the residence time scaling distortion, PHL scaling distortion is not one specific to FHR experiments. Due to the reduction in flow areas in SETs/IETs compared to their prototypical reactor counterparts, the solid-structure outer-surface-area-to-volume ratio is increased proportional to D_R^{-1} — significant because PHL is proportional to this solid-structure outer surface area. This means reduced-area experiments suffer an increased roll of PHL in system thermal behavior — in other words, the PHL distortion is inherent to reduced-area scaled systems.

Parasitic heat loss distortion analysis is less important to consider for the purpose of informing experimental design, as conserving A_R between systems is not practical, and more important for the purpose of quantifying the distortive effects and analyzing impacts on system behavior. To achieve this, the N_{PHL}^o can be applied to any component of interest for PHL distortion analysis. However, the amount of PHL distortion need not be accepted outright.

Typically, scaled down experimental systems utilize insulation to mitigate PHL. In terms of the N_{PHL}^o , the experimental h_∞ value will be decreased. However, overcoming the surface-area-to-volume ratio discrepancy between systems is a difficult task for insulation alone. There is another method for decreasing the impact of PHL.

Revisiting the residence time scaling distortion, there is another practical benefit of accelerated time beyond conducting experiments in a shorter time span — mitigating PHL. Strictly at steady-state conditions, one possible expression for the proportion of energy lost through system-level PHL per unit ND time is shown on the LHS of the equation below.

$$\left(\frac{\dot{Q}_{gen} - \dot{Q}_{HX}}{\tau} \right)_R = \left(\dot{Q}_{gen} - \dot{Q}_{HX} \right)_R t_{o,R} \quad (2.132)$$

The RHS shows this PHL metric evaluated as a ratio between experimental and prototypical systems, which reveals a direct relationship to the characteristic time-scale ratio. For scaled experiments with accelerated time, $t_{o,R} < 1$, thereby reducing the proportional impact of PHL per unit τ_e . Therefore, accelerated time can be used as another method to combat exaggerated PHL in scaled experiments for FHRs and augment its impact closer to that experienced by the prototypical reactor.

2.6.7 Thermal inertia scaling distortion

Thermal inertia plays a significant role in the heat transfer behavior of FHRs due to the relatively high thermal inertia of materials in the core [1]. Additionally, the high volumetric heat capacity of fiibe and high core graphite volume renders the balance between core fluid and solid structure thermal inertia on the order of unity. This point can be reinforced by evaluating the N_{ThI}^0 for the Mk.I core.

$$N_{ThI}^0 \Big|_{Mk.I} = \frac{(\rho c_p)_{graphite}[V_{core}(1 - \varepsilon) + V_{reflectors}]}{(\rho c_p)_{fiibe} V_{core}(\varepsilon)} \quad (2.133)$$

Here, ε represents the void fraction of a randomly packed pebble bed, ≈ 0.4 . Using values from Forsberg, Peterson, and Pickard [1] and the Mk.I Design Report [3],

$$\begin{aligned} N_{ThI}^0 \Big|_{Mk.I} &= \frac{3230 \text{ kJ}/(\text{m}^3 \text{ K})}{4540 \text{ kJ}/(\text{m}^3 \text{ K})} \left(\frac{0.6}{0.4} + \frac{28.3 \text{ m}^3}{7.2 \text{ m}^3} \right) \\ &= 3.86 \end{aligned} \quad (2.134)$$

For FHR scaled experiments, the thermal inertia interplay between the surrogate fluid and solid-structures in the heater section should have the same impact on system thermal response as that between fiibe and graphite in the FHR core. However, the materials historically used for FHR experiments typically produce a thermal inertia distortion. While the primary purpose of $N_{ThI,R}^0$ remains quantifying those distortive effects, there remains the possibility of utilizing this parameter for thermal mass augmentation, or artificially adjusting the thermal structures in components of interest by adding or removing solid structures.

Take, for example, a hypothetical comparison between CIET as the experiment and the Mk.I as the prototype. Using thermophysical properties for 304L stainless steel and Therminol[®] VP-1 at 80 °C [55] to describe the CIET heater section,

$$\begin{aligned} N_{ThI}^0 \Big|_{CIET} &= \frac{3774 \text{ kJ}/(\text{m}^3 \text{ K})}{1761 \text{ kJ}/(\text{m}^3 \text{ K})} \left(\frac{680.9 \text{ cm}^3}{1832 \text{ cm}^3} \right) \\ &= 0.80 \quad , \end{aligned} \quad (2.135)$$

which produces a 79 % distortion compared to the Mk.I core N_{ThI}^0 . If CIET were being designed as an IET for the Mk.I, the thermal inertia balance in the heater section could be augmented by adding thermal mass for the purpose of matching N_{ThI}^0 between systems.

$$\left[1 - \left(\frac{N_{ThI}^0 \Big|_{CIET}}{N_{ThI}^0 \Big|_{Mk.I}} \right) \right] \times 100 \% = 0 \% \quad (2.136)$$

$$\frac{3774 \text{ kJ}/(\text{m}^3 \text{ K})(680.9 \text{ cm}^3) + (\rho c_p V)_{aug}}{1761 \text{ kJ}/(\text{m}^3 \text{ K})(1832 \text{ cm}^3)} = 3.86 \quad (2.137)$$

$$(\rho c_p V)_{aug} = 9886 \text{ J/K}$$

$$V_{aug} = \begin{cases} 3757 \text{ cm}^3 & , \text{ Pyrex} \\ 373 \text{ cm}^3 & , \text{ 9:1 Teflon:Cu} \end{cases} \quad (2.138)$$

The two examples for additional solid-structure materials I provided, Pyrex [6] and Teflon doped with copper, are materials recommended for FHR experiments' solid structures. Materials should be chosen to match pertinent solid-structure scaling numbers from Tbl. 2.5. Additionally, these added structures should be entirely submerged in the coolant to avoid increasing experimental PHL. Ideal placement for these structures is surrounding the heater element to simulate FHR core geometry. If that placement is not practical, immediately following the heater is okay as long as effects on the characteristic height-scale are taken into account (see Pg. 38) to avoid distorting the Fr .

2.6.8 Radiative heat transfer scaling distortion

The issue of radiative heat transfer scaling distortion in FHR experiments is discussed at length in Ch. 1. I will summarize here. The rate of radiative emission is proportional to the fourth power of absolute temperature, so any reduced-temperature scaled experiment will suffer an inherent reduction in radiative heat transfer. However, radHT distortion is of particular interest to FHR experiments because flibe acts as a participating medium, further enhancing radHT in the experimental system. For FHR-based radiation-dominant heat transfer scenarios, reduced-temperature, surrogate fluid experiments will be physically unable to replicate that radHT behavior.

Quantifying this discrepancy requires approximating the system-level impact of radHT at prototypical conditions. However, the lack of radiative property data for flibe [25] makes approximating the role of radHT in FHRs a difficult task. Previous approximations were mentioned in Sec. 1.2.2. Future progress in characterizing the absorption properties of flibe in conjunction with the development of radHT modeling capabilities for system codes [63] will enable more accurate predictions of the role thermal radiation plays in the system-level heat transfer behavior of FHRs. Even without well-defined radiative properties for flibe, sensitivity studies can be (and are) carried out with various thermophysical property values to explore the impact of a participating medium coolant in a diverse range of FHR scenarios. With numerical approximations provided by system codes, the distortion quantification metrics proposed in Sec. 2.7 can be used to capture the impact of radHT discrepancies on scaled heat transfer and overall IET behavior.

2.7 Quantifying Radiative Heat Transfer Scaling Distortion between FHRs and their Experiments

Heat transfer scaling analysis for FHRs is carried out on the component level with the St . For some FHR components, there are scenarios where radHT is significant when compared to convective transfer. In terms of ND scaling parameters, this can be described as $St_{rad}/St_{mod} \sim \mathcal{O}(0)$. This behavior will not be inherently replicated by scaled systems, so quantifying the distortion in St_{rad} is necessary for understanding discrepancies in heat transfer behavior between FHRs and their experiments.

I have previously discussed the St_{rad} and its role in the scaled fluid energy equation in [Sec. 2.4.1](#). This scaling number is typically analyzed in conjunction with the convective St_{mod} , as shown by [Eq. \(2.86\)](#) and [Tbl. 2.4](#). However, if the radHT scaling distortion is anticipated to be significant, [Eq. \(2.129\)](#) should be used to quantify radHT scaling distortion. There are two ways to capture radHT scaling distortion depending on what the scaling analyst seeks to capture.

The **first approach** for analyzing radHT distortion is the most straightforward one. This approach compares the **isolated impact of radHT** between systems. Unlike convective transfer, thermal radiation cannot be isolated from its temperature dependencies, so the St_{rad} changes with temperature. Therefore, the correct metric for capturing total ND radHT in a component is represented by $St_{rad}(\overline{\varphi_w - \theta})$, previously defined in [Eq. \(2.85\)](#). The distortion quantification expression produced with this metric is shown by [Eq. \(2.139\)](#).

$$[St_{rad}(\overline{\varphi_w - \theta})]_{dist} = \left[1 - \left(\frac{L_{o,R} \int_e \frac{q_{rad}'''}{\rho u c_p} \partial \mathcal{X}_e}{\Delta T_{o,R} \int_p \frac{q_{rad}'''}{\rho u c_p} \partial \mathcal{X}_p} \right) \right] \times 100 \% \quad (2.139)$$

The **second approach** drops the ND temperature difference factor $(\overline{\varphi_w - \theta})$ in favor of treating **radHT as if it can be characterized by geometry and flow conditions, separate from temperature**, in the same way convective heat transfer can. Therefore, this behavior is best captured at steady state or at other well-defined characteristic conditions. The metric used here is the bare St_{rad} parameter previously shown in the penultimate row of [Tbl. 2.4](#). Inserting this metric into [Eq. \(2.129\)](#) produces a distortion quantification parameter, [Eq. \(2.140\)](#), useful for analyzing radHT distortion in the same manner as convective heat transfer distortion. The only difference between [Eqs. \(2.139\)](#) and [\(2.140\)](#) is the ΔT_R . However, this small change alters the meaning of the radHT distortion quantification parameter, which subsequently changes the situations in which it is appropriate for use.

$$(St_{rad})_{dist} = \left[1 - \left(\frac{L_{o,R} \int_e \frac{q_{rad}'''}{\rho u c_p} \partial \mathcal{K}_e}{\Delta T_{Nu,R} \int_p \frac{q_{rad}'''}{\rho u c_p} \partial \mathcal{K}_p} \right) \right] \times 100 \% \quad (2.140)$$

As discussed previously these two radHT distortion metrics will demonstrate a non-zero distortion value between FHRs and their experiments. In some circumstances, the radHT distortion will be significant enough to warrant compensation through other heat transfer means, specifically convection. To carry out “convective compensation”, it is necessary to contextualize radHT scaling distortion within the total heat transfer distortion (St_{dist}) for the component of interest. An example is shown below, assuming negligible radiative transfer in the experiment component.

$$St_{dist} = \left[1 - \frac{St_{mod,e}}{St_{mod,p} + St_{rad,p}} \right] \times 100 \% = 0 \% \quad (2.141)$$

$$Nu_e = (D_h Pe)_R Nu_p + \frac{(D_h Pe)_e}{4 \Delta T_{Nu,p}} \int_p \frac{q_{rad}'''}{\rho u c_p} \partial \mathcal{K}_p \quad (2.142)$$

Using this expression, convective heat transfer in the SET/IET heater section can be adjusted to compensate for the radHT distortion. Recall this convective compensation only holds true for the convective $\Delta T_{Nu,p}$.

Example distortion quantification calculation

For some, an example calculation can assist in making these distortion quantification parameters more tangible and comprehensible. To promote generalizability with this example, I produce and utilize arbitrary St values — some based on values calculated in [Sec. 4.2](#) — for an unspecified component in some nondescript scenario. All numbers and calculations discussed are summarized in [Tbl. 2.9](#).

For this example scenario, I assume participating media radHT constitutes 26 % of total solid-to-fluid heat transfer in the FHR prototype and 2 % in the scaled down experiment. If this analysis were conducted in a conventional manner for experimental design, these percentages would need to be ascertained for the FHR prototype for the situation at hand, and separately for the experiment (once it were designed). As radHT is impractical to measure, these values would most likely be acquired through system-level radHT simulation, such as those enabled by the work conducted in [Ch. 3](#). I proceed with this example pretending the 26 % and 2 % values were found through such simulations.

Assuming component-specific characteristic parameters are properly representative of conditions in the FHR component, $[St_{rad} (\overline{\varphi_w - \theta})]_p$ will likely equal unity. The St_p will depend

on component values for $\Delta T_{o,c}$ and the heat transfer $\Delta T_{Nu,c}$. For this example, I substitute a value calculated in Sec. 4.2 — 0.275. Incorporating the assumed radHT contributions, the convective and radiative St values in Tbl. 2.9 can be populated, completing the “prototype” column.

Table 2.9: Stanton number values used for radiative heat transfer scaling distortion quantification example.

	Prototype	Experiment	Distortion [%]
$St (\overline{\varphi_w - \theta})$	1.00	1.02	-2.0
$St_{mod} (\overline{\varphi_w - \theta})$	0.740	1.00	-35
$St_{rad} (\overline{\varphi_w - \theta})$	0.260	0.020	92
St	0.275	0.208	24
St_{mod}	0.204	0.204	0.0
St_{rad}	0.0715	0.00415	94

With the prototypical St values defined, I now move on to exemplifying the determination of an experimental design scaled down from the FHR system. Here, I assume the experimental designer neglects radHT and solely addresses the dominant heat transfer mechanism — convection. This is achieved by achieving perfect similitude in the St_{mod} , as shown by the associated 0% distortion in Tbl. 2.9. As the focus is on convection in this example, characteristic parameters would be selected such that $St_{mod} (\overline{\varphi_w - \theta}) = 1$. The St and St_{rad} values are found using the assumed 2% proportion of radHT. Again, this value would likely be found via system-level modeling.

The St distortion values, shown in the right-most column of Tbl. 2.9, are calculated in a manner consistent with the methods repeated throughout this chapter. The bolded values, radiative St terms, are found consistent with Eqs. (2.139) and (2.140). Exclusively seeking convective similitude, as carried out in this example, conveniently results in minimal scaled heat transfer behavior — made apparent by the -2% distortion for $St (\overline{\varphi_w - \theta})$. However, this small value is the result of almost-negligible experimental radHT and well-selected temperature-scales. The contribution of radHT is poorly scaled. By the first approach discussed in this section, the distortion is 92%. Thermal radiation, being a significant heat transfer mechanism in the prototypical scenario, is thus not represented by the experiment, and any deviation from this characteristic behavior set-point will likely result in increased heat transfer distortions in St and $St (\overline{\varphi_w - \theta})$.

2.8 This Scaling Methodology and FHR Development

There previously existed scaling methods purposed for FHR scaling, but none designed specifically to accommodate the analysis of inherent radHT scaling distortion between FHRs and their associated experiments. In this chapter, I present a cohesive scaling methodology that fills that persistent gap in the field of FHR scaling analysis.

In [Secs. 2.2 to 2.5](#), I show how this methodology’s scaling numbers arise from the system-level momentum and energy equations, explain the theoretical meaning and phenomenological interplay captured by these various parameters, and discuss the implications of applying these equations to component and system scaling approaches. The ND numbers produced from these derivations constitute the metrics of this scaling methodology, but do not constitute a methodology in their own right. In [Sec. 2.6](#), I culminate these numbers into a cohesive methodology by providing a three-step framework for FHR scaling. This includes steps for component and integral system scaling in addition to addressing the scaling distortions anticipated to be present in FHR experiments. The most important distortion addressed by this methodology is radHT scaling distortion, for which I discuss quantification and convective compensation methods in [Sec. 2.7](#).

Some example applications of scaling analysis are interspersed throughout this chapter. However, the bulk of example applications are included in [Ch. 4](#). Beyond applications constrained to this thesis, I developed this methodology for the purpose of scaling real world FHR prototypes. While radHT distortion does remain the focus here, this methodology is generalizable enough to be used for any FHR system-level scaling analysis, and I recommend considering it for that use. Either for applications in academia or industry, this methodology can provide the necessary scaling analysis methods while avoiding the need to independently develop one’s own.

Chapter 3

The Development of Radiative Heat Transfer Simulation Capabilities for System Analysis Module

An advanced system-level thermal hydraulics code (system code) is necessary to conduct scaling analysis for fluoride-salt-cooled high-temperature reactors (FHRs), which includes the radiative heat transfer (radHT) scaling analysis that is conceptually at the core of this thesis. However, before I conducted the work discussed in this chapter, the leading advanced reactor system code — System Analysis Module (SAM) — could not simulate radHT in any substantial manner. Therefore, since I chose to use SAM, I needed to develop this simulation capability. This chapter discusses the development of radHT modeling capabilities for SAM and further improvements I made to expand those capabilities and add new features.

Following a literature review on previous system-level radHT modeling (Sec. 3.1.2), I derived a radHT formulation (Sec. 3.2.1) that could permit the desired modeling scenarios and still be implemented into SAM (Sec. 3.2.2). The code I developed can simulate a one- or two-surface radiative enclosure with or without a participating fluid, all of which can be constructed from many compatible, preexisting SAM components (Sec. 3.2.4). For the predefined geometry options I enabled, the developed code can even determine the amount of participating fluid interaction (Sec. 3.2.3) without the user needing to calculate that parameter themselves. To make this radHT modeling capabilities a more useful tool for thermal hydraulic analysis, I added post-processing capabilities to output heat transfer rates for radiating bodies in the system (Secs. 3.2.5 and 3.2.6). Additionally, I verified the developed code (Sec. 3.3) to instill confidence in SAM's radHT modeling. Because of the work discussed in this chapter, SAM now has the ability to simulate radiative heat transfer, which means this tool can be incorporated into advanced reactor safety analysis to investigate radHT effects on the system-level.

This work constituted the bulk of the technical component of my dissertation work, so I

have given this chapter substantial emphasis. However, it should be noted I developed these simulation capabilities as a means of procuring the tools necessary to perform some of the analysis present in other chapters such as quantifying the radHT scaling distortion discussed in [Sec. 2.7](#) and modeling radHT in FHR simulations.

3.1 System Codes

System-level thermal hydraulics is integral to nuclear reactor safety analysis. Without analyzing the interplay of reactor components and safety systems across the entire reactor, safety analysis cannot effectively capture reactor behavior. Just as safety analysis is vital to nuclear reactor analysis, system analysis codes are vital to modern safety analysis. These codes are relied on to demonstrate reactors will maintain system integrity during both regular operation and postulated transients — when reactors could be faced with potentially strenuous conditions. In this way, “reduced-order modeling approaches... facilitate rapid turn-around for design and safety optimization studies” [64].

System-level thermal hydraulics codes have been developed and used extensively for Light Water Reactors (LWRs) in the past. However, these “legacy codes” are difficult to validate and maintain due to outdated software development methods and coding languages. Now, efforts to design advanced reactors which differ from traditional LWRs in many ways (coolant type, core configuration, accident scenarios, etc.) introduce new considerations to reactor safety analysis. For example, advanced reactors introduce conditions such as high temperatures in some designs, different types of coolants such as molten salts and liquid metals, and other phenomena more prevalent in advanced reactor analysis — such as participating media radiative heat transfer. There is a strong need to develop advanced modeling tools to address these simulation challenges unprecedented in regards to traditional water-cooled reactor analyses and, by extension, to previous safety analysis tools as well.

As part of the process for preparing to support the licensing efforts of advanced reactors, the United States Nuclear Regulatory Commission (NRC) has proposed a suite of codes for non-LWR safety analysis called the Comprehensive Reactor Analysis Bundle (CRAB)¹, which is comprised of both NRC- and DOE-based simulation tools. These codes will be used in conjunction “for evaluating normal operating conditions” along with “conduct[ing] safety analysis to verify safety margins and allowable operational limits” [65]. As it is widely expected the CRAB suite will be heavily utilized for advanced reactor safety analysis in the United States for the foreseeable future, special consideration should be paid to the CRAB codes. Of those codes, the one favored by CRAB for advanced reactor system-level thermal hydraulics is System Analysis Module, or SAM.

¹CRAB codes: SAM, PRONGHORN, Nek5000, BISON, MAMMOTH, TRACE, SCALE, PARCS, FAST, SERPENT, and FLUENT [65]

3.1.1 SAM and its need for radiative heat transfer modeling

SAM is a system-level thermal hydraulics code under active development by Argonne National Laboratory (ANL) — a United States Department of Energy (DOE) lab — for advanced reactor safety analysis “aim[ing] to provide fast-running, modest-fidelity, whole-plant transient analyses capabilities, which are essential for fast turnaround design scoping and engineering analyses of advanced reactor concepts” [66]. The “ultimate goal of SAM is to be used in advanced reactor safety analysis for design optimization and licensing support” [64]. Advanced reactors require different modeling approaches from LWRs because of “their use of single-phase, low-pressure (except high-temperature gas reactors), high-temperature, and non-unity Prandtl number coolants. This simple yet fundamental change has significant impacts on core and plant design, the types of materials used, component design and operation, fuel behavior, and the significance of the fundamental physics in play during transient plant simulations” [64]. As a result, any advanced system modeling tool will need to differ from traditional system codes. SAM is no exception, and has been developed to “distinguish the modeling needs of advanced reactor concepts from light water reactors” [67] while simultaneously taking advantage of advances in computing power and numerical methods.

Like most other DOE-based reactor codes, SAM utilizes the Multiphysics Object Oriented Simulation Environment (MOOSE) computational framework developed by Idaho National Laboratory. Some of the benefits of being a “MOOSE application” include being able to utilize MOOSE for all the behind-the-scenes operations of finite element method (FEM) solvers, domain meshing tools, and the input/output interface [66]. Another massively useful benefit is the inherent capability to couple MOOSE applications to each other, enabling truly “multiphysics” simulations between SAM and other MOOSE applications developed to model separate physical phenomena, even those occurring on entirely different scales [68]. However, there is one drawback. MOOSE is based on FEM numerical solvers, which subsequently makes SAM an FEM code — a fact that requires some explanation: While FEM is great for modeling the types of functions used to describe the physics behind conductive heat transfer and solid mechanics [69], this numerical method is not as good at modeling the hyperbolic functions behind physics like waves and fluid propagation, resulting in spatially unstable numerical oscillations when modeling fluids. However, due to the benefits of utilizing the MOOSE computational framework, SAM was built as a MOOSE application and incorporates numerical stabilization schemes to dampen out those oscillations in the solution. The final result is “a system-level modeling and simulation tool with higher fidelity (compared to previous system analysis tools), and with well-defined and validated simulation capabilities for advanced reactor systems. [SAM] provides fast-running, modest-fidelity, whole-plant transient analyses capabilities” [64].

Compared to traditional LWRs, advanced reactor concepts are typically designed to operate in a higher temperature region to achieve higher thermal efficiency. Additionally, some advanced reactor coolants, particularly molten salts, further enhance the significance of radiative transfer due to their propensity to absorb and emit thermal radiation at a rate

substantially higher than water. For these conditions, radiative heat transfer becomes important enough to necessitate its inclusion in system-level analysis. Therefore, SAM requires the ability to simulate radiative heat transfer for complete safety analysis to be conducted for these reactor types. However, before I completed the work described in this chapter, no substantial radiative heat transfer modeling capabilities existed in SAM. Solid-to-fluid radHT was entirely absent, and code users were restricted to a simple surface-to-surface fuel rod gap conductance model (more on this on [Sec. 3.1.2](#)).

Additionally, the advanced reactor design community has expressed a wide range of interest in SAM and has confirmed the need for SAM to simulate radiative heat transfer. For example, Kairos Power is developing its own version of SAM, i.e. KP-SAM, as its design and licensing tool [8, 70]. The NRC has also chosen SAM as its primary tool for advanced reactor system-level analysis, specifically listing SAM as the ideal analysis tool for FHR thermal hydraulics [65]. As for FHRs in particular, multiple validation studies for salt-cooled systems have already been completed [71, 72] in addition to the full FHR models that have been successfully built and simulated [73], making SAM the front runner for FHR system-level analysis. As SAM further established itself as the de facto FHR system-level

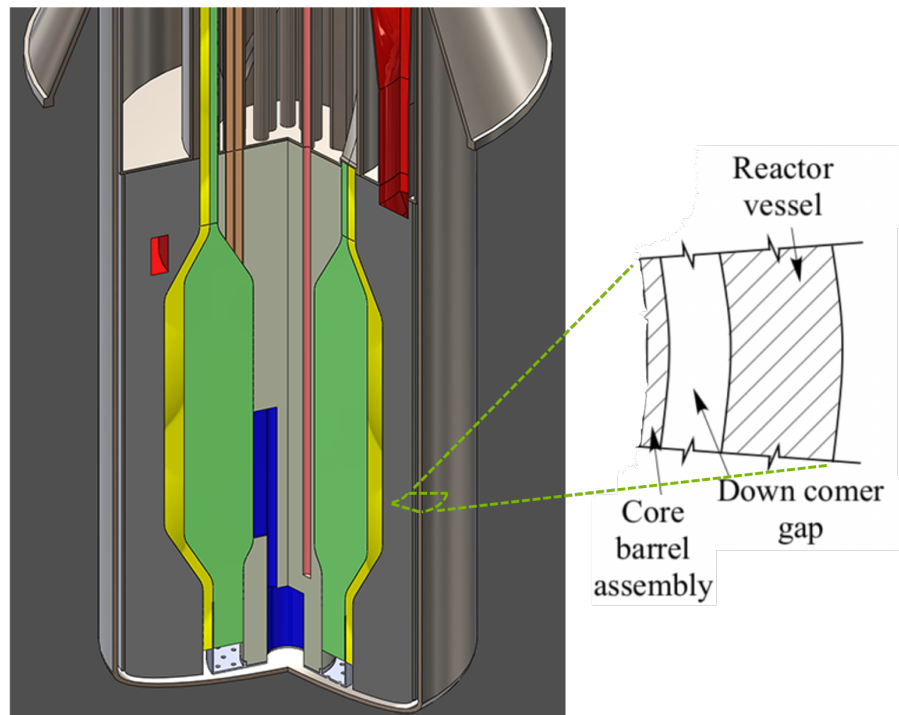


Figure 3.1: Composite image showing an expanded bird's-eye view of a Mk.I FHR downcomer. The radial slice view [3] is shown expanded from its in-core location on the left.

simulation tool, so too grew my predilection towards using SAM as the primary tool for my research. Avoiding SAM could have even prescribed my work on system-level effects of radHT in FHRs to irrelevance or outdatedness before it was even completed. However, the glaring issue remained: SAM could not yet simulate participating media radiative heat transfer. Conveniently for my dissertation work, the code is still under active development and new capabilities are being added to address various modeling and simulation challenges for advanced reactor analysis. This opened the door for my research to contribute to SAM by developing its radHT modeling capabilities.

For some, a more concrete example would be useful for justifying the need for radHT modeling in an FHR. For this discussion, I chose a scenario which includes a multi-surface enclosure with a participating fluid: the downcomer of the Mark 1 (Mk.I) FHR [3], a pre-conceptual reactor design from the University of California, Berkeley (UC Berkeley), following some loss of forced flow. [Figure 3.1](#) shows the downcomer region of the Mk.I. The inner surface of the downcomer, the core barrel, dissipates heat from the reactor core. For the chosen scenario, the outer surface of the enclosure, the reactor vessel, sits close to the bulk salt temperature of 600 °C [74], rendering convective heat transfer minuscule. In this example, the inclusion of a multi-surface radHT enclosure with participating media is the only way to derive an accurate model of the component-level heat transfer between the core barrel and the reactor vessel — one of the primary means for decay heat to leave the core. This example demonstrates a scenario for which SAM’s radHT modeling capability must be developed to provide code users the tools necessary to properly simulate heat transfer behavior. For scenarios like these, radiative heat transfer modeling is a necessary tool for performing accurate safety analysis. For other applications, the significance of radHT can be ascertained by using radHT simulation to perform sensitivity studies, revealing whether thermal radiation need be modeled in detail or neglected if unimportant.

$$\frac{\partial(\rho H)}{\partial t} + \frac{\partial(\rho u H)}{\partial x} = \nabla(k \nabla T) - \nabla \cdot q''_{rad} + q''' + \frac{Dp}{Dt} + \Phi \quad (3.1)$$

[Equation \(3.1\)](#) shows the one-dimensional (1D) fluid energy conservation equation represented in the SAM Theory Manual [67], where H here is used to represent enthalpy. This equation is defined as “1D” in terms of fluid flow because the spacial derivative of fluid advection is taken exclusively in the direction of axial flow (∂x). Other vector terms are left in formulation to capture heat transfer between the fluid and solid structure(s), but the axial fluid nodes are never discretized radially or azimuthally. Solid structures however can be two-dimensional (2D) — discretized radially and axially — and the code still considered 1D. Significant to this discussion, [Eq. \(3.1\)](#) includes the radiative term $\nabla \cdot q''_{rad}$, which is promptly neglected in subsequent derivation due to restrictions stemming from SAM’s computational framework. To maintain the radiative term in the fluid energy equation for SAM modeling, a modeling approach had to be developed to not only capture the radiative contribution to heat transfer, but to also respect the modeling limitations in SAM.

3.1.2 Previously implemented methods for modeling radiative heat transfer in system codes

To understand previous expectations for system-level radHT modeling, and to assist in developing an implementation approach suitable for radHT development in SAM, I conducted a literature review on the radHT implementation strategies in legacy codes for system-level thermal hydraulics, TRACE [75, 76] and RELAP5 [77]. In these codes, the default treatment of thermal radiation relies on LWR-specific radiative parameter values and correlations dependent on flow regime to calculate solid-to-fluid radHT. In other words, these methods were implemented specifically for LWR analysis and cannot be recycled and reused for (non-LWR analysis in) SAM. These codes additionally implement a radiative simulation component based upon the net radiation method, which performs radiative heat transfer analysis in axial planes along the flow path for surfaces and a radiatively-absorbing fluid. Due to the computational intensity of this component, calculation is limited to scenarios in which some surface in the system is in post-critical heat flux. Therefore, a complex component framework which leads to high computational intensity should be avoided in SAM. Nevertheless, this methods' use of the net radiation method does provide some valuable insight for how a more general and flexible radHT model could be developed for an advanced reactor system code.

The high-level takeaways from this literature review pertinent to SAM radiative heat transfer modeling are discussed in the previous paragraph. In summary, TRACE and RELAP5 radHT computational models are too reliant on LWR-specific scenarios and are too computationally intensive to be used for SAM. However, the math behind one of those models (the net radiation method) is promising for developing SAM radHT modeling. Readers satisfied with that discussion can proceed to the next section. For those who desire more details on previous system-level radHT modeling, read on.

Radiative heat transfer in TRACE is modeled by two separate modes, the default mode and the radiation enclosure (RADENC) model. The default radiation mode primarily models single-surface to fluid radiative transfer. The only exception is fuel-to-cladding gap conductance, which models two surfaces and does not incorporate a participating medium. The RADENC model is purposed for many-surface enclosures such as fuel rods in a boiling water reactor fuel bundle. However, due to the computational intensity of this model, there are several restrictions that guarantee RADENC is not utilized unless radiative transfer is significant.

Default radiation mode

Implementation of the default radiation mode in TRACE is highly specific to LWRs. Treatment of radiative transfer differs based on flow regime, but all regimes rely on empirical modifications to the wall heat transfer coefficient. This representation of radiative transfer effectively treats thermal radiation as augmented convection, which is necessitated by

the energy equations in TRACE. Firstly, for inverted annular film boiling, wall-to-vapor radiative heat flux is neglected, with the wall-to-liquid heat transfer coefficient containing the augmentation for radiative flux. Flow-regime-specific correlations dictate the wall and liquid emissivities. Secondly, for dispersed flow film boiling in which fluid void fractions exceed 90 %, wall-to-liquid and wall-to-vapor radiative transfer are modeled. For this flow regime, LWR-specific assumptions are integral to calculation: wall emissivity is set to 0.7, representative of Zircaloy; the liquid and vapor are assumed optically thin, resulting in no post-emission re-absorption by the participating fluid; and radiative path lengths are all set to $0.9D_h$, an assumption specific to this geometry and flow regime. Fluid and vapor emissivities are derived upon the latter path length assumption, utilizing correlations from a source marked “sensitive”, which The US NRC Public Document Room refused to release to me. Thirdly, fuel rod gap conductance models are used to simulate radiative transfer between the fuel and cladding. Here, the known emissivities of LWR fuel and Zircaloy cladding are enforced. No participating media are modeled here.

RADENC model

The RADENC component model is based on the net radiation method, in which two or more solid surfaces arranged as a complete enclosure can be modeled with or without fluid interaction. In this mode, radiative transfer occurs in axial planes along the flow path - no axial radiative transfer is modeled. Additionally, radiative transfer calculation is restricted to scenarios in which at least one surface is in post-critical heat flux, some surface is 100°C above the fluid saturation temperature, and surface temperatures within the axial plane differ by more than 10°C . If these criteria are met, TRACE calculates view factors between each unique surface and accompanying path lengths to specify fluid interaction. If the user desires, these values can be input manually. However, the complex nature of two-phase flow transients means these fluid path lengths will vary in time. For the most accurate analysis, these values should be determined by the code. Non-zero path lengths indicate the intermediary fluid must absorb and emit thermal radiation. Based on the calculated or inputted path lengths, the code determines energy transfer to and from the participating media based on correlations for fluid absorption and emission for steam-water mixtures.

SAM’s gap conductance model

To better contextualize the applicability of deductions from TRACE and RELAP5 radHT modeling, this literature review should include a discussion on SAM’s existing capabilities. Before I began my dissertation work, SAM was severely limited in its abilities to simulate radiative heat transfer. SAM was restricted to a simplified gap conductance model originally developed for surface-to-surface radHT across fuel rod gaps. SAM lacked the ability to model radHT in more complicated scenarios: fluids could not act as a participating media, the grey assumption was always enforced for solid surfaces, and the enclosure geometry always resembled an annular fuel gap. The model I developed, described in [Sec. 3.2](#), is far more

flexible than SAM's gap conductance model. However, because this method enables quick modeling of simple radHT across fuel-cladding gaps, it remains available to code-users for such scenarios.

3.1.3 Other prominent radiative heat transfer modeling methods not applicable to system-level modeling

In addition to the conducted literature review on previously implemented radHT modeling methods in system codes, I would like to acknowledge prominent radiative heat transfer modeling methods and discuss why I have not pursued these methods for implementation in SAM. This general investigation of common radHT modeling methods, particularly those utilized for molten-salt-cooled nuclear reactor applications, provided valuable insights on modern radHT analysis techniques, some of which were applicable to the process of developing radHT modeling capabilities for SAM.

Two commonly-used methods for participating media radHT modeling are the spherical harmonics method and the discrete ordinates method. It is out of the context of this thesis to discuss these methods in depth, so I would point readers to Chs. 16 and 17 of Modest [17] for discussion on spherical harmonics and discrete ordinates, respectively. In short, these methods approximate the radiative transfer equation (which requires known spacial temperature information) as partial differential equations to solve for local radiative heat fluxes. They "are today probably the most popular radiative transfer equation solvers... and some version of them is incorporated in most commercial computational fluid dynamics (CFD) codes" [17]. It then follows these methods would be popular for molten salt radHT analysis. While investigating the impact of radHT in advanced reactor applications from the molten salt FLiNaK, Chaleff developed a computational tool in MATLAB using the spherical harmonics method [28, 78]. He then verified his simulated radiative heat flux results with a simulation built in Ansys Fluent, a commercial CFD simulation tool that utilizes the discrete ordinates method for radHT analysis [78]. Abou Dbai used the same method as Chaleff (spherical harmonics) to explore the role radHT might play in the thermal hydraulic behavior of molten-Li₂BeF₄-salt-cooled (flibe-cooled) FHR heat exchangers [79]. For his modeling purposes, he used the commercially available COMSOL Multiphysics simulation tool, similarly verifying his results with a discrete ordinates method simulation. Derdeyn also used COMSOL to simulate radHT in FHR heat exchangers [26]. Coyle, who sought to enhance understanding of radHT in molten salts both through obtaining physical radiative property salt data and by modeling radHT in molten salts, modeled the radiative flux in higher fidelity using the discrete ordinates method with the commercial CFD tool STAR-CCM+ [25].

For all these modeling scenarios, simulations calculate the local radiative flux. There are alternatives. For instance, Zhang developed an analytical model to calculate the role of radHT in various flibe-filled tube geometries [80] using Derdeyn's approximation for the

wavelength-dependent fiber absorption coefficient [26]. However, this approach cannot be used for general FHR radHT simulation because the analytical model is specific to tubes, uses wavelength dependent properties, and uses a mean beam length approx which disagrees with SAM (explained in Sec. 3.2.3). Implementing separate analytical models for each and every modeling scenario is not practical and does not support the modeling needs identified for SAM radHT. Therefore, this approach will not be utilized for SAM code development.

Returning to the aforementioned radiative-flux-calculating simulation methods, the discrete ordinates method in CFD applications, as Coyle puts it, “can be thought of as a finite differencing of the angular dependence in the radiative transfer equation”, which inherently requires a well-defined three-dimensional (3D) space with 3D temperature information — information a 1D system code like SAM purposefully lacks. Even the lower fidelity spherical harmonics application employed by Chaleff and Abou Dbai assumed 2D axisymmetric geometries, an assumption that still requires more spacial information than SAM can always provide. All these individuals pursuing molten salt radHT modeling for advanced nuclear reactor applications, and all these commercial codes (Ansys Fluent, COMSOL Multiphysics, and STAR-CCM+), use either spherical harmonics or discrete ordinates to model radiation. These higher-fidelity methods are more accurate, as they strive to model the photon field, but they are also too computationally- and informationally-expensive to implement in a system-level code like SAM.

Because of the code-based limitations inherent to system codes, I had to choose the net radiation method over the other higher-fidelity codes I reviewed. However, there are still insights to be gained from the discrete ordinates and spherical harmonics methods. Primarily, meaningful deductions can be made about the information *lost* by modeling radHT via the net radiation approach — local radiative heat flux information within the participating fluid is neglected, as is the wavelength dependence of surfaces and fluids alike. These are two glaring omissions present in a system-level description of radiative heat transfer, and two omissions I kept in mind to compensate for when deriving my approach to modeling radHT in SAM.

3.2 SAM Radiative Heat Transfer Code Development

This section details my development of radHT modeling capabilities for SAM. For the sake of maintaining a cohesive narrative, I have broken down the development process into major tasks. I start off with a mathematical discussion on the radiative heat transfer equations I derived for SAM in Sec. 3.2.1. Then, in Sec. 3.2.2, I discuss the initial code framework development for radHT in SAM, which directly enables the implementation of my derived equations. Between these two task discussions, I describe the theory behind how radHT simulation in SAM works before progressing into describing more concrete development tasks, such as in-code radiative property calculations and code compatibility enhancements, that further built upon the capabilities of SAM radHT modeling. These more-concrete

developments are discussed in Secs. 3.2.3 to 3.2.6.

I discuss development tasks in this order to best contextualize each task and therefore help the reader best understand the final product. In reality however, I sometimes pursued several of these tasks in parallel or in a different order than I present them. To avoid any confusion that might arise from my non-chronological development progress, I accompany all SAM-produced data with the version number of the SAM code used for that simulation.

Where applicable, I describe the verification tests I used to verify the functionality of simulation capabilities produced through each task. These tests serve only to verify specific code developments, not radHT simulation in SAM as a whole. Those verification tests are important enough to be reserved for their own section, Sec. 3.3.

Section content introduction

The radiative term in Eq. (3.1) explicitly represents the divergence of the radiative flux ($\nabla \cdot q''_{rad}$), which inherently requires generating and solving for a radiative flux function — a function dependent on three-dimensional geometric and temperature information for all radiating bodies in the system. First and foremost, SAM is a system-level code that represents fluid flow in a one-dimensional form. Therefore, the fluid heat source from radiation (i.e. radiative energy absorbed by the fluid less its own emission to surrounding surfaces) cannot be found from the divergence of a multi-dimensional radiative flux function. Additionally, this means no axial change in the radiative flux will be calculated either. In other words, no axial radHT. Thermal radiation must be isolated to separate axial planes along stipulated components, in which node-averaged temperature values must be used.

System-level codes previously developed for LWRs include the ability to simulate radHT (see Sec. 3.1.2). However, these functions are computationally expensive to the point of being purposefully excluded whenever radHT can be assumed insignificant — for instance in TRACE [75]. Furthermore, they rely heavily on LWR-specific correlations and were built to successfully simulate radHT in LWR-specific conditions. Radiative heat transfer simulation capabilities in SAM would ideally not mimic these particular attributes. SAM requires a flexible framework in which radHT simulation could be successfully carried out for various advanced reactor concepts and requires the ability to properly model radiative behavior without being computationally expensive. This further necessitates spectrally- and geometrically-averaged radiative properties for radHT modeling. Code users must spectrally average radiative properties for their systems before modeling them with SAM. Previous discussion on spectral averaging surrounds Eq. (1.7).

Taking these restrictions into consideration, in addition to the motivations discussed in Sec. 3.1.1, I derived a general formulation for radHT calculation based off the net radiation method, which is applicable to SAM.

3.2.1 Adapting the net radiation method for radiative heat transfer modeling in SAM

What the net radiation method does well is simultaneously account for emission, reflection of that emission off multiple surfaces, and the absorption of radiation at each surface. Using spectrally-averaged radiative parameters, easily manageable equations simultaneously solve for the total heat flux at each user-defined surface, the formulation of which is well suited to SAM's heat transfer code framework and therefore well suited for implementing as SAM's radiative heat transfer simulation capabilities.

$$\sum_{j=1}^N \left[\frac{\delta_{kj}}{\varepsilon_j} - F_{kj} \left(\frac{1 - \varepsilon_j}{\varepsilon_j} \right) \right] q_j'' = \sum_{j=1}^N (\delta_{kj} - F_{kj}) E_{b,j} \quad (3.2)$$

The net radiation method applied to N surfaces is described mathematically by Eq. (3.2). For the derivation of this equation, the reader is invited to peruse sections 5.3.1 and 10.7 of Howell, Mengüç, and Siegel [16]. The Kronecker delta, δ_{kj} , is utilized to assist in visualizing the matrix formulation for this system of N equations — one for each surface k .

$$\delta_{kj} = \begin{cases} 1 & , k = j \\ 0 & , k \neq j \end{cases} \quad (3.3)$$

To allow more flexibility in radHT modeling, I rederived the net radiation method equation with modifications to compensate for the lack of spectral variation in radiative properties. Namely, the grey assumption is not enforced, meaning spectrally-averaged radiative properties of an interacting body can be separated to represent different wavelength bands of incoming and outgoing radiation; emissivity and reflectivity need not be related. Radiative parameters that contain no spectral variation, but are not bound to other parameters by relations such as Eqs. (1.2) and (1.5), are called “pseudo-grey”. By allowing these user-specified parameters to be separated from the grey assumption, a more accurate radHT solution can be found. However, the user should keep in mind this is only a mathematical compensation for the true lack in spectral dependence of radiative parameters. Without properly averaging radiative properties over the pertinent wavelength bands, a pseudo-grey solution is no better than implementing the grey assumption. As an alternative to calculating and utilizing pseudo-grey radiative properties, truly grey surfaces and fluids may be modeled instead.

$$\sum_{j=1}^N \left[\frac{\delta_{kj}}{1 - \rho_j} - F_{kj} \left(\frac{\rho_j}{1 - \rho_j} \right) \right] q_j'' = \sum_{j=1}^N (\delta_{kj} - F_{kj}) \left(\frac{\varepsilon_j}{1 - \rho_j} \right) E_{b,j} \quad (3.4)$$

$$\sum_{k=1}^N q_k'' A_k = 0 \quad (3.5)$$

The net radiation method modified to allow pseudo-grey surfaces is called the “Rad+” model to distinguish it from the basic “net rad” method and is shown by Eq. (3.4). However, this equation still lacks the ability to account for solid-to-fluid radHT, which is the capability determined as the priority for this SAM code development effort. Again, the Rad+ model can be rederived to enable modeling of a single pseudo-grey participating fluid in conjunction with N surfaces — Eqs. (3.6) and (3.7). To further distinguish this approach from the solid-only capabilities of the Rad+ model, I denote these equations by the “Rad++” model or, more accurately, the “Rad++” expression of the net radiation method.

$$\sum_{j=1}^N \left[\frac{\delta_{kj}}{1 - \rho_j} - F_{kj} \bar{t}_{kj} \left(\frac{\rho_j}{1 - \rho_j} \right) \right] q_j'' = \sum_{j=1}^N (\delta_{kj} - F_{kj} \bar{t}_{kj}) \left(\frac{\varepsilon_j}{1 - \rho_j} \right) E_{b,j} - \sum_{j=1}^N F_{kj} \bar{\alpha}_{kj} E_{b,f} \quad (3.6)$$

Rad+ heat fluxes calculated from Eq. (3.4) will satisfy the energy conservation condition shown in Eq. (3.5). In contrast, the Rad++ heat fluxes do not necessarily satisfy this condition due to the \bar{t}_{kj} and $\bar{\alpha}_{kj}$ terms in Eq. (3.6). Physically speaking, this is due to the introduction of absorption and emission by the participating fluid. Then, the net volumetric heat source of the fluid can be found by accounting for this “non-zero” energy. Mathematically speaking, that requires taking the sum all surface heat transfer equations and dividing by fluid volume. Taking the opposite sign of the radiative source then produces the net energy *emitted* by the participating fluid,

$$q_f''' = \frac{-1}{V_f} \sum_{k=1}^N q_k'' A_k \quad . \quad (3.7)$$

The significance of the Rad++ equations in terms of SAM radHT modeling should not be understated. While an argument in semantics could even be made that SAM does not model radiative heat transfer, but rather Eqs. (3.6) and (3.7), it is more clear to make the point that Rad++ physically describes the radHT modelled by SAM. The left hand side of Eq. (3.6) holds the all-important radiative heat flux q_j'' outwards from each surface j in the enclosure, where the Kronecker delta δ_{kj} has already been discussed, ρ_j “≡” reflectivity of surface j , F_{kj} is the view factor from surface k to j , \bar{t}_{kj} “≡” transmittance of radiation from surface k through the participating fluid to surface j . The first term on the right hand side contains the blackbody emission $E_{b,j}$ of each surface j mitigated by that surface’s emissivity ε_j , while the final term in Eq. (3.6) contains the blackbody emission $E_{b,f}$ of the participating fluid

f mitigated by the fluid emittance $\bar{\alpha}_{kj}$, which is geometrically averaged to represent the emittance only from surface k to surface j .

I use the variable $\bar{\alpha}_{kj}$ to describe fluid emittance, which is not necessarily conventional for participating fluid radiative analysis. Typically, α is used for fluid *absorptance* while ε is used for fluid *emittance*. The nomenclature adopted by the Rad++ method stems from the grey fluid assumption, where $\bar{\alpha}_{kj} = \bar{\varepsilon}_{kj}$. While the fluid modeled here is not necessarily grey, the use of $\alpha \equiv$ "emittance" is maintained to avoid convoluting fluid emittance with surface emissivity, another property denoted by ε .

Equation (3.7), which calculates the volumetric radiative fluid emission, uses all solved heat fluxes of each surface k multiplied by that surface's area and normalized by the participating fluid volume V_f .

The assumptions made to arrive at Eqs. (3.6) and (3.7) include a fully-enclosed radiative geometry, pseudo-grey surfaces and participating fluid, isothermal surfaces, a homogeneous and isothermal fluid, negligible scattering by the fluid, constant radiative properties (as functions of wavelength and temperature), and diffusely-emitting surfaces.

The Rad++ equations, Eqs. (3.6) and (3.7), mathematically describe the radiative transfer physics modeled by SAM. However, for the sake of *implementing* them into SAM as lines of code, it is beneficial to separate the heat fluxes into individual expressions for each q_k'' . I used Eq. (3.6) to generate a matrix of N equations which, when solved, produce the total heat flux at each of the N surfaces. Equation (3.10) shows the final form for the set of equations solved for heat flux. For each surface k , an equation can be found for the surface's heat flux. The first term describes the total radiative flux outwards from surface k in the enclosure. The second term can be interpreted as the emission and reflection from each surface k combined with the incident radiation from all other surfaces impinging each surface k — having been reflected around by all surfaces and attenuated in transit by the participating medium. The third term can be interpreted as the radiative flux emitted from the participating medium that impinges upon each surface k — having been reflected around by all surfaces and attenuated in transit by the participating medium itself.

$$\sum_{j=1}^N B_{kj} q_j'' = \sum_{j=1}^N C_{kj} E_{b,j} - \sum_{j=1}^N D_{kj} E_{b,f} \quad (3.8)$$

$$\begin{bmatrix} B_{11} & \cdots & B_{1N} \\ \vdots & \ddots & \vdots \\ B_{N1} & \cdots & B_{NN} \end{bmatrix} \begin{bmatrix} q_1'' \\ \vdots \\ q_N'' \end{bmatrix} = \begin{bmatrix} C_{11} & \cdots & C_{1N} \\ \vdots & \ddots & \vdots \\ C_{N1} & \cdots & C_{NN} \end{bmatrix} \begin{bmatrix} E_{b,1} \\ \vdots \\ E_{b,N} \end{bmatrix} + \begin{bmatrix} D_1 \\ \vdots \\ D_N \end{bmatrix} E_{b,f} \quad (3.9)$$

$$\mathbf{B} \mathbf{q}_k'' = \mathbf{C} \mathbf{E}_{b,k} + \mathbf{D} E_{b,f}$$

$$\mathbf{q}_k'' = \mathbf{B}^{-1} \mathbf{C} \mathbf{E}_{b,k} + \mathbf{B}^{-1} \mathbf{D} E_{b,f} \quad (3.10)$$

Equation (3.7) is then implemented by utilizing the solutions of Eq. (3.10) and geometric properties of the enclosure. Equation (3.11) shows the final form of the radiative fluid heat source as implemented in SAM, where A_k is the surface area of surface k and V_f is the fluid volume.

$$q_f''' = \frac{-1}{V_f} \begin{bmatrix} A_1 \\ \vdots \\ A_N \end{bmatrix}^T \mathbf{q}_k'' \quad (3.11)$$

The vector \mathbf{q}_k'' in Eq. (3.10) is the total radiative flux outwards from each surface in the enclosure. The first matrix-term on the right hand side can be thought of as the radiative flux from all surfaces impinging each surface, having been reflected around by non-black surfaces and attenuated in transit by the participating medium. The final matrix-term is interpreted as the radiative emission from the participating medium impinging each surface, accounting for re-absorption by the medium in transit.

While deriving, I took special care to ensure Eqs. (3.10) and (3.11) would remain mathematically generalizable to all desired modeling scenarios shown in Tbl. 3.1. In this manner, the utilized mathematical approach need not change between various radHT modeling scenarios; both single- and multi-surface enclosures can be modeled by the same equation. To accomplish this generalizability, the constituent coefficients for non-existent surfaces or fluids in Eq. (3.10)'s $\mathbf{B}^{-1} \mathbf{C}$ and $\mathbf{B}^{-1} \mathbf{D}$ result in a value of zero by default, primarily through initializing “non-existent” view factors to zero and “non-existent” transmittances to one.

In addition to achieving generalizability of Rad++ in relation to the number of modeled surfaces, there are further considerations which must be heeded to guarantee SAM properly

calculates and applies the same Eqs. (3.6) to (3.11) to all scenarios — considerations which include how to systematically generate these equations’ constituent coefficients. These considerations diverge from the current mathematical discussion and are more so influenced by the code framework upon which SAM’s radHT capabilities must be built.

3.2.2 Code framework considerations for adapting Rad++ to SAM

The previous section details the derivations for Eqs. (3.6) and (3.7) — also known as Rad++ — which enable pseudo-grey modeling of a single participating fluid in conjunction with N surfaces. However, a code framework for radHT modeling needed to be developed to implement Rad++ and ultimately enable simulation of the physics represented in SAM. To reach that end, the information necessary to calculate Eqs. (3.10) and (3.11) must be obtained, managed, and distributed. This information logistics handled by the code requires a robust, generalizable framework to guarantee Rad++ can be implemented in SAM and can properly simulate all desired modeling scenarios.

Reactor design companies who were utilizing SAM for molten-salt-cooled reactor analysis — Kairos Power and TerraPower — informed the extent of user-desired functionality for radiative heat transfer modeling, summarized in Tbl. 3.1. The general consensus was that it was strongly desired for SAM to be able to model participating media radHT. TerraPower requested “radiative heat transfer in cavities”, implying a lumped-wall single-surface approximation would suffice. Kairos listed reactor regions and specific conditions for which two-surface radHT enclosures were deemed necessary [81]. No modeling scenarios involving three or more surfaces were desired by either company. Moving forward with radHT development, SAM would need to be able to simulate radiative enclosures with one to two surfaces and a participating medium.

Table 3.1: User-desired capabilities for SAM radiative heat transfer modeling.

Surfaces	Participating Medium	
	No	Yes
1	✗	✓
2	✓	✓
3+	✗	✗

It is critical to note there are restrictions specific to the computational framework SAM is built on (MOOSE) which limit radHT implementation approaches. Specifically, thermally-

interacting bodies are coupled together via a prebuilt, information access framework. By this approach, information sharing is restricted to two interacting entities — for instance temperature information for a convectively interacting solid-fluid pair can be accessed and used for calculating convective heat fluxes. The results of calculation can then be returned to these interacting bodies. However, net heat fluxes for radHT analysis require information from *all* participating bodies in the system, which can produce complications when utilizing a coupling framework inherently structured for only two interacting bodies.

$$q_k'' = f(T_1) + f(T_f) \quad (3.12)$$



Figure 3.2: Two-body constraint infographic showing one constraint linking both bodies in the system.

To illustrate how this thermal-coupling restriction impacts Rad++ implementation in SAM, I will compare and contrast code framework descriptions for two- and three-body radiative systems. For two thermally radiating bodies, implementation is straightforward. Equation (3.12) shows the heat flux from some surface k as a function of the first surface’s temperature, $f(T_1)$, summed with a function of the fluid body’s temperature, $f(T_f)$. Both the surface and fluid can inherently access their own temperature information already. However, to perform full heat flux calculations, they both need to access temperature information from the other radiating body. The required passing-of-information can be accomplished by a single instance of the coupling framework (also known by SAM nomenclature as a “constraint”), visualized by the set of arrows in Fig. 3.2. Here, the blue, upper arrow shows the temperature information being accessed from Surface 1 and passed to Fluid, while the green, lower arrow shows Fluid information being accessed and sent the other direction. In this system, each body can now construct a complete heat flux calculation using its own temperature information, which is inherently accessible, and the other’s temperature information, which has been accessed and fed to it by the constraint. Two bodies, one “coupling”, no redundancies.

Complications arise when the radiative system is expanded to include three bodies, as all participants require information from themselves and two others. Equation (3.13) shows the complete heat flux calculation for this scenario, which is constituted by functions of Surface 1’s temperature $f(T_1)$, Surface 2’s temperature $f(T_2)$, and the Fluid’s temperature $f(T_f)$. One constraint cannot access all this information at once. The workaround is shown in Fig. 3.3, where three individual constraints (each shown by a pair of arrows) are called to

access and pass information such that heat flux calculations can be performed for all bodies in the system. Under this method, temperature information from each radiating body must be accessed and passed by two separate constraints. Each body has its information accessed a redundant, second time by its second constraint, giving rise to three redundant instances of information passing. However, these redundancies are a necessary outcome of the coupling framework upon which thermal interaction in SAM is built. This problem grows with the number of interacting bodies until input complications would necessitate $3(N^2 - N)/2$ couplings for N surfaces and a participating fluid, which provides ample discouragement from enabling SAM to simulate radHT for a system with more surfaces than those shown to be desired in Tbl. 3.1.

$$q_k'' = f(T_1) + f(T_2) + f(T_f) \quad (3.13)$$

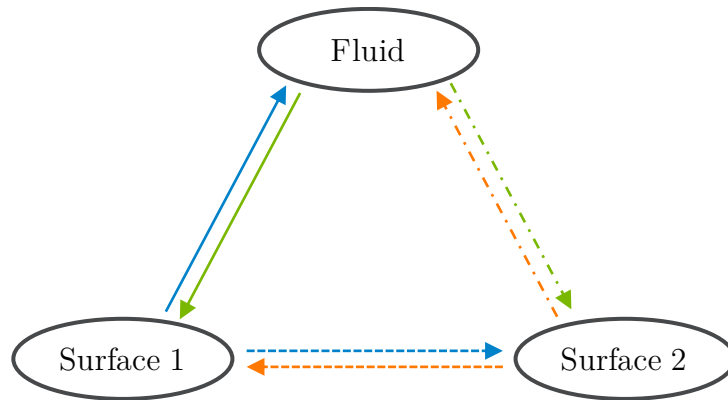


Figure 3.3: Three-body constraint infographic showing three constraints (opposite arrow pairs) linking both surfaces and a participating fluid.

Taking this coupling framework restriction into consideration, a radHT modeling framework was developed and subsequently implemented to enable all user-desired modeling capabilities as shown in Tbl. 3.1. Figure 3.4 details this code framework implemented as a radHT SAM component (hereafter frequently referred to by its SAM component name — RadiativeHeatTransfer), showing all pieces of code with brief function descriptions. Implementation of the multi-surface Rad++ equations into SAM requires multiple constraints, as demonstrated previously by Fig. 3.3. Depending on the user-specified number of surfaces and inclusion of a participating fluid, some combination of constraints will be called. Users do not interface with the radHT constraints. Rather, user-inputs are taken in by the component portion of RadiativeHeatTransfer, represented by the left-most box in Fig. 3.4. RadiativeHeatTransfer then performs input checks for completeness, calculates the Rad++ coefficients shown in



Figure 3.4: RadiativeHeatTransfer code framework showing component for interfacing with user and constraints called for Rad++ calculation.

Eq. (3.10), and feeds those to the constraints as shown by the three small boxes in Fig. 3.4. The necessary constraints are then applied at every axial node along the radiative geometry.

The framework developed in this section was built to support Rad++, as SAM’s 1D fluid flow modeling prohibits calculating the divergence of the radiative flux term from Eq. (3.1). As a result, RadiativeHeatTransfer models an effective 2D radiative enclosure at every node along the 1D flow path and, therefore, radiative parameters (in Eq. (3.6)) must be restricted to their 2D counterparts to properly calculate radHT as it is implemented and simulated in SAM. While spectral averaging cannot be performed by SAM, the code *can* automatically derive 2D view factors and transmittances based on a preset geometry options to decrease burden on the user. For instance, while RadiativeHeatTransfer supports modeling cylindrical and annular pipes, view factors are procured for their 2D axial projections — circles and annuli respectively — without regarding radiative interaction with pipe ends or even interaction between nodes. Maintaining this 2D interpretation of geometric properties not only simplifies analysis, but achieves mathematical consistency between the RadiativeHeatTransfer frame-

work and the radiative coefficients used for modeling. More on this theoretical justification will be explored in the next section surrounding the derivation of 2D transmittance values.

3.2.3 Deriving in-component transmittance calculations for predefined RadiativeHeatTransfer geometry options

For RadiativeHeatTransfer to properly model Rad++ physics, all constants shown in Eq. (3.6) must be either acquired or generated by the “component” box shown in Fig. 3.4. The specific variables that enable participating fluid interaction with radiating surfaces is \bar{t}_{kj} — the radiative parameter “transmittance”. This section details the derivations and development process behind enabling RadiativeHeatTransfer to generate these \bar{t}_{kj} -values for SAM simulation, and thereby enabling participating media radHT modeling in SAM.

Transmittance is a geometry-specific radiative property applied to a participating medium to describe the amount of incident radiation which passes through, or is transmitted by, the fluid along a line of sight along some path length S . The green line in Fig. 1.8 qualitatively demonstrates the transmitted radiation along some path length and can be quantitatively described by dividing the transmitted radiation by the incident radiation (using the relation provided by Eq. (1.4)), which produces Eq. (3.14).

$$t(S) = \frac{I(S)}{I_0} = \exp(-\kappa S) \quad (3.14)$$

This equation, albeit utilizing spectrally-averaged parameters, is only a description of transmitted radiation along a line of sight and therefore meaningless to any analysis based on the Net Radiation Method. Equation (3.14) is not useful for performing radiative heat transfer analysis for entire systems, such as that implemented in RadiativeHeatTransfer, due to its variation along both the emitting and receiving surfaces. To come by a system-wide applicable transmittance, such as the one utilized by Eq. (3.6), the local transmittance must be averaged along both surfaces to remove locational- and directional-dependence, thus yielding the geometric mean transmittance.

The geometric mean transmittance can be defined as the radiation departing from one surface, passing through a participating medium, and reaching another surface, normalized by the total radiation leaving the initial surface. The benefit of having a geometric mean value, once it is found, is being able to easily determine the heat transferred between emitting surfaces $E_i F_{ij} \bar{t}_{ij}$ and the energy absorbed along the way $E_i F_{ij} (1 - \bar{t}_{ij})$. These relations are relied upon by RadiativeHeatTransfer’s Rad++ computational implementation, so geometric mean transmittances must be found for radiative geometries modeled in SAM.

RadiativeHeatTransfer utilizes preset geometries (see Fig. 3.33), for which geometric mean transmittance and emittance $\bar{\alpha}$ values for a participating fluid are automatically found based

on geometric parameters and the absorption coefficient of the fluid. These in-code calculations are performed to reduce burden on the user by avoiding the need to manually calculate, and then input, the radiative parameters that govern solid-to-fluid radHT for every simulated radiative system or every time a design parameter is changed. However, there is one drawback. Due to SAM's preexisting constraints framework, upon which simulated heat transfer is built, radHT between radiating bodies is restricted to 2D axial planes along the flow path. Components are subdivided into axial nodes along the flow path, in which heat transfer is calculated using node-averaged temperature values. In other words, axial radHT is not possible.

One interpretation of modeling 3D geometries via 2D axial cross-sections is not neglecting axial heat transfer, but rather modeling infinitely-long geometries with no axial change in temperature. This interpretation holds true when all heat transfer from each node is forced to occur only at that node, because, for these infinitely-long geometries, all axial heat transfer that should be *arriving* at the node of interest (from other nodes) is identical to the axial transfer that should be *leaving* the node of interest. Therefore, modeling the 2D axial plane in this manner produces an identical mathematical solution to the 3D semi-infinite analog with no change in axial temperature. While these unrealistic 3D scenarios may not be of interest, except to those performing mathematical exercises, they do somewhat resemble some real-world scenarios. Those scenarios being very long components, where the components' lengths greatly outweigh characteristic measures of their cross sections, $L/D_o \gtrsim 10$, and components in which cross-sectional radiative temperature differences greatly outstrip their axial counterparts,

$$\frac{\Delta_r(T_o^4)}{\Delta_x(T_o^4)} \sim \left| \frac{T_w^4 - T_f^4}{T_x^4 - T_{x\pm D_o}^4} \right| \gtrsim 10 \quad . \quad (3.15)$$

For components complying with these relations, small path lengths and small axial temperature changes induce minimal axial heat transfer, therefore allowing 2D radHT solutions to be extrapolated to their 3D real-world counterparts with minimal distortion.

The means by which these extrapolatable 2D solutions are found fall to the responsibility of the geometric mean transmittance. Theoretically, an average geometric path length can be found that, when plugged into Eq. (3.14), produces a geometric mean transmittance or emittance value equal to the correct value. This theoretical, surrogate value exists and is called the mean beam length L_e . Three-dimensional mean beam lengths can be found in the literature for a wide variety of geometries, including the pertinent semi-infinite slab, infinitely-long cylinder [16], and infinitely-long annulus [82]. Correction factors can even be found to adjust the application of these mean beam lengths between optically thin and thick scenarios. Using correction factors C and mean beam lengths, the geometric mean transmittance is easily found as $\bar{t}_{L_e} = \exp(-\kappa C L_e)$. This transmittance can then be plugged into Eq. (3.6), thereby producing a 3D-applicable solution from a 2D-posed problem. Significantly, a computationally inexpensive transmittance solution can be quickly found by SAM and applied to radHT simulation. However, some major issues discourage the use of mean

beam lengths to find \bar{t} values for RadiativeHeatTransfer.

Issues utilizing mean beam lengths for RadiativeHeatTransfer

The use of mean beam lengths for SAM \bar{t} calculation has several flaws inherent to the derivation of L_e itself. Firstly, the mean beam length is actually derived to describe the *emittance* of a participating medium ($\bar{\alpha}_{L_e} = 1 - \exp(-\kappa CL_e)$) in scenarios without any surface emission or reflection, and therefore cannot describe fluid transmittance and absorptance unless that fluid is considered grey. While it is unlikely SAM users would rely on in-code transmittance calculations for non-grey fluids, this is still a potentially misleading detail that could cause users to utilize inappropriate transmittances for their simulated scenarios. Secondly, and more concerningly, the aforementioned correction factor for mean beam length is simply an average of the true correction factor, which varies across fluid absorption coefficient and geometric parameters. For instance, the listed $C = 0.9$ for a semi-infinite slab is only an approximation of the real correction factor,

$$C = \frac{0.9 - 1.8E_3(\kappa\delta)}{1 - \exp(-1.8\kappa\delta)} \quad , \quad (3.16)$$

where $E_3(\psi)$ represents the exponential integral function of the third kind [16].

Most troublesome of all, severe non-physical implications for SAM radHT simulation arise when the small path length and small axial heat transfer assumptions break down, which is likely to happen for SAM code users modeling radHT geometries. Recall, SAM simulates a 2D radiative enclosure at each axial node. When axial temperature change becomes significant, axial radHT is no longer constant along the component. Therefore, performing all energy exchange in axial planes diverges from being physically representative of the simulated scenario when either assumption breaks down. If 3D mean beam lengths are used, the amount of fluid each surface “views” will be more accurate, but the actual heat transfer with out-of-node fluid volumes is impossible to calculate.

To visualize the non-physical nature of applying 3D mean beam lengths, observe Fig. 3.5, which shows an example radiative path length between two axial nodes along a pipe. This S is one of many non-planar path lengths to be incorporated into the 3D mean beam length. With a temperature gradient between dA_n and dA_{n+5} , the assumptions for the mean beam length derivation begin to break down. Heat transfer occurs between the two nodes while depositing energy into the fluid, and receiving emission from the fluid, all along S . Using a correlation that takes this S into account, there should be solid-to-solid heat transfer from dA_n to dA_{n+5} . However, SAM would only be able to perform this calculation with cold wall temperatures at dA_{n+5} , understating solid heat transfer between the nodes while depositing all fluid-absorbed radiation at dA_{n+5} . Looking along S from dA_{n+5} to dA_n , there should be radiative emission from the fluid depositing itself at dA_n , but SAM would only see the fluid and wall temperatures at dA_n , leading to an inflated fluid-to-wall contribution. These are

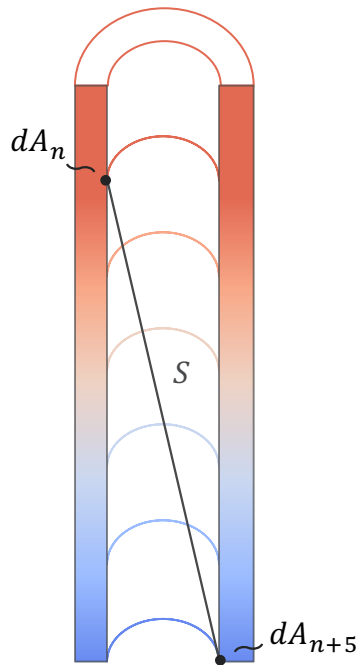


Figure 3.5: Radiative path length between axial nodes shown in a cutaway view of a 3D cylindrical radiative geometry. The color gradient shows the pipe wall and fluid at dA_n to be hotter than the colder wall and fluid at dA_{n+5} . Any radiative transfer along this S would require all fluid and wall temperatures between nodes n and $n + 5$.

but two examples of radHT errors that would arise from using mean beam lengths in SAM. As long as variables derived for 3D systems are imposed on SAM's 2D radiative geometries, the path lengths may be more accurate, but the radHT calculations and energy deposition will not be correct.

Unfortunately, there is no remedy for this conundrum. SAM has no way to determine *where* (i.e. in which node) to place energy absorbed and transmitted by the fluid, nor any mechanism to access up- or down-stream temperatures necessary to calculate that energy transfer. Therefore, this issue of calculating heat transfer solutions with a method mathematically inconsistent with SAM's computational framework ultimately deterred me from using mean beam lengths entirely. I decided that instead of incorrectly forcing 3D transmittance values onto a 2D SAM simulations, thereby depositing energy in erroneous locations along the radiative geometry, it was more desirable to pursue correlations for 2D fluid transmittance values to apply to the 2D simulated system instead.

Application of 2D transmittance correlations does not produce perfectly accurate solutions either. These correlations do, after all, misconstrue radiation as a phenomenon occurring

exclusively perpendicular to the axial direction. Imagine the radiation path length of photons emitted from a point on a pipe wall, traveling directly across the pipe, and hitting a point on the opposite side. Those photons traveled in the 2D cross-sectional plane, went a distance equal to the pipe diameter D , and a proportion equal to $1 - \exp(-\kappa D)$ of them were absorbed along the way. Now imagine other photons emitted still across the pipe, but slightly angled upstream or downstream. These photons, which are *not* traveling in the 2D cross-sectional plane, hit the other side slightly upstream or downstream of the previous photons' landing point, meaning they have to travel a little further before they hit the other side of the pipe, leading to a larger proportion of these photons getting absorbed along the way. Radiative path lengths are longer for any emission angle diverging from the cross-sectional plane. Therefore, imposing all radHT onto a 2D geometry effectively shortens path lengths, thereby reducing solid-to-fluid radHT in addition to already neglecting the axial solid temperature smoothing affects that would arise from axial radHT. In effect, utilizing 2D geometric mean transmittance correlations produces a conservative estimate for radiative path lengths. Nevertheless, the favorability of this approach holds true despite this consequence. The benefit — math-to-code consistency — outweighs the detriment of conservatism in the radHT solution. Ultimately, I decided if SAM has to simulate radiative heat transfer in two spacial dimensions, the transmittance values governing that transfer should be derived for 2D as well.

To implement geometric mean transmittances for 2D geometries, I needed to first derive them, as the literature lacks correlations for the pertinent geometries. For cylindrical geometries, there does exist 2D mean beam correlations [83]. However, these correlations exist in three parts — a mean beam length each for weak, strong, and very strong band limits, respectively. I am unaware of any available correlation simultaneously applicable to all optical thicknesses, which is desirable for SAM application. To derive the pertinent transmittance correlations for preset radiative geometry options (i.e. Cylinder, Annulus, and Slab), special considerations must be taken for each. The remainder of this section will discuss how I determined the geometric mean transmittance for each geometry, focusing on the Cylinder and Annulus transmittance derivations. Quantified comparisons between the derived correlations and existing mean beam length values will be made. Additionally, my code implementation strategy for the derived correlations will be discussed.

General 2D transmittance derivation considerations

Revisiting the definition of geometric mean transmittance made at the beginning of this section, it is “defined as the radiation departing from one surface, passing through a participating medium, and reaching another surface, normalized by the total radiation leaving the initial surface.” So to derive this parameter, the energy leaving the emitting surface must first be found. Let me define the energy leaving a differential surface $d\ell_i$ as $dQ_{d\ell_i}$. To determine the total energy leaving $d\ell_i$ in our 2D space, the 2D directional emissive power $E_i(\theta)$ must be determined.

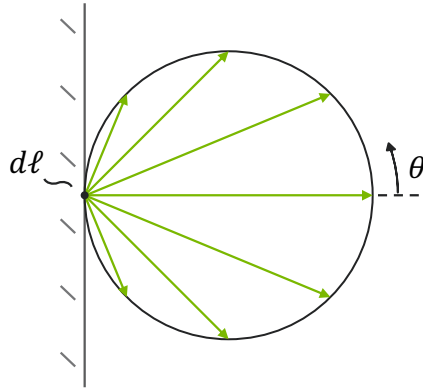


Figure 3.6: Lambert cosine law applied to a 2D diffuse surface. Vectors emanating from $d\ell$ show directional emissive power, $E(\theta)$.

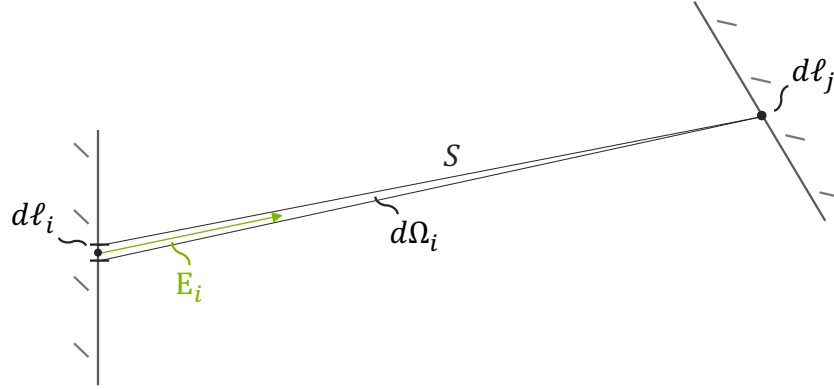
The diffuse approximation for surfaces, for which the Lambert cosine law is applied to emission and reflection, is commonly used for radHT analysis and is a good baseline depiction of radiative heat transfer behavior. Surfaces assumed to exhibit diffuse behavior are also referred to as Lambertian. Applying the Lambert cosine law to a 3D geometry can be visualized by placing a hollow sphere on a differential area dA , where a vector drawn from dA to any point on that sphere demonstrates the emissive power in the vector's direction. The surface normal vector shows maximum directional power emitted from dA . The analog for visualizing Lambertian emission in 2D can be visualized by placing a circle on a differential surface $d\ell$, as shown by Fig. 3.6. Again, a vector drawn from $d\ell$ to any point on this circle shows the directional emissive power, where $E(\theta)$ reaches a maximum at $\theta = 0$. Due to radiative intensity I remaining constant along emission angle, the 2D Lambert cosine law manifests as

$$E = \int_{-\pi/2}^{\pi/2} I \cos \theta d\lambda \quad . \quad (3.17)$$

Instead of integrating to find total hemispherical emissive power, $E_{3D} = \pi I_{3D}$, we get total semicircular emissive power as $E = 2I$ — a jarring relation for those familiar with basic radHT analysis. Luckily, I soon drops out of derivation, so we do not have to consider the wide-ranging implications of altering radiative intensity. For now, we can continue to define the energy leaving $d\ell_i$.

$$dQ_{d\ell_i} \equiv E_i d\ell_i = 2I_i d\ell_i \quad (3.18)$$

With the energy leaving $d\ell_i$ determined, the next step towards finding \bar{t} is determining the energy leaving $d\ell_i$ in the direction of a differential surface called $d\ell_j$. The proportional “view” $d\ell_i$ has of $d\ell_j$ can be called the differential view factor, $dF_{d\ell_i \rightarrow d\ell_j}$. Then the part of $dQ_{d\ell_i}$ that “views” $d\ell_j$, defined as $dQ_{d\ell_i} dF_{d\ell_i \rightarrow d\ell_j}$, is shown by Fig. 3.7. The differential view factor

Figure 3.7: Proportion of energy emitted from dl_i in the direction of dl_j .

can be broken down into the “view” dl_i has of the solid angle from dl_i to dl_j divided by dl_i ’s entire “view”, where the 2D analog of solid angle is shown by $d\Omega_i$.

Defining θ_i as the angle between dl_i ’s surface normal and I_i , $dF_{dl_i \rightarrow dl_j}$ can be defined as well.

$$dF_{dl_i \rightarrow dl_j} \equiv \frac{\cos \theta_i d\Omega_i}{\int_{-\pi/2}^{\pi/2} \cos \theta_i d\theta_i} \quad (3.19)$$

$$d\Omega_i \equiv \frac{\cos \theta_j dl_j}{S} \quad (3.20)$$

Then, using Eq. (3.18), an expression for the energy leaving dl_i in the direction of dl_j is found.

$$dQ_{dl_i} dF_{dl_i \rightarrow dl_j} = \frac{I_i \cos \theta_i \cos \theta_j dl_i dl_j}{S} \quad (3.21)$$

The fraction of energy transmitted $t(S)$ along a line of sight decays exponentially, as shown by Eq. (1.4), so the amount of energy emitted by dl_i in the direction of dl_j that reaches dl_j is described by the expression $t(S) dQ_{dl_i} dF_{dl_i \rightarrow dl_j}$. Moving to define a non-differential version of this expression, the total view factor of surface i to surface j is $F_{ij} \equiv \int_{\ell_i} \int_{\ell_j} dF_{dl_i \rightarrow dl_j}$ and the entirety of energy emitted from all of surface i is $Q_i \equiv \int_{\ell_i} dQ_{dl_i}$. Then, to define the mean geometric transmittance between surfaces i and j , $t(S) dQ_{dl_i} dF_{dl_i \rightarrow dl_j}$ must be found for all dl_i and for all dl_j in relation to every dl_i . This expression will equate to all energy leaving ℓ_i that reaches ℓ_j .

$$\bar{t}_{ij} Q_i F_{ij} \equiv \int_{\ell_i} \int_{\ell_j} t(S) dQ_{dl_i} dF_{dl_i \rightarrow dl_j} \quad (3.22)$$

Solving Eq. (3.22) for \bar{t}_{ij} , an general expression for 2D mean geometric transmittance between two surfaces can be found.

$$\bar{t}_{ij} = \frac{\int_{\ell_i} \int_{\ell_j} \frac{t(S) I_i \cos \theta_i \cos \theta_j}{S} d\ell_j d\ell_i}{F_{ij} \int_{\ell_i} 2I_i d\ell_i} \quad (3.23)$$

$$\bar{t}_{ij} = \frac{1}{F_{ij} \ell_i} \int_{\ell_i} \int_{\ell_j} \frac{t(S) \cos \theta_i \cos \theta_j}{2S} d\ell_j d\ell_i \quad (3.24)$$

All pertinent RadiativeHeatTransfer geometries are symmetrical, meaning all emission at all $d\ell_i$ s will behave the same way in regard to all $d\ell_j$ s. This results in length ℓ_i popping out of Eq. (3.24) as a constant and producing the simplified, general expression for geometric mean transmittance for 2D geometries. New correlations for the Cylinder and Annulus preset geometry options for RadiativeHeatTransfer have been derived using Eq. (3.25) assuming 2D radiative enclosures with diffuse surfaces and a homogeneous participating fluid.

$$\bar{t}_{ij} = \frac{1}{F_{ij}} \int_{\ell_j} \frac{t(S) \cos \theta_i \cos \theta_j}{2S} d\ell_j \quad (3.25)$$

Cylinder geometric mean transmittance

Fluid flow along a pipe creates a cylindrical radiative enclosure, which can then be broken down into circular axial cross-sections (Fig. 3.8). Known parameters for the Cylinder geometry are D , and fluid κ . The inner surface of the pipe constitutes the sole surface in this enclosure, meaning this surface (named surface 1) will serve as both surface i and surface j in terms of deriving \bar{t}_{ij} . The derived geometric mean transmittance will describe the transmittance of radiation from surface 1 to itself — \bar{t}_{11} .

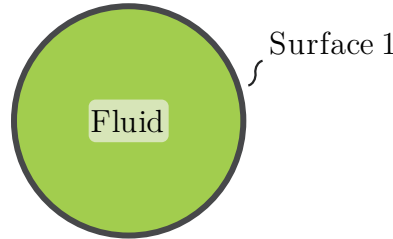


Figure 3.8: Two-dimensional axial cross-section of the Cylinder radiative enclosure.

Figure 3.8 can be dissected to assist in applying Eq. (3.25) to the Cylinder geometry. Several helpful relations can be noted in regard to determining S in Fig. 3.9. By symmetry, it can

be seen that $\theta_i = \theta_j$ and therefore this angle can simply be called θ . Using the law of cosines, $S^2 = r^2 + r^2 - 2r^2 \cos(\pi - \beta)$. Knowing for the interior angles of a triangle $\sum \angle = \pi$, the previous cosine relation can be rewritten as $S^2 = 2r^2[1 - \cos(\pi - 2\theta)]$. Applying the angle-difference and double-angle identities for cosine, this relation can be further rewritten to produce a simple formula for path length.

$$S = 2r \cos \theta = D \cos \theta \quad (3.26)$$

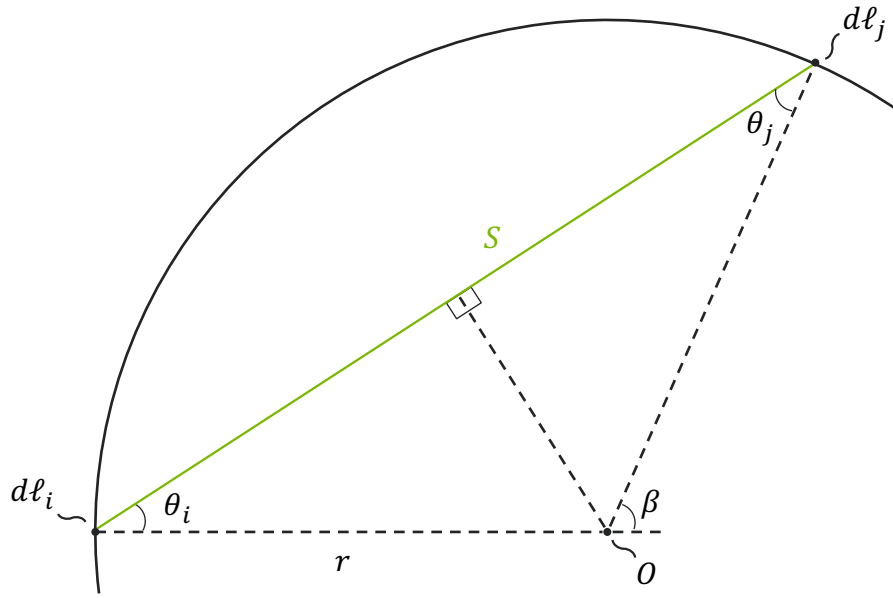


Figure 3.9: Dissection of the Cylinder radiative geometry showing the radiative path length between dl_i and dl_j .

Before substituting Eq. (3.26) into Eq. (3.25), the integral must be formulated in a way to cover all of surface j from dl_i . This can be accomplished by integrating θ_i across its entire view angle but requires translating the integral $\int dl_j$ into an expression of $d\theta$. Using the definition for arc length of a circle, and referencing Fig. 3.9, $dl_j = r d\beta$. Again, using the sum of interior angles, $2\theta + (\pi - \beta) = \pi$, which can be used to state $d\beta = 2d\theta$. Combining this statement with the arc length relation, the derivative with respect to l_j can be translated into one with respect to θ .

$$dl_j = 2r d\theta = D d\theta \quad (3.27)$$

Surface 1 can see all of itself, so $F_{11} = 1$. Substituting Eqs. (3.26) and (3.27) into Eq. (3.25),

an expression for geometric mean transmittance can be found.

$$\bar{t}_{11} = \int_{\theta} \frac{t(\theta) \cos \theta}{2} d\theta \quad (3.28)$$

Defining the angle of integration to be $\phi = [-\pi/2, \pi/2]$ and substituting in $t(S) = \exp(-\kappa S)$ produces a final expression for geometric mean transmittance of the Cylinder geometry.

$$\bar{t}_{11} = \frac{1}{2} \int_{-\pi/2}^{\pi/2} \exp(-\kappa D \cos \phi) \cos \phi d\phi \quad (3.29)$$

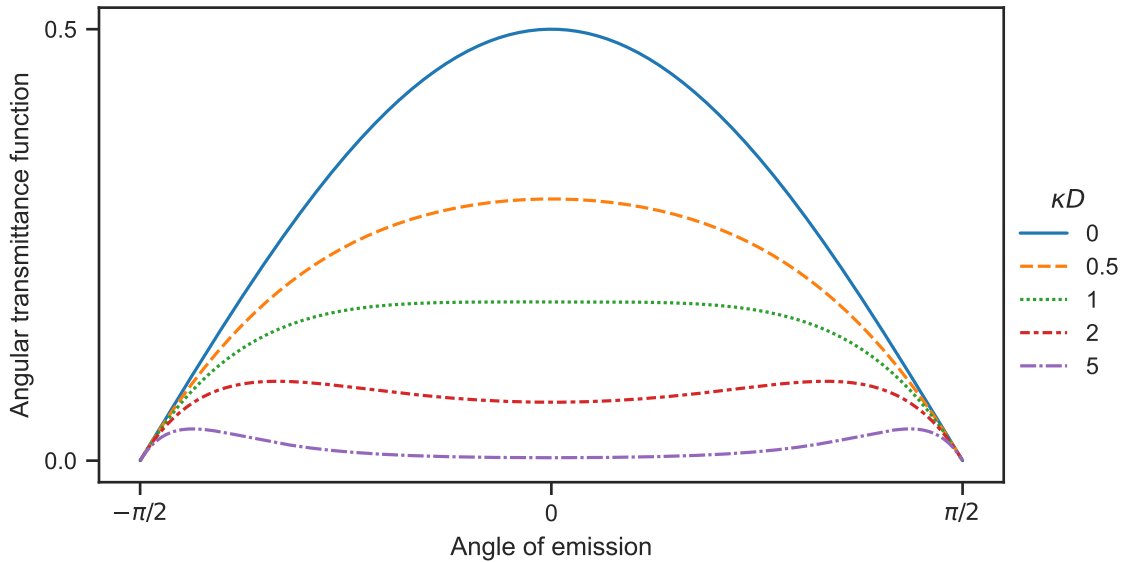


Figure 3.10: Cylinder geometric mean transmittance broken down by angle of integration, capturing the cumulative effects of emission, transmission, and arrival of radiation per emission angle. Several optical thicknesses are shown, where the area under each curve equals its respective \bar{t}_{11} .

A quick check of Eq. (3.29) can be performed by evaluating $\bar{t}_{11}|_{\kappa=0}$. Without a participating medium, all energy emitted from surface i towards surface j will reach surface j , so this

value should equate to one.

$$\begin{aligned}
 1 &\stackrel{?}{=} \frac{1}{2} \int_{-\pi/2}^{\pi/2} \exp(0) \cos \phi \, d\phi \\
 &= \frac{1}{2} \sin \phi \Big|_{-\pi/2}^{\pi/2} \\
 &= 1 \quad \checkmark
 \end{aligned}
 \tag{3.30}$$

Further investigation of Eq. (3.29) can be conducted by analyzing how \bar{t}_{11} changes with emission angle. Figure 3.10 shows $d\bar{t}_{11}/d\phi$, where the integral across plotted angles generates \bar{t}_{11} . As optical thickness κD increases, peaks appear near the emission limits. Although less energy is emitted in these directions, smaller optical paths lead to more energy reaching surface j than emission through the optically-thicker middle regions.

While Fig. 3.10 provides insight on general transmittance behavior for the Cylinder geometry and boosts confidence \bar{t}_{11} is properly derived, a comparison to established cylindrical trans-

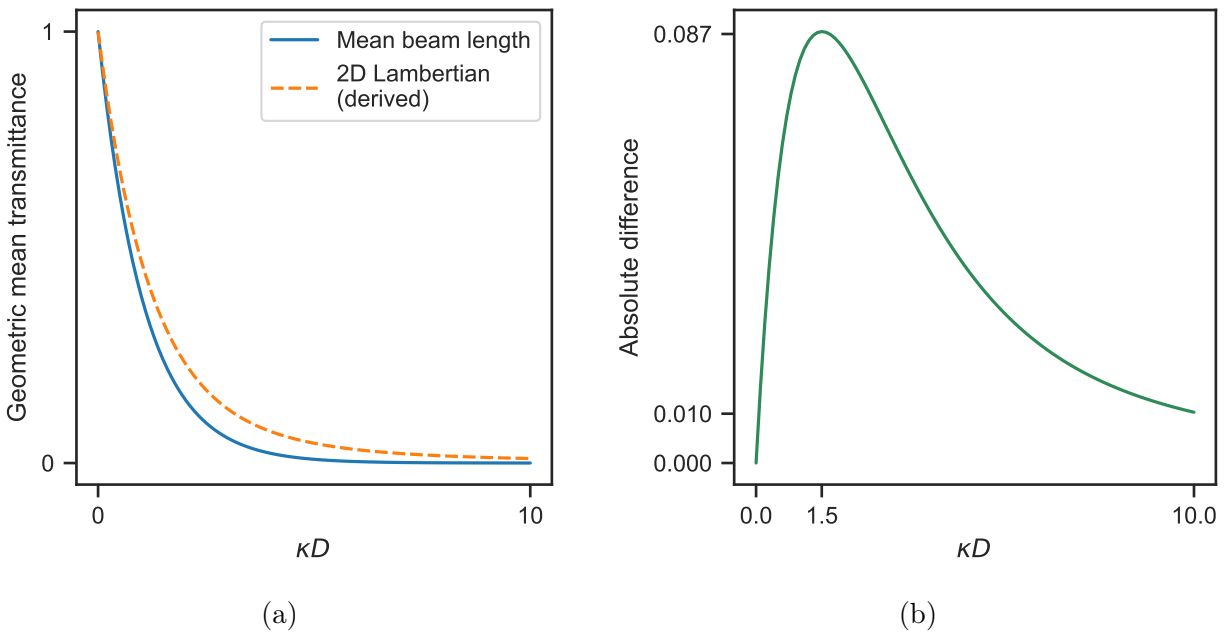


Figure 3.11: Comparison of geometric mean transmittances for the Cylinder geometry between the 3D mean beam length method [16] and the 2D diffuse derivation, Eq. (3.29). The expected higher transmittance values from the 2D method can be seen in (a) the calculated transmittance values and (b) the difference between them.

mittance values is more helpful for understanding the impact this newly derived parameter will have on radHT simulation.

The previously discussed 3D mean beam length method for deriving geometric mean transmittance provides a good comparison because it attempts to capture 3D radHT effects and is the only other method computationally inexpensive enough to implement in SAM. As mentioned, casting radiative enclosures as 2D geometries leads to a systematic shortening in radiative path length, and therefore an increase in transmitted radiation. This effect is noticeable in Fig. 3.11a, but does not appear significant. This qualitative analysis can be more accurately analyzed in Fig. 3.11b, where the % difference was not chosen as a metric because \bar{t} in both cases is already normalized to the total emitted radiation from surface 1 by definition. The maximum discrepancy between \bar{t}_{11} calculation methods appears around $\kappa D = 1.5$, and translates to 8.7% more emitted energy deposited in the fluid than reaches the wall when using the mean beam length method compared to the derived 2D Lambertian.

Annulus geometric mean transmittance

Fluid flowing between two concentric cylinders, or in the space between two coaxial pipes, generates an annular radiative enclosure, which can be subdivided into flat, donut-shaped axial cross-sections (Fig. 3.12). Known parameters include the geometric parameters r_i , δ , and r_o (because $r_i + \delta = r_o$), and the fluid parameter κ . For this geometry, two geometric mean transmittances must be found: the transmittance from surface 1 to surface 2 and that from surface 2 to itself. The transmittance from surface 2 to surface 1 need not be calculated because \bar{t} s between surfaces are reciprocally equivalent — $\bar{t}_{ij} = \bar{t}_{ji}$.

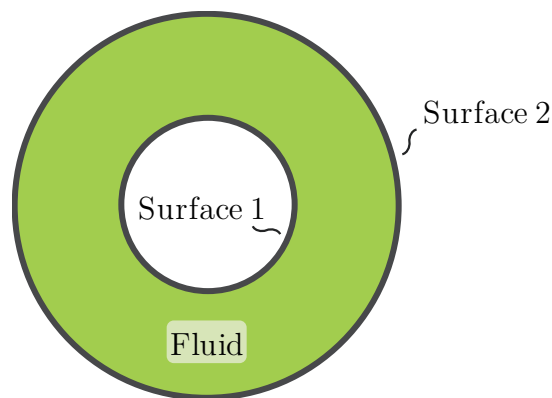


Figure 3.12: Two-dimensional axial cross-section of the Annulus radiative enclosure.

Starting with \bar{t}_{22} , much can be borrowed from the derived transmittance correlation for cylindrical geometries. The only differences are the view factor and bounds of integration.

The entirety of surface 1's view consists of surface 2, so the view factor $F_{12} = 1$. Then, the reciprocity rule, $A_i F_{ij} = A_j F_{ji}$, and summation of view factors, $\sum_k F_{ik} = 1$, can be used to acquire F_{22} .

$$\begin{aligned} \ell_1 F_{12} &= \ell_2 F_{21} \\ F_{21} &= \frac{\ell_1}{\ell_2} = \frac{r_i}{r_o} \end{aligned} \quad (3.31)$$

$$\begin{aligned} F_{22} &= 1 - F_{21} \\ &= 1 - \frac{r_i}{r_o} = \frac{r_o - r_i}{r_o} \\ &= \frac{\delta}{r_o} \end{aligned} \quad (3.32)$$

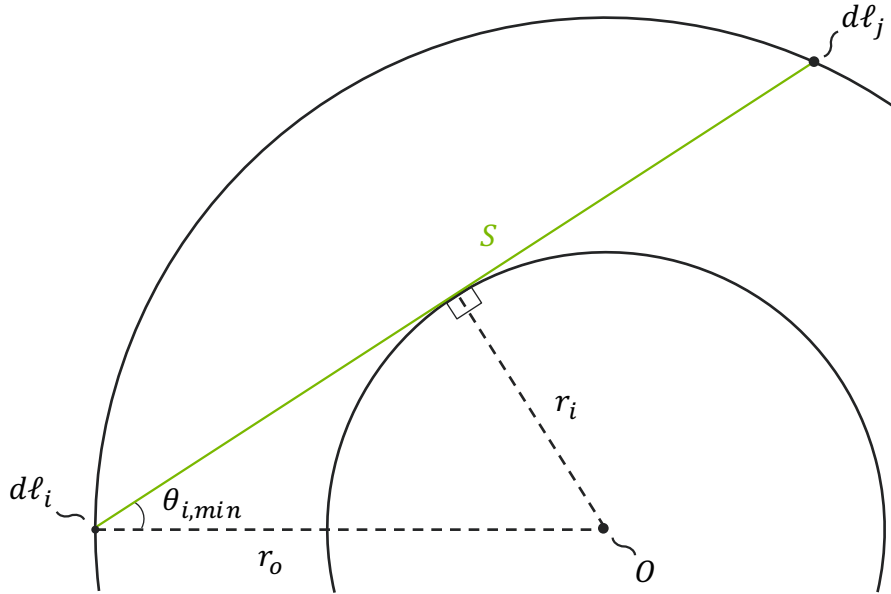


Figure 3.13: Dissection of the Annulus radiative geometry showing the radiative path length between $d\ell_i$ on surface 2 and $d\ell_j$ on surface 2. The shown S and angle $\theta_{i,min}$ show the maximum radiative path length and the minimum angle, respectively, for this geometry.

The same integration scheme from Eq. (3.29) can be borrowed for \bar{t}_{22} to sweep across all visible elements of surface 2. However, to avoid incorporating radiative paths that collide with surface 1, new bounds of integration should be used. Observing Fig. 3.13, the minimum available angle for emission from $d\ell_i$ is $\theta_{i,min} = \arcsin(r_i/r_o)$, while the maximum bound

remains $\theta_{i,max} = \pi/2$. Substituting ϕ as the angle of integration, Eq. (3.25) can be applied to \bar{t}_{22} as $\int_{-\pi/2}^{-\theta_{i,min}} f(\phi) d\phi + \int_{\theta_{i,min}}^{\pi/2} f(\phi) d\phi$ or, because of symmetry, as $2 \int_{\theta_{i,min}}^{\pi/2} f(\phi) d\phi$. Utilizing the latter expression, with $\phi = [\arcsin(r_i/r_o), \pi/2]$, a final expression for geometric mean transmittance of the Annulus geometry is found.

$$\bar{t}_{22} = \frac{r_o}{\delta} \int_{\arcsin(r_i/r_o)}^{\pi/2} \exp(-2\kappa r_o \cos \phi) \cos \phi d\phi \quad (3.33)$$

Again, a quick check of Eq. (3.33) can be performed by evaluating $\bar{t}_{22}|_{\kappa=0}$, which should equal one.

$$\begin{aligned} 1 &\stackrel{?}{=} \frac{r_o}{\delta} \int_{\arcsin(r_i/r_o)}^{\pi/2} \exp(0) \cos \phi d\phi \\ &= \frac{r_o}{\delta} \sin \phi \Big|_{r_i/r_o}^{\pi/2} \\ &= \frac{r_o}{\delta} \left(1 - \frac{r_i}{r_o} \right) \\ &= \frac{r_o}{\delta} \left(\frac{\delta}{r_o} \right) \quad \checkmark \end{aligned} \quad (3.34)$$

As for the behavior of Eq. (3.33) as a function of emission angle, Fig. 3.10 can be referenced. The only differences between that figure and one produced for the Annulus transmittance function is that the plotted function for \bar{t}_{22} would equal zero from $\phi = -\arcsin(r_i/r_o)$ to $\phi = \arcsin(r_i/r_o)$. A comparison with established 3D mean beam length correlations could be carried out. However, since the derived \bar{t}_{22} (Eq. (3.33)) is consistent with \bar{t}_{11} (Eq. (3.29)), deductions from Fig. 3.11 should pertain to this correlation as well. A comparison to mean beam length-derived transmittance values will be conducted for the remaining Annulus geometric mean transmittance, that from surface 1 to surface 2.

Deriving a correlation for \bar{t}_{12} requires a new approach. The Cylinder \bar{t}_{11} and Annulus \bar{t}_{22} derivations conveniently utilized an equivalency between θ_i and θ_j , which subsequently produced a simple expression for dl_j . The difficulty here lies in finding expressions to cast θ_j and dl_j as functions of θ_i . A simpler approach involves casting θ_i and θ_j as functions of β and integrating across $\beta = [-\arccos(r_i/r_o), \arccos(r_i/r_o)]$ to cover all emission angles from dl_i (see Fig. 3.14 for clarification). However, this introduces complications when integrating the derived correlations into SAM, an issue that will be discussed in ‘‘implementation’’ (Pg. 130). The geometric mean transmittance between surface 1 and surface 2 will be derived by converting all variables in Eq. (3.25) into functions of angle θ_i , and integrating this angle across dl_i ’s entire view. Throughout the following derivation, Fig. 3.14 should be referenced to contextualize all mathematical relations and surrounding discussion.

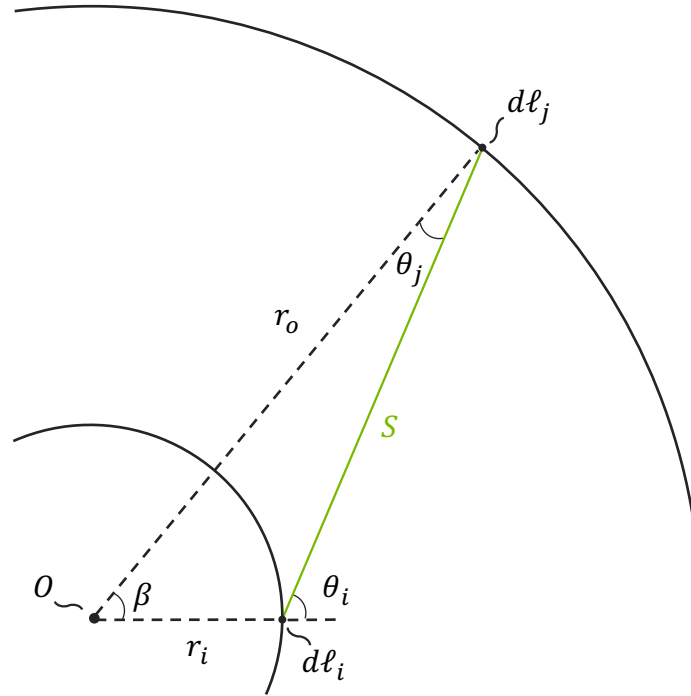


Figure 3.14: Dissection of the Annulus radiative geometry showing the radiative path length between dl_i on surface 1 and dl_j on surface 2.

To determine the length of S as a function of known variables, the center of the Annulus will be considered the origin of a coordinate grid. Then dl_j is located along the circle $(r_i + S \cos \theta_i)^2 + (S \sin \theta_i)^2 = r_o^2$. Rearranging as $S^2 + (2r_i \cos \theta_i)S - (r_o^2 - r_i^2) = 0$ and subsequently applying the quadratic formula generates an expression for radiative path length.

$$S = \frac{-2r_i \cos \theta_i \pm \sqrt{4r_i^2 \cos^2 \theta_i + 4(r_o^2 - r_i^2)}}{2} \quad (3.35)$$

In this case, S cannot be negative, so the previous expression can be simplified.

$$S = -r_i \cos \theta_i + \sqrt{r_o^2 - r_i^2 \sin^2 \theta_i} \quad (3.36)$$

The next term in Eq. (3.25) not a function of θ_i is $\cos \theta_j$, which appears when describing r_i with the law of cosines as $r_i^2 = r_o^2 + S^2 - 2r_o S \cos \theta_j$. Rearranging produces an expression of $\cos \theta_j = f(\theta_i, S)$, where $S = f(\theta_i)$.

$$\cos \theta_j = \frac{r_o^2 - r_i^2 + S^2}{2r_o S} \quad (3.37)$$

The integral over ℓ_j can be converted to an integral over all angles viewed by $d\ell_i$, which ranges from $-\pi/2$ to $\pi/2$.

$$d\ell_j = r_o d\beta \quad (3.38)$$

However, β is not known. Using the y -coordinate for $d\ell_j$,

$$\begin{aligned} r_o \sin \beta &= S \sin \theta_i \\ \beta &= \arcsin\left(\frac{S}{r_o} \sin \theta_i\right) \end{aligned} \quad (3.39)$$

$$d\beta = \frac{\sin \theta_i \left(\frac{r_i}{r_o} \sin \theta_i - \frac{r_i^2 \sin \theta_i \cos \theta_i}{S r_o + r_i r_o \cos \theta_i} \right) + \frac{S}{r_o} \cos \theta_i}{\sqrt{1 - \left(\frac{S}{r_o} \sin \theta_i \right)^2}} d\theta_i \quad (3.40)$$

The above expression is a function of θ_i and $S(=f(\theta_i))$, so plugging this expression for $d\beta = f(\theta_i)$ into [Eq. \(3.38\)](#) yields an equation for $d\ell_j = f(\theta_i)$.

$$d\ell_j = \frac{r_i \sin^2 \theta_i \left(1 - \frac{r_i \cos \theta_i}{S + r_i \cos \theta_i} \right) + S \cos \theta_i}{\sqrt{1 - \left(\frac{S}{r_o} \sin \theta_i \right)^2}} d\theta_i \quad (3.41)$$

Now, [Eqs. \(3.36\)](#) to [\(3.41\)](#) must be substituted into [Eq. \(3.25\)](#). Defining the angle of integration as $\phi = [-\pi/2, \pi/2]$, this derivation arrives at an expression for the geometric mean transmittance from surface 1 to surface 2 in the Annulus geometry.

$$\bar{t}_{12} = \int_{-\pi/2}^{\pi/2} \frac{\exp(-\kappa S) \cos \phi (r_o^2 - r_i^2 + S^2) \left[r_i \sin^2 \phi \left(1 - \frac{r_i \cos \phi}{S + r_i \cos \phi} \right) + S \cos \phi \right]}{4r_o S^2 \sqrt{1 - \left(\frac{S}{r_o} \sin \phi \right)^2}} d\phi \quad (3.42)$$

Ideally, [Eq. \(3.42\)](#) could be quickly checked by evaluating $\bar{t}_{12}|_{\kappa=0}$, but unfortunately this expression is not elegant enough to be solved by hand. A numerical integration scheme is used to solve this integral, which shows all emitted radiation from surface 1 passing through

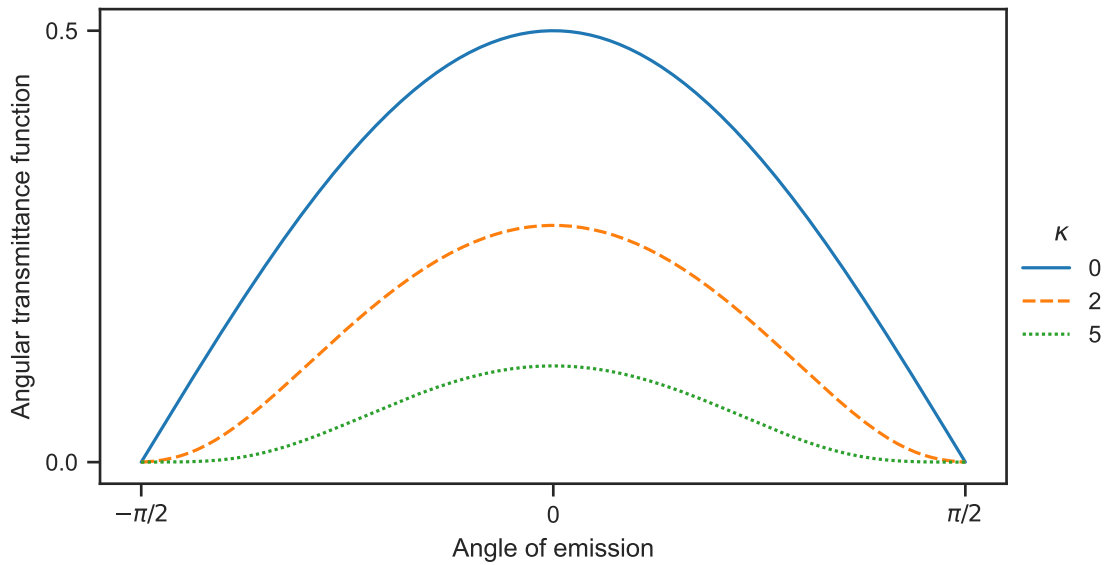


Figure 3.15: Annulus geometric mean transmittance between surfaces broken down by angle of integration in a geometry where $r_i = 5$ m and $\delta = 0.3$ m. Several plots for various optical thicknesses capture the cumulative effects of emission, transmission, and arrival of radiation per emission angle. The area under each curve equals its respective \bar{t}_{12} .

an optically transparent fluid reaches surface 2. Further discussion on the utilized integration scheme is provided on Pg. 130.

$$1 \stackrel{?}{=} \int_{-\pi/2}^{\pi/2} \frac{\exp(0) \cos \phi (r_o^2 - r_i^2 + S^2) \left[r_i \sin^2 \phi \left(1 - \frac{r_i \cos \phi}{S + r_i \cos \phi} \right) + S \cos \phi \right]}{4r_o S^2 \sqrt{1 - \left(\frac{S}{r_o} \sin \phi \right)^2}} d\phi \quad (3.43)$$

= 1 ✔

For transmittances calculated in Cylinder geometries, path lengths emitting near surface normal must travel the furthest distances and therefore undergo the highest absorption rates. This effect was discussed in relation to Fig. 3.10. In contrast, as can be seen in Fig. 3.14, emission near surface normal from $d\ell_i$ must travel the *shortest* distance of all available path lengths. Therefore, when analyzing how \bar{t}_{12} changes with emission angle, it is the optically-thicker peripheral regions which face depression. Figure 3.15 shows these depressive effects on $d\bar{t}_{12}/d\phi$ for several fluid absorption coefficients in a set annular radiative geometry. While

the validity of $\bar{t}_{12}|_{\kappa=0} = 1$ is not easy to see in equation form, it is easy to see graphically. The solid line for $\kappa = 0$ in Fig. 3.15 seems to closely resemble a cosine curve with an amplitude of 0.5, where $\int_{-\pi/2}^{\pi/2} (0.5) \cos \phi \, d\phi = 1$.

The values of \bar{t}_{12} from Eq. (3.42) are shown in Fig. 3.16a. Smaller annular gap widths (δ) contribute to lower radiative paths and less absorption. So too do lower κ s. As expected, the 2D Lambertian approach induces a systematic S -shortening and transmittance-inflation compared to its 3D mean beam length counterpart [82], which manifests as differences in Fig. 3.16b. The maximum difference appearing between these two methods arises at $\delta = 0.14$ m, $\kappa = 5$, where 12% more emitted energy is deposited in the fluid than reaches the wall when using the mean beam length method compared to the derived 2D Lambertian. Due to the relatively significant ($\mathcal{O}(-1)$) maximum difference between the two methods, RadiativeHeatTransfer code users modeling in this regime ($r_i \approx 5$ m, $\delta \approx 0.14$ m, and $\kappa \gtrsim 5$) should consider which method best suits their simulated scenario. If the simulated radiative

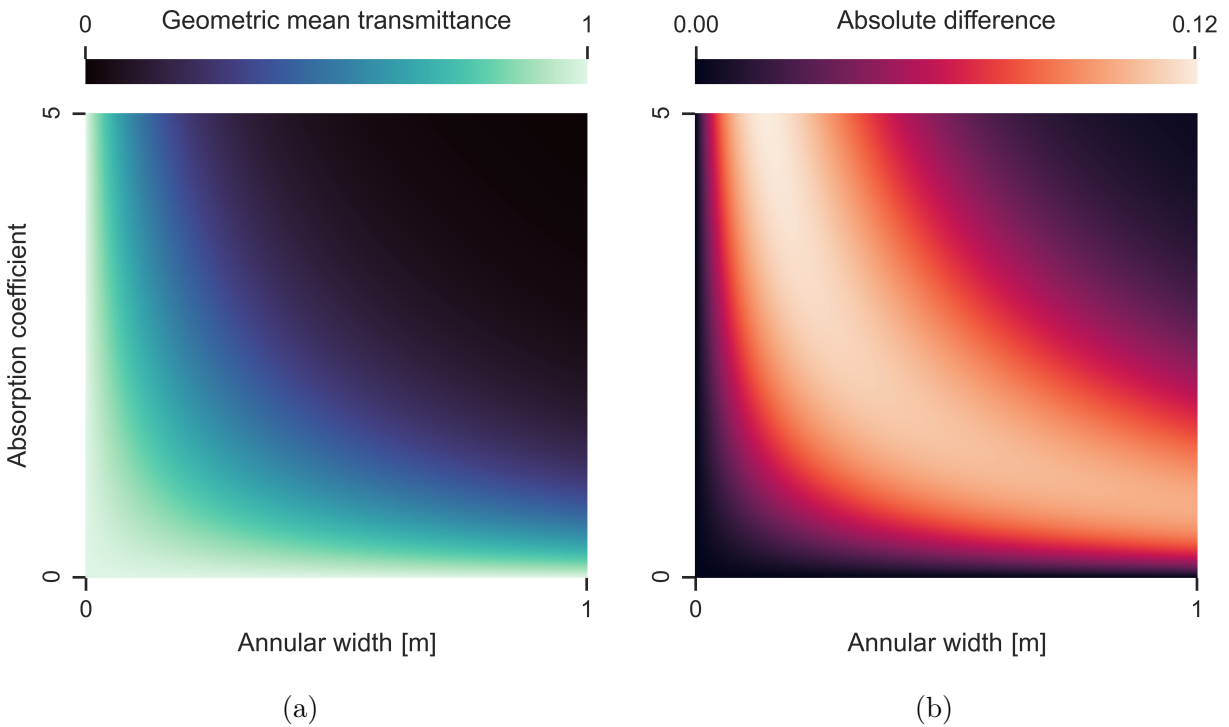


Figure 3.16: Geometric mean transmittances between surfaces for an Annulus geometry with $r_i = 5$ m and $\delta = [0, 1]$ m. The derived 2D diffuse transmittance (Eq. (3.42)) is (a) itself shown for a range of κ and subsequently (b) compared to the same \bar{t}_{12} derived from the 3D mean beam length method [82].

system is long with small axial temperature differences, and the user prefers to capture 3D radiative path lengths at the expense of math-to-code consistency, the 3D \bar{t}_{12} [82] should be manually calculated and entered into SAM as a user-input, which overrides any code-calculated 2D Lambertian transmittance value.

Semi-infinite Slab geometric mean transmittance

In terms of ascertaining a geometric mean transmittance, the Slab geometry can be placed in a class of its own. This option is inherently a semi-infinite geometry, as the fluid extends to infinity in the direction parallel to, and in one of the two directions perpendicular to, the fluid flow. As such, this geometry option is typically used for limiting case scenarios or mathematical exercises and is not meant to accurately model real-world systems. To that end, a derived 2D \bar{t} is not necessary. Howell [16] derives an expression for fluid emittance in a 3D semi-infinite slab, which is sufficient for implementing in SAM. This expression can be manipulated to produce the transmittance between surfaces, where δ is defined as the gap width across the Slab geometry. Note mean beam length is not necessary for this equation.

$$\bar{t}_{12} = 2E_3(\kappa\delta) \quad (3.44)$$

The term E_3 is the exponential integral function of the third kind. Utilizing an approximation for E_3 [84], the above expression can be simplified to produce the geometric mean transmittance for the Slab geometry as implemented in RadiativeHeatTransfer.

$$\bar{t}_{12} = \exp\left(-\frac{3}{2}\kappa\delta\right) \quad (3.45)$$

SAM implementation of geometric mean transmittance correlations

I chose to implement a trapezoidal integration scheme to calculate Eqs. (3.29), (3.33) and (3.42) in SAM. Equation (3.45) is calculated exactly with no integration required. The trapezoidal integration approximation method is well-established, so I leave it to the reader to find resources for further elaboration if desired. The equation below is the one I implemented to approximate a function from ϕ_0 to ϕ_N with N trapezoids of equal width.

$$\int_{\phi_0}^{\phi_N} f(\phi) d\phi \approx \frac{\phi_N - \phi_0}{N} \left(\frac{f(\phi_0) + f(\phi_N)}{2} + \sum_{i=1}^{N-1} f(\phi_i) \right) \quad (3.46)$$

Application of Eq. (3.46) can be visualized by reducing curves in Figs. 3.10 and 3.15 into $N + 1$ equally spaced points. Instead of drawing the curve as-shown, imagine straight lines between adjacent points. The areas underneath these straight lines are added together to approximate the true integral.

I previously mentioned an issue formulating the Annulus \bar{t}_{12} transmittance function as an integral with respect to β . This issue comes down to utilizing trapezoids of *equal width*. Referencing Fig. 3.14, the change of θ_i with respect to β is clearly not constant. While β would be divided equally by Eq. (3.46), angle θ_i , where radiative emission from the inner surface occurs, would not be. This means calculating $\bar{t}_{12} = f(\beta)$ with Eq. (3.46) would not take an equally-spaced sampling of the radiative emission at $d\ell_i$, which is part of the physics \bar{t}_{12} must properly capture.

When determining the number of trapezoids to use in Eq. (3.46), there is a trade-off to consider. Increasing N improves accuracy, but comes at the cost of increasing computation time. To understand how well trapezoidal approximation error is reduced by increasing N , at least for the derived \bar{t} correlations in this section, a convergence study was conducted. Approximations of the Cylinder \bar{t}_{11} and the Annulus \bar{t}_{12} were calculated using a varying number of trapezoids and then compared to their respective approximations using $N = 10^6$. Geometric mean transmittances calculated with 10^6 trapezoids should have negligible error when compared to the true integral value.

Figure 3.17 shows, to more accurately calculate \bar{t}_{11} , an increased number of trapezoids are necessary for optically-thicker scenarios. This behavior could be expected, as Fig. 3.10 shows increased optical thickness leading to curves less-suited to linear approximation. All curves

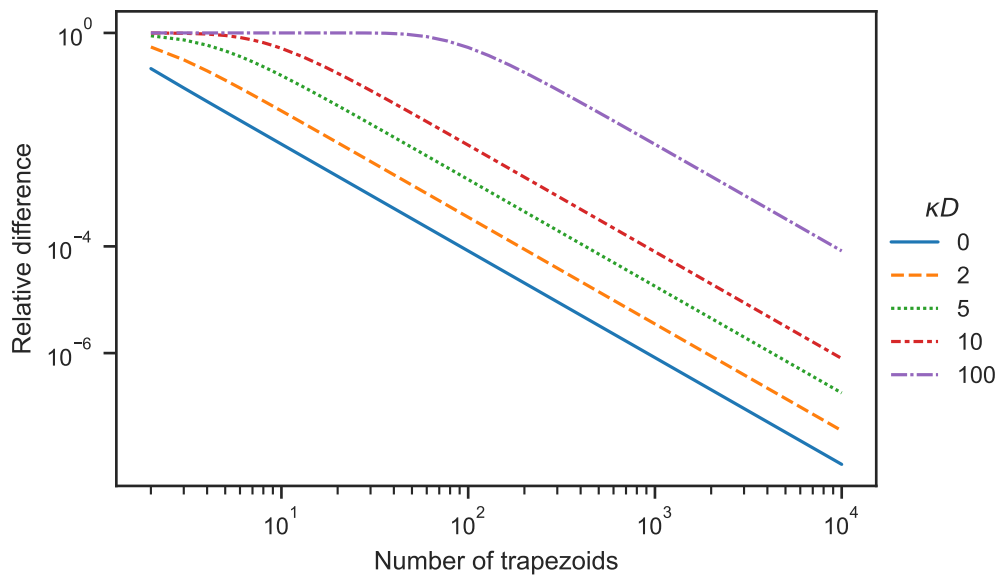


Figure 3.17: Convergence of the Cylinder \bar{t}_{11} (Eq. (3.29)) trapezoidal integration approximation for various optical thicknesses using $\bar{t}_{11}|_{N=10^6}$ as the reference solution.

in Fig. 3.17 show relative solution differences dropping below 10^{-4} at $N = 10^4$. However for scenarios with optical thicknesses in the range of $\kappa D = 100$, it is far more likely code-users will want to manually input $\bar{t}_{11} = 0$ than ask the code to calculate some minuscule transmittance value. For all other optical thicknesses, relative solution differences drop below 10^{-6} at $N = 10^4$ and either satisfy, or nearly satisfy, a relative difference of 10^{-4} at $N = 10^3$.

Despite jumpy convergence behavior below $N = 40$, Fig. 3.18 shows *fewer* trapezoids are necessary for more absorptive fluids in the Annulus geometry. Comparing convergence data with Fig. 3.15, the results here make sense as well. The more absorptive the fluid, the closer curves get to resembling a flat line. Here, code-users will likely model scenarios with $\kappa = 0$ without a participating fluid at all, in which case RadiativeHeatTransfer will not calculate any \bar{t} s. All approximations for \bar{t}_{12} with a participating fluid satisfy a relative difference of 10^{-6} by $N = 10^3$.

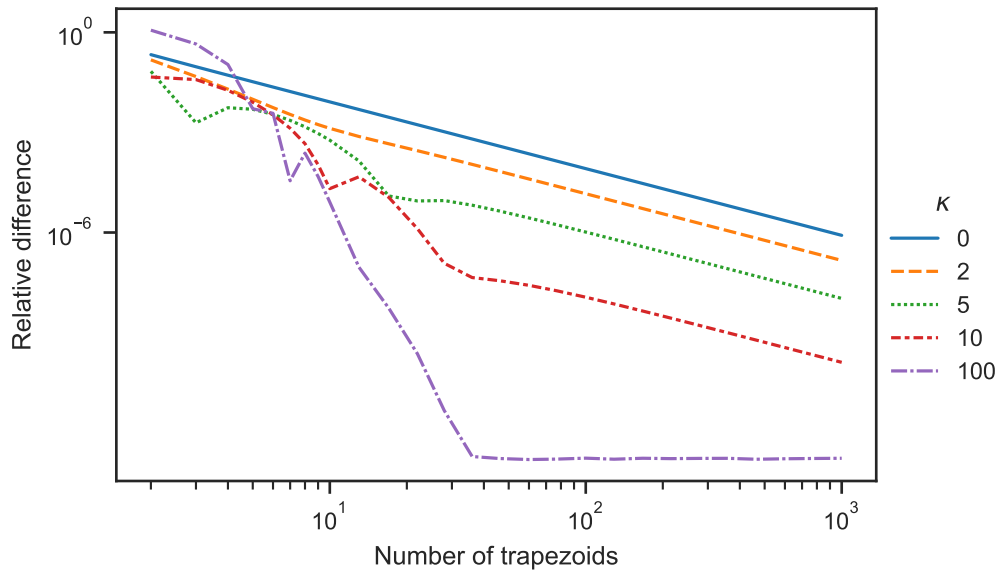


Figure 3.18: Convergence of the Annulus \bar{t}_{12} (Eq. (3.42)) trapezoidal integration approximation for various fluid absorption coefficients using $\bar{t}_{12}|_{N=10^6}$ as the reference solution. The modeled geometry for all κ curves is defined by $r_i = 5$ m and $\delta = 0.1$ m.

Based on the relative solution differences achieved with 10^3 trapezoids in both Figs. 3.17 and 3.18, I decided RadiativeHeatTransfer should utilize $N = 10^3$ for \bar{t} trapezoidal integration. Originally however, through a lack of foresight, Eqs. (3.29), (3.33) and (3.42) were implemented in SAM² with $N = 10^2$. While generating $10 \times$ fewer trapezoids does reduce

²SAM version number and git commit ID: v0.9.5.1-174-g57ccca98

computation time, \bar{t} calculations are only performed once at the beginning of each simulation. Therefore, increasing the number of trapezoids to 10^3 improves calculation accuracy with minimal increase in computation cost. In light of this realization, the number of trapezoids was increased to $N = 10^3$ and implemented in SAM with the RadiativeHeatTransfer development tasks discussed in Secs. 3.2.5 and 3.2.6.

3.2.4 Enabling RadiativeHeatTransfer compatibility with existing SAM components

During the primary RadiativeHeatTransfer development phase, I focused on utilizing two preexisting SAM components for radHT simulation - PBOneDFluidComponent and PBCoupledHeatStructure. These components were chosen because they serve as the basic building blocks upon which many other SAM components are built (referred to in this section as sub-components). Due to these components serving as building blocks, they must be flexible in application and are therefore well-purposed for building simulation geometries from the ground up, such as was done for the SAM Code Validation study using UC Berkeley's Compact Integral Effects Test [71]. By utilizing these basic components during code development, I developed RadiativeHeatTransfer to be inherently compatible with PBOneDFluidComponent and PBCoupledHeatStructure. This means any simulations utilizing either of these guaranteed-compatible components could properly model radHT, pending verification (see Sec. 3.3). However, there are scenarios in which the SAM user might not desire building their simulation from such a low level and would then opt for utilizing more specialized components for modeling. For purposes of radHT scaling distortion quantification, I am interested in heat transfer components. Therefore I identified several heat transfer components I anticipated using for future modeling purposes and expanded RadiativeHeatTransfer compatibility to include them. The names of these "specialized" heat transfer SAM components of interest include PBCoreChannel, PBHeatExchanger, and PBPipe.

Theoretically, enabling RadiativeHeatTransfer simulation compatibility with low-level components subsequently enables compatibility with those components built upon them as well. One such example of the inherent RadiativeHeatTransfer compatibility automatically extending from PBOneDFluidComponent and PBCoupledHeatStructure to a higher-level component (or a SAM component constructed from multiple lower-level sub-components) comes from PBPipe, which is simply constructed of a single PBCoupledHeatStructure linked to a single PBOneDFluidComponent. I realized simulation compatibility with PBPipe early enough on, I included this component in one of the initial regression tests used for testing new SAM code builds (see radHT_cylinder in Sec. 3.3). However, not all components of interest provided such little resistance towards working with RadiativeHeatTransfer, the most notorious example being PBHeatExchanger. This section will describe the process of enabling PBHeatExchanger-RadiativeHeatTransfer simulation compatibility. By showing the entire process, I hope to not only instill confidence that component coupling has been properly achieved, but to also lay out a compatibility development road-map that might be helpful

to others down the road who might be performing similar tasks or perhaps scrutinizing the RadiativeHeatTransfer component.

PBHeatExchanger compatibility

Upon concluding RadiativeHeatTransfer’s primary development phase, my brief attempt to model radHT within PBHeatExchanger had failed - I had not yet figured out how to set the solid structure walls as radiatively-interacting surfaces in RadiativeHeatTransfer. At that time, I described compatibility with PBHeatExchanger as being “of the utmost desirability to develop” [85] and listed it at the top of my future tasks list. Several subsequent attempts resulting in additional failures prompted me to create and follow a structured development plan to address this development task:

- Step 1. Build the heat exchanger geometry utilizing PBHeatExchanger
- Step 2. Negate convective heat transfer to isolate radHT effects
- Step 3. Build RadiativeHeatTransfer geometries and observe behavior
- Step 4. Check radiative coupling by outputting surface and fluid names
- Step 5. Check heat flux calculations by outputting radiative heat fluxes
- Step 6. Verify PBHeatExchanger-RadiativeHeatTransfer simulation solution

Step 1 sets the stage for investigating RadiativeHeatTransfer compatibility in later steps, so foresight into which radiative geometries will be built can be helpful for informing heat exchanger design. To ensure RadiativeHeatTransfer properly captures both surface-to-fluid and surface-to-surface transfer, both should be tested. One geometry which enables testing both forms of radHT at once is that of concentric tubes with fluid flowing both between the tubes and within the inner tube. The inner tube exclusively tests surface-to-fluid transfer, and the annular region between tubes, while technically simulating both forms, can be made to emphasize surface-to-surface interaction. Of this geometry, shown in Fig. 3.19, both fluids and the inner tube between them can be constructed with PBHeatExchanger (abbreviated here to “HX”), while the outer shell tube must be constructed with PBCoupledHeatStructure (abbreviated to “Shell”).

Some geometric properties too were selected with this foresight towards step 3. To emphasize the surface-to-fluid transfer within the tube, the optical thickness there should be large. Since optical thickness is a function of radiative path length, and path length is loosely related to cavity width, the proportion of surface-to-fluid transfer (compared to surface-to-surface transfer) can be emphasized by increasing the tube diameter. Whereas in the annular shell-side region, surface-to-surface transfer can be emphasized by doing the opposite - decreasing

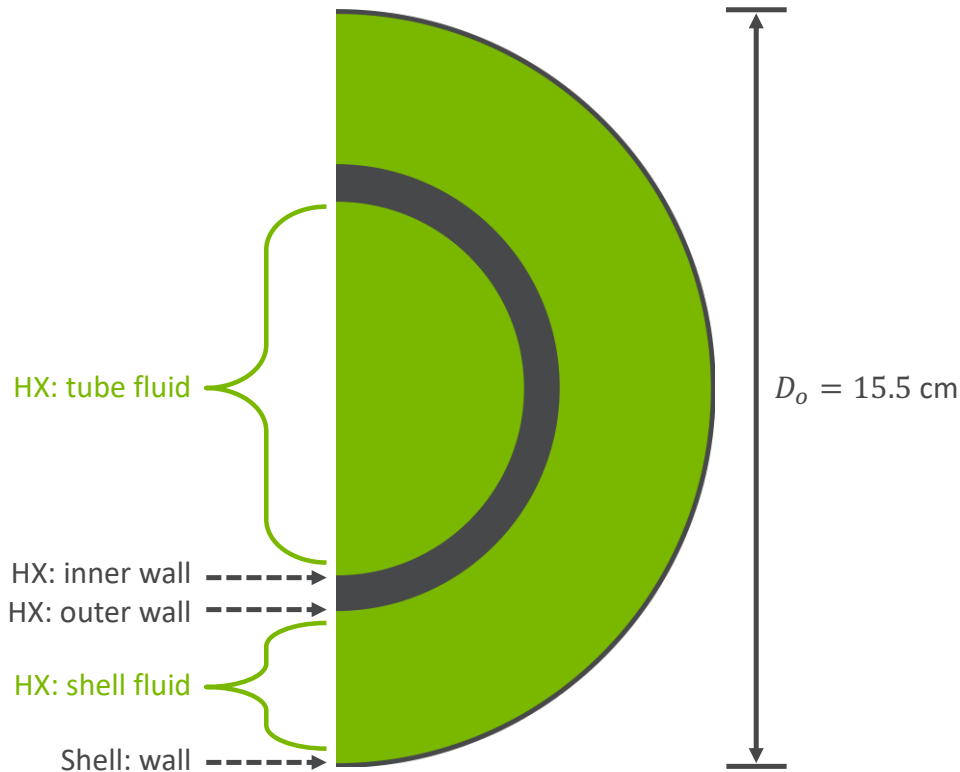


Figure 3.19: Axial cutaway view of RadiativeHeatTransfer-PBHeatExchanger compatibility testing geometry (not drawn to scale).

the annular width. This discussion is, at best, a rough qualitative description of one method for influencing different forms of radiative transfer, and further manipulation via radiative properties will be discussed in step 3 of this test plan. Nevertheless, these considerations still informed test geometry. A summary of all geometric parameters chosen for these simulations can be found in [Tbl. 3.2](#).

Beyond geometric properties, other simulation parameters had to be selected as well. For instance, the number of axial elements was set to fifty for all components, and the number of radial elements for solid structures was set to three. Thermophysical properties had to be chosen. As can be seen in [Tbl. 3.2](#), the fluid thermophysical properties were calculated within SAM as a function of temperature in accordance with [flibe](#) equations of state (EOS) [67], whereas the solid structure thermophysical properties were held constant on the order of that of 316 stainless steel [86] - a reasonable construction material for HX tubes. The initial conditions (ICs) and boundary conditions (BCs), however, were selected more deliberately in an attempt to simulate easily predictable behavior that would provide equally decipherable plots for quick visual analysis. The shell outer wall was made adiabatic to guarantee heat

Table 3.2: Simulation parameters for RadiativeHeatTransfer-PBHeatExchanger compatibility testing.

	Geometric Properties		Thermophysical Properties		Radiative Properties		Initial and Boundary Conditions				
Fluid	ℓ [m]	A_f [cm ²]	SAM EOS		κ [m ⁻¹]	T_0 [K]	T_{in} [K]	u_{in} [$\frac{m}{s}$]			
Tube	10	78.5	Flibe		100	900	900	0.2			
Shell	10	81.7	Flibe		10	800	800	0.2			
Solid	ℓ [m]	D_i [cm]	δ [mm]	k [$\frac{W}{mK}$]	ρ [$\frac{kg}{m^3}$]	c_p [$\frac{J}{kgK}$]	ε	ρ	T_0 [K]	$BC_{w,i}$	$BC_{w,o}$
Tube	10	10	5	15	8000	500	1	0	800	coupled	coupled
Shell	10	15	5	15	8000	500	1	0	800	coupled	adiabatic

losses there were not convoluting interior heat transfer behavior. All sub-components except the inner fluid were set to an initial temperature of 526.85 °C, or the system cold temperature, to allow those components to rise sequentially (from the center outwards) towards their steady-state values.

With all parameters chosen, a simulation was run to ensure the PBHeatExchanger geometry had been built properly. If each component in the simulation behaves intuitively with respect to the others, this indicates the simulation components are correctly built and coupled. Since the purpose of this exercise is limited to demonstrating correct simulation setup, the practice of guaranteeing correct heat transfer behavior will be left to SAM verification and validation studies. Qualitatively, the anticipated “intuitive” heat transfer behavior consists of an immediate rise in tube inner wall temperature up towards the tube fluid temperature (due to the large temperature difference between the two), followed closely by the tube outer wall (due to the non-insignificant $k = 15 \text{ W}/(\text{m K})$ and small $\delta = 5 \text{ mm}$). Once the tube outer wall rises above the shell fluid temperature, the fluid temperature should rise and subsequently deposit heat into the adiabatic shell. The extent to which observable changes in the shell fluid and wall temperatures will be seen depend on the steady-state solution and time required to get there, both of which are unknown before simulation results are obtained. Figure 3.20 shows fluid outlet and maximum wall temperatures for this simulation check,

³SAM version number and git commit ID: v0.9.5.1-19-g5d5c3e68

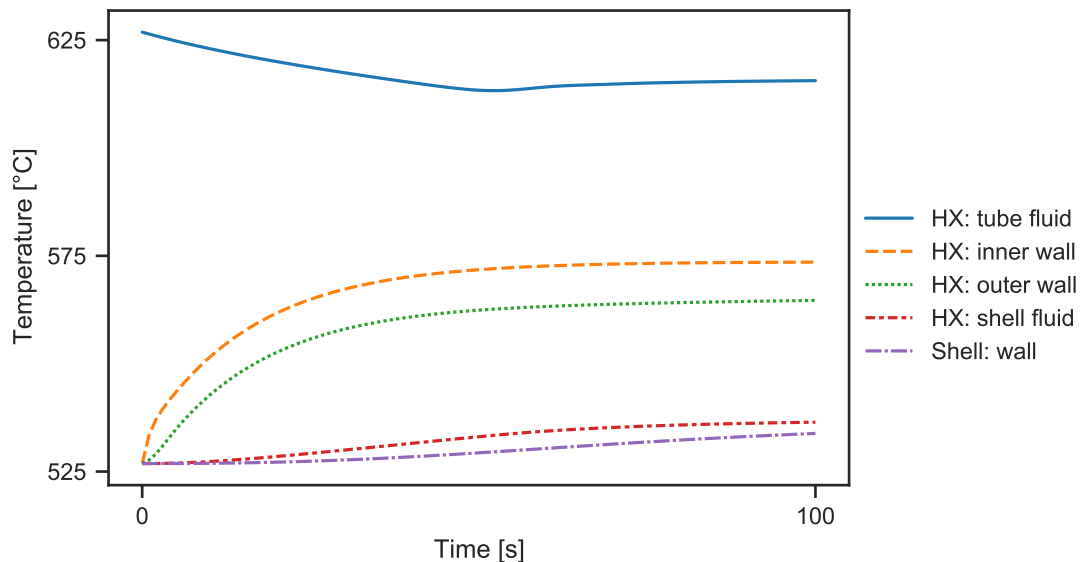


Figure 3.20: Fluid-outlet- and wall-maximum-temperatures for transient PBHeatExchanger-RadiativeHeatTransfer compatibility testing demonstrating intuitive convective behavior.³

which neglects axial behavior but captures the information necessary to give confidence in proper simulation build and component coupling. As a reminder, Fig. 3.19 shows a diagram of how the sub-components in this geometry is arranged. As one can see, the anticipated behavior is well represented in Fig. 3.20. The relatively large temperature gaps between walls and their adjacent fluids indicate a small heat transfer coefficient. This is further reinforced by the $\Delta T_f \sim 10^\circ\text{C}$ between inlet (see Tbl. 3.2) and outlet for both fluid sub-components, which amounts to only $dT_f/dx \approx 1^\circ\text{C}/\text{m}$. Regardless, the qualitative match between anticipated and demonstrated behavior instills strong confidence the simulation is properly built, and I can therefore proceed to the next step of the compatibility test plan.

Step 2, removing convective heat transfer from the simulation, went forward without any complications arising — all components stayed at their initial temperatures for the duration of the simulation. Step 3, building the RadiativeHeatTransfer geometry, requires furthering the previous discussion on optical thickness. As can be inferred from Tbl. 3.2, the radiative cavity within the tube has a $D = 10\text{ cm}$, while the annular radiative cavity between the concentric pipes has a smaller $\delta = 2\text{ cm}$. This decision was taken to increase optical thickness within the tube section — emphasizing solid-to-fluid radHT, and to decrease optical thickness within the annulus — emphasizing solid-to-solid transfer. However, beyond path length, optical thickness is further related to fluid absorption coefficient. To further emphasize these different radHT modes in each radiative cavity, the tube-side fluid was given an absorption coefficient ten times that of the shell-side fluid. While these radiative property considerations were made strictly for testing purposes, a realistic justification for this κ discrepancy could be that the primary, tube-side coolant in an FHR will inevitably end up “dirtier” than the secondary side coolant due to higher corrosion rates [29] leading to a glut of photon absorption spikes [87], potentially in a wavelength band of interest for FHR radHT simulation.

With the RadiativeHeatTransfer geometries built, simulation behavior could be observed, completing step 3 of the testing plan. As a slight diversion, I should mention some flaws in my execution of this step. To break down the reintroduction of heat transfer and avoid the two modes of radHT convoluting simulation results, I tried to nullify the annular RadiativeHeatTransfer component by artificially setting $\kappa = 0$ and $F_{io} = 0$, which did not work. For quite some time, I did not realize the RadiativeHeatTransfer code I had written gave no option to overwrite code-calculated view factors for preset radiative enclosures, such as the “Annulus” enclosure option I employed for this particular geometry. Upon finding the source of my mistake, I revisited the RadiativeHeatTransfer source code to write in additional input checks to warn the user in the case their view factor values were being overwritten.

Turning my attention to the results of step 3, I noticed a glaring issue which can be observed in Fig. 3.21: the PBHeatExchanger fluid was losing energy, but the PBHeatExchanger solid structure was staying put at its initial value of $T_0 = 526.85^\circ\text{C}$. Furthermore, experimentation revealed altering the solid temperature affected the rate and direction (positive or negative) of fluid heat transfer. This experimentation indicated the PBHeatExchanger sub-components

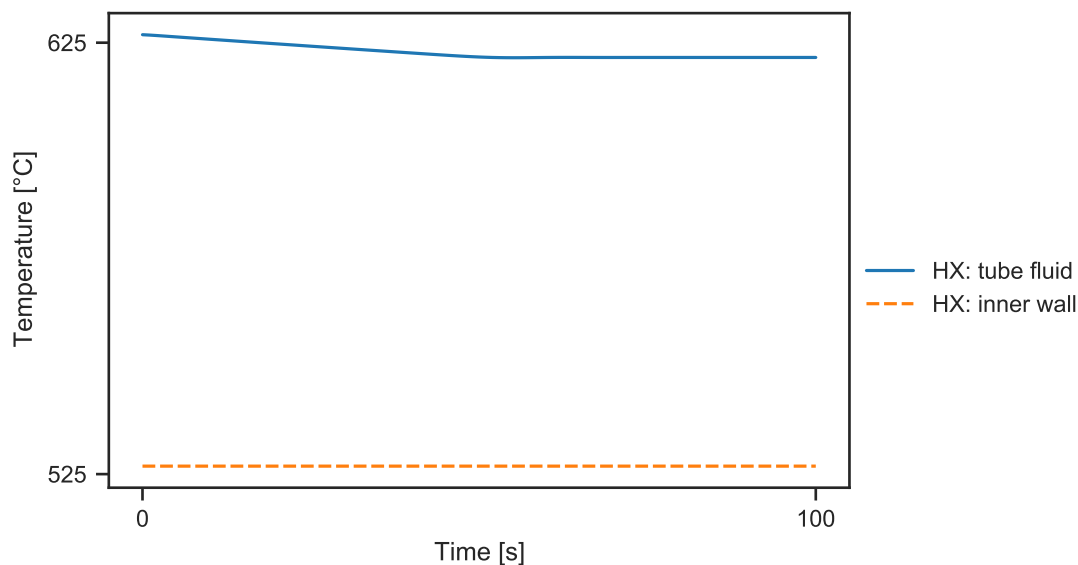


Figure 3.21: Fluid-outlet- and wall-maximum-temperatures for transient PBHeatExchanger-RadiativeHeatTransfer compatibility testing demonstrating incorrect radiative behavior.³

were coupled by the simulation in some manner, but the solid wall was not being passed the necessary information to calculate a heat flux. Somewhere in the code between the RadiativeHeatTransfer component and its RadHTFluidConstraint (the bit that calculates radiative heat flux for solid-to-fluid radHT configurations), the line of information was being severed. Suddenly [steps 4](#) and [5](#), initially meant as checks for the simulation, would instead serve as debugging steps to isolate where information was being lost.

As previously mentioned, I did not suspect sub-component coupling to be the issue. Nevertheless, I progressed with [step 4](#) of the plan. To debug the sub-components being used, I added lines in RadiativeHeatTransfer to output the names of all surfaces being utilized in simulation. If these strings were incorrect, code pointers being used to grab sub-component information would instead point to nothing, which would explain the SAM component compatibility error. However, after seeing the code output the surface name correctly as “HX:solid:inner_wall”, I proved my suspicions correct — surface coupling was not the issue. The final debugging step would have to yield the problem.

[Step 5](#) was conducted the same way as was [step 4](#) — adding debug lines to output suspicious variable values. [Table 3.3](#) shows how the bug was tracked down from the end of the line, the heat flux being applied to the wall by RadHTFluidConstraint, to its source, a missing line in PBHeatExchanger. In short, PBHeatExchanger must create its wall sub-component using the PBCoupledHeatStructure SAM component, which requires sending this component

Table 3.3: Locating the code bug causing PBHeatExchanger-RadiativeHeatTransfer coupling error (sorted by investigation order).

Code Location	Variable (incl. pseudocode)	Issue Description
RadHTFluidConstraint	$q''_w = f(RZ)$	Inner wall heat flux equals 0. 0-value tracked down to RZ , cylindrical-coordinates-multiplier
RadiativeHeatTransfer	$RZ = 2\pi r$	Radius equals 0
	$r = \begin{cases} r_i & , \text{ inner wall} \\ r_i + \delta & , \text{ else} \end{cases}$	Inner wall radius equals 0, and outer wall radius equals wall width
	$r_i \rightarrow \text{getInnerRadius}()$	Function returning 0 from PBHeatExchanger walls
PBHeatExchanger	$\text{wall} \rightarrow \text{getInnerRadius}()$	Function not returning PBHeatExchanger r_i values
	$r_{i,wall}$	PBHeatExchanger creating wall without setting r_i value

all pertinent information, such as heat structure geometric properties. When packaging up all these variables, the heat structure inner radius was being neglected entirely. This is exactly where the line of information was being severed between the code user specifying a PBHeatExchanger surface for radHT and the code calculating a q''_{rad} for that surface. The effects of this bug were propagating all the way back to RadHTFluidConstraint. Upon packaging up r_i with the other pertinent geometric parameters, the fix propagated back as well. The stagnant behavior demonstrated by the solid wall in Fig. 3.21 disappeared. Instead, the solid sub-component continued to rise in temperature throughout the simulation as expected. With this bug fix, steps 3 to 5 were satisfied and considered complete.

Figure 3.22 demonstrates behavior that gives confidence this simulation calculates radiative heat transfer in the expected fashion — the tube fluid transfers heat to the inner wall and the outer wall distributes that heat to the shell wall and shell fluid. The shell wall temperature rises above that of the shell fluid because the shell fluid is optically thin ($\sim \kappa\delta = 0.2$). However, to guarantee simulation parity with previously-verified SAM components, a benchmark study had to be performed.

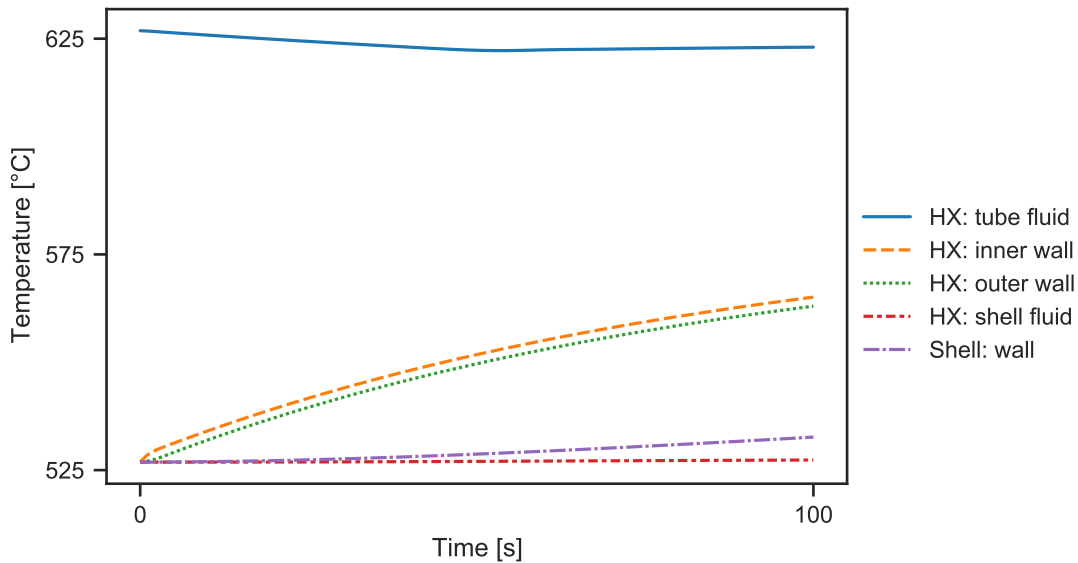


Figure 3.22: Fluid-outlet- and wall-maximum-temperatures for transient PBHeatExchanger-RadiativeHeatTransfer compatibility testing demonstrating properly-coupled radiative heat transfer.⁴

PBHeatExchanger compatibility verification testing

The final step to satisfying the testing plan on Pg. 134 consisted of verifying the radiative heat transfer solution being calculated by the code. The bug in PBHeatExchanger was easily noticeable because a value of zero was being calculated when it should have been nonzero. Now that the code was producing a nonzero solution, I wanted to make sure that solution was correct. Thanks to previous RadiativeHeatTransfer verification studies [85], I already have several SAM components verified to work with RadiativeHeatTransfer — namely PBOneDFluidComponent and PBCoupledHeatStructure. Instead of re-performing analysis similar to that found in Sec. 3.3, I decided to recreate the PBHeatExchanger test geometry with these lower-level verified components and compare both simulation solutions against each other. If the PBHeatExchanger solution matched that of the basic components simulation, I would consider the test plan complete and PBHeatExchanger compatible with RadiativeHeatTransfer.

To quantify solution differences, I computed the percent relative difference between the two temperature solutions using the basic components simulation as the reference:

$$\% \Delta(T) = \frac{T_{HX} - T_{basic}}{T_{basic}} \times 100 \% \quad . \quad (3.47)$$

⁴SAM version number and git commit ID: v0.9.5.1-20-g1babf375

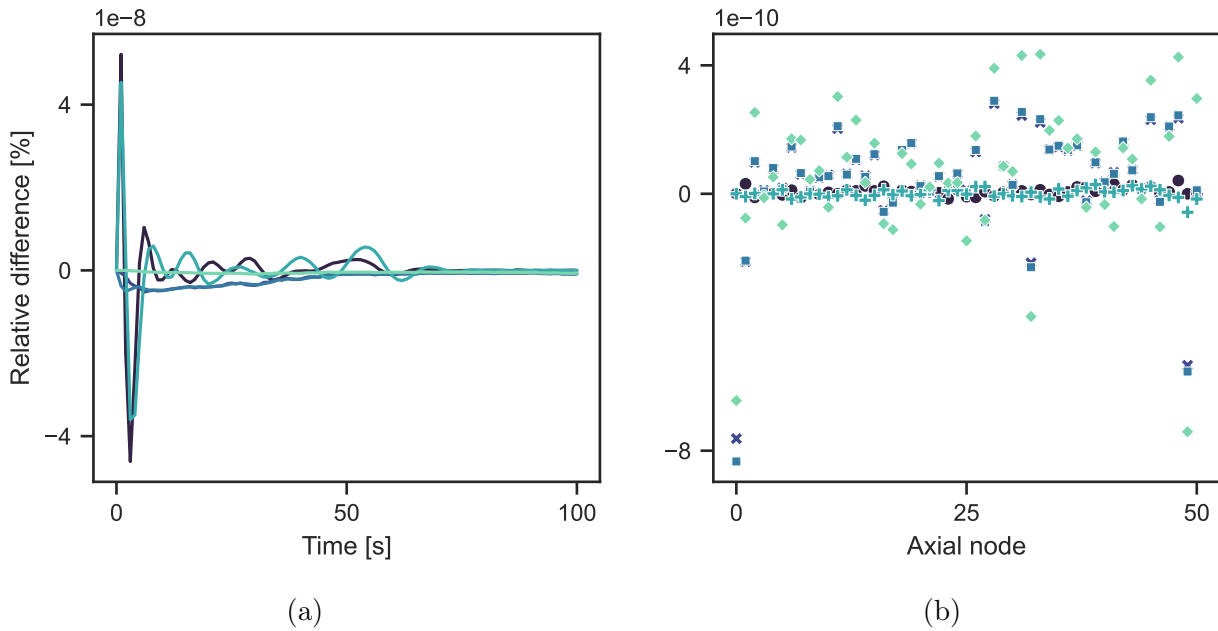


Figure 3.23: Temperature solution differences for PBHeatExchanger-RadiativeHeatTransfer compatibility testing compared to basic SAM components simulation. Fluid-outlet and wall-maximum (a) transient differences and node-by-node (b) axial differences at $t = 100$ s demonstrating identical radiative behavior.⁵

A maximum solution difference of $\% \Delta(T) \sim \mathcal{O}(-8)$, as seen in Fig. 3.23a, can be found during the first few time-steps of simulation. Discerning values for specific simulation sub-components is irrelevant, which motivates the lack of legend and line markers in these plots. These values are reassuring but do not tell the full story, as these simulation-to-simulation transient comparisons are performed with fluid outlet temperatures and surface-maximum temperatures. A more complete analysis entails the inclusion of a node-to-node comparison between simulations, which is displayed in Fig. 3.23b. The comparison is taken after two fluid residence times. If there are discrepancies between simulations resulting from erroneous component coupling, this amount of time would allow errors to compound and affect solution results in an obvious manner. Here, a maximum $\% \Delta(T_n) \sim \mathcal{O}(-9)$ almost certainly guarantees the solution difference can be chalked up to convergence error. To make sure, one could compare the solution difference to the convergence criterion specified in the simulation input file. The relative and absolute tolerances for each Newton solve are set at 10^{-7} and 10^{-6} , respectively. Although $\% \Delta(T)$ expresses a difference between separate solutions, the results shown in Fig. 3.23 are several orders within the allowable convergence cutoff (accounting

⁵SAM version number and git commit ID: v0.9.5.1-21-g45eabbe6

for $\% \Delta(T)$ being expressed as a percentage). This means for my purposes, the simulation solutions match, and the PBHeatExchanger SAM component is deemed compatible with RadiativeHeatTransfer.

PBCoreChannel compatibility

Following the success of the PBHeatExchanger-RadiativeHeatTransfer compatibility effort, I could turn my attention to the last remaining non-compatible heat transfer component of interest as identified at the beginning of this section — PBCoreChannel. I will keep the ensuing discussion short to avoid replicating discussion from the PBHeatExchanger compatibility process, which is the focus of this section.

Component compatibility with RadiativeHeatTransfer is characterized by being able to produce correct heat transfer between various solid structure surfaces and fluid sub-components. Therefore, there is no need to procure a PBCoreChannel simulation which simulates nuclear heat generation, despite that being the intended purpose of this component. To streamline

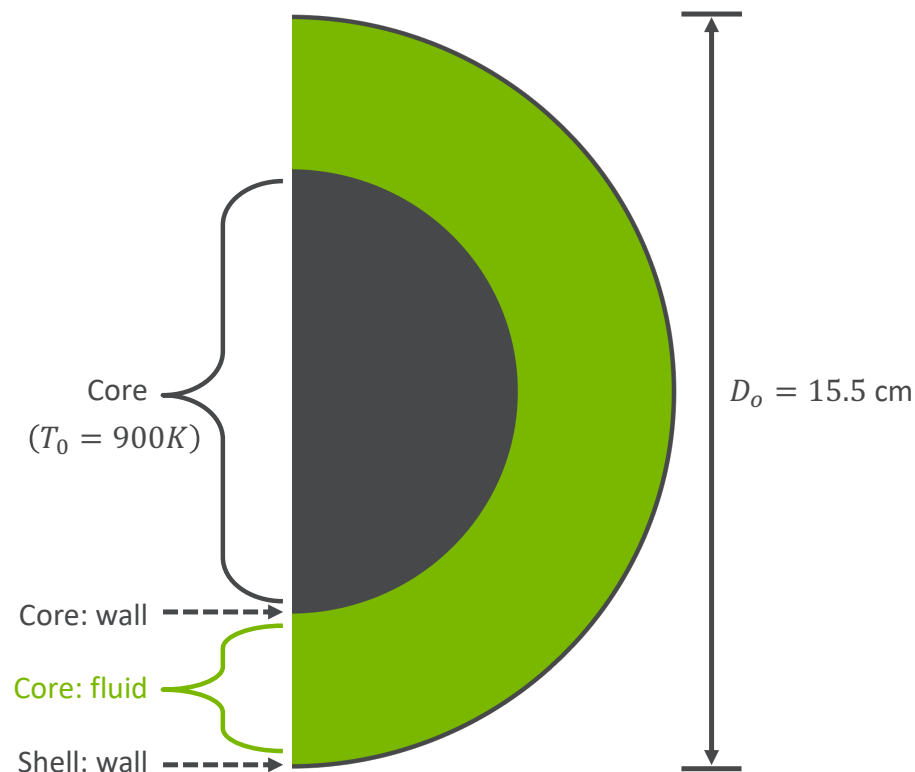


Figure 3.24: Axial cutaway view of RadiativeHeatTransfer-PBCoreChannel compatibility testing geometry (not drawn to scale).

the process of guaranteeing PBCoreChannel-RadiativeHeatTransfer compatibility, the test plan on Pg. 134 was repurposed for PBCoreChannel. As for test geometry, changes had to be made due to PBCoreChannel being constructed from one fewer fluid sub-component and a heat structure with one fewer wall compared to PBHeatExchanger. Referencing Fig. 3.24, the annular *shell-side* geometry from PBHeatExchanger testing (Fig. 3.19) was exactly replicated, with the tube and tube-side fluid replaced by a single, solid-filled cylinder. This cylinder and the adjacent fluid constitute the PBCoreChannel component, while the shell was, again, constructed with a PBCoupledHeatStructure. The simulation parameters in Tbl. 3.2 applicable to the shell-side annulus were retained. However, to include a source of heat, the core cylinder was given an IC of $T_0 = 900$ K, 100°C above the fluid and shell.

Upon completing test plan steps 1 to 6, this time for PBCoreChannel, a solution comparison can be made with an identical simulation constructed with basic SAM components. Figure 3.25 shows results strikingly similar in magnitude to those in Fig. 3.23, lending assurance PBCoreChannel is equally compatible with RadiativeHeatTransfer. In Fig. 3.25a, there is only a single line with a magnitude relatively large enough to provide discernible features. While discerning between sub-components here is irrelevant, explaining this be-

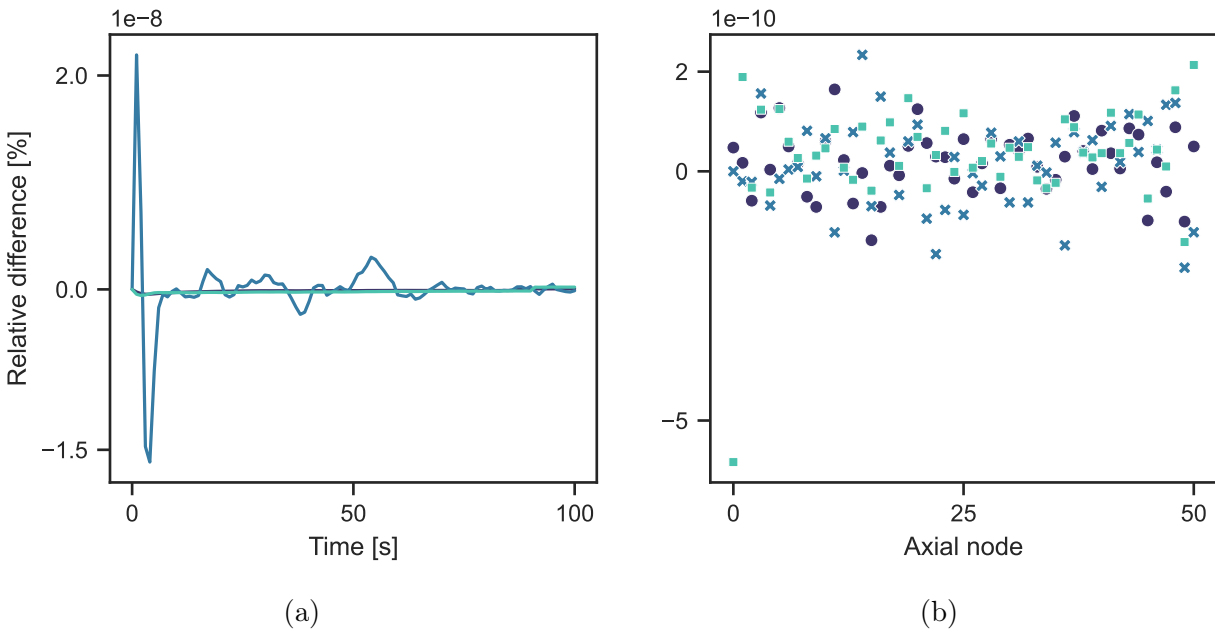


Figure 3.25: Temperature solution differences for PBCoreChannel-RadiativeHeatTransfer compatibility testing compared to basic SAM components simulation. Fluid-outlet and wall-maximum (a) transient differences and node-by-node (b) axial differences at $t = 100$ s demonstrating identical radiative behavior.⁵

havior benefits from acknowledging this line displays $\% \Delta(T_f)$. This outstanding behavior can be attributed to the simulation scaling factors, which supplement the simulation convergence criteria by serving as a factor to the observed residuals in the eyes of the numerical solver. For all simulations in this section, the fluid temperature scaling factor was set to 10^{-6} , effectively inflating the solver tolerance criterion for all fluid temperatures by 10^6 . The solid structure temperature solution, whose solution difference percent values in Fig. 3.25a (expressed by the seemingly-flat line at 0.0%) are of $\mathcal{O}(-10)$, receives no such treatment. The different scaling factors come as a result of precedence — those more experienced with SAM have found simulations typically run smoother when the fluid temperature convergence criteria is more relaxed than that of solid structures.

The sheer magnitude of all $\% \Delta(T)$ found for both PBHeatExchanger and PBCoreChannel when modeling radHT suggests the only differences between these simulations and their basic-components counterparts is the convergence error. Due to previous success carrying out verification exercises with the basic SAM components used for comparison — PBOneDFluidComponent and PBCoupledHeatStructure, and the successful benchmark study performed here against those verified components, both PBHeatExchanger and PBCoreChannel may now be considered verified-compatible with RadiativeHeatTransfer.

Modeling radHT in SAM is now possible for those users who desire building their simulation from more specialized components. Furthermore, the testing plan laid out on on Pg. 134 was successful in enabling inter-component compatibility and clarifying the process necessary to reach that goal. For others attempting similar tasks, following the process I described in this section could prove helpful.

3.2.5 Restructuring the RadiativeHeatTransfer code framework with a userObject to enable postProcessor development

It is highly likely those simulating radHT in SAM will want to know radiative heat transfer rates for surfaces and participating fluids in their systems — information useful for performing energy balances or even informing design decision. However, with the component-constraints code framework shown in Fig. 3.4, there was no method for the code to output radHT rates. These values *could* be produced by what are called postProcessors in SAM [88] — pieces of code that generate and output user-desired simulation behavior — but none of them were designed to produce radiative heat transfer rates. If I wanted RadiativeHeatTransfer to be able to output heat transfer rates, I needed to develop a postProcessor specifically for that task. However, if RadiativeHeatTransfer directly produced postProcessors in the same fashion it produces constraints (see Fig. 3.4), this would introduce a redundancy in how component information is managed. This section will discuss the code framework change made to avoid this redundancy and enable postProcessor development — namely, the introduction of a RadiativeHeatTransfer userObject.

The aforementioned information management redundancy is directly related to what the component used to do immediately prior to generating constraints: calculate, package up, and assign Rad++ coefficients in a form accessible by these constraints. This task was previously alluded to in the context of the original code-structure discussion about simultaneously gathering and assigning information from three bodies with three constraints (see Pg. 110). The issue of redundancy arises from the fact that those constants must be available to postProcessors as well, meaning the component would have to manually add every necessary constant to each parameter set for every constraint and postProcessor — an inefficient method of managing information. Instead of convoluting information logistics within the component, the responsibility of managing and assigning these constants should rest outside the component entirely. The ideal manager for this task is called a userObject. Under this framework, all constraints and postProcessors will obtain their coefficients from the userObject directly, and the code for requesting these coefficients can be called as many times as necessary.

A userObject can be envisioned as a collection of functions, which can be made to perform a wide range of tasks. In this case, the RadiativeHeatTransfer userObject will include functions for assigning Rad++ coefficients, which will then be made available to RadiativeHeatTransfer constraints and postProcessors. The code framework to accommodate the userObject can be seen in Fig. 3.26. Every RadiativeHeatTransfer component created by the code user now creates a userObject before creating its constraints and postProcessors. By simply letting these constraints and postProcessors know how to find their associated userObject, the component passes all coefficient logistics off to the new piece of code.

A RadiativeHeatTransfer userObject was built in accordance with the discussion in this section and was implemented into SAM⁶. The userObject picks up from the component by importing radiative parameters from Eqs. (3.6) and (3.7) already grouped into the matrix variables \mathbf{B} , \mathbf{C} , and \mathbf{D} from Eq. (3.10) and the surface area-to-volume ratios from Eq. (3.11). The userObject then performs the \mathbf{B} -matrix inversion and matrix multiplication necessary to generate the final radHT constants required by Fig. 3.26’s solid-to-fluid (s2f) and solid-to-solid (s2s) constraints — $\mathbf{B}^{-1}\mathbf{C}$ and $\mathbf{B}^{-1}\mathbf{D}$.

While the responsibility of requesting sets of pertinent constants is left to individual constraints and postProcessors, the userObject goes so far as to sort generated constants into ready-to-be-requested sets. This way, the calculations and sorting of variables conducted by the userObject are generalizable to all modeling scenarios and can therefore be performed the same way every time regardless of how many constraints or postProcessors are created by RadiativeHeatTransfer.

Reformatting the production and distribution of radiative parameter constants into a framework controlled by a userObject enables multiple requests for the same information while

⁶SAM version number and git commit ID: v0.9.5.1-373-g37a71a1bd

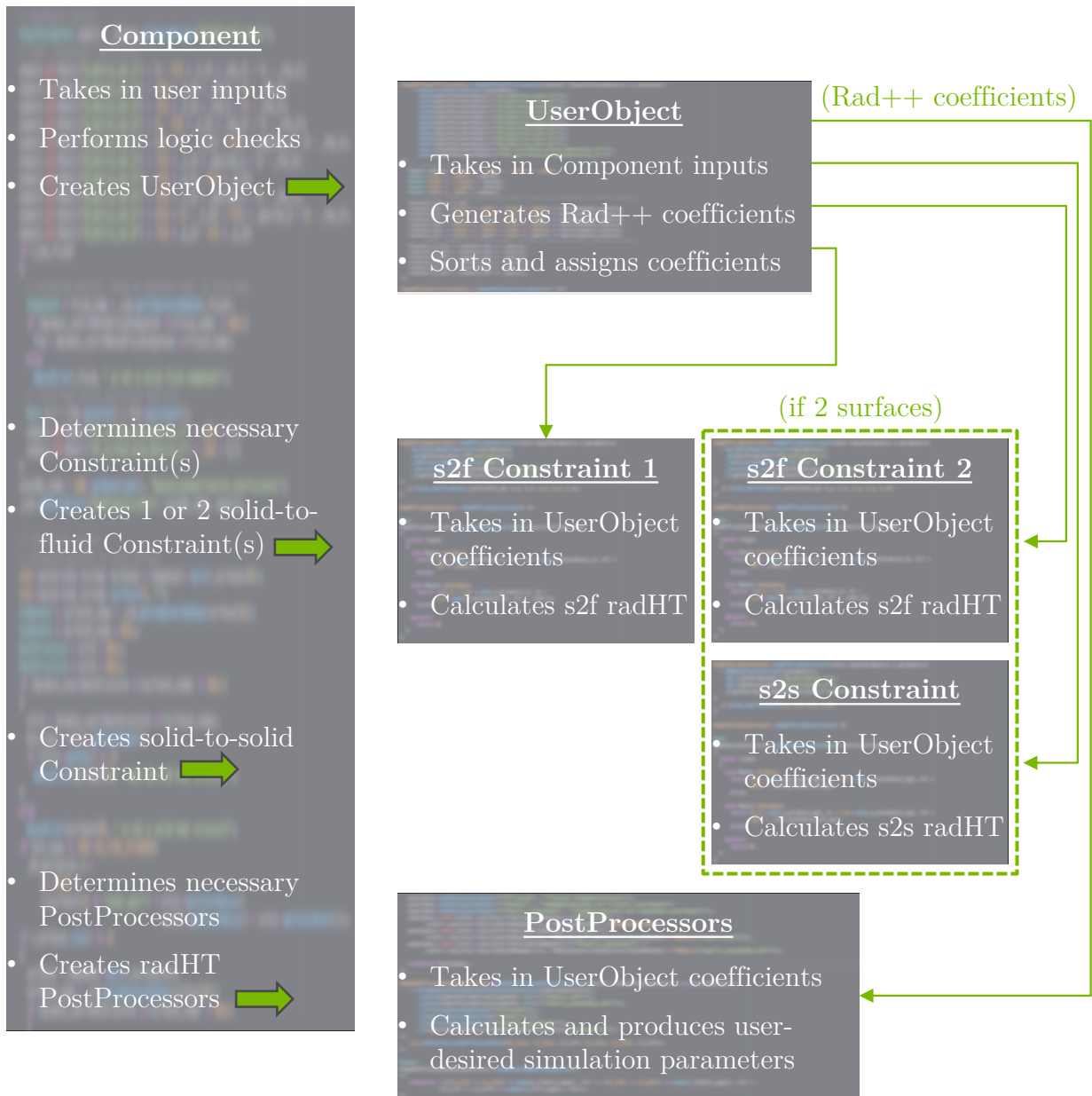


Figure 3.26: RadiativeHeatTransfer code framework utilizing a userObject for Rad++ coefficient management and information logistics. This code framework superseded the one shown in Fig. 3.4.

avoiding in-code redundancies. Specifically, this new framework permits the incorporation of postProcessors for RadiativeHeatTransfer, a vital tool for SAM code users simulating radHT while conducting sensitivity analysis or performing reactor safety analysis.

3.2.6 Developing heat transfer rate postProcessors for RadiativeHeatTransfer

The previous section discussed the code framework development work that enabled the expansion of RadiativeHeatTransfer capabilities — specifically, the use of a userObject to enable postProcessors. This section will discuss the development of the now-enabled postProcessors for RadiativeHeatTransfer.

To reiterate the purpose of these postProcessors, RadiativeHeatTransfer code user will want to know heat transfer rates for radiating bodies in their systems. In equation form, the radHT rate for each surface k is represented by Eq. (3.48), while the radHT rate for a participating fluid is represented by Eq. (3.49).

$$\dot{Q}_{rad,k} = \int q_k'' dA_k \quad (3.48)$$

$$\dot{Q}_{rad,f} = \int q_f''' dV_f \quad (3.49)$$

The information provided by these equations could be useful for anything from checking simple energy balances to informing design decisions.

Dependence of \dot{Q} postProcessor on SAM's convective coupling

There were, of course, obstacles to implementing Eqs. (3.48) and (3.49) in SAM. Previously, q_k'' and q_f''' values were only calculated in parts by constraints, as shown by Eq. (3.13) in conjunction with Fig. 3.3. Complete heat flux calculations for radiating bodies were only superficially consolidated as an effect of the SAM radHT component applying all pertinent constraints for all existing nodes in that simulation. This node-specific, partial heat flux information was then applied to its node, and subsequently abandoned without saving. To properly calculate Eqs. (3.48) and (3.49), the \dot{Q} postProcessor needed to somehow be able to associate nodal q_k'' and q_f''' calculations with their respective radiating bodies before summing them all together (integrating) to arrive at a total \dot{Q} . However, there did not yet exist any identifying information that could have been used to sort and accumulate the myriad constraint calculations into meaningful heat transfer rates.

To make matters worse, the inner workings of component integral postProcessors in SAM, upon which I needed to rely on to perform the integrals in Eqs. (3.48) and (3.49), only knows how to obtain information from a single body. I have described a similar issue before — Eq. (3.13) is a function of three temperatures, and constraints can only access two temperatures at a time, which is bad enough. This component integral postProcessor can only access one.

The two issues impeding \dot{Q} postProcessor development are summarized below. Solutions needed to be found to bypass both.

- Issue 1. Restriction limiting \dot{Q} postProcessor to accessing information from a single body
- Issue 2. Lack of identifying information available to associate calculations with the radiating bodies they describe

The solution for [issue 1](#) came from making use of a relatively obscure byproduct of convective coupling in SAM, which results in surface temperatures being briefly stored together with fluid temperatures. Because all these surface temperatures are stored in one location, under the auspices of the fluid body, \dot{Q} postProcessors would be able to access all necessary fluid and surface temperatures for Rad++ calculation. It should be noted that this information access method requires the RadiativeHeatTransfer surfaces to be coupled to a RadiativeHeatTransfer participating fluid. This means the \dot{Q} postProcessor was henceforth restricted to operating in RadiativeHeatTransfer enclosures in which there is a participating fluid, and that fluid is convectively coupled to the radiating surface(s). However, this convective coupling byproduct provided the only means by which multiple bodies' temperatures could be accessed from a single source, so I made the decision to proceed despite the dependence on convective coupling. Unfortunately, even with [issue 1](#) solved, [issue 2](#) still remained.

To explain how I addressed [issue 2](#), I need to describe in more detail how the coupled surface temperature information is stored. When a SAM simulation creates a fluid body, SAM effectively creates a matrix for node-by-node temperatures of the fluid. I have created a

Table 3.4: Visual representation of fluid-based temperature information matrix produced by convective coupling in SAM, and used for \dot{Q} postProcessor calculation. All these coupled-surface nodal temperatures can be accessed from one location — the fluid body.

Node #	Fluid	Surface ID (WH_ID)			
		0	1	...	k
0	$T_{f,0}$	$T_{0,0}$	$T_{1,0}$		$T_{k,0}$
1	$T_{f,1}$	$T_{0,1}$	$T_{1,1}$		$T_{k,1}$
⋮	⋮	⋮	⋮		⋮
N	$T_{f,N}$	$T_{0,N}$	$T_{1,N}$		$T_{k,N}$

visual demonstration of that matrix in [Tbl. 3.4](#). When SAM couples surfaces to that fluid body via convection, SAM increments a Surface ID variable called `WH_ID` and adds those surfaces to the matrix in the column number equal to `WH_ID`. At every timestep in the simulation, all fluid and coupled surface temperatures in [Tbl. 3.4](#) are updated to reflect their nodal temperature profiles at that timestep. However, while the fluid body knows in which column to copy down each surface’s temperatures, there was no information available to otherwise keep track of which surface was associated with which `WH_ID`. This meant that before my \dot{Q} postProcessor development work, it was impossible for `RadiativeHeatTransfer` to know which column was storing temperature information for a given radiating surface.

The previous paragraph is essentially a restatement of [issue 2](#) in the context of my solution to [issue 1](#). However, I provide that description to support my plan of action: to utilize the information stored in [Tbl. 3.4](#), I needed to develop a method for SAM to keep track of which surface was associated with which `WH_ID`. The method I implemented utilized a C++ “map”, which is similar to a two-column matrix. However, unlike a matrix, one column is designated as “map keys” while the other is designated as “mapped values”. Provide the map with any key, and the map will return the associated mapped value. I built a map and mapping functions into SAM’s fluid component, `PBOneDFluidComponent`. I then tracked down all instances in which any SAM component would convectively couple a surface to a `PBOneDFluidComponent` and wrote in my mapping functions to map the surface name as the key and the `WH_ID` as the mapped value. Now, anytime anyone wants to access coupled surface temperatures, they need only provide the `PBOneDFluidComponent` map with the coupled surface name, and the `WH_ID` will be returned. This is exactly what I implemented into the \dot{Q} postProcessor, solving [issue 2](#).

Implementation of the \dot{Q} postProcessors

After solving both [issues 1](#) and [2](#), I could proceed with developing the \dot{Q} postProcessor, which I named `RadHTHeatRemovalRate`. I designed `RadiativeHeatTransfer` to grab the participating fluid’s nodal temperatures, call on that fluid’s mapping functions to access all pertinent surface temperature information, grab `Rad++` coefficients from the `radHT` component’s associated `userObject`, and then create a postProcessor for every radiating body requested by the user. Then, at every timestep, each `RadHTHeatRemovalRate` performs its \dot{Q} calculation and outputs the amount of heat radiatively emitted from the body for each timestep. However, due to `RadHTHeatRemovalRate`’s dependence on convective coupling to the fluid body, and due to the inner workings of how component integral postProcessors work in SAM, the \dot{Q} calculations actually performed differ from their integral forms (previously shown by [Eqs. \(3.48\)](#) and [\(3.49\)](#)).

Knowing n means fluid node n of N total nodes and $\sum_{n=0}^N L_n = L_f$, the calculations conducted by `RadHTHeatRemovalRate` are shown by [Eqs. \(3.50\)](#) and [\(3.51\)](#). The surface area A_k is the user-input `RadiativeHeatTransfer` area for surface k , and L_f is specified by the

user when creating the fluid body, whether as a standalone `PBOneDFluidComponent` or as a sub-component of a SAM component.

$$\dot{Q}_{rad,k} = \sum_{n=0}^N q_k'' \left(\frac{A_k}{L_f} \right) L_n \quad (3.50)$$

$$\dot{Q}_{rad,f} = \sum_{n=0}^N \sum_k -q_k'' \left(\frac{A_k}{L_f} \right) L_n \quad (3.51)$$

The `PBOneDFluidComponent` mapping functions, which enable `RadHTHeatRemovalRate` to function, were hard-coded into all pertinent SAM components. Subsequently, these components are fully compatible with `RadHTHeatRemovalRate`, and therefore fully compatible with `RadiativeHeatTransfer` (because of the work performed in [Sec. 3.2.4](#)):

- `PBOneDFluidComponent`
- `PBCoupledHeatStructure`
- `PBPipe`
- `PBHeatExchanger`
- `PBCoreChannel`
- `PBDuctedCoreChannel`
- `ReactorCore`
- `HeatPipe`

Verification of `RadHTHeatRemovalRate`

To test the post-processing capabilities of `RadHTHeatRemovalRate`, I designed a test case for which I could easily calculate analytical radiative heat transfer values. I then used these analytical values to verify \dot{Q} outputs. The test geometry I decided on is shown in [Fig. 3.27](#), with an annular radiative enclosure consisting of a participating fluid (built with a `PBOneDFluidComponent`) situated between an inner cylinder and an outer shell (built with `PBCoupledHeatStructures`). Convective heat transfer is switched off. The inner cylindrical solid structure, which includes surface 1, produces heat homogeneously throughout its volume. The outer shell, which bounds the radiative enclosure, is subject to a constant heat flux on its outer surface (surface 2).

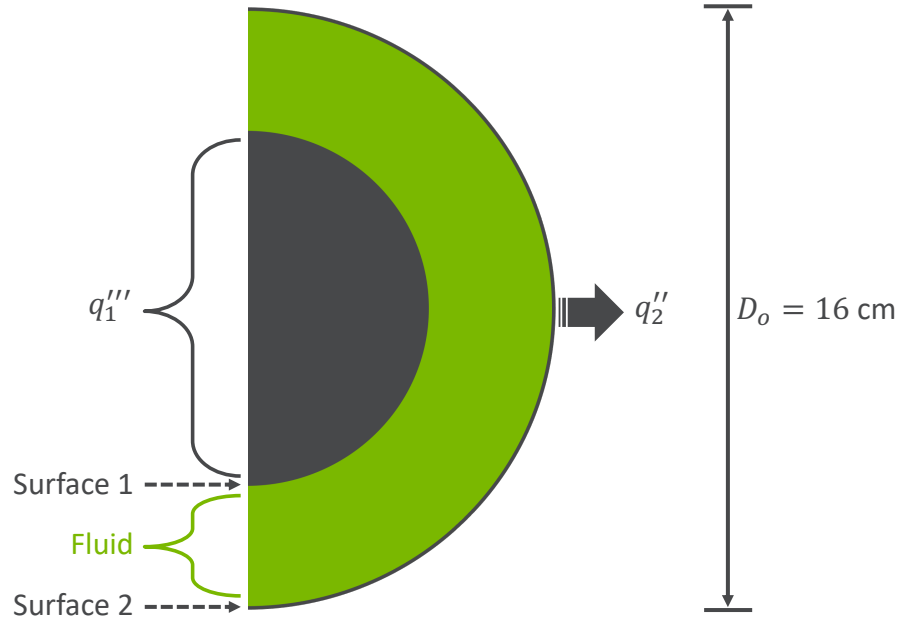


Figure 3.27: Axial cutaway of RadHTHeatRemovalRate verification test geometry (not to scale). Surface 1 bounds a region of volumetric heat generation q_1''' , while a constant heat flux q_2'' removes heat from Surface 2.

At steady-state, the q_1''' and q_2'' boundary conditions induce two analytically reproducible heat transfer rates: (1) surface 1 will emit radiation at a rate equal to the volumetric heat generation of the inner cylinder multiplied by its volume and (2) the inner surface of the shell will absorb radiation at a rate equal in magnitude to the heat flux on surface 2. Using Eq. (3.51), a third analytical solution can be produced for the fluid — (3) the rate of fluid emission should be equal in magnitude, but opposite in sign, to the total sum of surface emission. Mathematically, these three analytical conditions can be written as

$$\dot{Q}_1 = \left(\ell \frac{\pi D_{o,1}^2}{4} \right) q_1''' \quad , \quad (3.52)$$

$$\dot{Q}_2 = (\ell \pi D_{o,2}) q_2'' \quad , \quad (3.53)$$

$$\text{and } \dot{Q}_f = -\ell \pi \left(\frac{D_{o,1}^2}{4} q_1''' + D_{o,2} q_2'' \right) \quad . \quad (3.54)$$

To quantify RadHTHeatRemovalRate postProcessor performance, I compared simulated postProcessor values to the analytical conditions listed above. For each of these verifica-

tion conditions, I found the percent relative difference between the analytically produced \dot{Q}_{anal} and that produced by the postProcessor, using the analytical value as the reference:

$$\% \Delta \left(\dot{Q}_{postP} \right) = \left| \frac{\dot{Q}_{anal} - \dot{Q}_{postP}}{\dot{Q}_{anal}} \right| \times 100 \% \quad . \quad (3.55)$$

Table 3.5 shows all geometric properties and boundary conditions of the conducted simulation necessary to calculate the analytical condition values for this verification test. Initial temperatures and thermophysical properties are omitted because, regardless, the solid structures will eventually converge upon the steady-state temperatures necessary to induce the analytical heat transfer solutions. To reach steady-state, I simulated out to 1000 s to smooth out any spacial temperature discrepancies and then used a steady-state solver using the transient solution at 1000 s as its input. Before calculating $\% \Delta \left(\dot{Q}_{postP} \right)$ s, I wanted to conduct an energy balance to make sure the developed postProcessor did not have any major bugs. RadHTHeatRemovalRate calculates component-wide heat transfer in units of power, meaning RadHTHeatRemovalRate values for both surfaces and the participating fluid should sum to 0 W, or

$$\dot{Q}_{\Sigma} = \dot{Q}_1 + \dot{Q}_2 + \dot{Q}_f = 0 \text{ W} \quad . \quad (3.56)$$

Table 3.5: RadHTHeatRemovalRate postProcessor testing simulation parameters and verification test results.⁶

	Geometric Properties		Boundary Conditions		Verification Conditions and PostProcessor Accuracy	
Surface	ℓ [m]	D_o [cm]	q''' [$\frac{\text{W}}{\text{m}^3}$]	q'' [$\frac{\text{W}}{\text{m}^2}$]	\dot{Q}_{anal} [W]	$\% \Delta \left(\dot{Q}_{postP} \right)$
1	10	5.5	10522.64		1000	7×10^{-3}
2	10	16		-159.1549	-800	8×10^{-3}
Fluid	ℓ [m]	A_f [cm^2]	T_{in} [K]	u_{in} [$\frac{\text{m}}{\text{s}}$]	\dot{Q}_{anal} [W]	$\% \Delta \left(\dot{Q}_{postP} \right)$
	10	81.7	800	0.2	-200	7×10^{-2}

Since all \dot{Q} calculations utilize the same temperature values, I want this energy balance test to produce a deviation from 0 W comparable to the rounding error in SAM. I do not know what that value is, but I do know SAM sets the FEM convergence at some threshold called the fluid temperature scaling factor. For this simulation, that factor was set to 10^{-6} , so I would have been satisfied with this energy balance test if the postProcessor-produced \dot{Q}_Σ deviated from the analytical \dot{Q}_Σ by less than 10^{-6} W. When performing an energy balance 1000 s into the simulation and at steady-state, $\Delta(\dot{Q}_{postP})_\Sigma \ll \mathcal{O}(-6)$ W for both cases. Results are summarized below.

$$\Delta(\dot{Q}_{postP})_\Sigma = |\dot{Q}_{anal} - \dot{Q}_{postP}| = \begin{cases} 4 \times 10^{-11} \text{ W} & , t = 1000 \text{ s} \\ 3 \times 10^{-11} \text{ W} & , \text{ steady-state} \end{cases} \quad (3.57)$$

Convinced RadHTHeatRemovalRate did not have any major bugs, I proceeded with determining postProcessor accuracy. The final column in [Tbl. 3.5](#) shows quantified postProcessor performance. To be satisfied with RadHTHeatRemovalRate, I was looking for a relative difference on the order of 10^{-1} % or smaller. All RadHTHeatRemovalRate postProcessors achieved values of $\% \Delta(\dot{Q}_{postP}) \sim \mathcal{O}(-2)$ or better, which means the postProcessor error is at least four orders of magnitude smaller than the heat transfer rate. These relative difference values demonstrate good performance and are sufficiently small to verify RadHTHeatRemovalRate indeed works as intended.

3.3 RadiativeHeatTransfer Verification Studies

Verification analysis is the process of ensuring correct code functionality and proves the code performs its duties as designed, error free [89]. Typically, this analysis includes code-to-code comparisons or comparisons to analytical solutions. Code verification should not be confused with code validation, in which solutions are compared against experimental data for the purpose of proving the code properly simulates real physics. Verification analysis for RadiativeHeatTransfer can demonstrate the component has been properly developed and implemented in SAM and is properly calculating radHT according to the Rad++ expression of the net radiation method. While I have utilized small, confined verification tests for each code development task from [Secs. 3.2.3](#) to [3.2.6](#) to guarantee proper implementation, this section demonstrates verification cases for the underlying RadiativeHeatTransfer code framework.

To satisfy the verifiability of RadiativeHeatTransfer, I carried out a series of test cases to investigate the effectiveness of SAM's new simulation capabilities to transfer energy via thermal radiation. Verification results demonstrate successful implementation of RadiativeHeatTransfer, meaning all desired modeling scenarios (originally shown in [Tbl. 3.1](#)) can be correctly simulated, which include the unprecedented capability of solid-to-fluid radHT modeling.

Initial conditions and thermophysical properties are included to facilitate reproducibility. For instance, all tests were conducted with a heat transfer coefficient of zero, which means no convective heat transfer — only radHT between participating bodies and conduction within heat structures. However, the conditions imposed upon these tests generate results that are numerically unimportant (beyond comparisons to analytical results). Rather, these imposed conditions elicit behavior qualitatively relevant to the demonstration of SAM's radHT capabilities. SAM RadiativeHeatTransfer users may utilize a large variety of initial conditions and physical properties to reproduce the behavior pertinent to this analysis.

Concentric pipes energy balance testing for solid-to-solid constraint

In this test problem, two black concentric pipes were coupled together in an annular radiative cavity. Looking at Fig. 3.28, the grey space between pipes represents the radiation field where adjacent surfaces are interacting via radHT. Both pipes utilized adiabatic boundary conditions on their non-interacting wall surfaces. Based on the initial temperatures and volumetric heat capacity of the walls, some steady-state homogeneous temperature should be reached based on energy conservation, or more specifically, the distribution of initial thermal energy stored in both pipes. Successfully matching the simulated homogeneous temperature solution with its analytically-found counterpart would justify a successful test, and would demonstrate correct solid-to-solid surface coupling via radHT. This test was also used to check in-code calculation of non-unity view factors based on user-input geometric parameters.

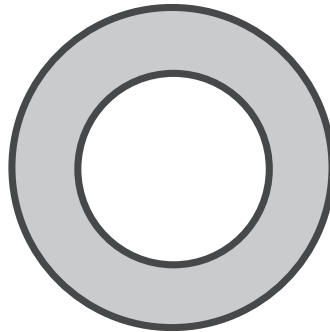


Figure 3.28: Concentric pipes with an annular radiation field (shown in grey) between radiatively interacting surfaces.

Table 3.6 shows the analytically-found temperature solutions T_{SS} based on thermal masses and initial temperatures, assuming constant density and specific heat. For all tests, the width of both heat structures remained 0.1 m. Each simulation was carried out until the temperature difference between pipes fell within 0.005 °C of its steady-state value. For each

Table 3.6: Geometric parameters, initial conditions, and analytical temperature solutions (in bold) for concentric pipes solid-to-solid testing.

Test #	$r_{o,1}$ [m]	$r_{i,2}$ [m]	$T_{0,1}$ [°C]	$T_{0,2}$ [°C]	T_{SS} [°C]
1	0.1	0.1001	1200	400	599.9
2	0.3	0.5	1200	400	908.67
3	0.5	0.9	226.85	1226.85	905.42
4	0.2	100	226.85	1226.85	1225.35

test case, the RadiativeHeatTransfer simulation⁷ produced solid temperatures identical to those shown in Tbl. 3.6, thereby verifying solid-to-solid radHT simulation in SAM, including in-code view factor calculation for the annular enclosure geometry.

Slab enclosure with participating fluid testing demonstrating convergence to analytical solution

For this test, an analytical radiative heat flux solution was calculated for contrived fluid and surface temperatures in a semi-infinite slab-type enclosure. Figure 3.29 shows an axial view of the test geometry — two slab walls and participating fluid. All simulation constituents are 1 m in length.

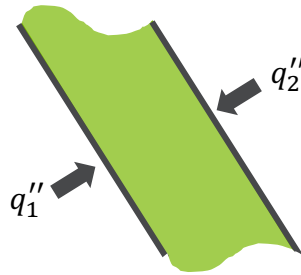


Figure 3.29: Semi-infinite slab geometry consisting of a participating fluid flowing between parallel walls.

The analytically found heat fluxes were implemented into the SAM model by applying them as boundary conditions on the non-radiatively-interacting outer slab surfaces. A successful

⁷SAM version number and git commit ID: v0.9.4-465-g6bdf02a0

test would result in the radiatively-interacting surfaces converging on the initial contrived surface temperatures.

The thermophysical radiative properties and fluid temperature shown in Tbl. 3.7 were implemented into a RadiativeHeatTransfer simulation. Note the pseudo-grey Surface 2. To test if these plates would converge to the desired steady-state temperatures, shown bolded in Tbl. 3.7, $38\,568\text{ W/m}^2$ was applied to the outer boundary of the wall which contains Surface 1, while $28\,029\text{ W/m}^2$ was removed from the outer boundary of the wall which contains Surface 2. To keep fluid temperature axially-constant in the flow direction, and therefore maintain the analytical solution along the walls, the fluid thermal inertia was inflated to an artificially large value, $10^8\text{ J/(m}^3\text{ K)}$, and the fluid velocity was set to 0.1 m/s . For comparison, the walls' thermal inertias were set to $1586.9\text{ J/(m}^3\text{ K)}$ with a thermal conductivity of 1500 W/(m K) . Other than for comparison, the walls' thermophysical properties are arbitrary to the steady-state surface temperatures observed in this test. Altering these parameters would simply affect the time taken to reach steady-state and the temperature gradients across the walls.

Table 3.7: Radiative parameters and analytical temperature solutions (in bold) for semi-infinite slab enclosure testing with a participating fluid.

Radiating Body	Radiative Properties		T_0 [°C]	T_{SS} [°C]
	ε	ρ		
Surface 1	0.8	0.2	500	800
Surface 2	0.5	0.3	700	400
	κ [m ⁻¹]			
Fluid	5		600	600

Regardless of the walls' initial temperatures, the radiating surfaces should converge to the temperature values used to produce the analytical solution. Figure 3.30 shows the surfaces approaching the expected temperature values listed in Tbl. 3.7. These results verify RadiativeHeatTransfer's capabilities to simulation multi-surface radHT with a participating fluid. Additionally, non-grey behavior of a radiatively-interacting surface is demonstrated.

The behavior demonstrated in Fig. 3.30 is notable for justifying the mathematical modeling approach chosen for SAM radHT simulation. One method of radHT modeling, utilized in TRACE for certain scenarios, implements surface-to-fluid radHT via a modification to the convective heat transfer coefficient. Before the code development work discussed in this chapter was conducted, that modified-convection method was heavily considered for SAM.

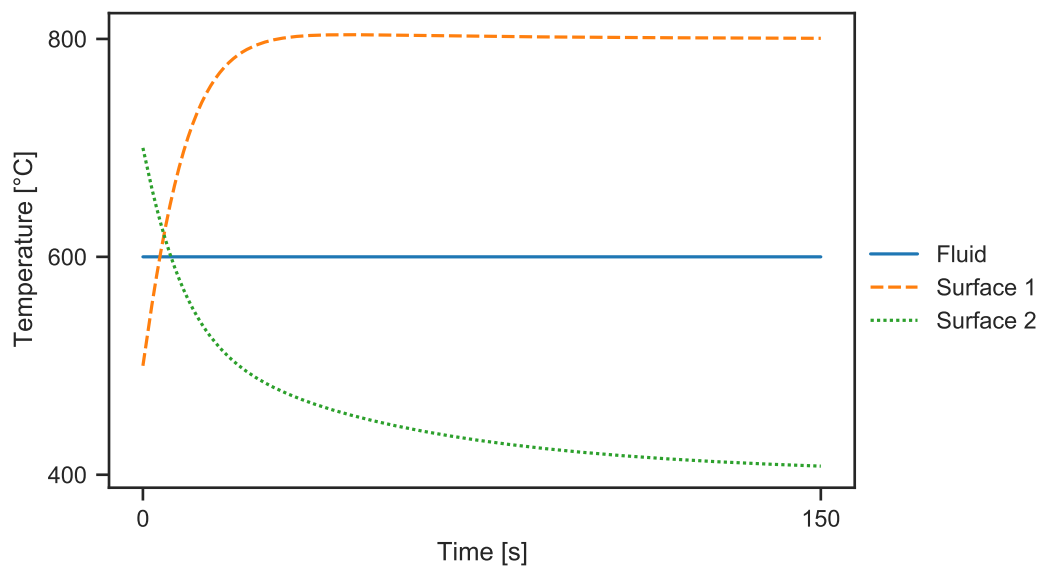


Figure 3.30: Semi-infinite slab testing with a participating fluid showing component temperatures converging towards the steady-state analytical solution.⁷

If that method had been implemented in SAM, Fig. 3.30’s Surface 1 temperature would not have been allowed to rise above the fluid temperature and Surface 2’s temperature would not have been able to drop below. As the fluid-to-surface temperature differences approached zero, the heat transfer coefficients required to alter surface temperatures would have hurdled towards infinity, and no heat transfer coefficient value could have forced the surfaces to gain or lose heat. In other words, modeling this radHT scenario with a modified convective heat transfer coefficient would not allow surfaces to switch from being colder to being hotter than the fluid, or vice versa.

Pipe flow testing demonstrating heating and cooling of walls by radiating fluid

This single-surface-with-participating-fluid test was executed to demonstrate both heating and cooling of a surface via radiative transfer with a fluid. Adiabatic outer surface conditions were imposed to ensure all heat transfer occurs via thermal radiation. The thermophysical properties of the pipe were manipulated so the surface’s temperature oscillations would more closely resemble that of the fluid (see Fig. 3.32) — solid structure thermal conductivity was set to $2 \text{ W}/(\text{m K})$ and thermal inertia was set to $10^4 \text{ J}/(\text{m}^3 \text{ K})$. Both the fluid and pipe were initialized at 600°C . The incoming fluid travels through the pipe at a velocity of 0.05 m/s with a temperature profile which follows $T [^\circ\text{C}] = 600 + \sin 0.5 \cdot t$.

Figures 3.31 and 3.32 are both snapshots of temperature profiles at some moment during the test, which periodically repeats throughout the course of the entire 100s simulation.

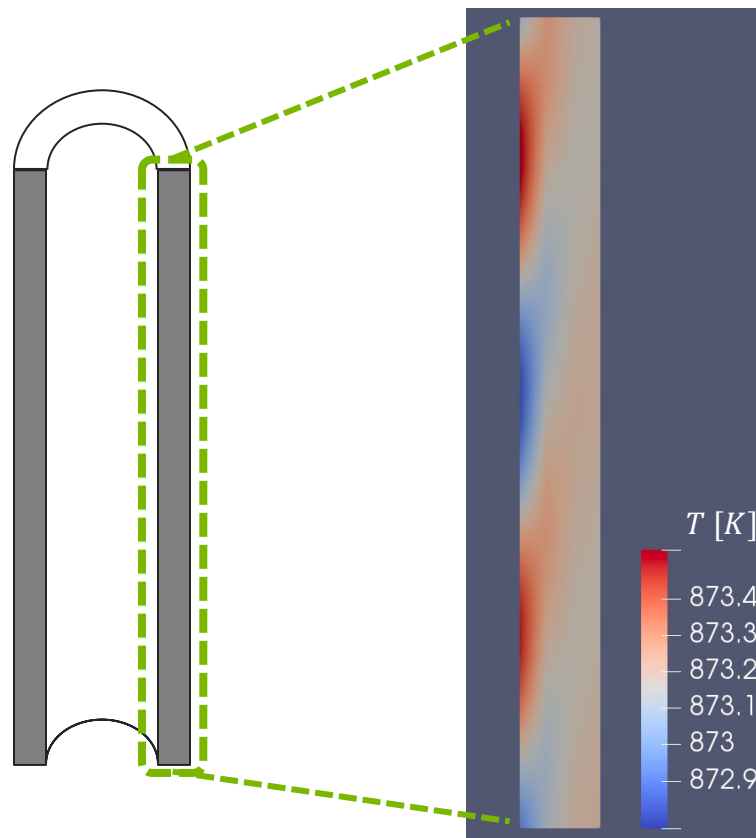


Figure 3.31: Two-dimensional wall temperature profile at time = 100 s in sinusoidal pipe heating and cooling testing. Plot generated in ParaView (note temperature scale in Kelvin).⁷

Figure 3.31 clearly shows the participating fluid can both heat and cool the pipe surface. In terms of this diagram's orientation, the fluid is flowing downwards and directly interacting with the pipe's inner surface, represented by the left side of the ParaView temperature plot.

Looking at Fig. 3.32, the regions of surface heating and cooling along the length of the test section can be demarcated by observing the temperature difference between the solid and fluid. While there is no analytical solution to benchmark these results against, direct solid-to-fluid radHT is clearly demonstrated. Without a second surface, the pipe wall temperature is directly influenced by the participating fluid temperature profile. The smooth sinusoid exhibited by the surface temperature in Fig. 3.32 lends confidence to RadiativeHeatTransfer in properly transferring heat both from the fluid to the solid (surface heating) and from the solid to the fluid (surface cooling). This is a significant deduction because, while the previous slab-type verification test incorporated a participating fluid temperature in the analytical solution, there was no observed fluid temperature change. Whether RadiativeHeatTransfer

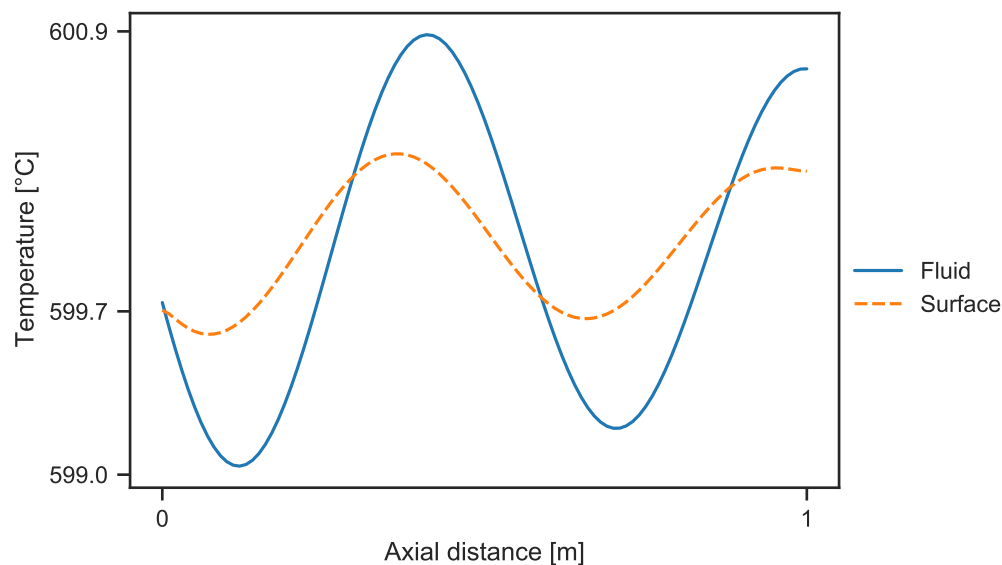


Figure 3.32: Axial temperature profiles demonstrating surface heating and cooling by the fluid in sinusoidal pipe heating and cooling testing.⁷

was actually adding or removing energy from the fluid component could be disputed when observing the test results. Here however, the existence of solid-to-fluid energy transfer via radiation is clearly shown. RadiativeHeatTransfer is undeniably capable of removing and adding energy to both solid and fluid simulation components.

Verification analysis conclusions

The three tests described in this section constitute the verification analysis performed for RadiativeHeatTransfer. The concentric pipes test verified solid-to-solid radHT, the sinusoidal pipe flow test verified the solid-to-fluid energy transfer abilities of the code, and the semi-infinite slab test verified SAM's new capability of performing radiative transfer in an enclosure with two surfaces and a participating fluid. Additionally, these tests proved the efficacy of modeling with RadiativeHeatTransfer's preset geometry options — Annulus, Cylinder, and Slab. The test results lend strong confidence to SAM's new radHT modeling capabilities, enough to state that Rad++ (Eqs. (3.6) and (3.7)) has been correctly implemented in SAM by RadiativeHeatTransfer. Furthermore, any additions or modifications made to the RadiativeHeatTransfer component beyond the execution date of these verification tests, which included some of the development activities discussed in Sec. 3.2, must undergo regression tests to demonstrate the produced radHT solutions still align with the reference solutions, three of which are the tests which have been discussed here. In affect, this verification analysis binds any and all RadiativeHeatTransfer simulations henceforth to

the level of verifiability demonstrated by these tests.

3.4 How to Use RadiativeHeatTransfer

I include this section as to clarify some of the necessary user inputs for various modelling scenarios. For more information on the input syntax, or for a comprehensive list of RadiativeHeatTransfer inputs, please refer to the most up-to-date version of the SAM User's Guide [88]. Additionally, logic checks built into RadiativeHeatTransfer generally guide the user towards the necessary inputs by issuing errors when parameters are amiss.

The component inputs can be broken down into three categories: geometry inputs, radiative property inputs for the participating fluid, and the same for radiating surfaces. RadiativeHeatTransfer is designed to “think” in terms of the radiative enclosure, so the most important input is geometry type. Figure 3.33 shows the available enclosure geometry options. Depending on the number of surfaces required by the selected geometry, one or two radiatively interacting surface(s) must be specified. RadiativeHeatTransfer is not a “geometric component”, meaning it does not create simulation objects. Therefore, the stipulated surfaces must already exist in the SAM simulation as other components, and are only selected by RadiativeHeatTransfer to be used in the radiative enclosure. Available options include any

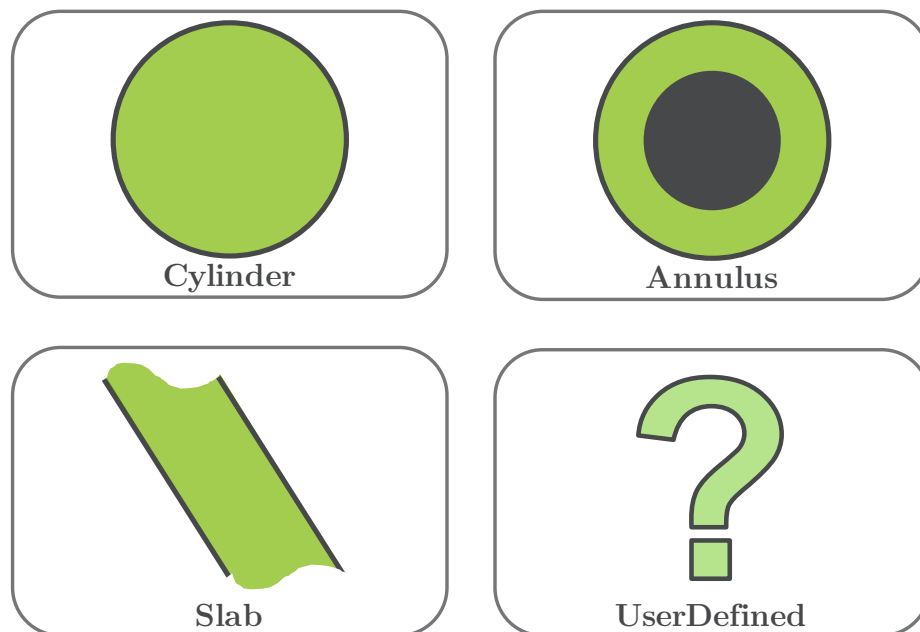


Figure 3.33: Geometry options for radiative enclosures built into the radiative heat transfer SAM component.

surface components compatible with RadiativeHeatTransfer (all of which are included in the list below). Depending on the component type, surfaces are accessed with various syntax. The User's Guide [88] can help guide code users towards the correct option.

Full list of SAM components compatible with RadiativeHeatTransfer:

- PBOneDFluidComponent
- PBCoupledHeatStructure
- PBPipe
- PBHeatExchanger
- PBCoreChannel
- PBDuctedCoreChannel
- ReactorCore
- HeatPipe

If the radiative system includes a participating fluid, the appropriate SAM fluid component must be stipulated in a manner similar to the interacting surface(s). Listing a fluid component will signify to RadiativeHeatTransfer that a participating fluid is present. Depending on the modeled scenario, the component will require further input(s) to determine the level of fluid interaction in the enclosure. If a predefined enclosure geometry is selected, the user can benefit from code-calculated fluid transmittance and emittance values. The only required input is the spectrally-averaged absorption coefficient, which needs to be predetermined by the user. However, if the user desires to override any transmittance or emittance values subsequently calculated from the absorption coefficient, the parameter to be overridden simply need be input.

Surface inputs include spectrally-averaged radiative properties, surface areas, and view factors. If no radiative properties are specified, the surfaces are considered black ($\varepsilon = 1$). If only emissivities or reflectivities are specified, the surface will be considered grey ($\rho = 1 - \varepsilon$). Additional surface properties may be specified along the lines of the pseudo-grey discussion concerning treatment of user-specified parameters for Eq. (3.4). Surface areas are only necessary in two cases. If there is a participating fluid, the surface area for each interacting surface must be provided because the fluid heat source Eq. (3.7) requires surface areas. The other case is the multi-surface UserDefined scenario, in which three inputs are required to calculate system view factors: surface area for surface 1, A_1 , surface area for surface 2, A_2 , and the view factor from surface 1 to surface 2, F_{12} .

A UserDefined radiative geometry necessitates more inputs. For a single-surface UserDefined enclosure, either a transmittance or emittance from surface 1 to itself needs to be stipulated. If the user inputs transmittance, emittance will be found in accordance with the grey fluid assumption via $\bar{\alpha} = 1 - \bar{t}$. If the user inputs emittance, transmittance will be found as $\bar{t} = 1 - \bar{\alpha}$. Again, an optional pseudo-grey modeling scenario is available if the user so desires. For this option, both transmittance and emittance need to be specified. The only difference for a multi-surface UserDefined geometry is that the same process will need to be additionally carried out for the transmittance/emittance from surface 1 to surface 2 and for the transmittance/emittance from surface 2 to itself. If a surface does not view itself, then the emittance between that surface and itself should equal zero.

Again, this section is only meant as a quick guide to describe necessary inputs. The SAM User's Guide [88] is more appropriate for helping code users build SAM simulations.

3.5 SAM Radiative Heat Transfer Simulation Capabilities

Before my development work, SAM lacked the ability to simulate radiative heat transfer in any significant fashion. Specifically, SAM lacked the ability to simulate participating media radHT. I, others at UC Berkeley, SAM code developers at Argonne, and advanced reactor design companies all saw the need for these simulation capabilities to be developed. Previous system codes specified their approach to LWR analysis, so I began with modifying previous applications of the net radiation method to complement a more flexible radHT modeling framework. I arrive at the Rad++ expression of the net radiation method, which allowed for simulating radiatively participating fluids in conjunction with non-grey surfaces. From there, I needed to create a code framework — how the code would work and be structured — to facilitate implementation of Rad++. Once that framework was in place, I developed the initial RadiativeHeatTransfer component in SAM and was subsequently able to simulate radHT for multiple radiative geometry types (Fig. 3.33).

Once SAM could simulate radHT, I turned my efforts to developing further capabilities for the RadiativeHeatTransfer component. I derived and implemented 2D transmittance correlations for the preset geometry options, which allows the code to more-accurately calculate participating fluid interaction in accordance with Rad++; I developed RadiativeHeatTransfer to be compatible with a number of preexisting SAM components, which allows for more widespread and flexible use of RadiativeHeatTransfer in SAM simulations; I developed radHT rate postProcessors, which makes RadiativeHeatTransfer a much more desirable reactor analysis tool for SAM code users; and when all these capabilities were added, I ran verification tests to prove RadiativeHeatTransfer was simulating Rad++ as intended, and all code improvements worked as well.

Following this work, SAM now includes radiative heat transfer simulation capabilities. Additionally, these code developments have been fully implemented in SAM, so code users can include radHT modeling in advanced reactor system analysis moving forward. For advanced reactor scenarios where thermal radiation is considered non-insignificant, RadiativeHeatTransfer should be built into SAM simulations to capture radHT effects. In conjunction with validation test data and higher-fidelity verification comparisons, the RadiativeHeatTransfer component will be a powerful tool for simulating a previously neglected phenomenon in system-level analysis for advanced reactors.

Chapter 4

The Mk.II Initiative or: System-Level Modeling of Scaled-Up FHRs to Demonstrate the Three-Step FHR Scaling Methodology

The Mark 1 (Mk.I) is a pre-conceptual fluoride-salt-cooled high-temperature reactor (FHR) design developed at the University of California, Berkeley (UC Berkeley) [3]. This design has established itself as an important reference design for FHR technology development and analysis studies. If scaling analysis were applied to the Mk.I to generate a reduced height, reduced area, surrogate fluid integral effect test (IET) design, the scaling approach would consist of the steps listed below:

1. Determine operational scenarios of interest for the Mk.I
2. Select parameters indicative of characteristic Mk.I behavior in the context of those predetermined scenarios
3. Incorporate those characteristic parameters into nondimensional (ND) scaling numbers, which is specified by the scaling methodology in use
4. Select rudimentary experimental design features
5. Approximate experimental characteristic parameters for the respective operational scenarios and calculate scaling numbers
6. Refine scaled-down experimental design by matching respective scaling number values between the Mk.I and experiment

These six steps could be carried out using the three-step FHR scaling methodology from Ch. 2, which would serve the additional purpose of providing an example application of the developed methodology. If there was interest in commercializing the Mk.I, and system codes needed to be validated for Mk.I simulation, that exact scaling analysis would be carried out. However, there is no interest in realizing the Mk.I, and any further benefits of designing a scaled experiment for the Mk.I would be limited due to an already-existing FHR-based IET at UC Berkeley — the Compact Integral Effects Test (CIET).

CIET is a reduced height, reduced area, surrogate fluid IET that was designed before the Mk.I design was finalized, so a 900 MW_{th} FHR called the PB-AHTR [48] was used as the primary reference design for CIET scaling analysis instead. CIET therefore does not properly capture the phenomenological behavior of the Mk.I [49]. Despite this deficiency, CIET is the closest thing that exists to a scaled-down Mk.I IET. It is a valuable resource for FHR development and opportunities to utilize CIET should be taken when possible. Still, having a family of prototypical FHR reference designs to relate experimental behavior to would improve the CIET concept.

To remedy this shortcoming, a novel scaling application was hypothesized — take a pre-existing IET and scale its behavior *up* to emulate hypothetical, prototypical-scale nuclear reactors. This proposed application gives CIET a true FHR reference, thereby allowing it the ability to imitate a family of full-scale FHRs while simultaneously providing a valuable opportunity to conduct a numerical demonstration of the three-step FHR scaling methodology I developed in Ch. 2. By then implementing CIET-to-FHR scaling relations into CIET’s control interface, CIET can emulate prototypical FHRs in real time, a novel application for molten-salt-cooled reactors.

4.1 The Mk.II Initiative

The hypothetical FHRs produced by scaling up CIET are given the designation Mark 2 (Mk.II) FHRs, evolving from the nomenclature assigned to the Mk.I. The culmination of scaling analysis and representing Mk.IIs in CIET is named “the Mk.II Initiative”.

The opportunity to carry out the Mk.II Initiative is ultimately enabled by the Advanced Reactor Control & Operations (ARCO) facility, which is used to operate CIET and serves as a testbed for advanced reactor instrumentation and control. The ARCO facility control displays feature indications for fluid temperature, fluid velocity, and heater power. By translating these indicators with scaling relations, control outputs can be modified to show Mk.II behavior, and CIET operators can perform their roles in the context of full-scale FHR operation.

The Mk.II Initiative also demonstrates a proof-of-concept application of the FHR scaling methodology to an FHR system. Test data from experiments can be used to investigate

the efficacy of scaling-distortion quantification methods. Additionally, proposed distortion mitigation methods can be iteratively examined and improved through experimentation. To accomplish this, the typical process of scaling down must be replaced by scaling up.

4.2 CIET Scaling Analysis for the Mk.II

The scaling parameters necessary for Mk.II Initiative scaling analysis are provided by the three-step FHR scaling methodology developed in [Ch. 2. Section 2.6](#) describes the methodology in detail and summarizes the scaling numbers included in each of the three steps.

To ascertain full-scale Mk.II FHR design parameters, scaling analysis must be applied in “reverse” of its intended design — instead of taking a prototypical FHR and scaling down to a separate effect test (SET) or IET, I took CIET and scaled up to a Mk.II. While “scaling up” for nuclear systems lacks precedence, there is no theoretical impediment facing this approach. The ND-ization of governing equations behind scaling theory indicate no preference for how produced scaling parameters are applied. Therefore in this chapter, the Mk.II scaling analysis actually begins by selecting CIET behavior of interest and then scaling up.

I made the choice to use System Analysis Module (SAM) simulations for CIET data rather than directly use the data gathered from real life CIET experiments. SAM is a system-level code, which means all data necessary for scaling analysis is generated in simulation. Furthermore, data acquisition in system-codes is not limited to the placement of instrumentation, which helps in calculating ND numbers. To guarantee the simulations provided accurate CIET data, I exclusively used SAM models from a successful CIET validation exercise [71]. I briefly describe these models below.

4.2.1 Description of SAM models

I used two SAM models as my CIET reference states for Mk.II scaling analysis — one for CIET’s forced circulation primary loop and another for CIET’s passive cooling natural circulation direct reactor auxiliary cooling system (DRACS) loop. As mentioned previously, both simulations were used for validation exercises. Therefore, both can be trusted to provide data reflective of the real life experiment.

\dot{Q} -step experiment model

The CIET primary loop power (\dot{Q}) step change experiment was a pump-driven, transient power test conducted in the CIET primary loop. A one-dimensional flow diagram for the CIET primary loop is shown in [Fig. 4.1](#). The behavior of this particular experiment is summarized in [Fig. 4.2](#), in which the heater power was gradually incremented step-wise from approximately 2.5 kW up to 7.6 kW, and then back down below 3 kW. The m was

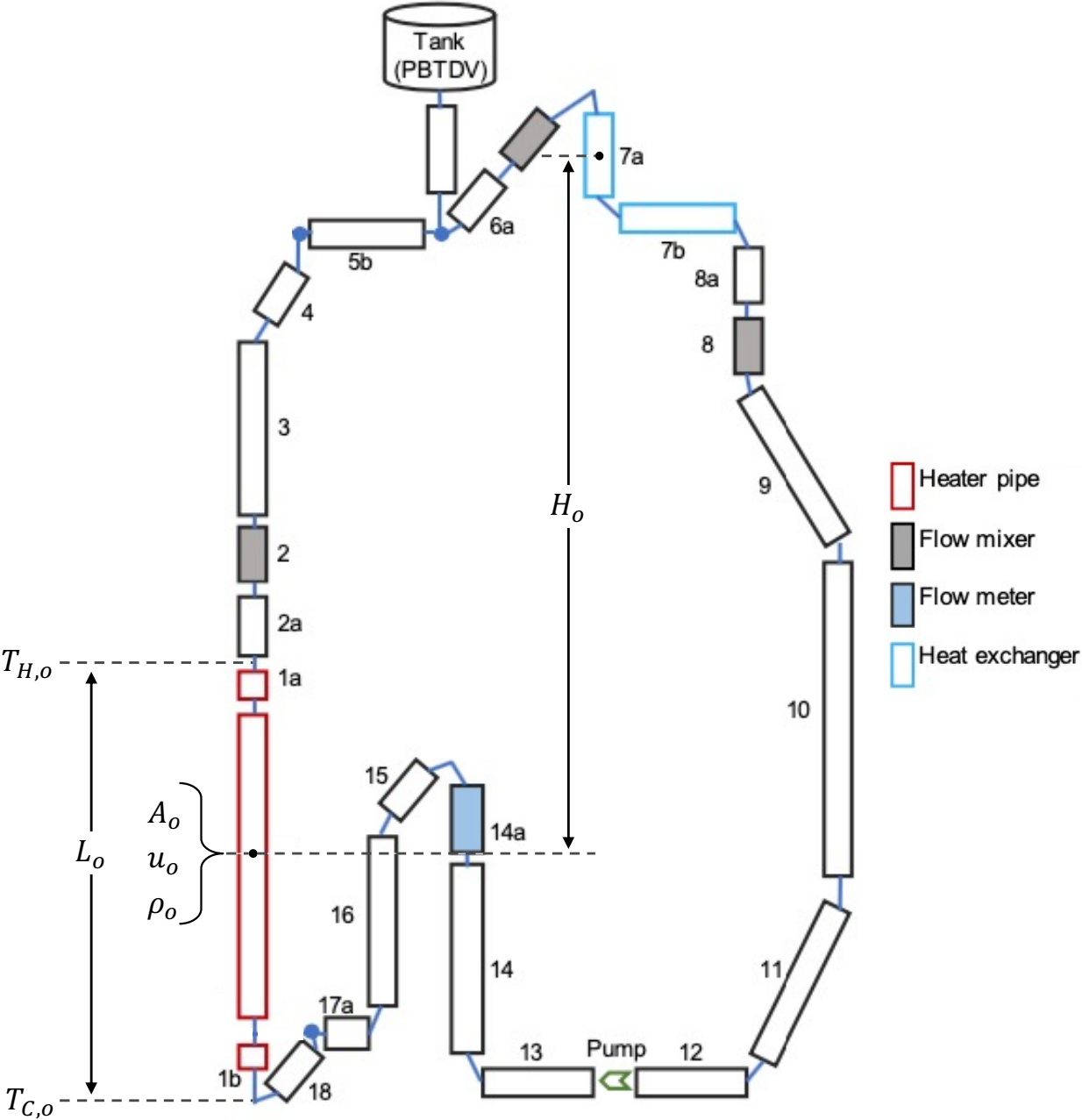


Figure 4.1: CIET primary loop flow path diagram showing where characteristic parameters are chosen for Mk.II scaling analysis. Fluid flow runs clockwise. Figure modified from Ling Zou et al. [55]. Component numbers shown here are irrelevant to this analysis.

maintained steady at 0.18 kg/s by the pump. These data were used for SAM molten salt simulation validation testing [71], whose results are also shown in Fig. 4.2.

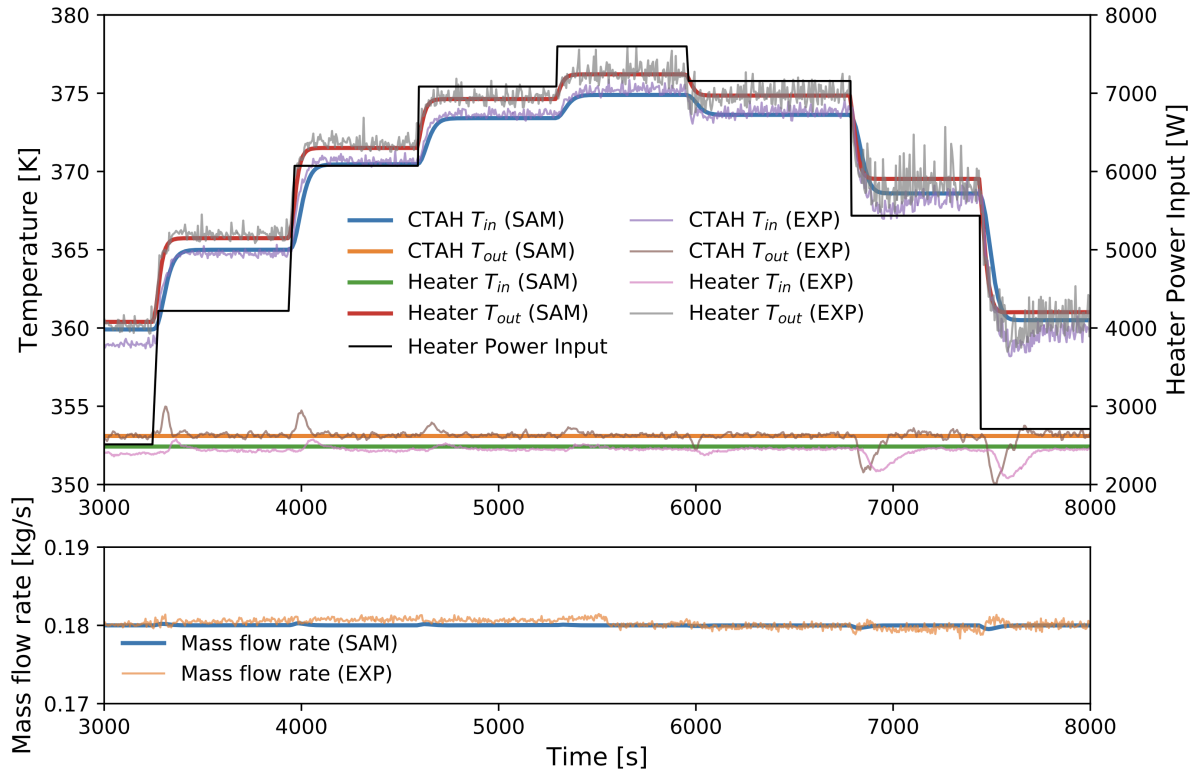


Figure 4.2: CIET power step change experimental data and SAM validation test results. Modified figure from Ling Zou et al. [55], with original data and plot from Zweibaum [49].

I conducted scaling analysis at steady-state full-power, specifically at $t = 5900$ s. At this moment, CIET’s heater power is set to the test maximum ($\dot{Q} = 7.6$ kW) and has yet to start incrementally dropping.

I chose $t = 5900$ s to allow as much time as possible to approach steady-state following the previous \dot{Q} -step up to 7.6 kW. Looking at Fig. 4.2, many of the real-life “EXP” deviations in temperature and mass flow rate are minimized at these steady-state conditions, which further enhances confidence in the accuracy of the SAM simulation data at $t = 5900$ s.

DHX-DRACS coupled-loop natural circulation experiment model

Direct reactor auxiliary cooling systems (DRACS) are passive cooling natural circulation loops in the Mk.I designed to remove decay heat from the core. Three of which are visible in

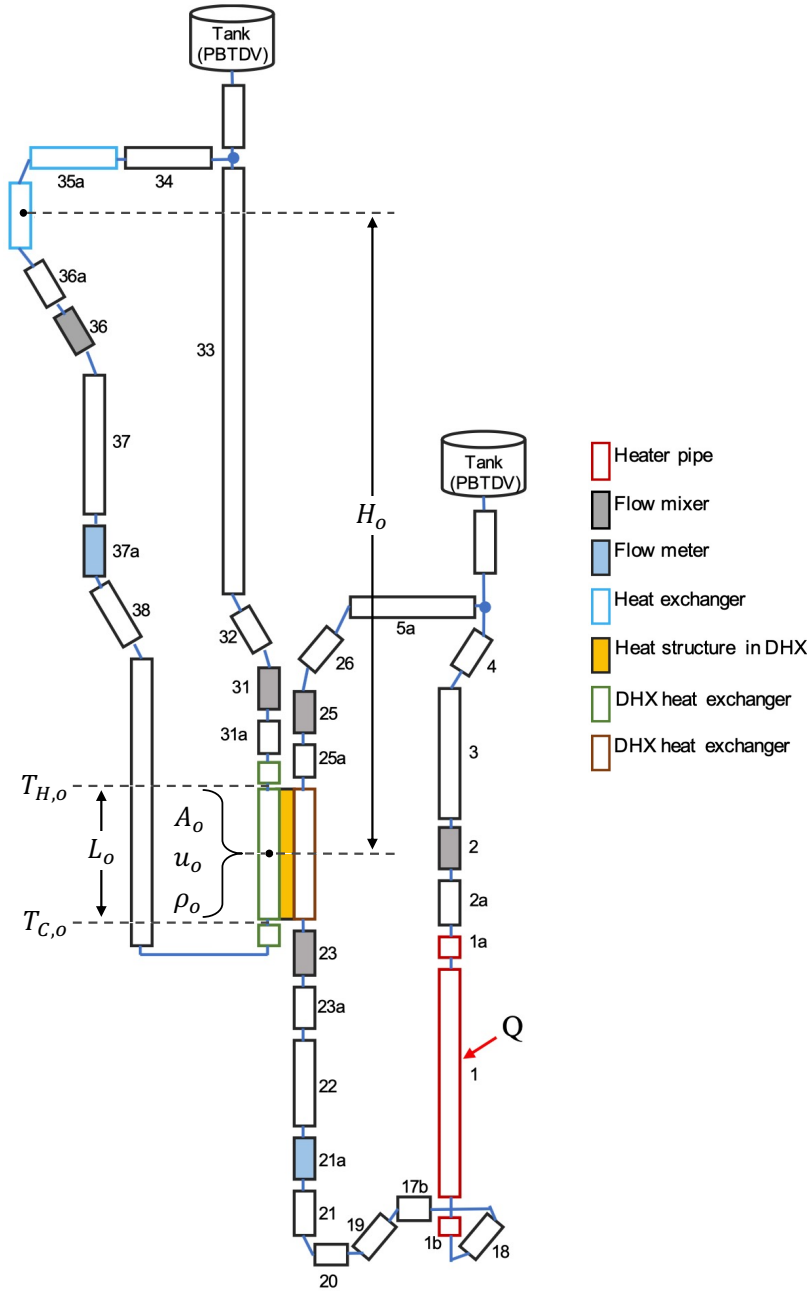


Figure 4.3: CIET natural circulation loop flow paths diagram. The DRACS loop (left), shown with characteristic parameter selection locations, is coupled to the primary loop natural circulation section (right). Fluid flow runs counterclockwise in both. Figure modified from Ling Zou et al. [55]. The component numbers shown here are irrelevant to this analysis.

Fig. 1.1. Each is coupled to the in-core coolant by a DRACS heat exchanger (DHX). CIET incorporated one scaled-down DRACS loop, coupled to a natural circulation section of the primary loop by a scaled-down DHX, to demonstrate the efficacy of passive cooling DRACS systems for FHRs. Both coupled natural circulation loops are shown in Fig. 4.3.

The SAM model I used simulated the development of natural circulation flow in both coupled loops as a result of a $\dot{Q}_{in} = 2400 \text{ W}$ generated by the primary loop heater and a \dot{Q}_{out} removed by the DRACS loop fan heat exchanger (HX). The fan HX enforced the \dot{Q}_{out} using an outer $T_{BC} = 46 \text{ }^\circ\text{C}$ and an artificially inflated inner heat transfer coefficient of $h_w = 8 \times 10^4 \text{ W}/(\text{m}^2 \text{ K})$. As discussed in Sec. 2.3.4, the system height-scale is chosen at the heater and HX midpoints, where temperature can be assumed to approximate T_{avg} . For this simulation, a proper height-scale is necessary to properly model buoyancy forces. To capture CIET buoyancy forces in the SAM simulation, the artificially inflated h_w was applied starting at the fan HX midpoint rather than the component inlet.

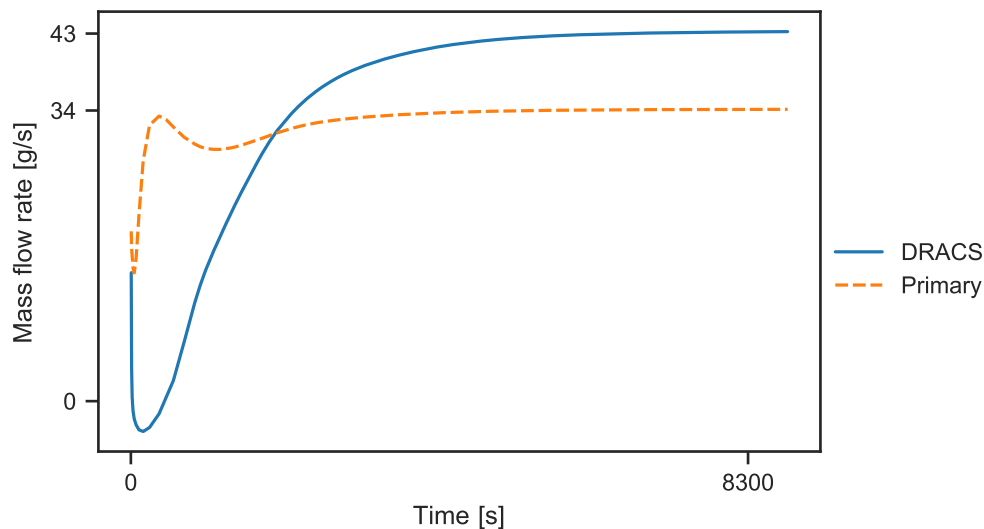


Figure 4.4: Development of steady-state flow rates for the DHX-DRACS coupled-loop natural circulation experiment. Data from SAM validation test simulation. Initial flow deceleration (and reverse DRACS flow) is a product of initial velocity and temperature conditions in the simulation.

Temperature-driven buoyancy forces drive natural circulation, so ample time was required to reach steady-state temperature profiles, particularly in the solid structures. The development of steady-state flow, which results from steady-state temperature development, is shown by Fig. 4.4. Note mass flow rate is expressed in units of [g/s], so flow is slow compared to the \dot{Q} -step experiment flow rate. I simulated the DHX-DRACS experiment validation simulation out to $t = 10^4 \text{ s}$ and used simulation data at the last timestep for Mk.II scaling analysis.

4.2.2 CIET primary loop forced circulation scaling analysis

In this section, I perform scaling analysis for the CIET primary loop using the scaling methodology outlined in Sec. 2.6. To accomplish this, I ND-ize CIET behavior using the \dot{Q} -step experiment as the reference. Using SAM simulation data for the \dot{Q} -step experiment, I identify characteristic parameters and calculate scaling numbers. I use this information in Sec. 4.3 to then scale up the CIET primary loop to that of a Mk.II.

Step 1) Intra-component scaling


The scaling parameters I wish to capture for this step are shown in Tbl. 2.4, with the N_{Th} shown in Tbl. 2.5. The characteristic parameters pertinent to calculating these scaling numbers are listed in Tbl. 4.1. For complete system scaling analysis, this step would be carried out for all major components. Here, intra-component scaling is carried out here for the CIET heater section.

Table 4.1: Component-specific characteristic parameters required for CIET primary loop intra-component scaling analysis. Values shown were found for the CIET heater section, excepting characteristic pump head.

Basic			Composite		
Parameter	Value	Units	Parameter	Value	Units
$L_{o,c}$	1.92	m	$\Delta T_{o,c}$	23.8	$^{\circ}\text{C}$
$H_{o,c}$	1.92	m	$(\rho c_p)_{s,o}$	3.80×10^6	$\frac{\text{J}}{\text{m}^3 \text{K}}$
$u_{o,c}$	0.495	m/s	$(\rho c_p)_{f,o}$	1.78×10^6	$\frac{\text{J}}{\text{m}^3 \text{K}}$
$T_{C,o}$	79.3	$^{\circ}\text{C}$			
$T_{H,o}$	103	$^{\circ}\text{C}$			
$h_{pump,o}$	1.33	m			

Using the characteristic parameters from Tbl. 4.1, in addition to other in-situ values, the CIET heater intra-component scaling parameters can be calculated. The scaling parameters of interest are shown in Tbl. 4.2. I decided to include the pump Eu as well to complete the parameters from Tbl. 2.4. Barring one exception (N_{Th}), I omitted the solid structure scaling parameters because I was not interested in scaling up CIET solid structures to the Mk.II.

Table 4.2: Intra-component scaling parameters of interest for the CIET primary loop. Values shown were found for the CIET heater section, excepting the Euclid number (pump).


	Scaling Number	Value
	Fr_c^{-1}	77.1
	$St (\overline{\varphi_w - \theta})$	1.00
	St_{mod}	0.275
	St_{rad}	0.00
	N_{ThI}^o	2.82
	Eu	53.4

Step 2) Inter-component scaling

To summarize, the inter-component scaling step reconciles ND mass flow values, ND energy fluxes, and ND time progression between adjacent components. Table 2.6 outlines the inter-component characteristic variable uniformity required to achieve this scaling step.

Carrying out inter-component scaling across every component in the entire CIET primary loop (all parts of Fig. 4.1) is akin to selecting integral-system characteristic parameters. As made apparent by Fig. 4.1, I determined these should be taken at the most important heat transfer component — CIET’s heater. Characteristic parameter values are shown in Tbl. 4.3.

Table 4.3: Inter-component scaling characteristic variable uniformity for the CIET primary loop. All values shown were defined by the CIET heater section.

	Characteristic Variable	Value	Units
	ρ_o	1000	kg/m ³
	u_o	0.495	m/s
	A_o	3.64×10^{-4}	m ²
	$T_{C,o}$	79.3	°C
	$T_{H,o}$	103	°C
	L_o	1.92	m

Step 3) Compatibility scaling


Scaling parameters for compatibility scaling are shown in Tbl. 2.7, of which only the Fr and \mathcal{F} are pertinent for forced circulation analysis. The necessary characteristic variables are identified in Tbl. 4.4, selected at the locations specified by Fig. 4.1.

Table 4.4: Integral-system characteristic parameters required for CIET primary loop forced-circulation compatibility scaling analysis.

Characteristic Parameter	Value	Units
L_o	1.92	m
H_o	3.12	m
A_o	3.64×10^{-4}	m^2
u_o	0.495	m/s
ρ_o	1000	kg/m^3

Based on the parameters in Tbl. 4.4, in addition to location-specific ρA values, the compatibility scaling parameters for forced circulation were found for the CIET \dot{Q} -step experiment at full-power steady-state conditions. The final scaling number values are shown in Tbl. 4.5.

Table 4.5: Compatibility scaling parameters of interest for CIET's primary loop.

	Scaling Number	Value
	Fr^{-1}	125
	\mathcal{F}	55.8

4.2.3 CIET DRACS loop natural circulation scaling analysis

In this section, I follow the same general scaling process shown in Sec. 4.2.2 but with the DHX-DRACS experiment as the reference instead. I still use the three-step FHR scaling methodology. However, due to the system-level-thermal-hydraulics focus inherent to natural

circulation analysis, I neglect some of the care typically given to intra- and inter-component scaling by using integral system characteristic parameters throughout all scaling steps. These parameters, listed in Tbl. 4.6, were determined as specified by Fig. 4.3.


Table 4.6: Characteristic parameters necessary for CIET DRACS loop natural circulation scaling and distortion analyses.

Basic			Composite		
Parameter	Value	Units	Parameter	Value	Units
L_o	1.48	m	P_o	42.9	kPa
H_o	4.25	m	ΔT_o	24.8	°C
A_o	6.02×10^{-4}	m ²	\dot{m}_o	4.44×10^{-2}	kg/s
u_o	7.18×10^{-2}	m/s	t_o	20.7	s
ρ_o	1030	kg/m ³			
β_o	8.26×10^{-4}	1/K			
$T_{C,o}$	45.7	°C			
$T_{H,o}$	70.5	°C			

Step 1) Intra-component scaling

Table 4.7 shows applicable intra-component scaling numbers for the DHX-DRACS experiment “heater”, which is simply the DRACS-side of the DHX in this case. The Eu is not

Table 4.7: Intra-component scaling parameters of interest for the CIET DRACS loop. Values shown were found for the DHX.

	Scaling Number	Value
	$St (\overline{\varphi_w - \theta})$	1.00
	St_{mod}	1.95
	St_{rad}	0.00

considered because there is no pump, and the Fr is left to the compatibility scaling step.


Step 2) Inter-component scaling

Due to the system-level focus taken for this section's scaling analysis, characteristic variable uniformity for DRACS loop scaling was already achieved by adopting the variables in Tbl. 4.6.

Step 3) Compatibility scaling

Compatibility scaling is the most important step for natural circulation scaling analysis due to the integral-system nature of buoyancy driving forces. Scaling numbers for this step are shown in Tbl. 4.8.

Table 4.8: Compatibility scaling parameters of interest for the CIET DRACS loop.

	Scaling Number	Value
	Fr^{-1}	8080
	Ri	165
	\mathcal{F}	306

4.3 Scaling Up to a Mk.II Design

Thus far, I have selected reference scenarios for CIET (in Sec. 4.2.1) and scaled their behavior (in Secs. 4.2.2 and 4.2.3). The next step of the Mk.II Initiative for these CIET reference scenarios is scaling them *up* to their Mk.II equivalents. In this section, I will demonstrate selection of design parameters for an example Mk.II. The primary loop will be based off CIET's primary loop forced circulation \dot{Q} -step experiment, and the DRACS loops will be based off CIET's DHX-DRACS natural circulation experiment.

Determining Mk.II design parameters requires utilizing the scaling parameters calculated from CIET. If I was conducting thorough component-by-component scaling analysis, I would start by conducting intra-component scaling for every component of interest. However for this Mk.II example, I am primarily interested in component scaling criteria for the heater sections and integral system scaling criteria otherwise. This section shows two examples for how to turn ND behavior of a CIET reference state into a Mk.II design.

4.3.1 Mk.II primary loop

The Mk.II is a prototypical scale FHR, which implies molten Li_2BeF_4 salt (flibe) coolant ($> 460^\circ\text{C}$) and a pebble bed core with graphite pebbles and outer reflector [6]. Unlike the Mk.I, this Mk.II does not include a central reflector in the core. A summary of this Mk.II's specific characteristic variables is provided in Tbl. 4.10. Below, I describe how those parameters were found.

For this Mk.II, I chose the global ratios $H_R = L_R = 2/3$. Recall a “ratio” ($_R$) is defined as the experimental value divided by the prototypical value, so $H_R = 2/3$ means this Mk.II primary loop is 1.5 times as tall as CIET's. From these ratios, all Mk.II component elevations and lengths were found. With the H_R defined, Fr_R^{-1} similitude dictates the u_R and, subsequently, loop-wide Mk.II fluid velocities.

$$\frac{1}{Fr_R} = \frac{gH_{o,R}}{u_{o,R}^2} = 1$$

$$u_{o,R} = \sqrt{\frac{2}{3}}$$
(4.1)

Time progression in the Mk.II is then set by $t_R = L_R/u_R$. I assumed \mathcal{F} similitude between CIET and the Mk.II. Form loss-inducing obstructions can be added or removed as necessary to obtain $\mathcal{F}_R = 1$, so I did not calculate \mathcal{F} for this Mk.II. However, I do find it useful to point out how \mathcal{F}_c would be approximated for a pebble bed. Using Ergun's correlation for pebble bed form losses [90] and Founeny's equation for pebble bed hydraulic diameter adjusted for wall effects [91],

$$\mathcal{F}_{PB} \approx \frac{L_o f_{[90]}}{2D_{h,[91]}} + \sum \frac{K}{2}$$
(4.2)

This approximation assumes ρ_o , A_o , and L_o are all defined by characteristic behavior of the pebble bed.

Transitioning away from integral scaling parameters, this paragraph shows how component scaling plays a vital role in determining scaled system behavior. Assuming Eu similitude, the $h_{pump,R} = H_R$. More importantly, having selected most CIET characteristic parameters at the heater midpoint, Mk.II core energy equation scaling yields many prototypical characteristic parameters for this scaling practice. The CIET heater St_{mod} value from Tbl. 4.2 can be used to determine characteristics of the Mk.II core, and therefore characteristic parameters for the entire Mk.II.

$$St_{mod} = \frac{4L_o}{D_h} \left(\frac{Nu}{Pe} \right) = 0.275$$
(4.3)

For the above equation, the Nu correlation can be supplied by Wakao [24] and D_h by Founeny [91]. The new variables ϵ and d_p represent pebbled bed void fraction and pebble diameter,

respectively.

$$Nu = 2 + 1.1Pr^{1/3}Re^{0.6} \quad (4.4)$$

$$D_h = \frac{2\epsilon d_p}{3(1-\epsilon)M} \quad (4.5)$$

where $M = 1 + \frac{2d_p}{3D(1-\epsilon)}$

I adjusted geometric properties and T_o (at which thermophysical properties were evaluated) until I approached $St_{mod} = 0.275$. The final distortion between CIET and Mk.II St_{mod} is 0.2%, which is only possible due to the impractical parameter selection available to a hypothetical reactor such as the Mk.II. The Mk.II ϵ is double that of a randomly packed bed. Unrealistic as that may be, it was necessary to increase D_h for St_{mod} similitude. The Mk.II parameters determined through core scaling analysis are shown in Tbl. 4.9.

Table 4.9: Mk.II core parameters determined via component scaling of the CIET heater.

Basic			Composite			Scaling	
Variable	Value	Units	Variable	Value	Units	Number	Value
T_{avg}	530	°C	\dot{m}	1.42×10^4	kg/s	Nu	2080
ΔT	60	°C	\dot{Q}	2060	MW _{th}	Pr	27.2
d_p	6.9	cm	A_f	11.6	m ²	Re	1.84×10^4
ϵ	0.8	—	$\delta_{refl.}$	2.36	m	N_{ThI}	2.82
D	5.3	m	δ_{DC}	0.981	m		
L	2.89	m					
L_{DC}	1.14	m					

Following the precedence set by many previous IETs, CIET was not designed to reproduce full-power prototypical operation — rather, CIET full-power represents approximately 10% power when the Mk.I is used as the prototypical reference. Scaling analysis for the Mk.II allows the flexibility to select prototypical plant designs that operate at a full-power state representative of CIET’s full-power state. As this can be helpful for ARCO studies, I chose to scale up the CIET \dot{Q} -step experiment to a full-power Mk.II. Note the \dot{Q} value in Tbl. 4.9 was produced by arbitrarily choosing a $\Delta T_o = 60$ °C. At a value of 2060 MW_{th}, the Mk.II power is almost an order of magnitude higher than the Mk.I (236 MW_{th}) [3].

The outer reflector thickness $\delta_{refl.}$ was determined by matching N_{THI}^0 with the CIET core and evaluating $(\rho c_p)_{graphite}$ and $(\rho c_p)_{flibe}$ at $T_{avg.}$ The Mk.II downcomer, abbreviated with the subscript “ $_{DC}$ ”, is scaled as an annular section surrounding the outer reflected. To maintain similitude in elevations, the downcomer only surrounds the bottom 1.14 m of the core, resulting in an unrealistic annular width (δ_{DC}) when $V_p = V_e/(A_R L_R)$ is enforced.

Table 4.10: Mk.II primary loop characteristic parameters at steady-state full-power.

Basic			Composite		
Parameter	Value	Units	Parameter	Value	Units
L_o	2.89	m	P_o	92.8	kPa
H_o	4.68	m	ΔT_o	60	°C
A_o	11.6	m ²	\dot{m}_o	1.42×10^4	kg/s
u_o	0.606	m/s	t_o	4.76	s
ρ_o	2020	kg/m ³	\dot{Q}_o	2060	MW
$h_{pump,o}$	2.00	m			
$T_{C,o}$	500	°C			
$T_{H,o}$	560	°C			

The final Mk.II primary loop characteristic parameters are summarized above.

4.3.2 Mk.II DRACS loop

The Mk.II DRACS loop is a flibe-filled passive-safety natural circulation loop designed to remove decay heat from the core via the DHX, which sits in the primary-side upper core region. This Mk.II is designed to emulate the coupled natural circulation behavior of the primary loop and three DRACS loops immediately following a reactor SCRAM, in which core power is reduced to $\approx 10\%$ of reactor full-power. Adjusting the full-power \dot{Q}_o value from Tbl. 4.10, this SCRAMed Mk.II core produces 206 MW of decay heat. Table 4.11 shows characteristic behavior of this Mk.II’s primary loop under natural circulation conditions following a SCRAM, while Tbl. 4.12 shows the same for each (one of three) Mk.II DRACS loop.

This Mk.II DRACS is scaled up from the CIET DHX-DRACS assuming perfect similitude with the compatibility scaling parameters in Tbl. 4.8. I started by selecting the same $H_R = L_R = 2/3$ as Sec. 4.3.1 to determine DRACS component lengths and height values. Further behavioral parameters were determined via scaling analysis. As with Mk.II primary loop

Table 4.11: Mk.II primary loop characteristic parameters for a post-SCRAM scenario at 10% power.

Basic			Composite		
Parameter	Value	Units	Parameter	Value	Units
L_o	2.89	m	P_o	46.5	kPa
H_o	2.39	m	ΔT_o	138	°C
A_o	2.74	m ²	\dot{m}_o	620	kg/s
u_o	0.114	m/s	t_o	25.3	s
ρ_o	1990	kg/m ³	\dot{Q}_o	206	MW
$T_{C,o}$	535	°C	\dot{Q}_{PHL}	47.0	MW
$T_{H,o}$	673	°C			

analysis, Fr similitude demands $u_R = \sqrt{H_R}$. Then, if $Fr_R = 1$, similitude in the Ri can be simplified to $Ri_R = (\beta_o \Delta T_o)_R$. Using the CIET DHX-DRACS data, and assuming a Mk.II DRACS loop average temperature of $T_o = 520$ °C, the fluid temperature increase across the DHX can be found.

$$\begin{aligned}
 Ri_R \Big|_{Fr_R=1} &= (\beta_o \Delta T_o)_R = 1 \\
 \Delta T_{o,p} &= \frac{(\beta_o \Delta T_o)_e}{\beta_{o,p}} \\
 &= 85 \text{ °C}
 \end{aligned} \tag{4.6}$$

The average DRACS-side DHX solid-to-fluid temperature difference in the CIET DHX-DRACS simulation was deemed to be $(\overline{T_w} - \overline{T})_e = 12.7$ °C. Multiplying that value by the newly-available $\Delta T_{o,R}$ produces the Mk.II average DHX solid temperature — $T_{s,o} = 564$ °C. The cold and hot solid DHX temperatures are shown in [Tbl. 4.12](#).

Applying the same \dot{Q}_R used for [Tbl. 4.11](#) to the CIET DHX-DRACS experiment, the three DRACS loops were found to be removing a cumulative total of 159 MW from the Mk.II primary side, while the three DRACS loop heat-removal HXs (named TCHXs) were removing 149 MW. Therefore, the primary loop loses 47 MW to parasitic heat loss, and the three DRACS loops lose a further 10 MW — a combined 28% of the Mk.II decay heat produced

Table 4.12: Mk.II DRACS loop characteristic parameters for a post-SCRAM scenario at 10% power. The values listed here represent the behavior of each DRACS, assuming a three-loop design.

Basic			Composite		
Parameter	Value	Units	Parameter	Value	Units
L_o	2.22	m	P_o	127	kPa
H_o	6.37	m	ΔT_o	85.0	°C
A_o	1.45	m ²	\dot{m}_o	258	kg/s
u_o	8.79×10^{-2}	m/s	t_o	25.3	s
ρ_o	2030	kg/m ³	\dot{Q}_o	53.0	MW
β_o	2.41×10^{-4}	1/K	\dot{Q}_{PHL}	3.36	MW
$T_{C,o}$	478	°C			
$T_{H,o}$	562	°C			
$T_{s,C}$	521	°C			
$T_{s,H}$	606	°C			

immediately post-SCRAM. This significant figure is a product of conserving parasitic losses in the scaling-up process and would likely not be as large in a real prototypical FHR. Nevertheless, the parasitic heat loss values are maintained for this Mk.II example. These values, along with other Mk.II DRACS behavioral parameters, are summarized in [TbIs. 4.11](#) and [4.12](#) for the primary and DRACS loops, respectively.

4.4 Realizing the Mk.II Initiative

The work presented in this chapter thus far does not satisfy all requirements of the Mk.II Initiative. This section provides a step-by-step implementation strategy for all steps required, path forward, and outcomes. To facilitate Initiative progress, I recommend using the work discussed in this chapter in lieu of supplanting with original Mk.II scaling analysis — at least for the first Mk.II iteration. Work in [Secs. 4.2](#) and [4.3](#) is directly referenced throughout this guide where pertinent to make clear when this chapter’s work can be used.

Step 1) CIET reference state selection

The first step of creating a Mk.II is deciding which CIET behaviors to capture — steady-state or transients, various power levels (full-power, decay heat, etc.), or even different forms of fluid flow. For example, [Sec. 4.2.1](#) identifies two operational modes, each with experiment-specific operational parameters, that could be selected as reference states. While those were previously-conducted experiments, the option remains to choose a reference state that has yet to be imposed on CIET.

Step 2) Mk.II scaling and design

With a CIET reference state chosen, a representative Mk.II can be designed by scaling up. For the CIET behavior one wishes to capture with that Mk.II design, the appropriate characteristic parameters must be identified and scaling numbers produced. To do that, one should follow the three-step FHR scaling methodology outlined in [Sec. 2.6](#). An example application of this is presented in [Secs. 4.2.2](#) and [4.2.3](#). Using the produced scaling numbers, Mk.II design characteristics can be selected, an example of which is provided by [Sec. 4.3](#).

Step 3) ARCO implementation and Mk.II operation

The developed Mk.II design(s) must be implemented in ARCO to complete the Mk.II Initiative. This step is crucial to allow the Mk.II to be emulated by real-world CIET operation. Using the Mk.II scaling parameters and characteristic parameters, CIET output data can be translated to representative Mk.II behavior in real time. To accomplish this, one must provide ARCO with those Mk.II translation functions. When implemented in ARCO, time-dependent Mk.II behavior will be output in real time. Thus CIET experimental operation can be treated as that of a full-scale prototypical FHR.

Step 4) Mk.II simulation and distortion analysis

Inevitably, scaling distortions will exist between CIET and the Mk.II. Some of those will be design distortions, resulting from Mk.II characteristic parameter selections that do not satisfy scaling number similitude with the CIET reference state. Those can be determined even before ARCO implementation. However, other distortions will arise during CIET/Mk.II operation — either transient deviations from the reference state or unexpected phenomenological interplay will produce behavioral discrepancies between CIET and the Mk.II design. To quantify those operational-mode distortions, one must compare fully-evaluated ND term values (e.g. those boxed in [Eqs. \(2.15\)](#), [\(2.37\)](#) and [\(2.81\)](#)) using CIET/Mk.II ND operational data and Mk.II simulation data. These Mk.II simulations should be created using a system-level thermal hydraulics code, preferably SAM. There already exists thorough FHR models developed in SAM [\[73\]](#), which could be appropriated for the Mk.II Initiative by altering the already-developed reactor model to reflect one's Mk.II design parameters and the experimental conditions imposed during Mk.II operation. Using these pre-existing models

would substantially reduce the burden required to quantify Mk.II scaling distortions and is, therefore, highly-recommended to those carrying out the Mk.II Initiative.

Mk.II Initiative outcomes

As discussed in [Sec. 4.1](#), the benefits of the carrying out the Initiative are substantial. By leveraging the facilities at UC Berkeley, and the work in this dissertation, CIET can be converted into a real, physical, prototypical FHR emulator. In addition to the benefits of emulating real-time FHR operation, the Mk.II Initiative provides meaningful applications of the three-step FHR scaling methodology to FHR systems and, most significant to this dissertation work, provides valuable context for carrying out FHR-based radHT simulations in SAM and conducting radHT distortion quantification practices for FHRs.

4.5 Final Words

This dissertation has addressed radHT scaling distortion between FHRs and their scaled down experiments, an important topic of study due to the increased significance of radHT expected at prototypical FHR conditions compared to their experimental counterparts. [Chapter 1](#) details the relevance of this issue by providing background on radHT physics and introducing the radHT distortion present in FHR scaling analysis. That narrative makes clear the need for an FHR scaling methodology that supports radHT distortion quantification and system-level radHT modeling tools, neither of which existed prior to the work presented in this dissertation. To that point, [Ch. 2](#) discusses the FHR scaling methodology I created, including radHT distortion quantification methods, while [Ch. 3](#) details the development of radHT simulation capabilities for SAM. [Chapter 4](#), then presents a case study for applying the scaling methodology and SAM to FHR systems via the Mk.II Initiative.

With FHRs now in commercial development, the work presented in this dissertation is immediately relevant to the engineering and design processes driving the FHR concept towards deployment. The radHT simulation tools I developed will contribute to FHR modeling efforts and are currently available to all SAM users. Once radiative property measurements have been more thoroughly conducted, these simulations can be validated for system-level FHR behavior. In addition to modeling and simulation, scaled experiments, SETs and IETs included, are critical to the FHR design process. The FHR scaling methodology presented in [Ch. 2](#) can be used to select design and operational parameters for those scaled experiments. An experiment designer need simply reference [Sec. 2.6](#) for a summary of the methodology's scaling parameters and distortion analysis methods. In addition to being directly useful to FHR-focused scaling analysts and thermal hydraulicists in academia and national laboratories, the radHT distortion quantification methods can be incorporated into the more-traditional scaling methodologies utilized by industrial entities pursuing molten-salt-cooled reactor commercialization by following the derivation process outlined in [Sec. 2.4](#) and quantification process outlined in [Sec. 2.7](#).

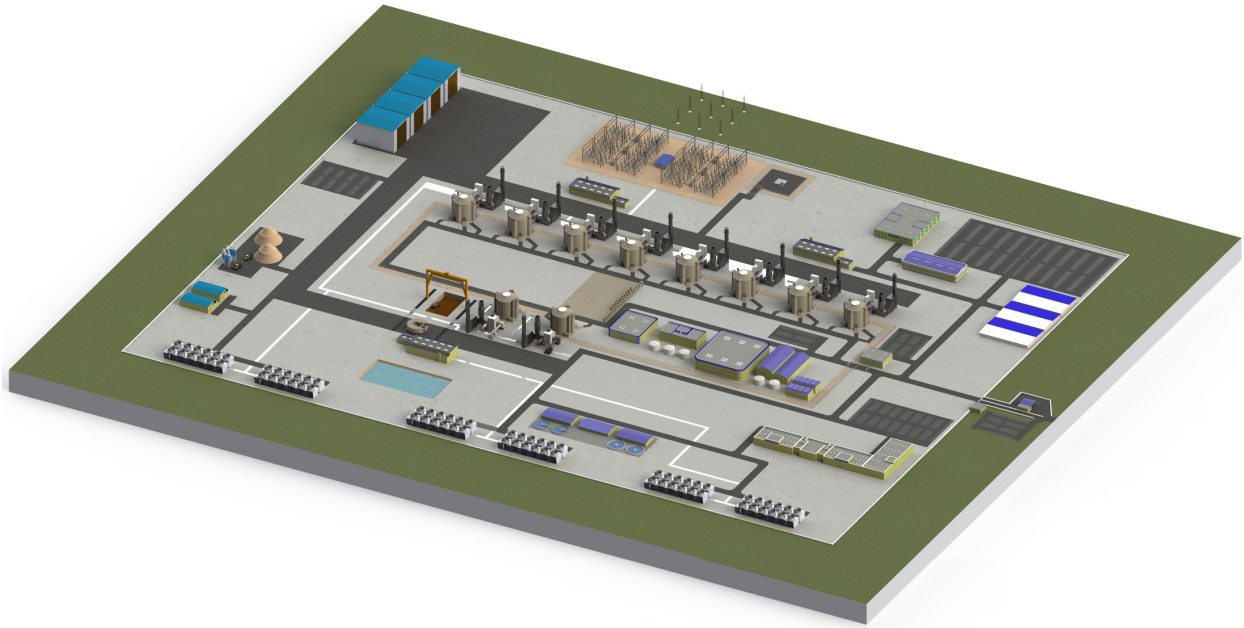


Figure 4.5: Nuclear power plant reference site showing 10 completed Mk.I FHRs with the 11th under construction. With a total of 12 complete units (reference site capacity), this site would be able to produce 1200 MW of nuclear-generated electricity. Figure from Andreades et al. [3, 74].

It is my hope this work will be utilized to facilitate FHR development and help realize the dream of building FHRs, such as those shown in Fig. 4.5, for clean energy production.

Bibliography

- [1] C. W. Forsberg, P. F. Peterson, and P. S. Pickard, “Molten-salt-cooled advanced high-temperature reactor for production of hydrogen and electricity”, *Nuclear Technology*, vol. 144, no. 3, pp. 289–302, 2003. [Online]. Available: <https://doi.org/10.13182/NT03-1>.
- [2] R. O. Scarlat, M. R. Laufer, E. D. Blandford, N. Zweibaum, D. L. Krumwiede, A. T. Cisneros, C. Andreades, C. W. Forsberg, E. Greenspan, L.-W. Hu, and P. F. Peterson, “Design and licensing strategies for the fluoride-salt-cooled, high-temperature reactor (FHR) technology”, *Progress in Nuclear Energy*, vol. 77, pp. 406–420, 2014. [Online]. Available: <https://doi.org/10.1016/j.pnucene.2014.07.002>.
- [3] C. Andreades, A. T. Cisneros, J. K. Choi, A. Y. Chong, M. Fratoni, S. Hong, L. R. Huddar, K. D. Huff, D. L. Krumwiede, M. R. Laufer, M. Munk, R. O. Scarlat, N. Zweibaum, E. Greenspan, and P. F. Peterson, “Technical description of the Mark 1 pebble-bed fluoride-salt-cooled high-temperature reactor (PB-FHR) power plant”, University of California, Berkeley, Berkeley, CA, USA, Tech. Rep. UCBTH-14-002, 2014. [Online]. Available: https://fhr.nuc.berkeley.edu/wp-content/uploads/2014/10/14-002-PB-FHR_Design_Report_Final.pdf.
- [4] Kairos Power, “Design overview for the Kairos Power fluoride salt-cooled, high temperature reactor”, Alameda, CA, USA, Tech. Rep. KP-NRC-1811-002, 2018. [Online]. Available: <https://www.nrc.gov/docs/ML1833/ML18337A040.pdf>.
- [5] —, *KP-FHR specifications*, 2022 [Online]. [Online]. Available: <https://kairospower.com/technology/>.
- [6] P. M. Bardet and P. F. Peterson, “Options for scaled experiments for high temperature liquid salt and helium fluid mechanics and convective heat transfer”, *Nuclear Technology*, vol. 163, no. 3, pp. 344–357, 2008. [Online]. Available: <https://doi.org/10.13182/NT163-344>.
- [7] NuScale Power, “NuScale SMR technology: An ideal solution for repurposing U.S. coal plant infrastructure and revitalizing communities”, Corvallis, OR, USA, Tech. Rep., 2021. [Online]. Available: <https://www.nuscalepower.com/technology/technical-publications>.

- [8] E. Blandford, K. Brumback, L. Fick, C. Gerardi, B. Haugh, E. Hillstrom, K. Johnson, P. F. Peterson, F. Rubio, F. S. Sarikurt, S. Sen, H. Zhao, and N. Zweibaum, “Kairos power thermal hydraulics research and development”, *Nuclear Engineering and Design*, vol. 364, 2020. [Online]. Available: <https://doi.org/10.1016/j.nucengdes.2020.110636>.
- [9] DOE Office of Nuclear Energy, *Energy Department’s Advanced Reactor Demonstration Program Awards \$30 Million in Initial Funding for Risk Reduction Projects*, Dec. 2020 [Online]. [Online]. Available: <https://www.energy.gov/ne/articles/energy-departments-advanced-reactor-demonstration-program-awards-30-million-initial>.
- [10] M. Davenport, *Kairos Power Selected by U.S. Department of Energy for Awards to Advance Nuclear Fuel and Materials Applications*, Jun. 2019 [Online]. [Online]. Available: https://kairopower.com/external_updates/kairos-power-selected-by-u-s-department-of-energy-for-awards-to-advance-nuclear-fuel-and-materials-applications/.
- [11] S. Mitchem, *Argonne leads award-winning collaboration with Kairos Power that unveils new simulation of nuclear power plants*, Feb. 2020 [Online]. [Online]. Available: <https://www.anl.gov/article/argonne-leads-awardwinning-collaboration-with-kairos-power-that-unveils-new-simulation-of-nuclear>.
- [12] DOE Office of Nuclear Energy, *U.S. Department of Energy Further Advances Nuclear Energy Technology through Industry Awards of \$19 Million*, Mar. 2019 [Online]. [Online]. Available: <https://www.energy.gov/ne/articles/us-department-energy-further-advances-nuclear-energy-technology-through-industry-awards>.
- [13] S. A. Neumann, *GAIN announces second-round FY-2019 Nuclear Energy Voucher recipients*, Apr. 2019 [Online]. [Online]. Available: https://gain.inl.gov/SiteAssets/2019VoucherAbstracts/19-088_NewsRelease_GAIN_announcesFY19-2ndRoundVouchers.pdf.
- [14] D. L. Krumwiede, R. O. Scarlat, J. K. Choi, T. M. Phan, and P. F. Peterson, “Three-dimensional modeling of the pebble-bed fluoride-salt-cooled, high-temperature reactor (PB-FHR) commercial plant design”, in *Transactions of the American Nuclear Society*, vol. 109, Washington, DC, USA, 2013, pp. 287–290. [Online]. Available: <https://www.ans.org/pubs/transactions/article-21632/>.
- [15] J. E. Bickel, N. Zweibaum, and P. F. Peterson, “Design, fabrication and startup testing in the compact integral effects test (CIET 1.0) facility in support of fluoride-salt-cooled, high-temperature reactor technology”, University of California, Berkeley, Berkeley, CA, USA, Tech. Rep. UCBTH-14-009, 2014. [Online]. Available: fhr.nuc.berkeley.edu/wp-content/uploads/2015/04/14-009_CIET-IRP-Final-Report.pdf.

- [16] J. R. Howell, M. P. Mengüç, and R. Siegel, *Thermal Radiation Heat Transfer*, 6th ed. Boca Raton, FL, USA: CRC Press, 2016. [Online]. Available: <https://doi.org/10.1201/b18835>.
- [17] M. F. Modest, *Radiative Heat Transfer*, 3rd ed. Oxford, England, UK: Academic Press, 2013. [Online]. Available: <https://doi.org/10.1016/C2010-0-65874-3>.
- [18] Unknown photographer, Accessed October, 2017. [Online]. Available: <https://www.berkeleyside.org/2011/01/24/uc-berkeley-is-ranked-the-worlds-greenest-university>.
- [19] J. Chimienti, Accessed October, 2017, 2017. [Online]. Available: <https://www.instagram.com/p/BaLJN1GnDcA/>.
- [20] R. M. Pope and E. S. Fry, “Absorption spectrum (380–700 nm) of pure water. II. Integrating cavity measurements”, *Applied Optics*, vol. 36, pp. 8710–8723, 1997. [Online]. Available: <https://doi.org/10.1364/AO.36.008710>.
- [21] P. F. Peterson, *Thermal Aspects of Nuclear Reactors*, Fall, 2016 ed. Berkeley, CA, USA: Department of Nuclear Engineering, University of California, Berkeley, 2016.
- [22] J. H. Lienhard IV and J. H. Lienhard V, *A Heat Transfer Textbook*, 5th ed. Mineola, NY, USA: Dover Publications, 2019. [Online]. Available: <http://ahtt.mit.edu>.
- [23] T. L. Shultz, “Westinghouse AP1000 advanced passive plant”, *Nuclear Engineering and Design*, vol. 236, pp. 1547–1557, 2006. [Online]. Available: <https://doi.org/10.1016/j.nucengdes.2006.03.049>.
- [24] N. Wakao, S. Kaguei, and T. Funazkri, “Effect of fluid dispersion coefficients on particle-to-fluid heat transfer coefficients in packed beds: Correlation of nusselt numbers”, *Chemical Engineering Science*, vol. 34, no. 3, pp. 325–336, 1979. [Online]. Available: [https://doi.org/10.1016/0009-2509\(79\)85064-2](https://doi.org/10.1016/0009-2509(79)85064-2).
- [25] C. Coyle, E. Baglietto, and C. Forsberg, “Advancing radiative heat transfer modeling in high-temperature liquid salts”, *Nuclear Science and Engineering*, vol. 194, pp. 782–792, 2020. [Online]. Available: <https://doi.org/10.1080/00295639.2020.1723993>.
- [26] W. Derdeyn, M. Abou Dbai, Scarlat, R. O., and M. Trujillo, “FLiBe radiative heat transfer”, in *Transactions of the American Nuclear Society*, vol. 118, Washington, DC, USA, 2018. [Online]. Available: <https://www.osti.gov/biblio/1471715>.
- [27] B. Bendow, “Transparency of bulk halide glasses”, in *Fluoride Glass Fiber Optics*, San Diego, CA, USA: Academic Press, Inc., 1991, pp. 85–140. [Online]. Available: <https://doi.org/10.1016/B978-0-12-044505-9.50007-3>.
- [28] E. S. Chaleff, T. Blue, and P. Sabharwall, “Radiation heat transfer in the molten salt FLiNaK”, *Nuclear Technology*, vol. 196, no. 1, pp. 53–60, 2016. [Online]. Available: <https://doi.org/10.13182/NT16-52>.

- [29] G. Zheng, B. Kelleher, G. Cao, M. Anderson, T. Allen, and K. Sridharan, “Corrosion of 316 stainless steel in high temperature molten Li_2BeF_4 (FLiBe) salt”, *Journal of Nuclear Materials*, vol. 461, pp. 143–150, 2015. [Online]. Available: <https://doi.org/10.1016/j.jnucmat.2015.03.004>.
- [30] F. Rahnema, B. Petrovic, P. Singh, P. Burke, D. Zhang, H. Noorani, X. Sun, G. Yoder, P. Tsvetkov, J. Zhang, and D. Ilas, “The challenges in modeling and simulation of fluoride-salt-cooled high-temperature reactors”, Georgia Institute of Technology, Atlanta, GA, USA, Tech. Rep. CRMP-2017-9-001, 2017. [Online]. Available: <https://smartech.gatech.edu/handle/1853/58808>.
- [31] K. Tasaka, M. Tanaka, H. Ito, K. Katada, K. Watanabe, C. Fineman, D. Bosley, and M. Shiba, “Conceptual design of large scale test facility (LSTF) of ROSA-IV program for PWR small break LOCA integral experiment”, Japan Atomic Energy Research Institute, Tokai, Ibaraki, Japan, Tech. Rep. JAERI-M-9849, 1981. [Online]. Available: https://inis.iaea.org/search/search.aspx?orig_q=RN:13708848.
- [32] G. Loomis, “Summary of the Semiscale program (1965-1986)”, Idaho National Engineering Laboratory, Idaho Falls, ID, USA, Tech. Rep. NUREG/CR-4945, 1987. [Online]. Available: <https://www.osti.gov/servlets/purl/6302855>.
- [33] L. Huddar, J. C. Kendrick, C. Poresky, X. Wang, and P. F. Peterson, “Application of frequency response methods in separate and integral effects tests for molten salt cooled and fueled reactors”, *Nuclear Engineering and Design*, vol. 329, pp. 3–11, 2018. [Online]. Available: <https://doi.org/10.1016/j.nucengdes.2017.11.045>.
- [34] G. E. Wilson, “Historical insights in the development of Best Estimate Plus Uncertainty safety analysis”, *Annals of Nuclear Energy*, vol. 52, pp. 2–9, 2013. [Online]. Available: <https://doi.org/10.1016/j.anucene.2012.03.002>.
- [35] N. Zuber, G. E. Wilson, M. Ishii, W. Wulff, B. Boyack, A. Dukler, P. Griffith, J. Healzer, R. Henry, J. Lehner, S. Levy, F. Moody, M. Pilch, B. Sehgal, B. Spencer, T. Theofanous, and J. Valente, “An integrated structure and scaling methodology for severe accident technical issue resolution: Development of methodology”, *Nuclear Engineering and Design*, vol. 186, pp. 1–21, 1998. [Online]. Available: [https://doi.org/10.1016/S0029-5493\(98\)00215-5](https://doi.org/10.1016/S0029-5493(98)00215-5).
- [36] N. Zuber, “An integrated structure and scaling methodology for severe accident technical issue resolution”, United States Nuclear Regulatory Commission, Washington, DC, USA, Tech. Rep. NUREG/CR-5809, 1991, ch. Appendix D: A Hierarchical, Two-Tiered Scaling Analysis. [Online]. Available: <https://www.nrc.gov/docs/ML0634/ML063400263.pdf>.
- [37] J. N. Reyes Jr. and L. Hochreiter, “Scaling analysis for the OSU AP600 test facility (APEX)”, *Nuclear Engineering and Design*, vol. 186, pp. 53–109, 1998. [Online]. Available: [https://doi.org/10.1016/S0029-5493\(98\)00218-0](https://doi.org/10.1016/S0029-5493(98)00218-0).

- [38] J. N. Reyes, J. Groome, B. G. Woods, E. Young, K. Abel, Y. Yao, and Y. J. Yoo, “Testing of the multi-application small light water reactor (MASLWR) passive safety systems”, *Nuclear Engineering and Design*, vol. 237, pp. 1999–2005, 2007. [Online]. Available: <https://doi.org/10.1016/j.nucengdes.2007.01.014>.
- [39] F. Mascari, G. Vella, B. Woods, and F. D’Auria, “Analyses of the OSU-MASLWR experimental test facility”, *Science and Technology of Nuclear Installations*, 2012. [Online]. Available: <https://doi.org/10.1155/2012/528241>.
- [40] M. Ishii, “Thermally induced flow instabilities in two-phase mixtures in thermal equilibrium”, Ph.D. dissertation, School of Mechanical Engineering, Georgia Institute of Technology, Atlanta, GA, USA, 1971. [Online]. Available: <http://hdl.handle.net/1853/16452>.
- [41] M. Ishii and I. Katoaka, “Scaling laws for thermal-hydraulic system under single phase and two-phase natural circulation”, *Nuclear Engineering and Design*, vol. 81, pp. 411–425, 1984. [Online]. Available: [https://doi.org/10.1016/0029-5493\(84\)90287-5](https://doi.org/10.1016/0029-5493(84)90287-5).
- [42] M. Ishii, S. T. Revankar, T. Leonardi, R. Dowlati, M. Bertodano, I. Babelli, W. Wang, H. Pokharna, V. H. Ransom, R. Viskanta, and J. T. Han, “The three-level scaling approach with application to the purdue university multi-dimensional integral test assembly (PUMA)”, *Nuclear Engineering and Design*, vol. 186, pp. 177–211, 1998. [Online]. Available: [https://doi.org/10.1016/S0029-5493\(98\)00222-2](https://doi.org/10.1016/S0029-5493(98)00222-2).
- [43] M. Ishii, S. Ravankar, R. Dowlati, M. Bertodano, I. Babelli, W. Wang, H. Pokharna, V. Ransom, R. Viskanta, T. Wilmarth, and J. Han, “Scientific design of Purdue University multi-dimensional integral test assembly (PUMA) for GE SBWR”, School of Nuclear Engineering, Purdue University, West Lafayette, IN, USA, Tech. Rep. NUREG/CR-6309, 1996. [Online]. Available: <https://doi.org/10.2172/220555>.
- [44] M. P. Heisler, “Development of scaling requirements for natural convection liquid-metal fast breeder reactor shutdown heat removal test facilities”, *Nuclear Science and Engineering*, vol. 80, pp. 347–359, 1982. [Online]. Available: <https://doi.org/10.13182/nse82-a19819>.
- [45] S. B. Seo, Y. Shin, and I. C. Bang, “Numerical analysis on spatial universality of similarity technique inside molten salt reactor system”, *International Journal of Heat and Mass Transfer*, vol. 116, pp. 569–580, 2018. [Online]. Available: <https://doi.org/10.1016/j.ijheatmasstransfer.2017.09.036>.
- [46] R. O. Scarlat, “Design of complex systems to achieve passive safety: Natural circulation cooling of liquid salt pebble bed reactors”, Ph.D. dissertation, Dept. Nuclear Eng., University of California, Berkeley, Berkeley, CA, USA, 2012. [Online]. Available: escholarship.org/uc/item/2x01b4v0.

- [47] L. Liu, P. Peterson, D. Zhang, I. Johnson, and G. Su, “Scaling and distortion analysis using a simple natural circulation loop for FHR development”, *Applied Thermal Engineering*, vol. 168, 2020. [Online]. Available: <https://doi.org/10.1016/j.applthermaleng.2019.114849>.
- [48] P. Bardet, E. Blandford, M. Fratoni, A. Niquille, E. Greenspan, and P. F. Peterson, “Design, analysis and development of the modular PB-AHTR”, in *Proceedings of the International Congress on Advances in Nuclear Power Plants (ICAPP) 2008*, Anaheim, CA, USA, 2008.
- [49] N. Zweibaum, “Experimental validation of passive safety system models: Application to design and optimization of fluoride-salt-cooled, high-temperature reactors”, Ph.D. dissertation, Dept. Nuclear Eng., University of California, Berkeley, Berkeley, CA, USA, 2015. [Online]. Available: <https://escholarship.org/uc/item/744882bt>.
- [50] N. Zweibaum, Z. Guo, J. C. Kendrick, and P. F. Peterson, “Design of the compact integral effects test facility and validation of best-estimate models for fluoride salt-cooled high-temperature reactors”, *Nuclear Technology*, vol. 196, pp. 641–660, 2016. [Online]. Available: <https://doi.org/10.13182/NT16-15>.
- [51] Kairos Power, “Scaling methodology for the Kairos Power testing program”, Alameda, CA, USA, Tech. Rep. KP-NRC-1903-001, 2019. [Online]. Available: <https://www.nrc.gov/docs/ML1906/ML19066A047.pdf>.
- [52] N. Zweibaum, E. Blandford, C. Gerardi, and P. Peterson, “Scaling methodology for integral effects tests in support of fluoride salt-cooled high-temperature reactor technology”, *Nuclear Science and Engineering*, vol. 194, pp. 793–811, 2020. [Online]. Available: <https://doi.org/10.1080/00295639.2019.1710976>.
- [53] P. A. Kottke, T. P. Ferguson, and A. G. Fedorov, “Scale analysis of combined thermal radiation and convection heat transfer”, *Journal of Heat Transfer*, vol. 126, pp. 250–258, 2004. [Online]. Available: <https://doi.org/10.1115/1.1677409>.
- [54] F. D’Auria and G. Galassi, “Scaling in nuclear reactor system thermal-hydraulics”, *Nuclear Engineering and Design*, vol. 240, pp. 3267–3293, 2010. [Online]. Available: <https://doi.org/10.1016/j.nucengdes.2010.06.010>.
- [55] L. Zou, R. Hu, and A. Charpentier, “SAM code validation using the compact integral effects test (CIET) experimental data”, Argonne National Laboratory, Argonne, IL, USA, Tech. Rep. ANL/NSE-19/11, 2019. [Online]. Available: <https://doi.org/10.2172/1571236>.
- [56] J. Dirker and J. Meyer, “Convective heat transfer coefficients in concentric annuli”, *Heat Transfer Engineering*, vol. 26, no. 2, pp. 38–44, 2005. [Online]. Available: <https://doi.org/10.1080/01457630590897097>.
- [57] V. Gnielinski, “Heat transfer coefficients for turbulent flow in concentric annular ducts”, *Heat Transfer Engineering*, vol. 30, no. 6, pp. 431–436, 2009. [Online]. Available: <https://doi.org/10.1080/01457630802528661>.

- [58] J. Lu, S. He, J. Liang, J. Ding, and J. Yang, “Convective heat transfer in the laminar–turbulent transition region of molten salt in annular passage”, *Experimental Thermal and Fluid Science*, vol. 51, pp. 71–76, 2013. [Online]. Available: <https://doi.org/10.1016/j.expthermflusci.2013.07.002>.
- [59] W. R. van Zyl, J. Dirker, and J. P. Meyer, “Single-phase convective heat transfer and pressure drop coefficients in concentric annuli”, *Heat Transfer Engineering*, vol. 34, no. 13, pp. 1112–1123, 2013. [Online]. Available: <https://doi.org/10.1080/01457632.2013.763550>.
- [60] W. A. Summers, Y. T. Shah, and G. E. Klinzing, “Heat-transfer parameters for an annular packed bed”, *Industrial & Engineering Chemistry Research*, vol. 28, no. 5, pp. 611–618, 1989. [Online]. Available: <https://pubs.acs.org/doi/pdf/10.1021/ie00089a018>.
- [61] L. Liu, D. Zhang, L. Li, Y. Yang, C. Wang, S. Qiu, and G. Su, “Experimental investigation of flow and convective heat transfer on a high-prandtl-number fluid through the nuclear reactor pebble bed core”, *Applied Thermal Engineering*, vol. 145, pp. 48–57, 2018. [Online]. Available: <https://doi.org/10.1016/j.applthermaleng.2018.09.017>.
- [62] W. Wulff, “Scaling of thermohydraulic systems”, *Nuclear Engineering and Design*, vol. 163, pp. 359–395, 1996. [Online]. Available: [https://doi.org/10.1016/0029-5493\(96\)01232-0](https://doi.org/10.1016/0029-5493(96)01232-0).
- [63] I. Johnson, R. Hu, L. Zou, and P. Peterson, “Solid-to-fluid radiative heat transfer modeling for System Analysis Module”, in *Proceedings of the 2021 International Congress on Advances in Nuclear Power Plants (ICAPP)*, Abu Dhabi, UAE, 2021.
- [64] R. Hu, G. Hu, L. Zou, G. Zhang, B. Hollrah, and M. Gorman, “SAM developments to support transient safety analysis of advanced non-LWRs”, Argonne National Laboratory, Argonne, IL, USA, Tech. Rep. ANL/NSE-19/31, 2019. [Online]. Available: <https://doi.org/10.2172/1577423>.
- [65] United States Nuclear Regulatory Commission, “NRC non-light water reactor (non-LWR) vision and strategy, volume 1 – computer code suite for non-LWR plant systems analysis”, Washington, DC, USA, Tech. Rep. ML20030A176, 2020. [Online]. Available: <https://www.nrc.gov/docs/ML2003/ML20030A176.pdf>.
- [66] R. Hu, G. Hu, L. Zou, A. Klingberg, T. Fei, and D. Nunez, “FY20 SAM code developments and validations for transient safety analysis of advanced non-LWRs”, Argonne, IL, USA, Tech. Rep. ANL/NSE-20/50, 2020. [Online]. Available: <https://doi.org/10.2172/1716517>.
- [67] R. Hu, “SAM theory manual”, Argonne National Laboratory, Argonne, IL, USA, Tech. Rep. ANL/NE-17/4, 2017. [Online]. Available: <https://doi.org/10.2172/1353375>.

- [68] C. J. Permann, D. R. Gaston, D. Andrš, R. W. Carlsen, F. Kong, A. D. Lindsay, J. M. Miller, J. W. Peterson, A. E. Slaughter, R. H. Stogner, and R. C. Martineau, “MOOSE: Enabling massively parallel multiphysics simulation”, *SoftwareX*, vol. 11, p. 100430, 2020. [Online]. Available: <https://doi.org/10.1016/j.softx.2020.100430>.
- [69] T. I. Zohdi, *A Finite Element Primer for Beginners*, 2nd ed. Cham, Switzerland: Springer, 2018. [Online]. Available: <https://doi.org/10.1007/978-3-319-70428-9>.
- [70] H. Zhao, L. Fick, J. Herter, and B. Haugh, “Overview of Kairos Power systems code KP-SAM development”, in *Proceedings of 18th International Topical Meeting on Nuclear Reactor Thermal Hydraulics (NURETH)*, Portland, OR, USA, 2019.
- [71] L. Zou, G. Hu, D. O’Grady, and R. Hu, “Code validation of SAM using natural-circulation experimental data from the compact integral effects test (CIET) facility”, *Nuclear Engineering and Design*, vol. 377, 2021. [Online]. Available: <https://doi.org/10.1016/j.nucengdes.2021.111144>.
- [72] D. O’Grady, T. Mui, A. Lee, L. Zou, G. Hu, and R. Hu, “SAM code enhancement, validation, and reference model development for fluoride-salt-cooled high- temperature reactors”, Argonne National Laboratory, Argonne, IL, USA, Tech. Rep. ANL/NSE-21/15, 2021. [Online]. Available: <https://doi.org/10.2172/1781830>.
- [73] G. Hu, D. O’Grady, L. Zou, and R. Hu, “Development of a reference model for molten-salt-cooled pebble-bed reactor using SAM”, Argonne National Laboratory, Argonne, IL, USA, Tech. Rep. ANL/NSE-20/31, 2020. [Online]. Available: <https://doi.org/10.2172/1674975>.
- [74] C. Andreades, A. T. Cisneros, J. K. Choi, A. Y. Chong, M. Fratoni, S. Hong, L. R. Huddar, K. D. Huff, J. Kendrick, D. L. Krumwiede, M. R. Laufer, M. Munk, R. O. Scarlat, N. Zweibaum, E. Greenspan, X. Wang, and P. F. Peterson, “Design summary of the Mark-I pebble-bed, fluoride salt-cooled, high-temperature reactor commercial power plant”, *Nuclear Technology*, vol. 195, pp. 223–238, 2016. [Online]. Available: <https://doi.org/10.13182/NT16-2>.
- [75] United States Nuclear Regulatory Commission, “TRACE V5.0 user’s manual — volume 2: Modeling guidelines”, Washington, DC, USA, Tech. Rep. ML120060402, 2008. [Online]. Available: <https://www.nrc.gov/docs/ML1200/ML120060402.pdf>.
- [76] ———, “TRACE V5.0 theory manual — field equations, solution methods, and physical models”, Washington, DC, USA, Tech. Rep. ML120060218, 2008. [Online]. Available: <https://www.nrc.gov/docs/ML1200/ML120060218.pdf>.
- [77] The RELAP5 Development Team, “RELAP5/MOD3 code manual — volume 1: Code structure, system models, and solution methods”, Idaho National Laboratory, Idaho Falls, ID, USA, Tech. Rep. INEL-95/0174-Vol.1, 1995. [Online]. Available: <https://doi.org/10.2172/105079>.

- [78] E. S. Chaleff, “The radiative heat transfer properties of molten salts and their relevance to the design of advanced reactors”, Ph.D. dissertation, The Ohio State University, 2016.
- [79] M. Abou Dbai, R. O. Scarlat, and M. F. Trujillo, “Radiative heat transfer in flibe molten salt participating medium in a vertical heated tube under forced and mixed convection laminar flows”, *Nuclear Engineering and Design*, vol. 368, 2020. [Online]. Available: <https://doi.org/10.1016/j.nucengdes.2020.110775>.
- [80] S. Zhang and X. Sun, “Convective and radiative heat transfer in molten salts”, *Nuclear Technology*, vol. 206, no. 11, pp. 1721–1739, 2020. [Online]. Available: <https://doi.org/10.1080/00295450.2020.1749481>.
- [81] H. Zhao (Kairos Power), private communication, Jul. 2019.
- [82] K. M. Andersen and S. Hadvig, “Geometric mean beam lengths for the space between two coaxial cylinders”, *Journal of Heat Transfer*, vol. 111, no. 3, pp. 811–813, 1989. [Online]. Available: <https://doi.org/10.1115/1.3250757>.
- [83] W. W. Yuen, “Evaluation of the geometric mean transmittance and total absorptance for two-dimensional systems”, *International Journal of Heat and Mass Transfer*, vol. 25, no. 7, pp. 1069–1071, 1982. [Online]. Available: [https://doi.org/10.1016/0017-9310\(82\)90083-7](https://doi.org/10.1016/0017-9310(82)90083-7).
- [84] R. D. Cess and S. N. Tiwari, “Infrared radiative energy transfer in gases”, *Advances in Heat Transfer*, vol. 8, pp. 229–283, 1972. [Online]. Available: [https://doi.org/10.1016/S0065-2717\(08\)70040-6](https://doi.org/10.1016/S0065-2717(08)70040-6).
- [85] I. Johnson, “Development of a SAM component for solid-to-fluid radiative heat transfer modeling”, unpublished internship report, 2019.
- [86] J. J. Valencia and P. N. Queded, “Thermophysical properties”, *ASM Handbook*, vol. 15, pp. 468–481, 2008.
- [87] J. P. Young, “Absorption spectra of several 3d transition metal ions in molten fluoride solution”, *Inorganic Chemistry*, vol. 8, no. 4, pp. 825–827, 1969. [Online]. Available: <https://doi.org/10.1021/ic50074a025>.
- [88] R. Hu, L. Zou, and G. Hu, “SAM user’s guide”, Argonne National Laboratory, Argonne, IL, USA, Tech. Rep. ANL/NSE-19/18, 2019. [Online]. Available: <https://doi.org/10.2172/1559541>.
- [89] R. Hu, “Verification and validation plan for the SFR System Analysis Module”, Argonne National Laboratory, Argonne, IL, USA, Tech. Rep. ANL/NE-14/14, 2014. [Online]. Available: <https://doi.org/10.2172/1168234>.
- [90] S. Ergun and A. Orning, “Fluid flow through packed columns”, *Chemical Engineering Progress*, vol. 48, pp. 89–94, 1952.

- [91] E. Foumeny, F. Benyahia, J. Castro, H. Moallemi, and S. Roshani, “Correlations of pressure drop in packed beds taking into account the effect of confining wall”, *International Journal of Heat and Mass Transfer*, vol. 36, pp. 536–540, 1993. [Online]. Available: [https://doi.org/10.1016/0017-9310\(93\)80028-S](https://doi.org/10.1016/0017-9310(93)80028-S).